Advanced light-sheet and structured illumination microscopy techniques for neuroscience and disease diagnosis

Jonathan NYLK

University of
St Andrews

This thesis is submitted in partial fulfilment for the degree of

Doctor of Philosophy

at the

University of St Andrews

June, 2016

UNIVERSITY OF ST ANDREWS

Abstract

Faculty of Science

Department of Physics and Astronomy

Doctor of Philosophy

Advanced light-sheet and structured illumination microscopy techniques for neuroscience and disease diagnosis

by Jonathan NYLK

Optical microscopy is a cornerstone of biomedical research. Advances in optical techniques enable specific, high resolution, sterile, and biologically compatible imaging. In particular, beam shaping has been used to tailor microscopy techniques to enhance microscope performance. The aim of this Thesis is to investigate the use of novel beam shaping techniques in emerging optical microscopy methods, and to apply these methods in biomedicine.

To overcome the challenges associated with high resolution imaging of large specimens, the use of Airy beams and related techniques are applied to light-sheet microscopy. This approach increases the field-of-view that can be imaged at high resolution by over an order of magnitude compared to standard Gaussian beam based light-sheet microscopy, has reduced phototoxicity, and can be implemented with a low-cost optical system. Advanced implementations show promise for imaging at depth within turbid tissue, in particular for neuroscience.

Super-resolution microscopy techniques enhance the spatial resolution of optical methods. Structured illumination microscopy is investigated as an alternative for electron microscopy in disease diagnosis, capable of visualising pathologically relevant features of kidney disease. Separately, compact optical manipulation methods are developed with the aim of adding functionality to super-resolution techniques.

Declaration of Authorship

Candidate's declarations:

I, Jonathan NYLK, declare that this thesis, which is approximately 50,000 words in length, has been written by me, and that it is the record of work carried out by me, or principally by myself in collaboration with others as acknowledged, and that it has not been submitted in any previous application for a higher degree.

I was admitted as a research student in June 2012 and as a candidate for the degree of Doctor of Philosophy in June 2012; the higher study for which this is a record was carried out in the University of St Andrews between 2012 and 2016.

Signed:

_____

Date:

_____

Supervisor's declarations:

I hereby certify that the candidate has fulfilled the conditions of the Resolution and Regulations appropriate for the degree of Doctor of Philosophy in the University of St Andrews and that the candidate is qualified to submit this thesis in application for that degree.

Signature of supervisor:

_____

Date:

_____

Permission for publication:

In submitting this thesis to the University of St Andrews I understand that I am giving permission for it to be made available for use in accordance with the regulations of the University Library for the time being in force, subject to any copyright vested in the work not being affected thereby. I also understand that the title and the abstract will be published, and that a copy of the work may be made and supplied to any bona fide library or research worker, that my thesis will be electronically accessible for personal or research use unless exempt by award of an embargo as requested below, and that the library has the right to migrate my thesis into new electronic forms as required to ensure continued access to the thesis. I have obtained any third-party copyright permissions that may be required in order to allow such access and migration, or have requested the appropriate embargo below.

The following is an agreed request by candidate and supervisor regarding the publication of this thesis:

PRINTED COPY

Embargo on all or part of print copy for a period of 2 years on the following ground(s):

- Publication would preclude future publication

ELECTRONIC COPY

Embargo on all or part of electronic copy for a period of 2 years on the following ground(s):

- Publication would preclude future publication

Signature of candidate:

_____

Signature of supervisor:

_____

Date:

_____

ABSTRACT AND TITLE EMBARGOES

An embargo on the full text copy of your thesis in the electronic and printed formats will be granted automatically in the first instance. This embargo includes the abstract and title except that the title will be used in the graduation booklet.

If you have selected an embargo option please indicate below if you wish to allow the thesis abstract and/or title to be published. If you do not complete the section below the title and abstract will remain embargoed along with the full text of the thesis.

a) I agree to the title and abstract being published YES/~~NO~~
b) I require an embargo on abstract ~~YES~~/NO
c) I require an embargo on title ~~YES~~/NO

05/06/17

Date ..... signature of candidate ..... signature of supervisor .....

Acknowledgements

I would like to thank my supervisors, Kishan and Frank, for their invaluable advice and support throughout my PhD. I would also like to thank my colleagues for their support, both academically and sociably. Those who were directly linked to research projects are acknowledged at the end of relevant Chapters, but some of the best revelations occur during conversations over coffee.

Special thanks go to my family, my Mum, Dad, and wife, Emma, for their support and belief in me.

List of Abbreviations

1D	one-**D**imensional
1PE	one/single-**P**hoton **E**xcitation
2D	two-**D**imensional
2PE	two-**P**hoton **E**xcitation
3D	three-**D**imensional
4D	four-**D**imensional
6D	six-**D**imensional
AAV	**A**deno**A**ssociated **V**irus/**V**iral
AO	**A**daptive **O**ptics
AOD	**A**cousto-**O**ptic **D**eflector
APC	**A**ntigen **P**resenting **C**ell
APS	**A**mmonium **P**er**S**ulfate
BB-LSM	**B**essel **B**eam based **L**ight-**S**heet **M**icroscopy/**M**icroscope
Bessel-CS	**Bessel** beam **C**onfocal line **S**canning
Bessel-SI-OS	**Bessel** beam **S**tructured **I**llumination for **O**ptical **S**ectioning
Bessel-SI-SR	**Bessel** beam **S**tructured **I**llumination for **S**uper **R**esolution
BSA	**B**ovine **S**erum **A**lbumin
COM	**C**entre-**O**f-**M**ass
cSMAC	**c**entral **S**upra-**M**olecular **A**ctivation **R**egion
cw	**c**ontinuous **w**ave
DAPI	4',6-**D**i**A**midino-2-**P**henyl**I**ndole
DM	**D**eformable **M**irror
DMD	**D**igital **M**icromirror **D**evice
DMEM	**D**ulbecco's **M**odified **E**agle's **M**edium
DMSO	**D**i**M**ethyl **S**ulf**O**xide
DNA	**D**eoxyribo**N**ucleic **A**cid
DNase	**D**eoxyribo**N**ucle**ase**
DOF	**D**epth-**O**f-**F**ocus
DSLM	**D**igitally **S**canned **L**ight-sheet **M**icroscopy/**M**icroscope
dSMAC	**d**istal **S**upra-**M**olecular **A**ctivation **R**egion
EELS	**E**lectron **E**nergy **L**oss **S**pectroscopy
EM	**E**lectron **M**icroscopy/**M**icroscope
(EM)CCD	(**E**lectron **M**ultiplied) **C**harge-**C**oupled **D**evice
f-actin	**f**ilamentous **actin**
FCS	**F**etal **C**alf **S**erum
FITC	**F**luorescein **I**so**T**hio**C**yanate
FOV	**F**ield-**O**f-**V**iew
FP	**F**oot **P**rocess
FRET	**F**örster **R**esonance **E**nergy **T**ransfer
FWHM	**F**ull **W**idth at **H**alf **M**aximum
GB	**G**iga**B**yte

GBM	**G**lomerular **B**asement **M**embrane
GFP	**G**reen **F**luorescent **P**rotein
GRIN	**GR**adient refractive **IN**dex
HIV	**H**uman **I**mmunodeficiency **V**irus
IS	**I**mmunological **S**ynapse
LFM	**L**ight **F**ield **M**icroscopy/**M**icroscope
LMP	**L**ow **M**elting **P**oint
LSM	**L**ight-**S**heet **M**icroscopy/**M**icroscope
MHC	**M**ajor **H**istocompatibility **C**omplex
MM	**M**ulti-**M**ode
MSC	**M**esenchymal **S**tem **C**ell
mSPIM	**m**ultidirectional **S**elective/**S**ingle **P**lane **I**llumination **M**icroscopy/**M**icroscope
MTF	**M**odulation **T**ransfer **F**unction
NA	**N**umerical **A**perture
ND	**N**eutral **D**ensity
NGS	**N**ormal **G**oat **S**erum
NL-SIM	**N**on-**L**inear **S**tructured **I**llumination **M**icroscopy/**M**icroscope
nPE	multi-**P**hoton **E**xcitation
NSOM	**N**ear-field **S**canning **O**ptical **M**icroscopy/**M**icroscope
OCT	**O**ptical **C**oherence **T**omography
OFT	**O**ptical **F**ibre **T**rap
OTF	**O**ptical **T**ransfer **F**unction
PAA	**P**oly(**A**cryl**A**mide)
PA-FP	**P**hoto-**A**ctivatable **F**luorescent **P**rotein
PA-GFP	**P**hoto-**A**ctivatable **G**reen Fluorescent **P**rotein
PALM	**P**hoto-**A**ctivation **L**ocalisation **M**icroscopy/**M**icroscope
PBS	**P**hosphate **B**uffered **S**aline
PC	**P**rincipal **C**omponent
PCA	**P**rincipal **C**omponent **A**nalysis
PDMS	**P**oly(**D**i**M**ethyl**S**iloxane)
PE	**P**oly(**E**thylene)
PFA	**P**ara**F**orm**A**ldehyde
PI	**P**ropidium **I**odide
PSD	**P**ower **S**pectral **D**ensity
PS-FP	**P**hoto-**S**witchable **F**luorescent **P**rotein
pSMAC	**p**eripheral **S**upra-**M**olecular **A**ctivation **R**egion
QPD	**Q**uadrant **P**hoto**D**iode
RESOLFT	**RE**versible **S**aturable **O**ptical **F**luorescence **T**ransitions
RNase	**R**ibo**N**ucle**ase**
ROI	**R**egion **O**f **I**nterest
RT	**R**oom **T**emperature
SCAPE	**S**wept **C**onfocally-**A**ligned **P**lanar **E**xcitation
sCMOS	**s**cientific **C**omplimentary **M**etal-**O**xide **S**emiconductor
SEM	**S**canning **E**lectron **M**icroscopy/**M**icroscope
SHG	**S**econd **H**armonic **G**eneration
SIM	**S**tructured **I**llumination **M**icroscopy/**M**icroscope
SLM	**S**patial **L**ight **M**odulator
SM	**S**ingle-**M**ode
SMA	**S**ub**M**iniature version **A**
SMAC	**S**upra-**M**olecular **A**ctivation **R**egion

SNR	**S**ignal-to-**N**oise **R**atio
SPIM	**S**elective/**S**ingle **P**lane **I**llumination **M**icroscopy/**M**icroscope
SR	**S**uper-**R**esolution
STED	**ST**imulated **E**mission **D**epletion
STORM	**S**tochastic **O**ptical **R**econstruction **M**icroscopy/**M**icroscope
TCR	**T**-**C**ell **R**eceptor
TDE	2,2′-**T**hio**D**i**E**thanol
TEM	**T**ransmission **E**lectron **M**icroscopy/**M**icroscope
THG	**T**hird **H**armonic **G**eneration
w.d.	**w**orking **d**istance
YFP	**Y**ellow **F**luorescent **P**rotein

Publications

Peer-reviewed publications

1. **Nylk J.**, Preciado, M. A., Mazilu, M., and Dholakia, K., "Attenuation compensation toolbox (ACT) for light-sheet microscopy with propagation-invariant beams" (in preparation).

2. **Nylk, J.**, McCluskey, K., Aggarwal, S., Tello, J., and Dholakia, K., "Characterization of enhanced imaging performance of Airy light-sheet microscopy in turbid tissue" (in preparation).

3. Pullman, J. M., **Nylk, J.**, Campbell, E. C., Gunn-Moore, F. J., Prystowsky, M. B., and Dholakia, K., "Visualization of podocyte substructure with structured illumination microscopy (SIM): a new approach to nephrotic disease" Biomedical Optics Express **7**(2), 302-311 (2016).

4. **Nylk, J.**, Kristensen, M. V. G., Mazilu, M., Thayil, A. K., Mitchell, C. A., Campbell, E. C., Powis, S. J., Gunn-Moore, F. J., and Dholakia, K., "Development of a graded index microlens based fibre optical trap and its characterization using principal component analysis", Biomedical Optics Express **6**(4), 1512-1519 (2015).

5. Yang, Z., Prokopas, M., **Nylk J.**, Coll-Lladó, C., Gunn-Moore, F. J., Ferrier, D. E. K., Vettenburg, T., and Dholakia, K., "A compact Airy beam light-sheet microscope with a tilted cylindircal lens", Biomedical Optics Express **5**(10), 3434-3442 (2014).

6. Vettenburg, T., Dalgarno, H. I. C., **Nylk, J.**, Coll-Lladó, C., Ferrier, D. E. K., Čižmár, T., Gunn-Moore, F. J., and Dholakia, K., "Light-sheet microscopy using an Airy beam", Nature Methods **11**(5), 541-544 (2014).

Conference proceedings

7. **Nylk, J.**, Yang, Z., Piksarv, P., Preciado, M. A. Mazilu, M., Vettenburg, T., Coll-Lladó, C., Ferrier, D. E. K., Čižmár, T., Gunn-Moore, F. J., and Dholakia, K., "Airy Beams for Light-sheet Microscopy", B06.P1 (poster) - Deep Tissue Imaging and Light Sheet Microsocpy, Microscopy and Microanalysis (2015).

8. **Nylk, J.**, Vettenburg, T., Yang, Z., Dalgarno, H. I. C., Coll-Lladó, C., Ferrier, D. E. K., Čižmár, T., Gunn-Moore, F. J., and Dholakia, K., "Shaped light for imaging and manipulation" (invited), Proc. Biophotonics III, Advanced Laser Technologies (2014).

9. **Nylk, J.**, Mitchell, C., Vettenburg, T., Gunn-Moore, F. J., and Dholakia, K., "Wavefront shaping of a Bessel-light field enhances light sheet microscopy with scattered light", Proc. SPIE 8949, Three-Dimensional and Multidimensional Microscopy: Image Acquisition and Processing XXI, 89490V (2014).

Contents

List of Figures

For Fiona, my daughter.

This was my contribution to biomedical science at the time of your birth. I hope it will be interesting to look back on.

Chapter 1

Introduction

1.1 Preface

For centuries, optical imaging has been a crucial tool for biomedical research, allowing observation of the constituent building blocks of life, cells, and their dynamic processes. Optical imaging enables contact free imaging with good spatial and temporal resolution, a wide range of bio-compatible contrast agents exist, and is ubiquitous in virtually all biomedical research laboratories.

When other biomedical imaging methods are considered, it is perhaps surprising that optical microscopy is still so prevalent. Electron microscopy (EM) has superior resolution when compared to light microscopy simply due to the higher energy, and therefore shorter wavelengths, associated with electrons rather than photons. Sub-nanometre resolution can be achieved by EM whereas optical techniques are diffraction limited to a resolution of about 200nm. EM additionally benefits from newly discovered genetically-encoded contrast agents [1, 2] and multi-colour imaging [3], areas in which EM has previously struggled. However, EM must be performed in a vacuum which necessitates dead and desiccated samples and prohibits live imaging. This desiccation removes proteins of interest from their natural environment, water, and may form structures that are functionally different from their natural conformations. Even if the challenges of vacuum and desiccation were overcome, contrast agents required for EM typically contain highly toxic heavy metals. The short wavelength of electrons provides high resolution, but also limits how much EM can penetrate into samples, EM requires very thin samples, often sectioned at a thickness on the order of 100nm.

At the other end of the spectrum is ultrasound imaging. Ultrasound imaging

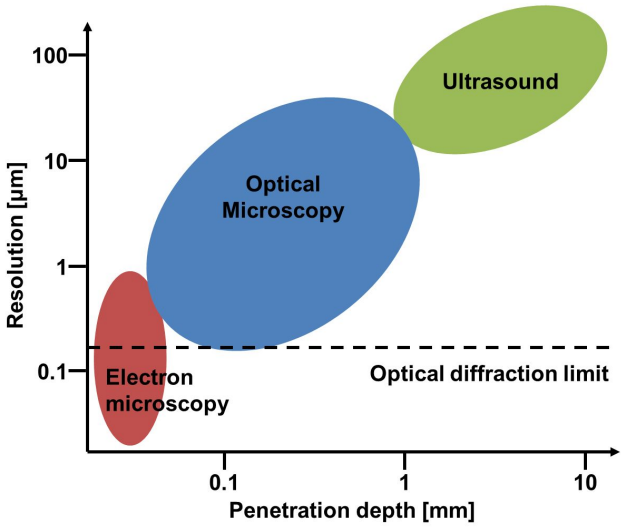

FIGURE 1.1: Illustration of ultrasound (green), optical (blue), and electron (red) imaging domains showing resolution and penetration depth from the surface of a specimen.

has relatively poor resolution but has excellent penetration depth, again owing to the greatly reduced wavelength of ultrasound waves compared to visible light. Ultrasound imaging allows visualisation of structures deep within the body, obscured by several layers of tissue and even whole organs without the need for surgery. Ultrasound imaging is therefore non-invasive, requiring only light contact with the patient in order to image within the body *in vivo*.

Optical microscopy occupies the middle ground, as shown in Fig. 1.1. The resolution of an optical microscope is limited by diffraction to about 200nm and so is suitable for observation of small organisms, organs (*ex vivo*), single cells, and some sub-cellular components. Light microscopy also retains some penetration depth, typically allowing observation through several cellular layers or even multiple tissue layers. As such, optical microscopy can also be non-invasive in that it can observe cell cultures without perturbation and superficial layers of organs can be observed without surgical incisions or sectioning. Light exposure can damage biological matter, but this effect is low across the visible spectrum and prolonged observation is possible. Additionally, a wide range of bio-compatible and highly specific contrast agents (such as fluorescent labels) exist.

However, optical microscopy has existed for hundreds of years, and microscope design has remained largely unchanged in that time. It begs the question:

What is the role of modern optical microscopy?

It is the ethos of this Thesis that optical microscopy is still an essential and relevant tool, particularly for live imaging where both high-resolution and good penetration depth are required. When imaging living specimens, the imaging method must be fast enough to capture a large enough view of the structure of the specimen without artefacts from motion blur, and the act of imaging must not harm the specimen. Modern optical microscopy requires photonic innovation to push back the boundaries of traditional microscopy.

Precise control of optical properties, such as wavelength, intensity, phase, and polarisation, collectively referred to as beam shaping is available through various techniques and allows optical microscopy techniques to be tuned and optimised, or even for entirely new techniques to surface. Figure 1.2 illustrates the extension of the optical imaging domain by selected prominent beam shaping techniques (discussed in detail in Chapter 2). The ultimate goal is to steer optical imaging techniques toward the lower right-hand region of this graph, realising an imaging modality capable of excellent resolution at great depth within a specimen. This would ultimately enable superior imaging across a range of length scales required for understanding of complex biological systems. The human brain features organised structure on the order of centimetres, down to individual synaptic connections between neurons on the order of 100s of nanometres, and further still to molecular distributions at synaptic connections on the nanoscale. All levels of structure must be visualised to understand the function of the brain, and will require such imaging techniques.

Light-sheet microscopy (LSM) shows promise as a fast technique for imaging large volumes at depth and does so in a very efficient way, thereby minimising damage to the specimen by unnecessary light exposure. Figure 1.2 shows LSM extending to the right, to greater imaging depth with reasonable resolution. Additional beam shaping techniques in combination with LSM are increasing the resolution of this method and can bring LSM closer to the goal region.

Super-resolution (SR) microscopy techniques are pushing the optical domain down, achieving resolution beyond the diffraction limit. SR microscopy techniques have the

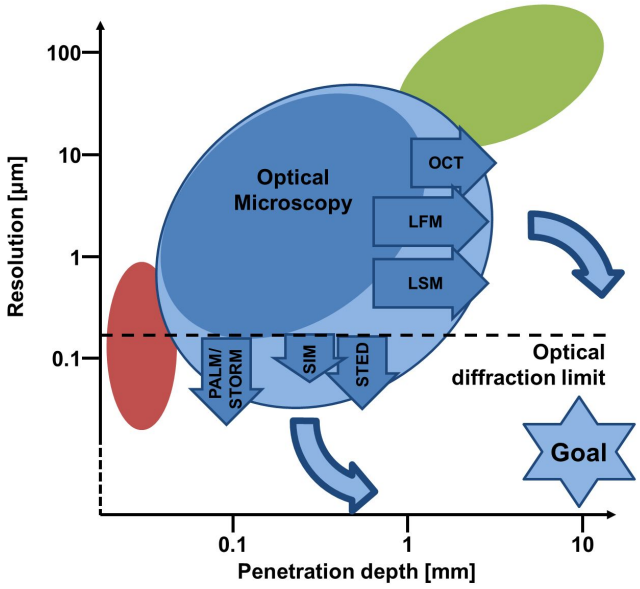

FIGURE 1.2: Illustration of the extension of optical techniques by beam shaping. Plot of resolution and penetration depth from the surface of a specimen. Approximate scope of ultrasound (green), optical (blue), and electron (red) imaging domains. Labelled arrows illustrate the new regions unlocked by each respective technique. OCT: Optical coherence tomography; LFM: Light field microscopy; LSM: Light-sheet microscopy; PALM: Photo activated localisation microscopy; STORM: Stochastic optical reconstruction microscopy; SIM: structured illumination microscopy; STED: stimulated emission depletion microscopy

potential to displace EM in particular applications, particularly because these techniques can be applied to living samples but also due to their greatly simplified sample preparation stages and the ability to image much larger intact volumes.

Separately, optical techniques for the manipulation of biological matter have been developed. Optical trapping enables non-contact, precise, three-dimensional (3D) positioning of small particles such as individual cells and can also be utilised to measure microscopic forces. Intense focussed laser beams can also be employed to precisely cut selected sections of tissue or to create transient holes, allowing the passage of foreign material into cells. These techniques can be complimentary to imaging techniques and combination of these techniques with advanced microscopy platforms adds a whole new dimension of functionality and enables truly ground-breaking studies.

1.2 Synopsis

This thesis describes the use of beam shaping in optical microscopy and optical manipulation, and the combination of such techniques for advanced functional imaging. Advanced wavefront shaping techniques are applied to extend the volumetric imaging capability of high-resolution light-sheet microscopy (LSM) and applied to brain imaging studies. Structured illumination microscopy (SIM) and optical manipulation are considered and a compact optical trapping system is developed and integrating into a microscope with SIM capability.

Chapter 2 introduces volumetric imaging techniques, in particular LSM and existing beam shaping approaches to enhance LSM, before discussing a number of prominent super resolution (SR) microscopy techniques. SIM is identified as an ideal SR technique for live imaging and is discussed in more detail. Chapter 3 covers background literature on the use of optical manipulation, particularly in combination with advanced microscopy techniques, and the calibration of optical traps.

Chapters 4 - 6 discuss new beam shaping innovations in LSM. Chapter 4 introduces the use of an Airy beam for light-sheet illumination to facilitate high resolution imaging over large volumes. A full theoretical analysis is performed and the optical system is designed, constructed and tested. The Airy LSM is applied to the topic of brain imaging in Chapter 5, the performance of standard and Airy light-sheet illumination schemes is analysed in both native and optically cleared tissue. Chapter 6 details advanced beam shaping techniques to compliment Airy LSM. Controlled aberrations from simple optical elements are exploited for low-cost implementations of Airy LSM, widening the availability of the technique. Separately, attenuation compensation techniques are investigated to counteract intensity loss of the Airy light-sheet on propagation within turbid media.

Chapter 7 turns to SR imaging, investigating the use of SIM for the rapid diagnosis of nephrotic disease from kidney biopsies. Chapter 8 details the design and characterisation of a compact optical trapping system based on a high quality gradient refractive index (GRIN) lens, the integration of this compact trapping solution into a SR microscope, and the demonstration of its use for biomedical applications.

Chapter 9 summarises and concludes on the results presented in this Thesis, discussing ways to expand upon and improve the investigations performed.

Chapter 2

Optical imaging in the biomedical sciences

2.1 Introduction

Optical imaging has enabled many powerful studies in biomedicine. For instance, optical techniques have facilitated observation of human immunodeficiency virus (HIV) transfer between cells [4], the separation of individual chromatids during cell division [5], transient activity throughout the whole brain of a larval zebrafish [6], and neuronal activity throughout an entire worm (*Caenorhabditis elegans*) [7], and many other powerful studies.

This Chapter will introduce basic principles of optical microscopy, describing Abbe's theory of image formation which defines the limitations of resolution, laser beam propagation, and the concept of fluorescence microscopy. Although many of the discussed techniques may be applied to other contrast mechanisms, fluorescence microscopy is particularly prevalent in the biomedical sciences and all techniques discussed will be discussed in the primary context of fluorescence imaging. Existing techniques for volumetric microscopy are introduced and discussed, from which LSM is selected as a technique for more investigation. Similarly, SR techniques are introduced before selecting and focusing on SIM as a technique of merit for live imaging.

2.2 Principles of optical microscopy

This section introduces important concepts in microscopy which underpin the work presented in this Thesis. Resolution is an important metric to quantify microscope performance and is introduced with Abbe's theory of image formation. This is an important concept in beam shaping and is discussed and compared to propagation characteristics of Gaussian and non-Gaussian light modes. The principle of fluorescence is introduced which is a foundation for all microscopy methods discussed in this Thesis, and finally, a description of resolution in the Fourier domain is introduced.

2.2.1 Abbe's theory of image formation and the diffraction limit

The first modern theory of image formation was put forward by Abbe in 1873 [8] and has influenced microscope design ever since. In this theory, fundamental limits were set out that predicted the best resolution that could be achieved with an optical microscope. Today, imaging techniques exist that beat this so-called diffraction limit. These techniques, some of which will be covered in later chapters, however do not break the diffraction limit, they bend it. Even in the age of SR microscopy, Abbe's theory of image formation is as relevant and important as it was in 1873 and is outlined below.

It can be shown that a lens performs a Fourier transform of the electric field distribution at its focal plane. The finite extent of the lens, however, means that the Fourier transform is band-limited and acts as a spatial low-pass filter.

Resolution is defined by considering the image of a infinitesimal point like object (a Dirac delta-function), called the point-spread function (PSF). The Fourier transform of the delta-function is constant but the lens truncates this, yielding a top-hat function. Re-imaging the captured field results in a sinc function and a sinc squared intensity profile, called an Airy disk.

From this understanding, Abbe determined the minimum lateral, $r_{x,y}$, and axial, r_z, size of feature that could be resolved by a microscope to be:

$$r_{x,y} = \frac{\lambda}{2\,\mathrm{NA}} \tag{2.1}$$

$$r_z = \frac{2\lambda n}{\mathrm{NA}^2} \tag{2.2}$$

where λ is the wavelength of light in vacuum and $\mathrm{NA} = n\sin(\theta)$ is the numerical aperture, a dimensionless figure of merit which describes the collection efficiency of a lens where n is the refractive index of the medium at the object side of the lens and θ is the half angle which defines the acceptance cone of the lens [9, 10]. Abbe's resolution limit, or diffraction limit, given by equations (2.1) and (2.2) are defined as the radius of the first intensity minimum of the Airy disk. This definition bounds 83.8% of the intensity spread out over the Airy disk.

There are many definitions for resolution that rely on different assumptions [11] but many of these are relative measurements. Abbe's criteria describes an isolated point and is an absolute measurement.

2.2.2 Gaussian beams

Since the invention of the laser in 1960, the landscape of microscopy techniques has evolved rapidly. The unique properties of the laser; high intensity, spatial and temporal coherence, and monochromaticity, have impacted greatly on microscopy techniques. The high intensities lasers can provide reduce exposure times and the energy densities can be large enough, particularly with ultrashort pulsed lasers, to induce nonlinear effects such as second [12, 13] and third harmonic generation [14] (SHG and THG respectively), and multi-photon excitation (nPE) fluorescence [15–17]. The high degree of spatial coherence and the monochromatic nature of laser light allow precise control of the beam wavefront and has enabled a wide range of beam shaping techniques to impact on microscopy [18–23].

The light emitted from a laser is generally a fundamental Gaussian mode. The Gaussian beam is a solution of the paraxial wave equation [24]. In this scenario it is assumed that, in the ray optics approximation of the propagating beam, all rays propagate close to the optic axis and at relatively small angles to the optic axis. The time-independent electric field distribution of a Gaussian beam propagating along the

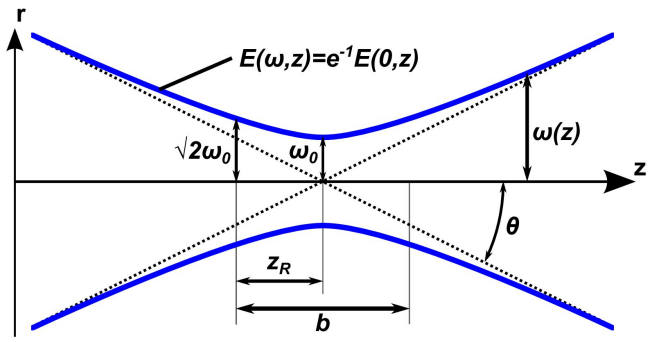

FIGURE 2.1: Propagation of Gaussian beam. Beam width of electric field (blue lines) around the beam waist (focus). Important dimensions; ω_0, z_R, b, and θ, are labelled. Dashed lines indicate ray optics propagation of a beam with the same divergence angle, θ.

z axis is described by:

$$\boldsymbol{E}(\boldsymbol{r},z) = \boldsymbol{E_0}\frac{\omega_0}{\omega(z)}\exp\left(\frac{-\boldsymbol{r}^2}{w(z)^2}\right)\exp\left(-i[kz + k\frac{\boldsymbol{r}^2}{2R(z)} - \Phi(z)]\right) \tag{2.3}$$

where $\boldsymbol{r}$ is a position vector transverse to beam propagation, $\boldsymbol{E_0}$ is the maximum electric field strength, ω_0 is the beam waist or minimum beam width, ω(z) is the beam width, $k = 2\pi/\lambda$ is the wave-number, $R(z)$ is the wavefront radius of curvature, and $\Phi(z)$ is the Gouy phase [24]. ω_0, $\omega(z)$, and $R(z)$ are defined as:

$$\omega_0 = \frac{\lambda}{\pi\theta} \tag{2.4}$$

$$\omega(z) = \omega_0\sqrt{1 + \left(\frac{z}{z_R}\right)^2} \tag{2.5}$$

$$R(z) = z\left[1 + \left(\frac{z_R}{z}\right)^2\right] \tag{2.6}$$

$$z_R = \frac{\pi\omega_0^2}{\lambda} \tag{2.7}$$

The beam width, $\omega(z)$, is defined as the transverse distance at which the electric field strength has dropped to e^{-1} of its on-axis value [8] and is shown in Fig. 2.1 with other important dimensions. The Rayleigh range, z_R, is defined as the axial distance

from the beam focus ($z = 0$) at which the beam width increases by $\sqrt{2}$, $b = 2z_R$ is known as the confocal parameter and generally defines the axial extent of a beam focus. For $|z| \gg z_R$ the beam width increases linearly with increasing $|z|$ and a ray optical treatment of beam propagation becomes valid with a divergence angle, θ.

w_0 and z_R are closely related to $r_{x,y}$ and r_z respectively, however, equation (2.3) relies on the paraxial approximation and so is invalid for describing beams with a large distribution of wavevectors. Additionally, Gaussian beams are typically truncated at some point on propagation through an optical system and so a treatment using Abbe's theory is generally more accurate.

2.2.3 Non-Gaussian beams

Although Gaussian beams are prevalent, a number of more exotic beam types can be produced and are finding many applications in imaging and optical manipulation. In this Thesis, Bessel and Airy beams are investigated. These are described in more detail when first encountered in later Chapters, but are introduced now to highlight the key differences between these beam types.

Bessel beams are a propagation-invariant solution of the Helmholtz equation [25], which is analogous to the paraxial wave equation. The electric field of an ideal Bessel beam is given by:

$$E(r, \phi, z) = A_0 \exp(ik_z z) J_n(k_r) \exp(\pm in\phi) \tag{2.8}$$

where r, ϕ, and z are radial, azimuthal and longitudinal directions in cylindrical coordinates, k_r and k_z are the radial and longitudinal wavevectors where $k = \sqrt{k_r^2 + k_z^2} = 2\pi/\lambda$, J_n is the n^{th}-order Bessel function, and A_0 is a scalar constant. A zeroth-order Bessel beam is described by $n = 0$. $n > 0$ yields higher order Bessel beams which have a singularity on axis and carry orbital angular momentum [26] but these are not considered here.

Bessel beams consist of a narrow cylindrical core, surrounded by a series of concentric rings. This profile is formed by interference from plane waves arranged on the

surface of a cone. As such, an approximation of a Bessel beam can be generated from the following pupil function (electric field distribution in the back focal plane of a lens):

$$P_{Bessel}(\boldsymbol{u_r}) = \frac{1}{\sqrt{\pi\beta(2-\beta)}} H(1-\boldsymbol{u_r})H(\boldsymbol{u_r}-1+\beta) \tag{2.9}$$

where $\boldsymbol{u_r}$ is the radial normalised pupil coordinate, H denotes the Heaviside step function, and β is the fractional width of annulus (width of annulus/radius).

The Airy beam is in analogue of a dispersion-free solution of the Schrödinger equation for a free particle [27]. The electric field of an Airy beam can be expressed as:

$$E(x,z) = \mathrm{Ai}\left(\frac{x}{x_0} - \frac{z^2}{4k^2x_0^4}\right) \exp\left(i\frac{xz}{2kx_0^3} - i\frac{z^3}{12k^3x_0^6}\right) \tag{2.10}$$

where Ai is the Airy function, x is the transverse coordinate, x_0 is a characteristic transverse length, z is the propagation distance, $k = 2\pi n/\lambda$ is the wavevector where n is the refractive index [28, 29]. At the origin, $E(x,0) = \mathrm{Ai}(x/x_0)$ and this remains invariant upon propagation. However, the Airy beam undergoes a transversal shift, or acceleration, upon free propagation [28] and the main lobe of the Airy beam following a parabolic trajectory (Fig. 4.1).

The Airy beam is separable in Cartesian coordinates. Equation (2.10) describes a 1+1D Airy beam (an Airy beam in a 2D space), and a 2+1D Airy beam can be described by multiplication by a similar expression for $E(y,z)$. A 2+1D Airy beam can be generated from the pupil function:

$$P_A(u,v) = \frac{H(1-\boldsymbol{u_r})}{\sqrt{\pi}} \exp[2\pi i\alpha(u^3+v^3)] \tag{2.11}$$

where u and v are normalised pupil coordinates corresponding to the x- and y-axes respectively, $\boldsymbol{u_r} = (u^2+v^2)^{1/2}$, and α is the strength of the cubic modulation.

Figure 2.2 shows key differences in propagation between Gaussian, Bessel, and Airy beams. All beams are simulated through an objective lens with $0.42\,\mathrm{NA}$ for a wavelength of 532nm.

Figure 2.2(b,e) shows a Bessel beam formed from equation (2.9) with $\beta = 0.05$. The central core has a diameter slightly smaller than the Gaussian beam, but has an

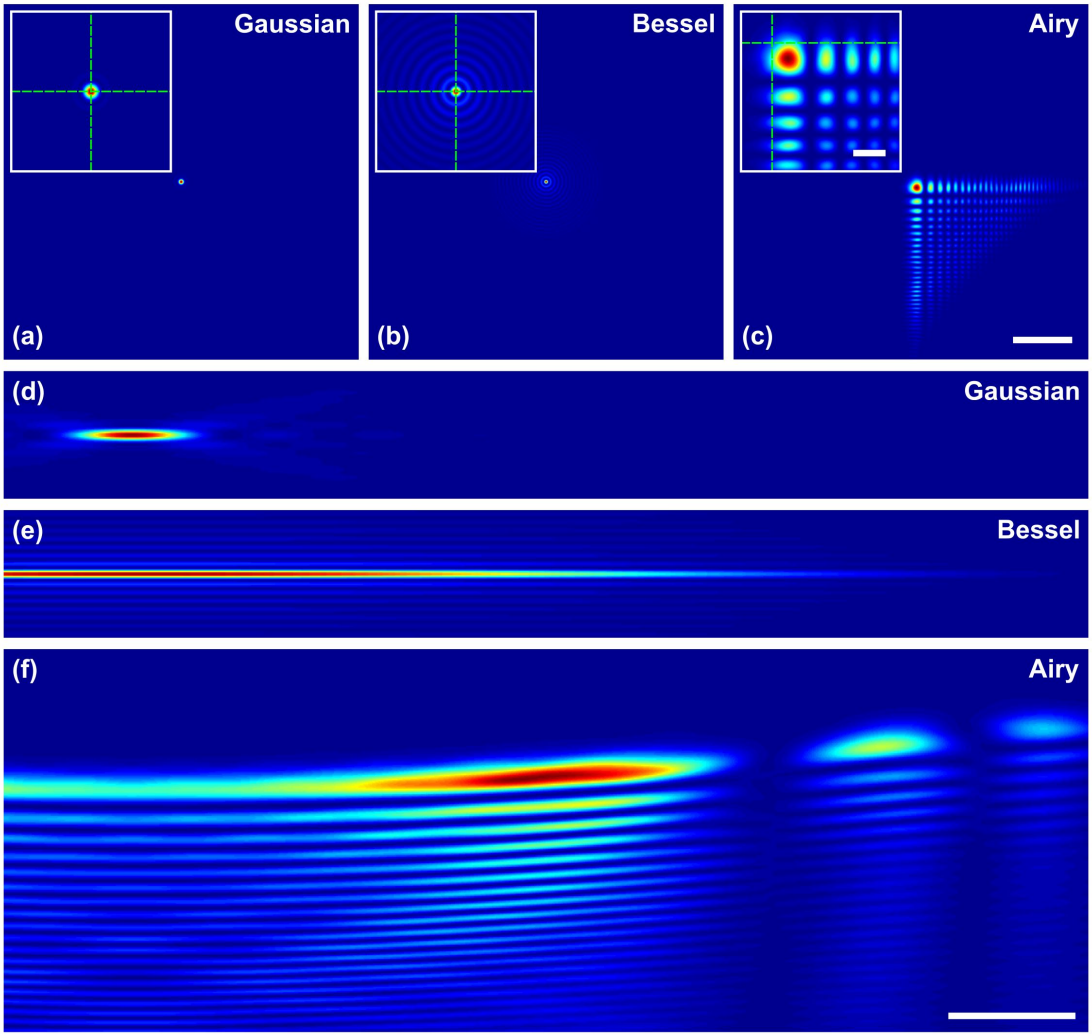

FIGURE 2.2: Propagation of Gaussian, Bessel, and Airy beams. Transverse intensity profiles of (a) Gaussian, (b) Bessel ($\beta = 0.05$), and (c) Airy ($\alpha = 7$) beams at the beam focus, showing the extended transverse structure of Bessel and Airy beams. Insert shows close up of central region, crossing dashed green lines indicate the origin. (d,f) Axial profiles of the beams. Scale bar is $10\,\mu\mathrm{m}$ ($2\,\mu\mathrm{m}$ in inserts).

extended transverse profile of concentric rings. The Bessel beam maintains this profile over a much larger longitudinal range than the Gaussian beam.

Figure 2.2(c,f) shows an Airy beam formed from equation (2.11) with $\alpha = 7$. The Airy beam has an asymmetric transverse profile an extended transverse profile compared to the Gaussian beam (and the Bessel beam). The Airy beam also exhibits propagation-invariance and maintains this profile over an extended longitudinal range. Figure 2.2(f) shows variation on propagation but this apparent variation is due to the transverse shift of the beam on propagation. It can be seen that the main lobe follows a parabolic trajectory.

2.2.4 Fluorescence microscopy

Different microscopy techniques rely on different physical properties of the sample to be imaged but most commonly rely on the absorption of transmitted light or the reflection of incident light, while more exotic schemes exploit the change in phase from passing through parts of the sample with different optical thickness [8]. With microscopic samples, these changes can be very small as the sample is very thin. Additional contrast agents may be added to the sample before imaging to enhance contrast, for example by selectively increasing the absorption of certain features for histological analysis by transmission microscopy.

Fluorescence as a contrast agent has, by far, had the greatest impact on biomedical microscopy. The field of fluorescence microscopy exploded in 1995 with the discovery of genetically encoded fluorescent proteins (green fluorescent protein; GFP) in the jellyfish *Aequorea victoria* [30] and is now common to almost all biomedical research laboratories. As will be seen in Chapter 2.4, most super-resolution microscopy techniques rely on manipulation of the spatiotemporal emission of embedded fluorophores to overcome the diffraction limit. Since the discovery of GFP, many mutations and other variants have been developed to yield fluorescent probes with excitation and emission peaks across the visible spectrum and into both the infra-red and ultra-violet [31].

Fluorescence is the process in which a fluorescent molecule, or fluorophore, absorbs light of one wavelength, exciting the fluorophore from its ground state, S_0, to an excited

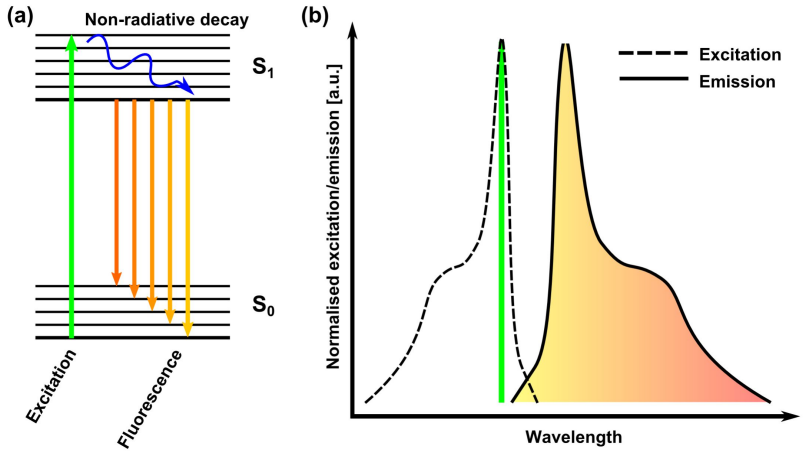

FIGURE 2.3: (a) Energy level diagram of fluorophore showing vibrational levels of ground (S_0) and excited (S_1) states, and excitation (green), non-radiative (blue), and fluorescence (yellow/orange) transitions. (b) Excitation and emission spectra of fluorophore showing spectral separation of excitation (green) and fluorescence (yellow/orange).

state, S_1 (Fig. 2.3(a)). The fluorophore then loses some energy through non-radiative processes and spontaneously emits a photon, returning to its ground state. The wavelength of the emitted photon is longer than the absorbed photon due to the energy loss within the fluorophore. Due to the fine structure of the fluorophore, a relatively broad range of wavelengths will excite the fluorophore, and the emission is equally broadband (Fig. 2.3(b)).

Fluorescence microscopy achieves a remarkably high contrast due to a very low background. GFP requires absorption of light at approximately 490nm to generate fluorescence, this corresponds to an energy bandgap of approximately 2.5eV. Thermal energy at room temperature corresponds to an energy of approximately 0.026eV and so spontaneous thermal excitation of a fluorophore is non-existent. Additionally, fluorophores can be conjugated to antigens, conformational proteins which only bind to highly specific antibodies, to target only specific antigens present in different cellular structures [31] which ensures high contrast due to low levels of residual fluorophores outwith the structures of interest. Multi-labelled specimens can, with appropriate choice of filters, avoid cross talk between the signals from different fluorophores if their excitation and emission spectra are kept spectrally distinct.

Image formation in a fluorescence microscope can be described by:

$$D(r) = (H \otimes [SI])(r) \tag{2.12}$$

where $\otimes$ is the convolution operator, $D(r)$ is the resulting image intensity, $H(r)$ is the point-spread-function (PSF) of the imaging system, $S(r)$ is the fluorophore distribution within the sample, $I(r)$ is the illumination intensity within the sample, and, for simplicity, r is a 1D vector in the lateral plane of the microscope [32]. $S(r) \cdot I(r)$ is the emission intensity from the sample, for uniform illumination, as is the case in a standard fluorescence microscope, $I(r)$ is unity. By spatially modulating $I(r)$, novel image acquisition methods can be developed. These are described in the following sections and are the main investigations of this Thesis.

2.2.5 Optical transfer function

Equation (2.12) expresses the image as a convolution with the PSF of the imaging system in real-space. In Fourier space, this can be expressed as:

$$\tilde{D}(k_r) = O(k_r)\mathcal{F}[(S(r)I(r))] \tag{2.13}$$

where $\mathcal{F}$ denotes the Fourier transform and $O(k_r)$ is the Fourier transform of $H(r)$, and is called the optical transfer function (OTF) of the imaging system [32].

The OTF describes the transmission of different spatial frequencies, k_r, through the optical system. Whereas better imaging typically requires an imaging system with the smallest PSF, an OTF with values above some noise threshold at the highest spatial frequencies is desirable.

As the OTF is typically complex valued, an optical system is often characterised by the modulation transfer function (MTF), which is the absolute magnitude of the OTF. This essentially gives the transmission coefficient of the imaging system as a function of spatial frequency.

Figure 2.4 shows the PSF and MTF for a typical microscope lens. The magnitude, or contrast, decreases as spatial frequency increases, reducing to zero at the spatial frequency corresponding to the diffraction limit. The resolution is determined by the

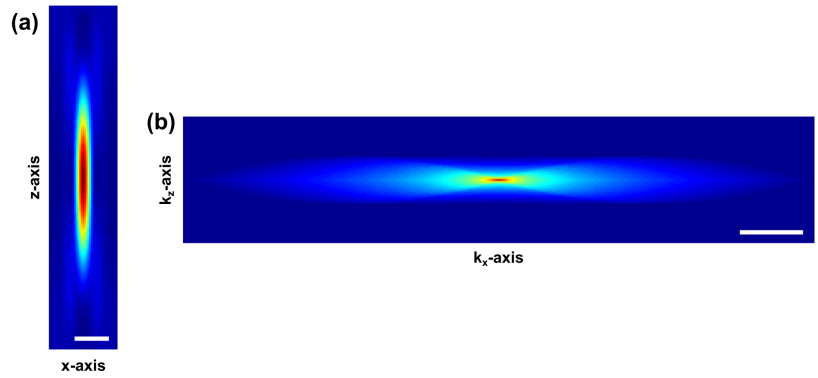

FIGURE 2.4: (a) Simulated PSF and (b) MTF for a typical microscope objective ($\mathrm{NA} = 0.4$, $\lambda = 532$nm). Scale bar in (a): $2\,\mu\mathrm{m}$. Scale bar in (b): 0.2 where units are normalised such that $1 = 2\,\mathrm{NA}\,/\lambda$ corresponds to the diffraction limit.

first zero in the MTF, or more practically, the lowest spatial frequency at which the MTF falls below the noise floor of the system [33]. Aberrations in the system will cause the MTF to fall at some spatial frequencies.

2.3 Volumetric imaging

Microscope design has tended to follow the rule that light collected from the sample is collinear with the light that is used to illuminate the sample, whether this is from opposing sides of the sample, as in transmission imaging, or in the more flexible case of reflection, or epi-fluorescence, imaging. This poses a great challenge for the imaging of thick specimens. The illumination generates fluorescence in the focal plane and also everywhere else in the sample along the path of the illumination and so the signal collected by the microscope contains the desired image from the focal plane of the microscope but also the blurred image from fluorescence excited anywhere else in the sample. In standard fluorescence microscopy this is generally everywhere in the sample and so the out-of-focus contributions to the image can be very large, especially in densely labelled samples. Biological imaging experiments have been designed around this fundamental limitation and so much biomedical research is carried out on two-dimensional (2D) cultures of biological material to ensure sufficient contrast in the image. Biology is intrinsically three-dimensional (3D) in nature and to truly understand

processes in development and disease, studies must be performed on model systems that recapitulate the natural environment of the specimen more accurately than a 2D culture or on an entire animal *in vivo*. Microscopy techniques must evolve to overcome their limitations and better suit the needs of the end user.

Microscopy techniques have, and continue to, evolve and a number of techniques have emerged to enable volumetric imaging. The primary requirement for volumetric imaging is optical sectioning, the ability to separate signals in one axially offset plane of the sample from another. The following sections describe a number of techniques designed to give optically sectioned, volumetric images of large specimens.

2.3.1 Confocal and multi-photon microscopy

Confocal microscopy is a technique for achieving optical sectioning based on selective detection of light [34], so-called because the method comprises a point light source which is imaged to a point in the sample and a detector which only accepts signal from one point in the sample. These points must be aligned in order to generate a signal from this point, which is scanned throughout the sample in 3D to produce an image. The method can give high-contrast, optically sectioned images at considerable depth into thick, scattering specimens because of this point-to-point principle. This is achieved generally using pinhole apertures and a simple confocal microscopy apparatus is shown in Fig. 2.5. The illumination is focused to a point, the intensity of the illumination will be concentrated at the focus but some signal will be generated throughout a cone converging on this point and another cone diverging from it which will generate some unwanted background signal. This extraneous background signal would lower contrast but is rejected by the detection pinhole; the pinhole only strongly transmits light which focuses at the centre of its aperture. Light which is focused in the aperture plane but laterally offset is strongly attenuated as it is not transmitted, light which is defocused from the aperture plane is only partially transmitted and so also attenuated.

By rejection of light that has originated from outwith the focal spot, or light from the focal spot which has scattered due to sample turbidity, only ballistic emitted photons

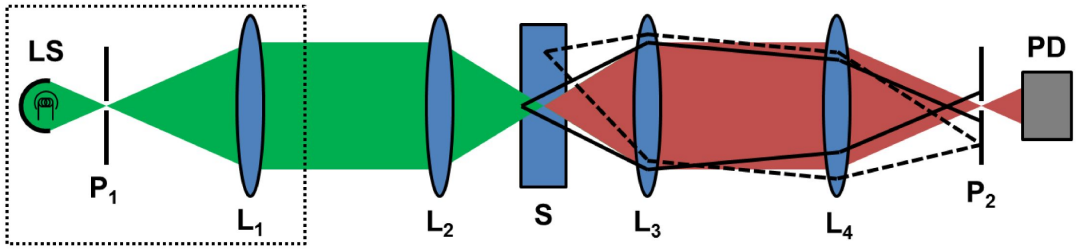

FIGURE 2.5: Schematic of confocal microscope shown in transmission configuration for simplicity. LS: Light source; Px: Pinhole; Lx: Lens; S: Sample; PD: Photodetector. Beam pathway in block colour shows light transmission from desired focal spot in sample. Pathways of unwanted signal form laterally and axially offset points are shown by dashed and full outlines respectively. The dashed box around LS indicates the components which may be replaced by a collimated laser beam. Beam steering optics and fluorescence filters have been omitted for clarity.

are efficiently collected and contribute to the image, offering good image quality at depth.

The resolution of the microscope can be partially controlled by varying the diameter of pinhole aperture. If the pinhole in made infinitely small, it is theoretically possible to achieve resolution 2 times better than the diffraction limit. In practice however, this is not possible due to the infinitely small signal that would be collected and resolution enhancement by a factor of approximately $\sqrt{2}$ is achieved [35].

The confocal microscope is a point scanning technique and so intrinsically slow for imaging large samples, the time required to image a cube of side a scales with a^3. With advances in photodetectors and beam scanning optics, the time taken to position the beam accurately at a point and acquire a signal can be sub-millisecond. Confocal microscopy is therefore best suited to small volumes where short scan times can be achieved. Video rate confocal microscopy can be performed using spinning-disk or Nipkow disk methods [36], where a spinning disk with an array of holes is used to rapidly scan the focal spot across a plane in the sample. Depending on the disk design, this can be parallelised and multiple, appropriately separated, focal spots can be imaged simultaneously [36].

Multi-photon microscopy, most commonly two-photon excitation (2PE) microscopy [15] is an extension of confocal microscopy that exploits the non-linear response of multi-photon excitation, the process of absorbing two photons of energy equal to half

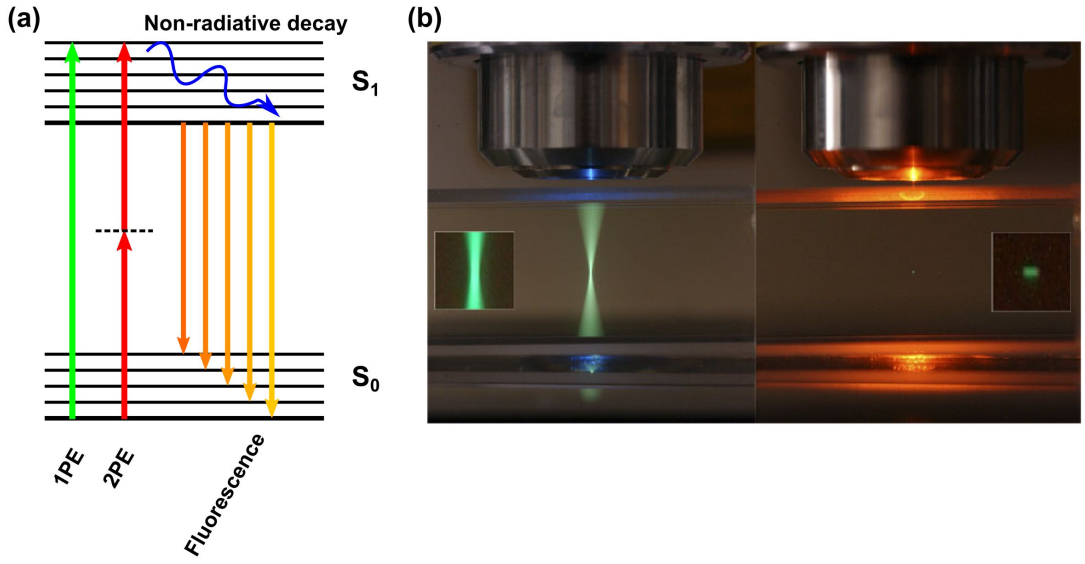

FIGURE 2.6: (a) Energy level diagram of fluorophore showing vibrational levels of ground (S_0) and excited (S_1) states, and 1PE (green), 2PE (red), non-radiative (blue), and fluorescence (yellow/orange) transitions. (b) Photograph of 1PE (left) and 2PE (right) fluorescence. Photo in (b) taken from [37].

the excitation energy, to the illumination intensity (2.6(a)). The probability of 2PE scales with the square of the intensity, so for a focused beam, occurs only in the focal volume (2.6(b)), yielding high SNR without requiring rejection pinholes. However, short-pulsed lasers are required to generate the required intensities which makes multi-photon microscopy expensive and limits the choice of excitation wavelengths available and therefore fluorophore choice. The spectral separation of excitation and emission is improved and the longer wavelengths used for illumination have greatly reduced Rayleigh scattering allowing imaging at increased depth which makes multi-photon microscopy particularly suitable for *in vivo* applications.

2.3.2 Light-sheet microscopy

Whereas confocal microscopy is based on both selective illumination and selective detection, LSM is based solely on selective illumination of the sample alone and is much more efficient in its use of the photon budget. If it is desirable to not collect fluorescence from outwith the focal plane, simply do not illuminate outwith the focal plane.

This is achieved by illuminating the sample with a beam perpendicular to the detection optics and is generally delivered into the sample through another lens [34, 38, 39]. With a weakly focused beam, this illumination scheme will illuminate a line within the focal plane. In order to capture an image from the entire focal plane simultaneously the beam must be made broad along one axis, this can be achieved by using a cylindrical lens as shown in Fig. 2.7. Alternatively, a quasi-light-sheet may be formed by rapid one-dimensional (1D) scanning of the beam, often referred to as digitally scanned light-sheet microscopy (DSLM) [40]. If the beam is scanned on timescales much shorter than the camera integration time, the scanned beam appears, to the camera, as a continuous sheet. Rapid scanning of a focused beam yields a more uniform intensity light-sheet than one formed by cylindrical lensing, as a cylindrical lens still maintains a Gaussian profile whereas rapid scanning can yield a flat intensity profile over a significant range. DLSM is also more resistant to shadowing artefacts [41] due to the increase in $k-$vectors associated with tightly focused beams, but requires a more complex optical system.

Figure 2.7 also highlights that the optical sectioning ability is dependent of the light-sheet thickness, or width. The insets in Fig. 2.7(a) show two standard modes of LSM operation; (i) the light-sheet thickness is matched with the depth-of-focus (DOF), or axial resolution, of the microscope objective used to collect fluorescence, and (ii) the light-sheet thickness is made much narrower than the DOF. In both scenarios the lateral resolution of the microscope remains the same and is given by equation (2.1).

In the first scenario, the axial resolution is given also by the Abbe criteria for the detection lens, as given by equation (2.2), the light-sheet width is approximately equal to, or a bit larger than, the DOF of the detection lens and so background fluorescence emission from outwith the focal plane is inhibited. As the light-sheet is fairly broad in this case, the divergence of the illumination is low and the light-sheet width remains approximately constant over a large propagation range, or field-of-view (FOV). The cut-off point used to define the limits of the FOV is the confocal parameter, b, of the light-sheet, at which point the beam width is $\sqrt{2}$ greater than at the beam waist.

In the second scenario, the light-sheet is focused such that the thickness is much narrower than the DOF of the detection lens. In this case, the greater divergence of

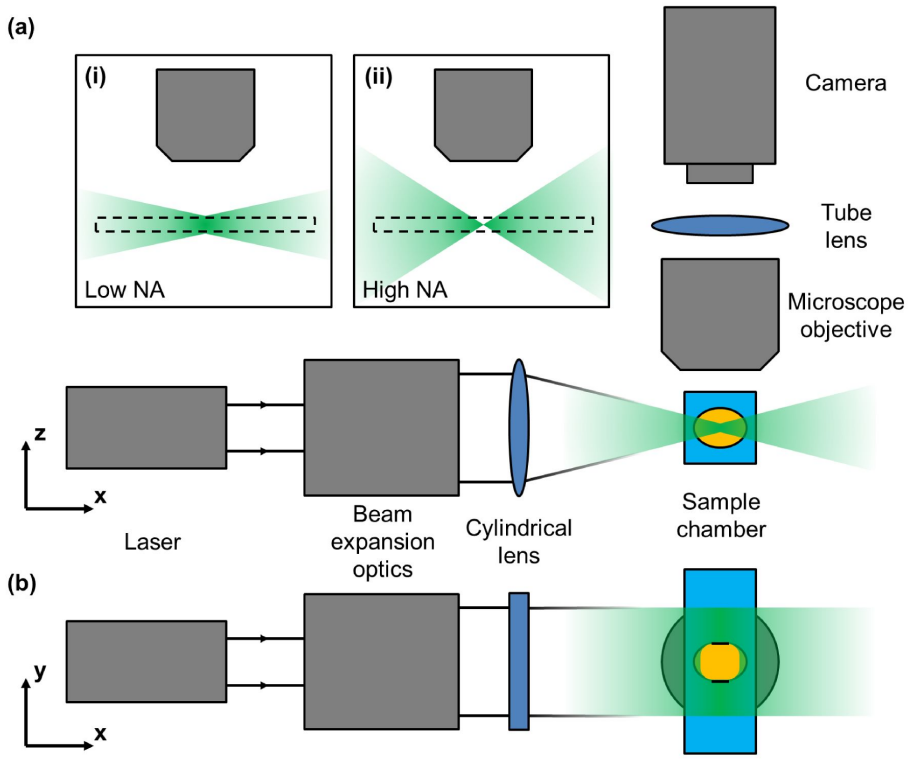

FIGURE 2.7: Simple light-sheet microscope design. (a) Top down ($x-z$) and (b) side on ($x-y$) views of the microscope setup. A collimated laser beam is expanded and two-dimensionally focussed into a thin sheet normal to the z-axis. This light-sheet intersects the sample (usually immersed in liquid within a chamber) and is co-aligned with the focal plane of the microscope objective, which collects fluorescence from the sample. The collected signal is imaged via the tube lens onto the camera. Insets in (a) show the two main classes of LSM; (i) low and (ii) high NA illumination. The dashed box indicates the depth-of-focus of the microscope objective.

the light-sheet results in a much shorter FOV but the axial resolution of the microscope can be greatly increased. If the illumination has the same NA as the detection optics, isotropic resolution can be achieved. This scheme was originally termed confocal-theta microscopy [42] and later evolved into the LSM technique described above in order to increase the FOV of the technique.

At the high-resolution limit of LSM, the requirement of two perpendicular objective lenses places a geometric limit on the resolution that can be achieved. With identical objective lenses for illumination and detection, as is required for isotropic resolution, the cone of acceptance cannot exceed an angle of $45°$ ($\mathrm{NA} = 0.71$ in air) or the focal points of the two objectives cannot be matched. Higher resolution implementations

have been achieved through the use of complimentary multi-view, structured illumination, and super-resolution techniques [5, 20, 41, 43–48].

Compared to point scanning methods, where the illumination is time-shared across each point of the sample, the illumination is incident on all points in the image continuously for cylindrical lensed LSM and only time-shared per line of the image for DSLM. As the illumination is present at each point in the sample for longer per image acquisition, the instantaneous illumination intensity can be lower to achieve the same signal-to-noise ratio (SNR), however, the total fluence for each method is the same. The wide-field nature of image acquisition in LSM and readily available fast and sensitive camera technology allows for very fast imaging, even over large volumes [6, 49]. Ahrens *et al* have reported sub-cellular resolution imaging of the entire larval zebrafish brain $(800 \times 600 \times 200)\,\mu\mathrm{m}^3$ with nearly 1s temporal resolution [6]. One drawback to wide-field image acquisition is that fluorescence emitted from planes deep into thick specimens is subject to scattering and so images from within turbid specimens will degrade with increasing depth.

2.3.3 Light-field microscopy

Light-field microscopy (LFM) is based on the concept of integral photography [50, 51] that exploits the use of an array of small lenses, or "lenslets", to acquire information about the angular distribution of light from a sample as well as the positional information [50].

Microscope objectives feature a physical stop (circular aperture) at the back focal plane of the lens which imposes a number of conditions on the image: that the images produced are orthographic rather than perspective views of the sample, the PSF of the lens is shift invariant in the lateral plane, and translation of the sample in the lateral plane does not cause parallax [50]. While these properties are, in general, very useful, a consequence is that no impression of the 3D distribution of the sample can be discerned without axially translating the sample relative to the focal plane of the microscope. Volumetric images are constructed by scanning the sample through the focal plane of the microscope and image of different planes are acquired sequentially, limiting the

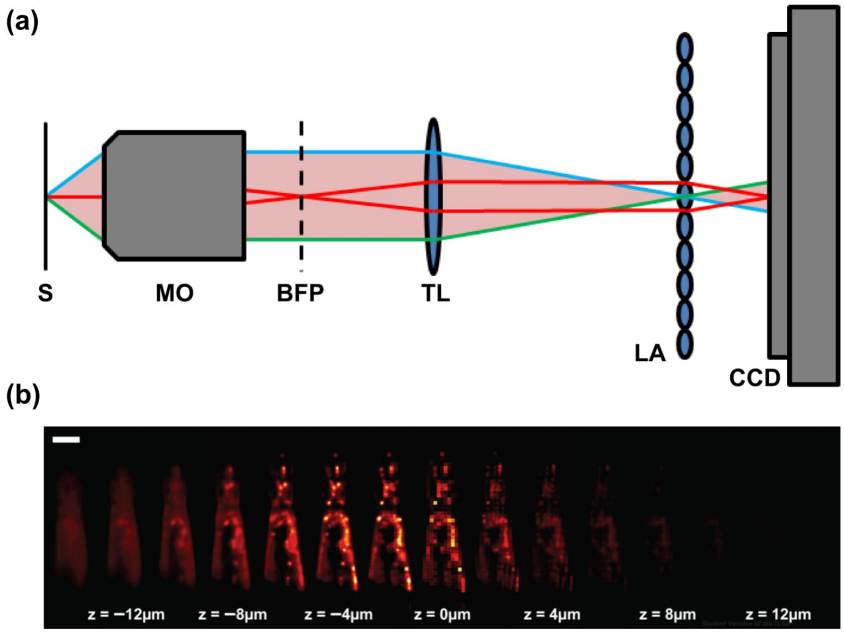

FIGURE 2.8: (a) Simple light-field microscope schematic. A lenslet array (LA) is placed at the image plane of a typical microscope and the camera is set back by the focal length of LA. Each lenslet images a different point in the sample plane, within the image produced by each lenslet each point corresponds to a view of that point from a different direction. Light propagation is shown from a single, on-axis point in the sample to the detector (pink), individual ray traces (red, green, blue) indicate the mapping of the angular views to pixels in the image. S: Sample; MO: Microscope objective; BFP: Back focal plane; TL: Tube lens; LA: Lenslet array; CCD: CCD camera. (b) Typical LFM image of Ca^{2+} in *C. elegans* showing 15 $z-$planes acquired from a single camera exposure. Scale bar in (b) is $50\,\mu\text{m}$. (a) adapted with permission from [50]. (b) used with permission from [7].

volumetric acquisition rate. For example, by any wide-field imaging technique of a cubic volume of side a, the imaging time scales linearly with a.

In LFM, positional information (i.e. lateral resolution) is sacrificed in order to simultaneously acquire angular information about the light emitted from a sample which can be used to reconstruct the image of the whole sample volume from a single snapshot image. This is achieved by placing a lenslet array at the traditional image plane of a microscope (Fig. 2.8(a)). An unusual image is then formed after the lenslet array consisting of an array of circles, one for each lenslet. Each circle in the image maps onto a point in the sample and each point in the circle corresponds to the view of that point from a different direction [50].

As each lenslet maps a point in the sample into the image, the spatial resolution

is much lower than if a traditional microscope had been used. Assuming 100% fill factor of the lenslet array, a LFM with $N \times N$ points per lenslet sub-image will yield an image with N^2 fewer pixels than a traditional microscope image [52]. The benefit gained is that N planes, axially offset by $r_z = (2 + N)\lambda n/2\,\mathrm{NA}^2$, can be retrieved from the recorded image [50]. This allows whole volumes to be imaged in a single camera acquisition and so very high temporal resolution can be achieved. Volumes of approximately $(700 \times 700 \times 200)\ \mu\mathrm{m}^3$ have been imaged at a rate of 20Hz [7] and, with future camera technology, could exceed 100Hz very easily. Figure 2.8(b) shows a typical LFM image [7].

The limited spatial resolution cannot be improved simply by increasing the pixel density due to diffraction, but can be recovered using 3D deconvolution. The algorithms for this are computationally demanding and reconstruction of a volumetric image can take 2-30 minutes depending on the size of the image, the resolution desired, and the computer hardware available [7]. This reconstruction highlights a major limitation of LFM, image post-processing is accepted, or tolerated, when the processing time is comparable to the time for image acquisition, when the image post-processing stage takes significantly longer than the image acquisition stage this introduces a bottleneck in the user workflow. Coupling this with extremely high acquisition rates, a huge amount of data may require processing at once. For example, for a 100s time-series experiment with the parameters given above [7], processing would take 67-1000 hours if processed serially and parallelisation again depends on available hardware. Other approaches have been developed to increase the spatial resolution of LFM, one technique utilises an additional transform lens to invert the light-field distribution [53]. In this case, the lenslet array and single camera was replaced by a macroscopic array of lenses, each focusing onto a different camera. Each "lenslet" captures a different angular view, and each point within this circle now corresponds to a different point in the sample. If limited viewpoints are acquired, a high spatial resolution can be achieved without deconvolution [53].

2.3.4 Discussion of volumetric imaging techniques for live imaging

The techniques introduced above are all currently used for volumetric imaging. Confocal microscopy, and its non-linear counterpart multi-photon microscopy, is the current gold standard technique because of the high resolution and high contrast it can achieve. With over 30 years of commercial development, confocal systems have many "bells and whistles" such as automated and incubated sample stages, simultaneous multi-colour acquisition, and user friendly control software, meaning end-users are quite happy to design their experiment and research questions around the limitations of the confocal microscope. This limits imaging experiments of dynamic specimens to small volumes or a series of fixed specimens at various stages of a process due to the point-scanning nature of the confocal microscope. Scan rates can be increased if the signal acquisition time at each point is reduced but this necessitates an increase in the illumination intensity which causes more photobleaching of fluorophores and can cause other phototoxic effects to the sample [5, 54, 55] and limits the number of times a specimen can be imaged before it is expended.

LSM is a wide-field acquisition method and so is much faster than confocal microscopy, limited only by the frame-rate of the camera and the number of frames to be imaged. With a LSM based on cylindrical lensing, each point of the sample imaged is continuously illuminated and so the illumination intensity can be kept low, reducing phototoxic effects [5, 54, 55]. With 1D scanning based LSMs, the illumination intensity is higher as it must be time-shared between each line of the image, but can still be minimised through synchronisation with rolling-shutter based cameras [56]. Volume scans can be acquired rapidly and temporal resolution of about 1s/volume has been demonstrated over the entire brain of a zebrafish embryo [6] "Scanless" methods, not requiring any translation of the sample have been developed to increase volumetric imaging speeds [57, 58]. Imaging deep within scattering tissues is still a challenge with LSM due to the wide-field acquisition; the parallel nature of the acquisition means that aberrations blur each PSF into its neighbours, lowering the resolution. This can be alleviated through use of structured illumination techniques [59] or confocal line apertures [56, 60, 61] which increase in-plane acquisition times (about $2-5$ times), and multi-view

methods [41, 45, 56, 62–64] which record multiple volumes of the sample from different orientations and require rotation of the sample which slows the method. Additionally, complex and computationally intensive volumetric image registration methods [63, 65] are required to combine different views and sample motion may introduce artefacts making multi-view LSM less suitable for monitoring of rapid processes but still suitable for long-term monitoring of slower changes such as embryonic development [45].

LFM has, by far, the best temporal resolution over large volumes of all three methods discussed. However, it also has the lowest spatial resolution, although it can still give 3D sub-cellular resolution over volumes approximately $(700 \times 700 \times 200)\,\mu\mathrm{m}^3$ [7]. This resolution is probably sufficient for rapid dynamical studies on the whole animal or embryo scale but for a full understanding of intricate processes, complimentary studies on smaller volumes with slower, but higher resolving techniques may be required. LFM is essentially a wide-field acquisition technique and so image quality at depth will degrade due to aberrations. This may be less severe in LFM as the spatial resolution is low and aberrations have more of an effect on the highly inclined rays associated with the outer-Fourier space and high-resolution.

One claim of LFM is that it has excellent light gathering power [50]. If, for example, a 10 plane z-stack of a sample was to be acquired, a conventional microscope would have to acquire 10 images sequentially whereas a LFM could acquire one image with an array of 100 lenslets and compute the image with a lateral resolution which is 10 times lower in x and in y. The LFM image would have 100 times less voxels (volumetric pixels) and so would have a SNR 100 times greater than the conventional image, additionally the frame-rate is 10 times faster and so a 10 times longer integration time could be used to increase the signal even further. This is beneficial in principle but the comparison assumes a scenario where there is no shortage of light and intense illumination will not adversely affect the sample. As previously mentioned, intense illumination does have a negative effect on the specimen [54, 55] and fluorescence microscopy is a situation where the photon budget is extremely limited. LFM is a low resolution but fast imaging method and fluorescence LFM will stay such until more robust fluorophores are developed. Short acquisition times equate to a low SNR and photo-bleaching and photodamage will result if the illumination intensity is increased.

Additionally, the light that is collected from each point is distributed over over many pixels on the detector such that the SNR on each pixel will be low.

Overall, although LFM is a very promising technique, some further progress is needed for high resolution volumetric imaging of biological material. Its power mainly stems from its excellent temporal resolution, but existing fluorophore photo-chemistry is not efficient to provide appreciable signal on these timescales. LSM, on the other hand, is based on an optimisation of existing fluorescence microscopy techniques and can generate sufficient signal for biomedical imaging. LSM puts limitations on temporal resolution back on the hardware but is still able to acquire four-dimensional (4D) datasets with high spatiotemporal resolution. It is also compatible with and complimentary to a wide range of fluorescent imaging techniques making it a powerful tool in almost any scenario. For this reason, LSM is chosen as a volumetric imaging technique to focus on and the use of beam shaping to improve upon LSM techniques is discussed in Chapters 4 - 6.

2.3.5 Further developments in light-sheet microscopy

A number of innovations have advanced the LSM technique as discussed below. As a strong emphasis of this Thesis is the use of beam shaping techniques for microscopy, techniques which exploit novel photonics, rather than simply addressing engineering challenges, are given focus.

Multi-view reconstruction in light-sheet microscopy

Light scattering in large specimens has precluded high-resolution LSM of large specimens such as millimetre sized zebrafish and drosophila (*Drosophila melanogaster*) embryos. Typically a standard LSM configuration, as shown in Fig. 2.7, can only yield a high-resolution image of the regions of such large samples that are nearest to the illumination lens, as the light-sheet is attenuated with propagation through the specimen, and nearest to the detection lens, as scattering from the sample distorts the fluorescence emitted from deeper layers [41]. These issues can be mitigated by acquiring multiple views of the specimen. This first issue was solved with the introduction of a second light-sheet projected into the specimen from the opposite side of the FOV [41]. As both light-sheets become broad on the distal side of the sample, simultaneous

imaging with both light-sheets reduces overall image quality and so images acquired with dual-light-sheet illumination must be sequentially acquired and computationally fused which lowers the acquisition speed and increases the computational burden of the method. This technique has been extended to utilise a second detection lens from the opposing side of the sample to capture high-resolution data from the "back" of the specimen [45, 62, 64]. Additionally, the sample can be rotated to acquire more views to fill in regions that are not adequately covered by the dual-illumination-dual-detection method alone. These methods necessitate enclosing the sample within a square of microscope objective lenses, while this is suitable for imaging small embryos, it is generally limiting specimen choice. Other methods have since been developed that allow multi-view LSM using the standard LSM geometry (Fig. 2.7) in which both objective lenses deliver light-sheet illumination and collect fluorescence [43, 44]. This system has limited use at depth in large specimens but has less constrained specimen choice than other multi-view LSM methods.

The confocal principle in light-sheet microscopy

The confocal principle has been applied to LSM. In this scenario the illumination is generally a 3D focussed beam which is scanned across the sample, illuminating a line of the sample at any given time. As this line is scanned across the sample, it is imaged onto a line aperture which rejects light not originating on the line of illumination [61]. Light scattering along the axis of the slit will still affect image quality and degrade the SNR but this is greatly reduced from the case of unfiltered LSM which is affected by scatting in any direction. The improved contrast comes at the price of reduced imaging speed, as the scanning of the illumination line and confocal slit aperture must be synchronised. Use of line scanning methods also allows the signal to be coupled into an imaging spectrometer instead of a camera to perform Raman [66] and hyperspectral [67] imaging, although this has also been demonstrated on full-field LSM images using the "spectral knife edge" method [68]. Alternatively, a digital slit can be applied to a series of images acquired for different illumination positions, or by using rolling shutter camera acquisition modes [56]. Also making use of the confocal principle is swept confocally-aligned planar excitation (SCAPE) microscopy [69]. SCAPE microscopy combines highly inclined and laminated optical sheet microscopy

[34, 70], oblique plane microscopy [34, 71], and a unique scanning-descanning system to achieve efficient LSM over large volumes through a single objective lens without translating the sample.

Adaptive optics in light-sheet microscopy

Adaptive optics (AO) for aberration correction has also been implemented in both the illumination [72] and detection [73] pathways of LSM to enable better contrast and resolution at depth within specimens. Aberration correction requires a pre-imaging phase where aberrations are measured which limits use with rapidly changing samples. Both spatial light modulators (SLMs) and deformable mirrors (DMs) have been used for AO in LSM. SLMs have low light efficiency but allow correction of severe aberrations, DMs conversely have a very high light efficiency but can only correct for low aberrations. Therefore SLMs have been exploited in the illumination pathway whereas DMs have been used to correct for aberrations in the detection pathway. Both methods utilised wavefront-sensorless correction procedures. Correction of the illumination pathway has demonstrated improved image quality in highly turbid samples within about $10\,\mu\mathrm{m}$ of the correction point [72]. Correction of the detection pathway revealed that aberrations were mainly caused by the mounting capillary and a systematic correction could be performed prior to the experiment [73].

Structured illumination in light-sheet microscopy

Structured illumination (see Chapter 2.4.3 and Appendix A) can be readily implemented with LSM to improve the axial resolution as described by Neil *et al* [74]. In LSM, the periodic grating required for SIM has been created by a four-faceted symmetric prism [75], but is more commonly generated by stepping a rapidly scanned light-sheet in discrete steps [76–79]. In some of these implementations, a modified structured illumination technique known as HiLo microscopy which combines images acquired with uniform and modulated illumination [77, 79]. Modified structured illumination algorithms have also been used to overcome aberrations occurring in the detection pathway when imaging at depth by filtering out the ballistic fluorescence signal from the scattered fluorescence background [59]. A number of raw image frames must be acquired and processed to yield a SIM image [74] which reduces the imaging speed of SIM based LSM methods.

Stimulated emission depletion in light-sheet microscopy

LSM has also been combined with stimulated emission depletion (STED) concepts (see Chapter 2.4.2) [80, 81]. STED allows the fluorescence emission volume to be restricted by use of a second beam which depletes excited fluorophores [22, 82]. The emission volume can be made much smaller than a diffraction limited spot. In LSM, STED has been used to narrow the width of a light-sheet produced by a cylindrical lens. The depletion beam is shaped to resemble a TEM_{01} Hermite-Gaussian mode and effectively forms a light-sheet either side of, but overlapping with, the excitation sheet, narrowing the thickness of the excitation light-sheet. This technique yielded an axial resolution of $0.68\,\mu\mathrm{m}$, 40% lower than the standard LSM setup with the STED beam off [80]. Other implementations have been proposed utilising scanned light-sheets and Bessel beams for depletion [83]. The low intensity, low phototoxicity view of LSM may jar with the high intensity and considerably high phototoxicity views of STED microscopy but the combination of these techniques could yield a balanced imaging method where the benefits of one mitigate the negative effects of the other.

Bessel beams in light-sheet microscopy

As mentioned previously, focusing of the light-sheet to widths much narrower than the DOF of the detection lens is possible and allows for isotropic resolution imaging, this beam shaping effectively gives a form of axial-super resolution although it is only valid over a short FOV. The extreme case of this is confocal-theta microscopy [42]. Perhaps the most common beam shaping technique utilised in LSM is the use of Bessel beams to extend the FOV over which high-resolution can be achieved and their properties are summarised below.

Bessel beams are a propagation-invariant solution of the Helmholtz equation [25], which is analogous to the paraxial wave equation. The electric field of an ideal Bessel beam is given by:

$$E(r, \phi, z) = A_0 \exp(ik_z z) J_n(k_r) \exp(\pm in\phi) \tag{2.14}$$

where r, ϕ, and z are radial, azimuthal and longitudinal directions in cylindrical coordinates, k_r and k_z are the radial and longitudinal wavevectors where $k = \sqrt{k_r^2 + k_z^2} =$

$2\pi/\lambda$, J_n is the n^{th}-order Bessel function, and A_0 is a scalar constant. A zeroth-order Bessel beam is described by $n = 0$. $n > 0$ yields higher order Bessel beams which have a singularity on axis and carry orbital angular momentum [26] but these are not considered here.

The Bessel beam is so-called "non-diffracting" because the cross section of its intensity profile, $I(r, \phi)$, is independent of its longitudinal position and resembles a central bright spot, surrounded by concentric rings. Each ring contains an equal fraction of the energy of the beam. In practice, a true Bessel beam cannot be created as it contains infinite energy but quasi-Bessel beams can be created which exhibit non-diffracting properties over a finite range[1]. A Bessel beam may be decomposed as a super-position of plane waves converging on a cone with angle corresponding to k_r. This can either be formed from a annular ring aperture in the Fourier plane of a lens, illuminated with a collimated beam of light (as shown in Fig. 2.9) or through the use of an axicon, a conical lens [26]. From the properties of the Bessel function and simple geometric arguments it can be shown that the size of the on-axis Bessel core has a radius, r_0, and a maximum propagation-invariant range, z_{max}, given by:

$$r_0 = \frac{2.405}{k_r} \tag{2.15}$$

$$z_{max} = \frac{R}{\arctan\left(r_A/f\right)} \qquad \textit{(Fourier annulus)} \tag{2.16}$$

$$z_{max} = \frac{\omega_0}{(n-1)\gamma} \qquad \textit{(Axicon)} \tag{2.17}$$

where R is the radius of the imaging lens, f is its focal length, r_A is the radius of the annulus, ω_0 is the beam waist of a Gaussian beam formed under spherical focusing using an equal power lens, n is the refractive index of the axicon, and γ is the opening angle of the axicon [26].

The Bessel beam profile is formed from interference of rays propagating at an angle to the optic axis. Therefore objects blocking the Bessel core do not permanently

[1] In this Thesis, all beams considered are the physical, finite aperture versions of the theoretical beam type. From now on, quasi-Bessel beams will simply be referred to as Bessel beams.

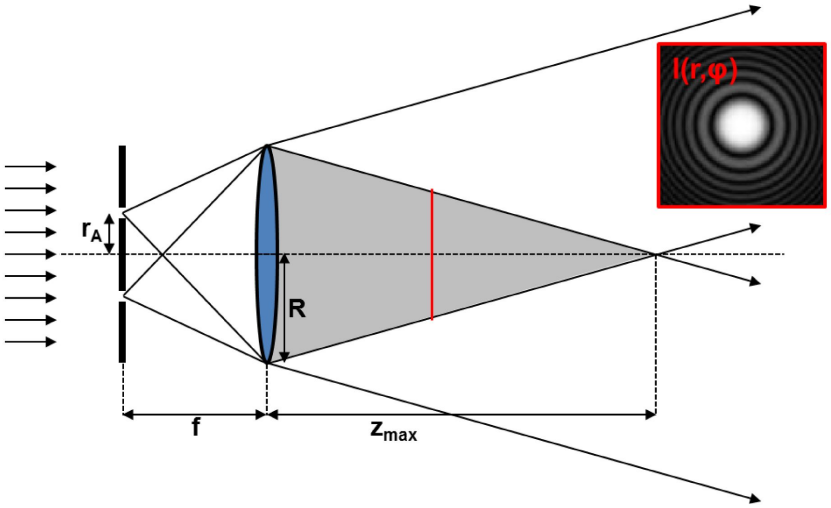

FIGURE 2.9: Bessel beam generation by annulus in the back focal plane of a lens. Selected light rays transmitted through the annulus of radius, r_A, is focused through a lens of radius, R, and focal length, f, and interferes within the shaded cone. z_{max} is the maximum propagation-invariant range, given by equation (2.16). The inset image (red box) gives an example of the cross-sectional intensity distribution within the cone (red line). Inset taken from [26]. Figure adapted with permission from [26].

halt beam propagation and the beam profile will be restored after some propagation. Bessel beams, and propagation invariant beams in general, are considered to be self-reconstructing and resistant to aberrations [26].

Bessel beam generation by an axicon is more light-efficient as all the light contributes to the Bessel beam. Annular generation of Bessel beams is very inefficient as most of the input light is blocked by the annulus. However, the axicon method is a near-field method whereas the annular method generates a Bessel beam in the far-field and is therefore more readily compatible with other Fourier plane beam manipulation methods and can be dynamically changed using programmable beam shaping devices such as spatial light modulators (SLMs).

Returning to LSM, as Bessel beams can give a small core size over extended longitudinal ranges compared to a focused Gaussian beam, it is perhaps an obvious choice to utilise for high-resolution LSM, thus solving the problem of beam divergence. However, Bessel beams cannot be passed through cylindrical lenses as the conical distribution of wavevectors is lost and a chequerboard pattern results [26, 84–86]. A Bessel

light-sheet must be generated by rapid scanning of the beam, this results in a very broad cross-sectional profile and leads to a low axial resolution. A comprehensive comparison between Gaussian and Bessel beam based DSLM in both single-photon excitation (1PE) and 2-photon excitation (2PE) modalities is presented by Olarte *et al* [87] and the theory underpinning this result is developed in Chapter 4. As the emission profile for 2PE fluorescence is proportional to the square of the illumination intensity, the side lobes of the Bessel light-sheet are greatly suppressed and yield excellent axial resolution and improved penetration depth due to the longer wavelengths used [87, 88] but at the cost of expensive pulsed laser sources required for multi-photon excitation, a more limited choice of excitation wavelengths, and a more limited choice of fluorophores which have strong multi-photon absorption cross-section.

Bessel beam based LSM (BB-LSM) in the 1PE regime must be combined with other techniques to mitigate the negative effects from the broad cross-sectional area of the beam. Line scanning confocal techniques have been used to reject light from all but the Bessel core [60], which benefit additionally from the self-healing property of the Bessel beam to preserve the illumination intensity across the image in scattering specimens but rejects significant amounts of fluorescence generated from the side-lobes and increases sample exposure and potentially increases photo-damage. Structured illumination can also support BB-LSM as was initially demonstrated by Planchon *et al* [20], but this technique has since been refined [5, 46, 89]. In this method, a linear array of Bessel beams is projected into the sample. For certain periodicities of the Bessel grating, the side-lobes interfere in such a way as to create a 2D array of lines comprised of a few discrete Fourier components and can be used to perform 3D-SIM (see reference [32], Chapter 2.4.3, and Appendix A). The light-sheet illumination scheme allows much higher SNR than can be achieved by normal SIM and with greatly reduced photo-damage, however, the SIM algorithm requires at least 3 images to be acquired per plane for reconstruction and so is expected to cause at least 3 times more photo-damage than other techniques [5].

2.4 Super-resolution microscopy

Abbe's theory of image formation sets fundamental limitations on resolution as discussed in Chapter 2.2.1. It has since been demonstrated that these limitations were only true in a certain specific context, and that these limitations can be relaxed if other image acquisition schemes are employed. The following sections summarise a number of techniques which go beyond Abbe's predicted limit of spatial resolution. SR will be defined as resolution beyond that which would be possible with a single objective lens and given by equations (2.1) and (2.2). The suitability of each technique for live imaging is then discussed.

2.4.1 4Pi microscopy

Although this technique is not strictly a SR technique as it exploits additional resolution through the use of additional objective lenses, it is included here as it vastly increases the axial resolution compared to traditional methods. Traditional microscopy has a limited resolution due to the finite aperture of the collection optics. Fluorescence is emitted isotropically from each point in the sample, and a typical microscope objective can capture, at most, half of the emission, in the case of high NA, oil immersion lenses. This corresponds to approximately one hemisphere of the spherical emission [8]. By utilising a second high NA objective lens, aligned anti-parallel and confocal, on the opposite side of the sample (Fig. 2.10(a)), the remaining hemisphere can also be collected and used to compose the image [90]. This technique is called 4Pi microscopy as it allows access to nearly the full solid angle of the spherical fluorescence emission.

This method can be extended to use the confocal principle, wherein an intense point light source is imaged through both objectives into a single point in the sample and then the emission from this point is imaged through both objectives onto a point detector. The interference of illuminating wavefronts from each objective lens produce side-lobes on axis situated $\lambda/2$ above and below the focal point which distorts the PSF. 2-photon excitation (2PE) is generally used to reduce the intensity of the side-lobes. (Fig. 2.10(c); type-A). Figure 2.10(e) shows the increased axial extent of the MTF, indicating increased axial resolution. The use of dual-confocal detection (Fig. 2.10(d,f);

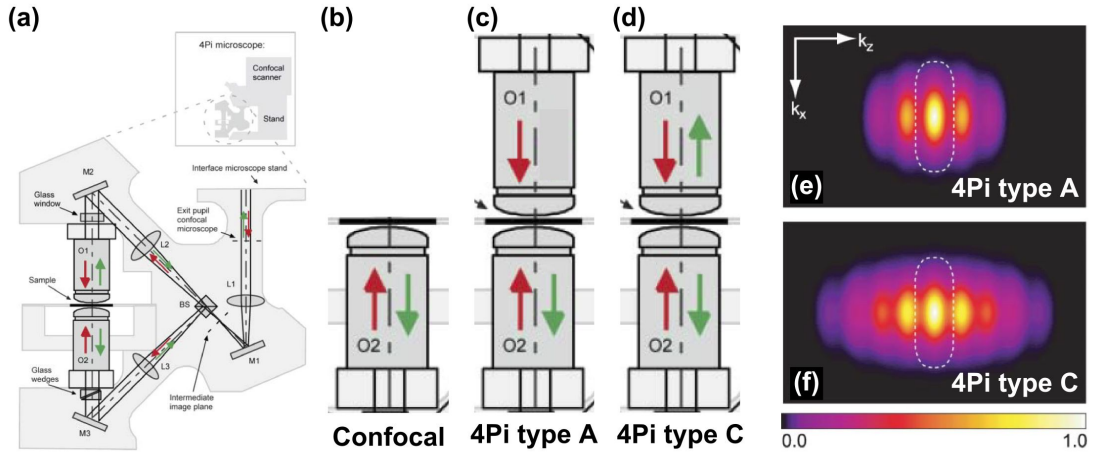

FIGURE 2.10: 4Pi microscopy schemes. (a) Optical system for a 4Pi microscope showing the dual confocal pathways above and below the sample. (b-e) Comparison of 4Pi illumination schemes. (b) Confocal microscope scheme for comparison, (c) dual-confocal 2PE illumination, single-confocal detection (Type-A), (e) Dual-confocal 2PE illumination, dual-confocal detection (Type-C). (e-f) MTF of (e) Type-A and (f) Type-C 4Pi microscopes showing increased axial extent. Dashed white line shows 2% threshold of a confocal microscope for comparison. Figure adapted with permission from [91].

type-C) further increases the axial resolution of the resulting image [90].

Due to the interference of the illuminating wavefronts, 4Pi microscopy does not extend the lateral resolution by two times as may be expected considering the NA of the microscope system has effectively doubled [90]. Instead, the lateral resolution is modestly enhanced by up to 1.5 times the resolution of a single objective illumination scheme. The main improvement is in the axial resolution, which can be improved by up to 5 times compared to the diffraction limit of a single lens system [90]. The 4Pi microscope is a point scanning method so imaging time scales with the volume to be imaged, it is most suitable for fixed samples where temporal resolution is not of importance or for imaging small volumes in dynamic samples.

The construction of a 4Pi microscope is very similar to that of a confocal microscope, and can therefore exploit the highly refined optical systems developed for this (e.g. scanning mirrors, pinhole selection). The additional complexity of the system stems from the precise alignment required between objective lenses, and of the optical pathways. The dual objective configuration limits the range of samples that can be imaged as only thin, coverslip-based samples will fit in the microscope.

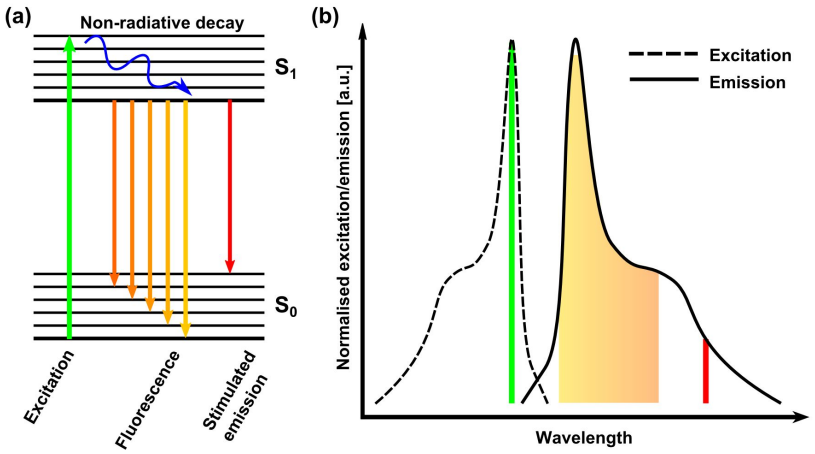

FIGURE 2.11: (a) Energy level diagram of STED fluorophore showing vibrational levels of ground (S_0) and excited (S_1) states showing excitation (green), non-radiative (blue), fluorescence (yellow/orange), and STED transitions (red). (b) Excitation and emission spectra of fluorophore showing spectral separation of excitation (green line), STED beam (red line) and fluorescence (yellow/orange area) which can be collected.

2.4.2 Stimulated emission depletion microscopy

Stimulated emission depletion (STED) microscopy exploits spatially selective promotion of non-fluorescent atomic transitions to achieve narrowing of the emission volume at the focus of a confocal microscope. Fluorescence emission is relatively broadband but the emission bandwidth is much narrower if the decay process is driven, as is the case in stimulated emission [22]. If a second laser (usually at a longer wavelength than the fluorescence signal to be collected) is used to illuminate the sample at a wavelength that drives stimulated emission of the excited state, fluorescence emission is inhibited. An energy level diagram (Fig. 2.11) illustrates the spectral separation required for STED. The STED principle normally requires precise temporal control of excitation and depletion beams to induce the correct photo-physical process at the correct time. The fluorophore must be excited to an upper state by the excitation beam, then irradiation by the depletion beam must occur before the fluorescence transition occurs. For this temporal control, pulsed lasers with precise pulse delays were used [22, 82] but implementations relying on stead-state conditions and utilising continuous wave (cw) lasers are also possible [92].

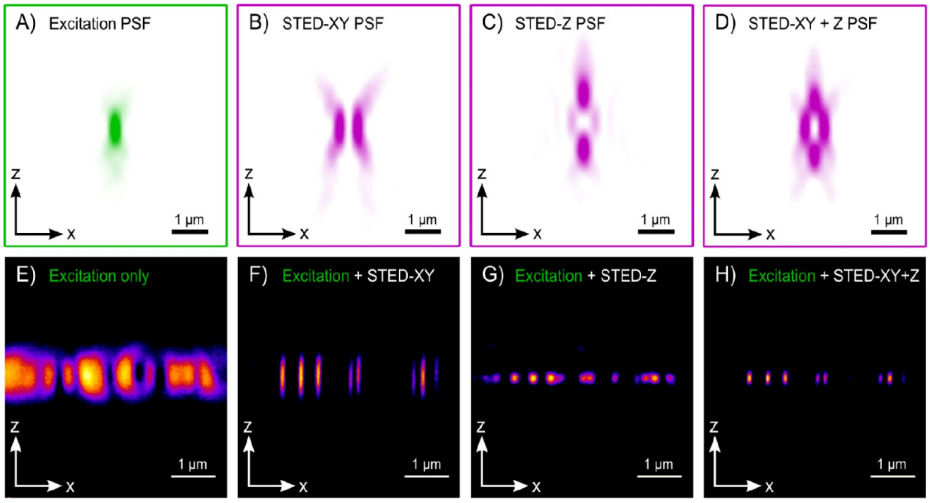

FIGURE 2.12: Experimentally determined excitation (a) and depletion (b-d) beam PSFs and their corresponding images of 100nm fluorescent beads below (e-h). (b,f) A Laguerre-Gaussian optical vortex narrows the PSF in x and y. (c,g) A bottle beam narrows the PSF along z. (d,h) Incoherent combination of (b) and (c) narrows the PSF in 3D. Figure used with permission from [93].

The concept of STED microscopy is to use different spatial distributions of fluorescence excitation and depletion light-fields to control and restrict the region of fluorescence emission [22]. This is demonstrated in Figure 2.12 which shows the excitation PSF (the same as for confocal microscopy; Fig. 2.12(a)) and the depletion PSFs most commonly used (Fig. 2.12(b-d)) along with the resulting images for each technique (Fig. 2.12(e-h)).

The depletion beam used in Fig. 2.12(b) is a Laguerre-Gaussian mode, or optical vortex, circularly symmetric in the $x - y$ plane. It is produced by imparting a spiral phase profile on a fundamental Gaussian mode [93] and contains a "dark core" of zero intensity. As inferred from its shape and evidenced by the image in Fig. 2.12(f), this depletion beam narrows the PSF laterally when the central intensity minimum of the depletion beam is aligned with the focal spot of the excitation beam. The other common depletion beam is shown in Fig. 2.12(c) and is the "bottle" beam [23, 94]. This beam has 2 intensity maxima, axially offset, which are connected by a weaker spherical shell of intensity. Figure 2.12(g) shows that this depletion beam gives mostly axial enhancement of the PSF, although some lateral improvement is gained from the weak shell. Figure 2.12(d) and 2.12(h) show the case of combining both depletion beams from

Fig. 2.12(b,c) to give maximum 3D resolution.

The resolution of a STED microscope is well approximated by [82]:

$$r_{x,y} = \frac{\lambda}{2\,\mathrm{NA}\,\sqrt{1 + I_{max}/I_S}} \tag{2.18}$$

where I_{max} is the maximum intensity of the depletion beam and I_S is the saturation intensity of the fluorophore. By increasing the intensity of the depletion beam, the resolution can be increased infinitely[2]. A limitation on the resolution that can be achieved with STED stems from engineering fluorescent dyes that can be excited and depleted at suitable wavelengths, and that can withstand prolonged exposure to high depletion beam intensities. STED has demonstrated resolutions of structures as small as 2.4nm in very specific scenarios [95] but in biological samples the lateral resolution is typically on the order of 40nm [92, 93, 96].

STED microscopy is a point-scanning method which limits the speed of imaging for large specimens, although it is a direct observation method in the sense that each point imaged has super-resolution and does not require combination of multiple images to achieve the enhanced resolution. Parallelised methods have been implemented which improve imaging speed but at the cost of increased optical complexity [97, 98].

2.4.3 Structured illumination microscopy

All microscopy techniques that employ the spatial control of illumination are technically structured illumination techniques; SIM is a term that describes a specific method where the illumination takes the form of a 1D or 2D periodic grid pattern consisting of only a few discrete Fourier components. SIM was originally developed as a method to yield optically sectioned images from a wide-field microscope [74] but was shown later by Gustafsson to be capable of lateral resolution enhancement also [99], and eventually extended to yield both lateral and axial resolution enhancement [32]. A summary of the SIM technique is presented below, a more detailed description of the theory can be found in Appendix A.

SIM was originally developed as a technique to achieve wide-field optical sectioning [74]. Neil *et al* illuminated the sample with light modulated in a sinusoidal pattern.

[2]The resolution of a fluorescent microscope cannot exceed the spatial extent of a single fluorophore.

This grating is sharply focussed only at the focal plane of the microscope, away from the focal plane each line of the grating is broadened and all blur together. This yields an illumination which illuminates only part of the focal plane, but gives uniform illumination to areas of the samples outwith the focal plane. Now if the grating is laterally translated, different regions of the focal plane will be illuminated at each position but the out of focus background signal will remain constant. Three images are acquired with $2\pi/3$ phase offsets to ensure that every point of the focal plane is maximally illuminated in at least one acquired image and fed into an algorithm. To use a simple analogy, the algorithm plays "spot the difference" with the images to separate out the modulated signal, originating from the focal plane, from the unmodulated signal, originating from the out of focus regions of the sample.

The use of patterned illumination was also found to enable higher resolution imaging than was previously possible. Gustaffson realised that the use of a periodic grating encodes high-frequency information, normally unobservable by the microscope, on a lower frequency carrier signal through the phonomenon of Moiré fringes [99]. This method is particularly beneficial in comparison to confocal microscopy because the resolution enhancement is achieved without rejecting any signal emitted by the sample. The principle of resolution enhancement by SIM is illustrated in Fig. 2.13.

Figure 2.13(a) shows the typical toroidal OTF of a microscope. Figure 2.13(b) demonstrates the principle of Moiré fringe formation. This difference frequency generation allows other regions of the sample's Fourier space to be observed by the microscope. Figure 2.13(c) shows the extended regions made accessible by sinusoidal illumination with a spatial frequency corresponding to half the diffraction limit, yielding optical section or an axial resolution benefit. Figure 2.13(d) shows the extended Fourier space imaged with a spatial frequency corresponding to the diffraction limit, yielding enhanced lateral resolution two times beyond the diffraction limit. Three images, each with the illumination grating laterally offset (a phase delay), are required in order to separate the information from each Fourier region and restore it to its original location [99]. The lateral resolution enhancement is only achieved along one axis, and must be repeated along other directions in order to fill a circle of the Fourier space, typically 3 orientations of illumination grating are used, mutually offset by 60° [99].

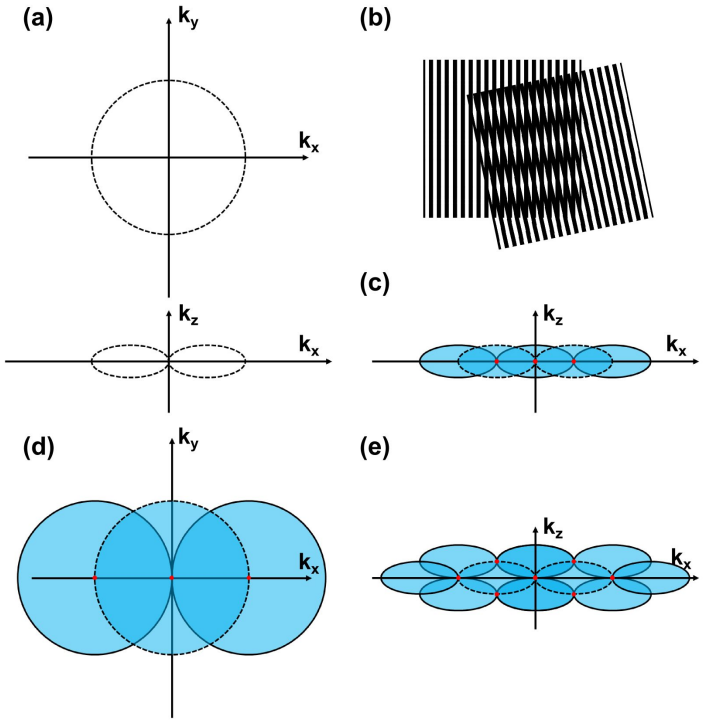

FIGURE 2.13: Extension of the OTF support range by structured illumination in various schemes. (a) $x-y$ (top) and $x-z$ (bottom) cross section of toroidal OTF. The dashed lines indicate the maximal extent of the OTF, corresponding to spatial frequencies of $2\,\mathrm{NA}\,/\lambda$ laterally and $\mathrm{NA}^2\,/2\lambda n$ axially. (b) Principle of Moiré fringe generation. (c) Extension of the OTF for optical sectioning (axial enhancement). (d) Extension of the OTF for lateral resolution doubling. (e) Extension of the OTF for lateral and axial resolution doubling. In (c-e) the dashed lines bound the traditional OTF, the extended OTF is shaded blue, and the Fourier components of the illumination are shown by red dots.

More complex illumination patterns, containing simultaneous lateral and axial modulations can achieve a 3D resolution enhancement. Figure 2.13(e) shows the extension of the Fourier space achieved using a grating with cross-section resembling a hexagonal lattice [32].

SIM is compatible with all standard fluorophores and only requires standard illumination intensities to yield a significant SNR. As a wide-field imaging method, SIM is intrinsically fast even if it is 15 times slower than standard wide-field microscopy. The main limitation to temporal resolution comes from the methods used to accurately shift the phase and orientation of the illumination grid.

Non-linear implementations of SIM (NL-SIM) rely on generating higher, harmonic Fourier components from the illumination pattern through the non-linear response of

the fluorophore to the illumination intensity [100]. A number of methods have been proposed to induce such a non-linear response, most notably fluorophore saturation [100, 101] and the use of photoswitchable fluorophores [102–104]. These methods can, in principle, give unlimited resolution but require an increasing number of raw images to be acquired with different grating phases and rotations to yield a SR image. To date, most uses of NL-SIM give lateral enhancement only and attain a resolution of approximately 45nm [100, 102].

2.4.4 Photoactivated localisation microscopy & stochastic optical reconstruction microscopy

Photo-activated localisation microscopy (PALM) and stochastic optical reconstruction microscopy (STORM) are both founded on the same principle but differ in their implementation. Consider the image of a single isolated fluorescent molecule. Although the image is diffraction limited, the knowledge that a only a single molecule constitutes the image allows more precise localisation of the molecules position through determination of the centre of the image spot. Neglecting background noise, the error in the estimation of the particle position is given by:

$$\sigma_{x,y} \approx \frac{s}{\sqrt{N}} \tag{2.19}$$

where s is the standard deviation of a Gaussian model of the microscope PSF and N is the total number of photons detected from the particle [105]. By this method, a single molecule may be localised to within nanometre precision. The concept of PALM and STORM is simple: if a number of images can be acquired sequentially, each containing a sparse subset of emitting fluorophores separated such that each diffraction limited image spot contains only one molecule, then a SR image may be obtained. This is simple for sparsely labelled specimens in which spatial resolution is not of strict importance [106, 107] but ensuring the sparsity of emitting fluorophores is challenging in microscopy, where fluorophore density can be as high as 10^5 $\mu\mathrm{m}^{-2}$ [105].

In PALM, the criteria that only a small subset of fluorophores can emit in a given

image frame is ensured through the use of photo-activatable fluorescent proteins (PA-FPs) - fluorophores which are naturally in a non-fluorescing conformation but which, by absorption of light, undergo a conformational change which allows fluorescence excitation and emission (for example photo-activatable green fluorescent protein (PA-GFP) [108], Kaede [109]). PA-GFP is a PA-FP which exists in a non-fluorescing state until exposed to light of $\lambda = 413$nm and can emit $\approx 10^{4-5}$ photons before permanently photobleaching [108]. By equation (2.19), this can potentially give very good localisation.

To acquire a SR PALM image, a small fraction of fluorophores are activated by irradiation with low intensity $\lambda = 405$nm light, the activation light is then turned off and fluorescence is excited in the sample. Multiple image frames are collected until the activated fluorophores become photobleached. The process is then repeated until all PA-FPs, or enough to construct an accurate image of the desired structure, have been activated and bleached. In each recorded frame, the isolated intensity spots are fitted with a Gaussian function to determine their centre and the results from all frames are combined to yield a single SR image [105, 110]. With PALM, the process is irreversible, as activated PA-FPs are permanently bleached during the acquisition process.

STORM maintains a sparse distribution of fluorescing molecules by exploiting different photophysical processes. STORM exploits photo-switchable fluorescent proteins (PS-FPs) which can be activated to a fluorescing state from exposure to light of a particular wavelength but can also be switched back to a non-fluorescing state by exposure to light of a different wavelength. The first such molecule was a pair of cyanine dyes, Cy5 bound in close proximity to Cy3 [111]. Red laser light, which produced fluorescence from the Cy5 molecule, would also switch the molecule to a non-fluorescing state, and the molecule could be re-activated by irradiation with green laser light [112]. More recently, photo-switching has been shown to be unnecessary for STORM imaging as a number of "blinking" dyes have been identified, which allows more standard fluorophores, in the presence of additional chemical buffers, to stochastically and reversibly switch between fluorescing and non-fluorescing states [113].

The acquisition process for STORM is very similar to that used for PALM. The sample is continually illuminated for fluorescence excitation. If PS-FPs are used, a low

intensity activation beam irradiates the sample such that a small but random fraction of the fluorophore population is continuously re-activated to produce a blinking effect. If naturally blinking samples are used, no additional steps are required. The intensity spots from each individual frame are then fitted and localised to compose a SR image as for PALM [112].

While PALM and STORM are very similar, they are fundamentally different and targeted for different applications. Due to the necessity for photobleaching of activated PA-FPs, PALM is not suitable for longitudinal studies on the same sample as the fluorophore population is depleted during the acquisition of a single SR image, whereas STORM continuously cycles the same fluorophores and so multiple STORM images can be acquired in series. The stochastic nature of STORM makes association of intensity spots across multiple recorded frames with a specific fluorophore difficult whereas in PALM, a fluorophore is bleached before acquiring information from others in close proximity and so greater photon statistics can be readily attributed to specific fluorophores.

2.4.5 Near-field scanning optical microscopy

The super-resolution techniques discussed so far are all far-field methods and are subject to diffraction. Light transmitted through a sub-diffraction limit aperture retains accurate information of the aperture shape in the near-field, and it is only upon propagation into the far-field that this information is lost. Hence, by using very small apertures to confine light, volumes smaller than the diffraction limit may be probed. Pohl *et al*, who were amongst the first to demonstrate this technique optically [114], compared this technique, somewhat incorrectly [115], to a doctor's stethoscope, however the analogy is still illustrative of the technique. With a stethoscope, a doctor may localise the position of the heart to within 10cm by scanning the stethoscope across a patient's chest, listening to the sound of the heartbeat. Pohl assumed a sound frequency of $30-100$Hz and a wavelength of 100m, therefore the resolving power of the stethoscope is approximately $\lambda/1000$, much more powerful than the $\lambda/2$ resolution of far-field microscopy. In a similar manner, near-field scanning optical microscopy (NSOM) involves scanning a sub-diffraction limited aperture across a sample [114, 116].

The intensity distribution remains comparable to the aperture shape, only over propagation of approximately half a wavelength so the NSOM probe must be very close to the sample (~ 250nm for visible light). Therefore it is preferable to have a probe that is sharply focussed and narrow in order to reach recesses of a rough sample surface. These probes generally consist of tapered glass pipettes, coated with a thin layer of aluminium [115]. The light is funnelled towards the pipette tip and the aluminium coating creates the aperture. Apertures much less than 100nm can be fabricated. A simplistic estimation of lateral resolution is given by the aperture width [114].

The near-field light is evanescent, and the intensity decay is approximately exponentially with increasing distance from the aperture. The axial response can therefore be very sensitive. The detected signal, which is back-scattered illumination or fluorescence emission, is collected back through the aperture and focused onto a detector, and is proportional to the exponentially varying illumination. Axial resolution can reach several nanometres due to this strong axial variation in signal [115, 117] but this limits the applicability of SNOM to the outer surfaces of structures.

NSOM scanning is point-by-point mechanical and so requires highly stable and accurate micro- and nano-positioning equipment and is generally slow [115, 117]. Long acquisition times are also common as the signal that can be emitted from such small volumes is typically very weak. Schemes exploiting multiple apertures to parallelise measurements have been explored [115] but the overall width of the probe is increased and makes structural recesses inaccessible.

2.4.6 Discussion of super-resolution techniques for live imaging

As summarised above, there are a wide range of SR imaging techniques available which all differ greatly in their implementation and their efficacy. The details of these techniques, as well as some examples of spatial and temporal resolution presented in literature are summarised in Table 2.1.

While the techniques discussed above differ significantly, they all share one common theme: spatial resolution may be gained at the cost of temporal resolution. Point scanning methods such as 4Pi microscopy, STED microscopy, and NSOM all directly

Method	Modality	Complexity	Fluorophore choice	Illumination intensity	Theoretical		
					$r_{x,y}$	r_z	r_t
4Pi	Point scanning	High	All	High	$\frac{\text{Abbe}}{1.5}$	$\frac{\text{Abbe}}{5}$	Low
STED	Point scanning	High	Limited	High	∞	∞	Low
SIM	Wide-field	Moderate	All	Moderate	$\frac{\text{Abbe}}{2}$	$\frac{\text{Abbe}}{2}$	$\frac{\text{Abbe}}{15}$
NL-SIM	Wide-field	Moderate	Limited	High	∞	∞	$\frac{\text{Abbe}}{30}$
PALM	Wide-field	Low	Limited	Low	∞	Abbe	V. Low
STORM	Wide-field	Low	Limited	Moderate	∞	∞	V. Low
NSOM	Point scanning	High	All	Moderate	20nm	2nm	V. Low

Method	Example				Additional notes
	$r_{x,y}$ [nm]	r_z [nm]	r_t [s]	Ref.	
4Pi	160	80	90	[90]	Thin samples only. Hard to align.
STED	35	90	2400	[93]	Low intensity methods becoming available (RESOLFT [82, 118]).
SIM	120	250	1.5	N/A	Example resolution given from performance of Nikon N-SIM
NL-SIM	45	100	0.5	[102]	TIRF used additionally in example to achieve enhanced axial resolution.
PALM	80	80	500	[105, 110]	Resolution limited by number of photons collected from each fluorophore. *A priori* knowledge of fluorophore density required.
STORM	25	50	120	[119, 120]	Resolution limited by number of photons collected from each fluorophore.
NSOM	20	2	6000	[117]	Surface imaging only. Slow due to physical (not optical) scanning.

TABLE 2.1: Summary of key parameters of selected super-resolution techniques. Theoretical estimations and examples from literature for the lateral, axial, and temporal resolutions, $r_{x,y}$, r_z, and r_t respecitvely. Due to differences in the exact imaging scenario, example resolution values may not be directly comparable across all imaging methods.

observe a sub-diffraction limited point, however this must be scanned to image a volume, and as a smaller point is used, the scan will take more time. Wide-field methods like SIM, PALM, and STORM capture an image of a large area simultaneously but multiple images must be acquired to construct a SR image. This may not be a drawback if fixed samples are to be imaged but presents challenges for live imaging. Live specimens require specific environmental conditions that may be difficult to replicate on a microscope stage for prolonged periods of time, and more importantly live specimens move which can cause image blur if long acquisition times are required.

Sample motion intrinsically couples the spatial and temporal resolution of a microscope. A spatial resolution of $x$nm is meaningless if the feature of interest in the sample moves greater than x in the time taken to acquire the image. For example, Table 2.1 shows that STORM has a lateral resolution of 25nm and a temporal resolution of about 2 minutes per SR image [119]. If a freely moving particle is imaged, a diffusion velocity of only 12.5 nm/min will be sufficient to blur the image and give an apparent resolution that is only 50nm, twice as large as expected. In terms of general live SR microscopy, this rules out NSOM and PALM/STORM, although they may be suitable for specific live imaging applications. Point scanning techniques are generally only suitable for imaging small sections of live specimens as the imaging time scales linearly with the volume to be imaged.

Point scanning methods typically utilise high intensity illumination in order to acquire an appreciable signal at each point in the scan. STED microscopy employs even higher intensity beams for depletion of fluorescence, and the sample can experience irradiation by cw intensities of over 100kW/cm^2 [82] and peak intensities up to 250MW /cm^2 have been reported [121]. Fluorophores are sensitive to light exposure and can photobleach very quickly in the presence of such high intensities [122]. Additional photo-damage to the biological specimen is often overlooked when quantifying imaging techniques but high intensity visible exposure has been shown to cause morphological defects during embryo development [54] and also to cause unwanted extraneous stimulation of the optic nerve [123]. For these reasons, it is preferential for live imaging to use a wide-field method which makes more efficient use of the photon budget.

Linear and non-linear implementations of SIM also require multiple images to construct a SR image but the number of images is relatively small - 9 images can yield 120nm lateral resolution across the entire image plane. Improvements in microscopy hardware are allowing faster and more sensitive image acquisition and more flexible control of beam shape. This can be seen in Table 2.1 which shows that the temporal resolution of a state-of-the-art NL-SIM system is faster than a commercial SIM system even though it must acquire at least twice as many raw image frames. Although other SR methods can achieve much higher spatial resolution, structured illumination methods have the best temporal resolution.

The demonstrated temporal resolution available with SIM, coupled with its wide-field acquisition and efficient use of the photon budget, its compatibility with all standard fluorophores, and its fairly low complexity, make SIM the current SR microscopy method of choice for live imaging applications. This Thesis explores the use of linear SIM for SR microscopy. Chapter 7 explores the use of SIM for diagnosis of fixed renal tissue sections. Though not a live imaging application, the speed of diagnosis can have a great impact on patient well-being and make more efficient use of finite man-power and hospital resources. Chapter 8 explores combination of SIM with optical manipulation to add functionality to the microscope.

2.5 Conclusions

This Chapter has described a range of optical (fluorescence) microscopy techniques developed for volumetric imaging and for SR imaging. Each technique has been discussed and compared for the purpose of live imaging where speed and photo-toxicity are critical parameters to consider.

For the imaging of large volumes, LSM is selected as the optimal technique, although LFM does show promise and merits future investigation. A number of methods have been exploited to overcome challenges associated with LSM, such as shadowing artefacts and limited axial resolution. The use of shaped light modes, most notably the Bessel beam, has shown the greatest potential in combination with LSM and so more beam shaping methods for LSM are considered in this Thesis. Chapter 4 considers the

properties required for high-resolution LSM over a large FOV and explores the use of an Airy beam for light-sheet illumination. Chapter 5 applies such an Airy beam based LSM to the problem of imaging at depth within turbid tissue (mouse brain slices) and compares performance against a Gaussian light-sheet in both normal and chemically cleared tissues. In Chapter 6, the Airy light-sheet principle is built upon with more advanced beam shaping strategies to increase light-sheet penetration depth and image uniformity in scattering tissue.

For imaging with excellent (super-) resolution, SIM is selected as the technique of choice for live imaging and long term observation. Although best suited for live specimens, the high temporal resolution offered by SIM can also be beneficial in a number of applications where fixed tissue is imaged but time constraints exist due to external factors rather than sample motion, such as medical diagnosis. Chapter 7 investigates the use of SIM to resolve diagnostically relevant features of nephrotic disease in kidney biopsy sections. In Chapter 8, optical trapping (see Chapter 3) is integrated into a microscope with SIM capability to give control over dynamic systems whilst imaging, working towards a functional SR microscope.

Although the challenges of large volumetric imaging, SR microscopy, and optical manipulation are addressed separately in this Thesis, a long-term goal would be to combine and integrate these techniques to achieve superior imaging techniques.

Chapter 3

Optical manipulation in the biomedical sciences

3.1 Introduction

The concept of moving and manipulating objects using only light originates from the 17th century when Johannes Kepler observed that the tails of comets always pointed away from the Sun and attributed this to a radiation pressure [124]. This idea was reinforced by developments in understanding at the turn of the 20th century: the Nichols-Hull experiment, demonstrating optical force [125, 126]; and Beth's experiment which demonstrated optical torque [127].

The magnitude of photon flux achievable in a laboratory setting is minuscule compared to that produced by the Sun and as such the optical forces which can be exerted are very small (on the order of a few picoNewtons) and were to remain unexploited for several decades. However, a smaller force simply needs a lighter object to act upon in order to yield significant acceleration and displacement. Moving from an astronomical scale to the laboratory necessitates the transition from macroscopic to microscopic objects.

In 1970, Ashkin performed the first demonstration of controlled optical manipulation of microscopic particles [128]. He demonstrated that focused laser light could propel microspheres ($1 - 2\,\mu\mathrm{m}$), and that two counter-propagating beams could be used to hold microparticles in place. Ashkin *et al* went on to show that a single, tightly focused laser beam is sufficient to optically trap particles in both the lateral and axial confinements of the beam's focal spot [129]. This 3D optical confinement has become

known as "optical tweezers". An optical trap is an overdamped harmonic oscillator [124], behaving like an ideal Hookean spring, and can be well characterised.

Advances in beam steering and beam shaping technology have greatly extended the potential applications of optical tweezers. Acousto-optical beam deflectors [130] and scanning mirrors [131] enable dynamical trapping of multiple particles in time-shared optical traps, much like spinning plates. Multi-beam interference [132] and spatial light modulators (SLMs) [133] also allow the creation of multiple dynamic traps. SLMs and fabricated diffractive and refractive optical elements, such as axicons [134], can generate non-Gaussian light modes which may be exploited for novel optical trapping applications. Laguerre-Gaussian beams [135], with an annular intensity profile with an optical vortex, or singularity, at its centre, have found applications in optical manipulation. These beams carry orbital angular momentum due to the helical wavefronts of the beam, and can cause particles to transit around the annulus [136]. The central intensity maximum of a Bessel beam can be exploited as an optical conveyor belt to passively transport microscopic particles over large distances [137]. In a similar manner, Airy beams can be used to move particles along curved trajectories and have been utilised to create an "optical snowblower" for moving particles between walled micro-chambers by transporting the particles up and over the wall [29].

Optical tweezers have revolutionised our understanding of the micro-world. The biological sciences in particular have benefited greatly from the ability to place and manipulate biological matter on a cellular scale in a sterile, non-contact way. This spatial and temporal control of populations of cells has enabled cell interaction studies, observation of phagocytosis [138–140], virus transfer [141], and the immunological synapse [142, 143] over the full evolution of these processes, and even the construction of synthetic tissue systems [144]. Optical tweezers can also be applied as force transducers, able to measure picoNewton [145] and even attoNewton forces [146] and have elucidated a number of biological mechanisms such as the motion of kinesin and dynein along cytoskeletal filaments [147–149], and even the growth of these filaments [150, 151].

This Chapter describes the origins of forces in optical traps and optical tweezers and how these can be quantified and characterised. The use of optical manipulation

in biomedical microscopy is also discussed, which leads on to a discussion of compact, fibre optical implementations of optical manipulation.

3.2 Forces from an optical trap

The mechanisms underpinning optical trapping depend on the relative size of the trapped object to the dimensions of the trap beam focus. When the diameter of the trapped particle is much smaller than the beam focus ($d \ll \lambda$), the Rayleigh approximation is valid and the particle can be considered a point dipole in an electric field gradient [129]; if the particle is much larger than the beam focus ($d \gg \lambda$), then the Mie approximation is valid and a geometric optics approach may be used to consider momentum transfer [152]; for particles of intermediate size ($d \approx \lambda$), the interaction falls into the Lorentz-Mie regime which requires complex modelling [124] and so will not be considered in this Thesis. However, it was shown that geometric optics reasonably approximates the angular intensity distribution as given by Mie theory for sphere sizes as low as $r = 10\lambda/\pi$ (see Chapter 12 of [153]) and that major discrepancies between methods occur at angles contributing very little to the total optical force [152].

3.2.1 Trapping in the Rayleigh regime

To consider optical forces in the Rayleigh regime, consider focused light incident on a transparent dielectric sphere with a diameter $2r \ll \lambda$ and refractive index n_2, immersed in a medium of refractive index n_1 such that the effective refractive index, $m = n_2/n_1$, is greater than unity. The sphere behaves like a point dipole in an inhomogeneous electric field. The forces acting on the dipole along the direction of light propagation are the scattering force, F_s, and the gradient force, F_g, which are given by:

$$F_s = \frac{I_0}{c}\frac{128\pi^5 r^6}{3\lambda^4}\left(\frac{m^2-1}{m^2+1}\right)^2 \tag{3.1}$$

$$F_g = -\frac{n_1 r^3}{2}\left(\frac{m^2-1}{m^2+1}\right)\nabla E^2 \tag{3.2}$$

where E is the electric field amplitude of the incident light and $I_0 \propto E^2$ is the light intensity [129]. Conservation of momentum dictates that the scattering force pushes the dipole forward along the optic axis of the incident light as the light is scattered isotropically from the particle. The scattering force increases linearly with the incident light intensity. The gradient force scales with the gradient of the intensity (∇E^2) and the force is directed towards the intensity maximum (i.e. the beam focus). This highlights the necessity for a tight beam focus and the use of high-NA microscope objectives to facilitate single-beam optical trapping; if a weakly focused beam is used it will not generate sufficient gradient force to overcome the scattering force and so the object will not be trapped stably. Another consequence of this force behaviour is that if the particle has a refractive index index lower than the surrounding medium ($m < 1$) then both F_s and F_g undergo a sign change and the particle will be repelled away from the beam focus. Figure 3.1(a) shows a schematic of the optical forces and their directions acting on a high-index ($m > 1$) Rayleigh sphere in a focused Gaussian beam.

3.2.2 Trapping in the Mie regime

For particles in the Mie regime, consider the Rayleigh sphere above now fulfills the criterion $2r \gg \lambda$. In this case geometrical optics can be used to determine the optical forces; the evolution of individual light rays can be traced as they scatter or refract from the surface of the sphere. As long as the Mie criteria is satisfied, there is no need to consider the Gaussian nature of the beam at focus, and rays that focus to an infinitesimal point are valid due to the large size of the sphere relative to the beam focus. Each ray has a defined intensity, direction, and polarisation; for a Gaussian beam which sufficiently overfills the input pupil of a lens, all rays will have similar intensity and uniformly fill a cone with maximum angle given by the numerical aperture of the lens.

Consider a pair of isolated rays incident of the sphere which are symmetric around the optic axis and act through the centre of the sphere. Light scattering from the particle will occur in the backwards direction, the change of momentum for each ray perpendicular to the optic axis will cancel each other whereas the parallel components will add, resulting in a forward acting force on the particle. Small displacements of the sphere from beam focus will still result in a force which has some component pushing

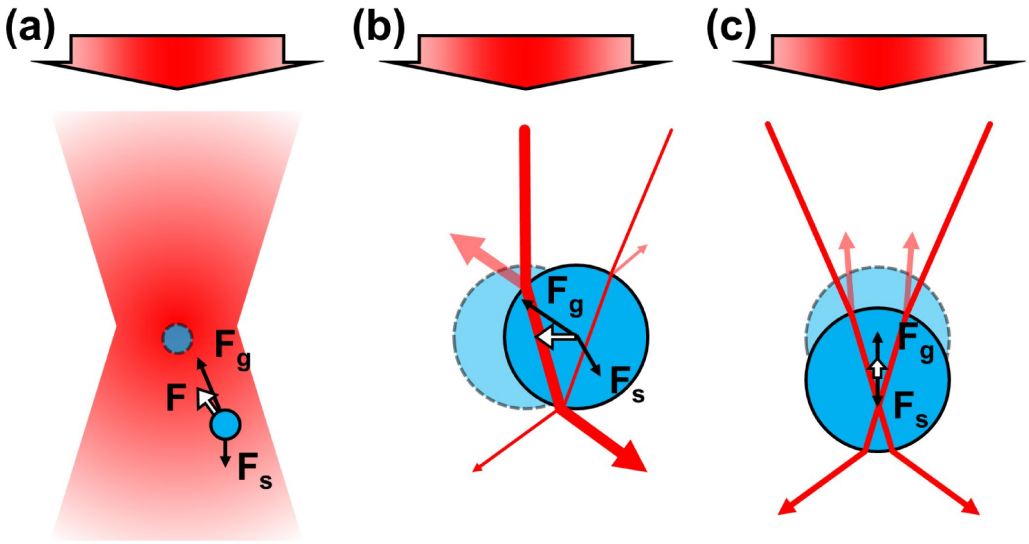

FIGURE 3.1: Schematic diagram showing optical forces acting on high-index ($m > 1$) dielectric spheres in the Rayleigh (a) and Mie (b-c) regimes. The scattering and gradient forces, F_s and F_g, are labelled by black arrows, The total optical force, F, is denoted by a white arrow, the equilibrium position is marked by a faint circle with dashed outline. (a) The scattering force acts in the direction of beam propagation whereas the gradient force is directed towards the beam focus. (b) Isolated rays from a Gaussian beam (intensity denoted by line thickness) reflected from and refracting through a sphere displaced to the right, the total force is directed to the left. (c) Isolated rays on a sphere displaced axially downwards, the total force is directed upwards.

the sphere in the direction of beam propagation. Light refracting through the particle centred on the beam focus will generate no force, the light rays will exit the particle with the same angle as they enter and there will be no net momentum transfer. Small displacements of the sphere from beam centre will result in a net momentum change in the light that causes a force on the sphere directed back to the beam focus. Figures 3.1(b,c) illustrate the forces on a high-index Mie sphere in a focused Gaussian beam which is displaced laterally and axially from the trap equilibrium position respectively.

Ashkin calculated the forces acting on a dielectric sphere using this model by considering the initial reflection, with power PR, and the infinite series of refraction events with power $PT^2, PT^2R, ..., PT^2R^n$, of an incident ray with initial power, P. R and T are the Fresnel reflection and transmission coefficients respectively for the medium-sphere interface at angle θ. Grouping all the contributions parallel to the optic axis as

the scattering force, F_s, and all the perpendicular contributions as the gradient force F_g yields the expressions:

$$F_s = \frac{n_1 P}{c}\left(1 + R\cos 2\theta - \frac{T^2[\cos(2\theta - 2\phi) + R\cos 2\theta]}{1 + R^2 + 2R\cos 2\phi}\right) \tag{3.3}$$

$$F_g = \frac{n_1 P}{c}\left(R\sin 2\theta - \frac{T^2[\sin(2\theta - 2\phi) + R\sin 2\theta]}{1 + R^2 + 2R\cos 2\phi}\right) \tag{3.4}$$

where ϕ is the angle of the refracted ray given by Snell's law [152]. R and T vary as a function of the input beam polarisation and as a function of the absolute refractive indices, n_1 and n_2. An effective index of refraction, m, greater than unity ensures the sphere acts as a positive lens and focuses the refracted light. For $m < 1$, R, T, θ, and ϕ are altered, create a negative lensing effect, and a repulsive gradient force [154, 155]. The balance of the scattering and gradient forces stably hold a particle in place close to the beam focus, but offset along the direction of beam propagation by a small distance.

Equations (3.3) and (3.4) can be re-expressed as:

$$F_s = Q_s \frac{n_1 P}{c} \tag{3.5}$$

$$F_g = Q_g \frac{n_1 P}{c} \tag{3.6}$$

where Q_s and Q_g are dimensionless parameters which depend on the geometry of the incident beam and the trapped particle. The total force acting on a particle is then:

$$F = Q \frac{n_1 P}{c} \tag{3.7}$$

where $|Q| = (Q_s^2 + Q_g^2)^{1/2}$. Figure 3.2 shows the dependence of incident angle on Q_s, Q_g, and Q for an isolated ray with circular polarisation and again highlights the necessity for high angle rays (i.e. a strong intensity gradient) in order to achieve a strong optical trap. The Q-factor gives a measure of force independent of the incident power and so can be considered as a measure of quality of the optical trap. The maximum theoretical value for Q is 2 but in practice this is much lower. Figure 3.2 shows that

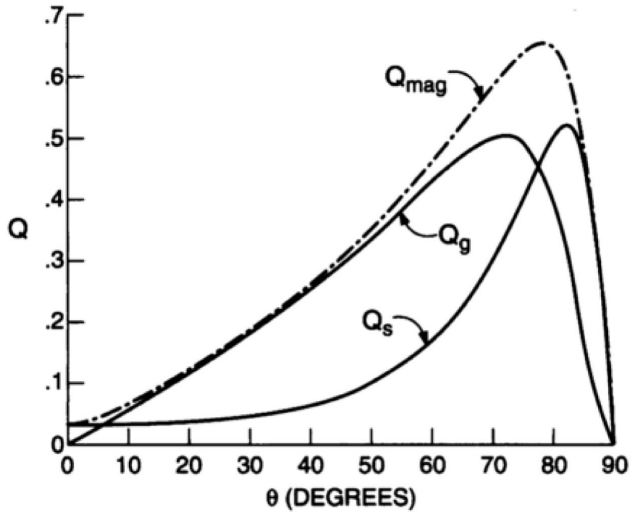

FIGURE 3.2: Plot of $|Q_s|$, $|Q_g|$, and $|Q_{mag}| \equiv |Q|$ versus incident angle θ for a single, circularly polarised ray incident of a sphere with $m = 1.2$. Figure used with permission from [152].

some highly inclined rays can achieve $Q \approx 0.5$ but, integrated over the incident beam, experimentally $Q < 0.3$ is typical [152].

3.3 Characterisation of an optical trap

It is interesting to consider that most optical trapping occurs in the Lorentz-Mie regime [124] despite the lack of accurate, analytic theory, and most studies adopt a characterisation and calibration based approach to determine the Q-factor and overall performance of their optical traps. The optical trapping probe presented in Chapter 8 is used to trap small microspheres and cells with diameters in the range $1 - 10\,\mu\text{m}$ and so fall into this category. Consideration is given to the methods commonly used to calibrate an optical trap.

An optical trap behaves as a microscopic Hookean spring and a linear restoring force will be felt by the particle for displacements up to several hundred nanometres from the equilibrium position. Optical trapping is generally performed in an aqueous medium and, in this case, the motion of a trapped particle is given by the Einstein-Ornstein-Uhlenbeck theory of Brownian motion and a Langevin equation with the

form:

$$m\frac{\partial^2 x(t)}{\partial^2 t} + \gamma_0 \frac{\partial x(t)}{\partial t} + k_{trap}x(t) = (2k_B T\gamma_0)^{1/2}\eta(t) \tag{3.8}$$

where x is the displacement of the particle from the equilibrium position of the trap, m is the mass of the trapped particle, γ_0 is the Stokes drag coefficient for a spherical particle in a fluid, k_{trap} is the trap stiffness and equivalent to the spring constant of a Hookean spring, $(2k_B T\gamma_0)^{1/2}\eta(t)$ is a random Gaussian function representing Brownian motion at temperature, T, and k_B is Boltzmann's constant [124, 156]. Equation (3.8) has been represented in one dimension for simplicity.

The inertial term in equation (3.8) can be neglected as the energy loss due to friction occurs on timescales given by the characteristic time, $t_{inert} \equiv m/\gamma_0$ which is typically $10 - 100ns$ whereas the characteristic relaxation time of the optical trap is on the order of milliseconds [156] and can be simplified to:

$$\gamma_0 \frac{\partial x(t)}{\partial t} + k_{trap}x(t) = (2k_B T\gamma_0)^{1/2}\eta(t) \tag{3.9}$$

which fully describes the observed motion of a trapped particle for small displacements from the trap equilibrium position.

3.3.1 Hydrodynamic-drag method

One of the simplest methods to calibrate an optical trap is to induce a fluid flow around the trapped particle. Neglecting the Brownian motion term in equation (3.9), the optical force on the trapped particle will be equal in magnitude to the Stokes drag force for small displacements of the particle from the trap equilibrium position. The trap stiffness will then be given by [157]:

$$k_{trap} = -\frac{\gamma_0 \nu_{flow}}{x} \tag{3.10}$$

The negative sign here is due to the opposing directions of the Stokes and optical forces. The flow velocity can be easily controlled using a motorised stage to move the sample chamber around a fixed optical trap at a known velocity. For this calibration method, the bead displacement, x, must be known, which requires accurate knowledge

of the trap and bead positions. These measurements are easily made with nanometre precision even with a simple CCD camera, as the centre-of-mass (COM) of the trapped particle can be easily determined from images of the bead with and without fluid flow. Brownian motion of the particle will result in a small experimental error that can be mitigated by repetition.

A measurement of trap performance that is independent of trap displacement, x, can also be performed using the hydrodynamic-drag method if the flow velocity is such that the Stoke's drag just overcomes the optical forces and the particle becomes freed. At this point, the linearity of the optical trap is invalid and so the trap stiffness, k_{trap}, is no longer a valid description of trap performance but by equating geometric and Hookean expressions for optical forces (equations (3.7) and (3.9) respectively) with equation (3.10) an expression for the Q-factor of the trap is determined:

$$Q = \frac{c}{n_1 P}\gamma_0 \nu_{flow} \tag{3.11}$$

Both implementations of the hydrodynamic-drag method above rely on good knowledge of the Stokes drag, γ_0 which is given by:

$$\gamma_0 = 6\pi\rho\nu r \tag{3.12}$$

where ρ and ν are the density and kinematic viscosity of the fluid respectively. Equation (3.12) is only valid in the bulk fluid, away from any interfaces, however, optical trapping is routinely performed in close proximity to a glass slide enclosing the fluid chamber. This restriction is generally imposed by the short working distances of high-NA microscope objectives required for high-quality trapping. Close to this interface the Stokes drag increases drastically and Faxen's correction must be included to modify γ_0. This modified drag coefficient for a spherical particle is given by:

$$\gamma = \frac{\gamma_0}{1 - \frac{9}{16}\left(\frac{r}{z}\right) + \frac{1}{8}\left(\frac{r}{z}\right)^3 - \frac{45}{256}\left(\frac{r}{z}\right)^4 - \frac{1}{16}\left(\frac{r}{z}\right)^5} \tag{3.13}$$

where z is the height from the surface to the centre of the bead [148, 157].

3.3.2 Equipartition method

The equipartition method relates energy with particle motion and uses this to infer the trap stiffness from the Brownian motion of a trapped particle in a static optical trap. The equipartition theorem is expressed as [157]:

$$\frac{1}{2}k_BT = \frac{1}{2}k_{trap}\langle x^2\rangle \tag{3.14}$$

where $\langle x^2\rangle$ is the variance of the displacement, x, from trap centre. From this expression, the trap stiffness may be determined from a trace of the bead centre coordinates with time acquired using either a CCD camera or calibrated quadrant photo-diode (QPD).

The equipartition method is only valid if the trap potential is harmonic which ensures the true distribution of x is Gaussian around the equilibrium position and if drift within the instrumentation is low compared to $\langle x^2\rangle$ otherwise this will broaden the distribution. Sufficient detector bandwidth is also required to accurately capture the behaviour of $\langle x^2\rangle$ otherwise the detector performs averaging of the particle position and the measured $\langle x^2\rangle$ is a low-pass filtered version of the true $\langle x^2\rangle$. Detectors with a low acquisition rate can be used to give accurate results for the equipartition method provided the integration time of the detector is taken into account [158].

3.3.3 Power spectral density method

Determination of the trap stiffness by the power spectral density (PSD) method is often considered the gold standard technique and has been used to give trap stiffness measurements with less than 1% calibration error [156, 157] whereas this error can be as much as 20% in some biological experiments [156]. This method analyses the motion of the trapped particle in the frequency-domain. The Fourier transform of the bead position with time has the form of a Lorentzian power spectrum:

$$S(f) = \frac{k_BT}{\pi^2\gamma_0(f_c^2 + f^2)} \tag{3.15}$$

where $[S(f)] = \text{nm}^2/\text{Hz}$, γ_0 is the Stokes drag and may be substituted by γ (equation (3.13)) whenever Faxen's correction is necessary, and $f_c = k_{trap}/2\pi\gamma_0$ is the corner, or roll-off, frequency which is dependent on the trap stiffness [157]. A harmonic trap potential is required for the PSD method which is expected as it is related to the equipartition method; using Parseval's theorem [159], the power spectrum can be integrated to yield the variance of trap position, $\langle x^2 \rangle$ [157]. A large detector bandwidth (in excess of $10 f_c$) is recommended to capture fine details in the spectral density. For this reason a QPD is generally used to perform PSD measurements but a fast camera may be utilised if correction for finite bandwidth [158] is applied. Interestingly, the power spectrum may be scaled by an arbitrary factor and this does not affect the corner frequency. As such, QPD measurements made in the linear range of the detector do not require a position calibration (V/nm) to determine the trap stiffness.

Instrument drift, anharmonic trap potentials, and other systematic imperfections in the trap apparatus will result in deviations away from a Lorentzian shape, and as such, the shape of the power spectrum may be used to elucidate the source of problems in the optical trap.

3.3.4 Discussion of optical trap characterisation methods

The hydrodynamic-drag method is the simplest method for characterisation of an optical trap. It requires only a very basic camera and a method to induce fluid flow around the trapped particle; either a motorised stage or microfluidic chip. However, only the Q-factor can be determined, and it is very difficult to accurately determine the trap stiffness from the hydrodynamic-drag method. Both the equipartition and PSD methods allow determination of the trap stiffness and are preferable to the hydrodynamic-drag method.

The equipartition and PSD methods both rely on the same experimental measurements for determination of the trap stiffness, traces of particle position as a function of time. The equipartition method is effectively a random sample of particle positions and so the time between samples is less crucial. Detectors with a long integration time will still smooth out high-frequency variation in particle position and short integration

times should be used if possible. The analysis of the data is also relatively straightforward.

The PSD method is considered to be the gold standard technique for trap stiffness determination [156]. Generally a QPD is used to acquire the data for PSD analysis as high temporal resolution yields more accurate results, this is necessary for very high quality traps. The data analysis for the PSD method is more involved than for the equipartition method but yields more accurate results as it is based on an accurate model of particle motion rather than simple random error.

The equipartition method relies on an assumed temperature of the trapped particle and so is prone to error in situations where significant heating may occur at the trap position [160]. The PSD method also relies on temperature but also includes details of the viscosity of the medium surrounding the trap, which is temperature dependent and reduces the impact of unknown temperature on the measurement [160].

3.4 Optical manipulation in microscopy

Almost all optical trapping experiments are integrated into some form of rudimentary microscope with brightfield illumination, but in most cases this is simply to locate targets to be trapped, verify trapping, and to perform COM localisations of these targets. Utilising more advanced forms of microscopy with optical manipulation can yield much more information from studies, indeed in the biological sciences, fluorescence microscopy techniques have been particularly revolutionary and present interesting opportunities for integration with optical manipulation. Even a basic epi-fluorescence microscope combined with optical tweezers can be used to observe Förster resonance energy transfer (FRET), indicating structural changes at the single molecule level in response to mechanical perturbation [157].

Although optical tweezers can provide sensitive force measurements, even the simple ability of optical manipulation to pick up or put down a cell at will within a spatio-temporal domain, coupled with advanced imaging methods, has enabled a number of studies into dynamic biological processes such as pathogen transfer [138], and virological [141] and immumological synapses [142]. These three studies all utilised confocal

microscopes with optical tweezers capability provided through the same high NA objective lens as was used for imaging, a technique first exploited by Hoffman *et al* [161]. One consequence of this configuration is that both the image plane and trapping plane within the sample move as the objective is scanned as they are delivered into the sample by a common objective lens. In this case, additional engineering solutions must be implemented in order to move the image plane independently from the trapping plane and acquire a volumetric image.

Hoffmann *et al* achieved this by axial translation of a fibre tip which is imaged into the sample and delivers the trapping laser [161]. The translation of the fibre had to be calibrated and moved synchronously with the microscope objective to keep the trapping plane fixed while the image plane was scanned. Other schemes have utilised the trapping geometry described by Fällman and Axner [162], with which the trapping plane can be axially translated by the axial translation of a lens in the trapping beam path with a static objective lens. This scheme has enabled confocal and multiphoton microscopy of tweezed samples, with volumetric images built up by scanning the trapped objects through the image plane [163], and super-resolution microscopy of protein dynamics on trapped DNA strands by stimulated emission depletion (STED) nanoscopy [164]. The trapping beam geometry of Fällman and Axner has also been applied to light-sheet microscopy [165], incorporating the reflected beam, or "macro-tweezers", geometry by Thalhammer *et al* [166, 167] to facilitate optical trapping of large specimens with a single, low-NA objective lens.

Other techniques include holographic generation of the trapping beam or beams via a programable device such as an SLM; the axial position of the trap can then be translated holographically by applying a quadratic phase across the beam profile [168]. This holographic trap generation has recently enabled three-dimensional imaging of trapped objects by temporal focusing [169]. Complete decoupling of the imaging and trapping optics can be achieved by delivering the trap beam through another microscope objective on the other side of the sample from the imaging optics [170].

All of the methods detailed above facilitate advanced microscopic imaging of optically trapped specimens but they all require a high degree of optical systems knowledge that the intended end-user for such a system will very rarely possess. Most proposed designs involved shared optics for the trapping and imaging beam paths [161, 163–165, 169] which requires synchronised scanning elements and may introduce aberrations to the imaging pathways. Having completely independent imaging and trapping beam paths [170] is highly desirable but places additional constraints on sample choice as two high-NA objective lenses are required.

3.5 Fibre based optical manipulation

Optical manipulation has relied on the use of high-NA objective lenses which are expensive, bulky, and, relative to their size, have a very short working distance. These factors severely restrict the use of optical tweezers and preclude endoscopic applications and integration with equipment which is in itself bulky and spatially constrained (e.g. an advanced microscopy platform). Optical fibres are low cost and have a very small size which make them an attractive prospect for optical trapping if sufficient gradient force can be generated. The first optical fibre traps (OFTs) utilised basic, low-NA optical fibres and circumvented the issue of low-NA in a dual-beam counter-propagating geometry [171]. In this setup, particles are trapped between two co-linear and anti-parallel optical fibres. The scattering force from both fibres cancel whereas the gradient force adds. This geometry is easily integrated into a microfluidic chip which can sit atop a microscope with both fibres and the trap location lying in the focal plane of the microscope and has been exploited for applications such as cell stretching [172]. Variations on this device, utilising laterally offset or angled fibres, have facilitated rotation of trapped particles, so-called "optical-spanners" [173, 174].

The low NA of optical fibres has precluded their use for full, 3D optical tweezers, but has still enabled 2D fibre optical trapping on or near the bottom of a sample chamber. Many cell-cell interaction studies can be carried out in 2D as biologists are familiar with working with cultures of 2D cell monolayers and 2D OFTs can still compliment biological experiments.

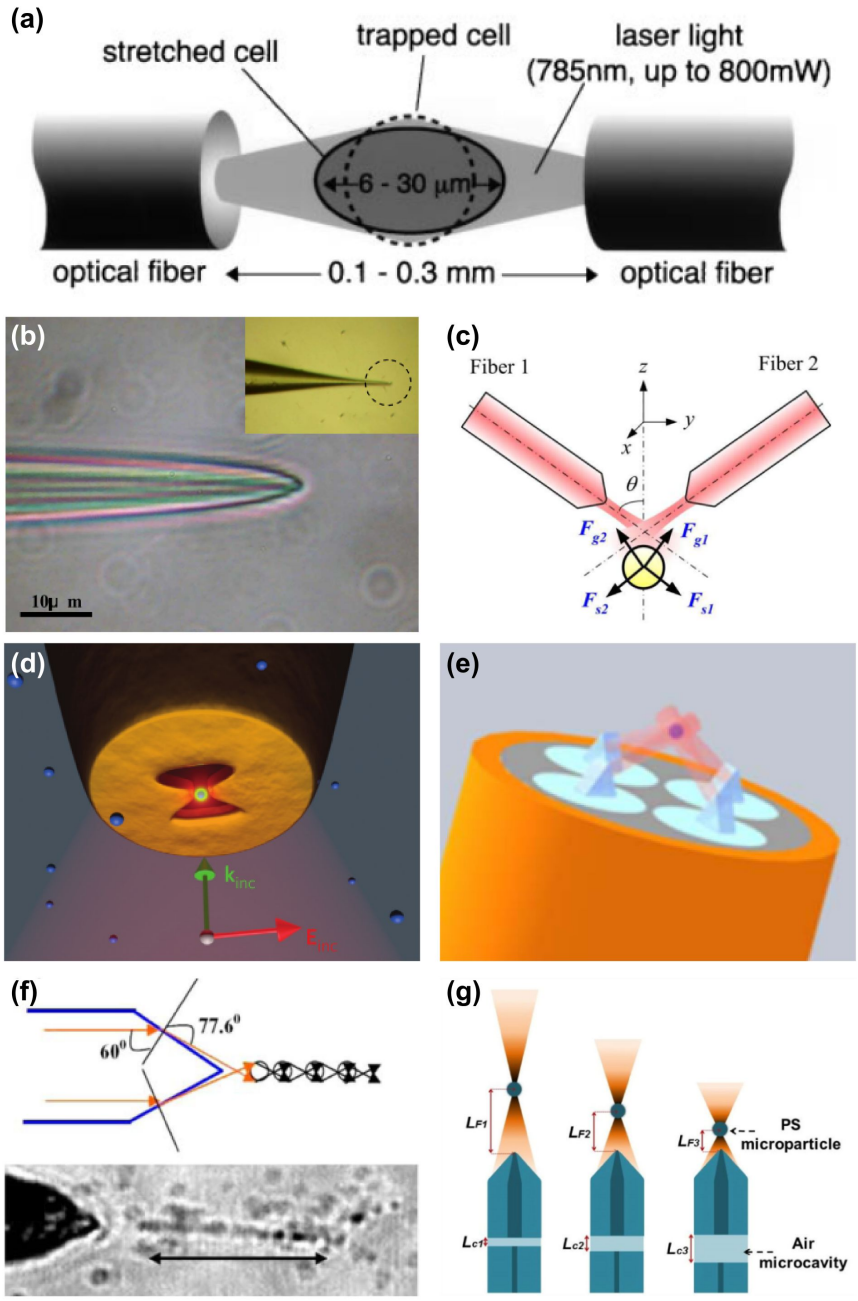

FIGURE 3.3: Schematics and artistic renderings of various optical fibre trapping probe designs. (a) Counter-propagating optical fibres trap and stretch cells in the area between the fibre tips [172]. (b) Microscopic brightfield image of a tapered OFT probe tip [175], insert shows larger section of probe. (c) Two tapered fibres are inclined relative to the z-axis to create a strong gradient force [176]. (d) Near-field optical tweezers with bowtie plasmonic aperture fabricated on the fibre tip [177]. (e) Reflected beam OFT with microfabricated micro-prisms centred on each of the 4 fibre cores [178]. (f) Schematic (top) and brightfield image (bottom) of trapped particle chains by optical binding [179]. (g) OFT based on a GRIN-MM fibre tip, effect of varying the air cavity length, L_{cj} on focal length, L_{Fj} [180]. PS: Polystyrene. All figures used with permission from their respective references.

There has been emphasis on engineering optical fibres with increased NA in order to facilitate 3D trapping with an OFT. A simple approach is to heat and draw the end of the fibre such that the fibre tapers and forms a fine point as demonstrated by Liu *et al* [175]. Their approach involved heating and pulling the fibre in multiple stages to reduce the diameter of the fibre from $125\,\mu\mathrm{m}$ to approximately $10\,\mu\mathrm{m}$ and achieve a parabolic tip shape. This focused the light to a $1\,\mu\mathrm{m}$ diameter focal spot at a distance of $1.2\,\mu\mathrm{m}$ from the end of the fibre tip which propagated with a divergence angle of $30°$. This highlights a major drawback of 3D OFTs; the working distance, or manipulation length, is cripplingly small. Optical trapping is favoured for being a sterile, non-contact method for manipulation of particles but all objects with a diameter of approximately $3\,\mu\mathrm{m}$ or greater will be in physical contact with the OFT probe described in [175]. Tapered OFTs can also be achieved through chemical etching processes [179, 181, 182] though the same drawback of short manipulation length is encountered. Other approaches to increase the NA of OFTs have included using multiple highly inclined fibres [176], micro-fabrication of angled mirrors [178, 183, 184] or plasmonic structures [177, 185] at the tip of the fibre, micro-lens tipped fibres [186], and optical binding [179] although these techniques still struggle to achieve manipulation lengths of more than a few tens of microns.

The OFT solutions above use a single-mode (SM) fibre, or an array of SM fibres which elucidates the intrinsically short manipulation length of these devices. A SM fibre has a core diameter typically less than $10\,\mu\mathrm{m}$, and is significantly smaller after tapering. From geometric considerations, a SM fibre with $\mathrm{NA} = 0.8$ and a core diameter of $10\,\mu\mathrm{m}$ yields a manipulation length of only $6.6\,\mu\mathrm{m}$. A recent approach utilising gradient-index (GRIN) multi-mode (MM) fibres by Gong *et al* [187] shows promise to achieve long manipulation lengths as the core diameter of MM fibres is an order of magnitude larger than for SM fibres. GRIN-MM fibres have a periodic lensing effect and this was combined with a chemically etched taper after an appropriate length of fibre to produce an optical trap with manipulation length of approximately $5\,\mu\mathrm{m}$ and with Q-factor of 0.095. This technique was built upon by introducing a tunable air cavity between the lead-in SM fibre and the GRIN-MM fibre which extended the manipulation length to approximately $50\,\mu\mathrm{m}$ [188], and up to $177\,\mu\mathrm{m}$ when optical forces

from the GRIN-MM fibre were balanced with a microfluidic flow [180], but these techniques still require precise shaping of the fibre tip. More sophisticated approaches have performed optical trapping at the tip of a MM fibre by characterising the transmission matrix of the fibre and shaping the light transmission through the fibre [189]. This technique allows manipulation at arbitrary distances from the fibre tip, however the trap strength decreases with increased manipulation length and requires complex optical systems to implement. Figure 3.3 shows the probe design and geometry for some of the OFTs described above.

3.6 Conclusions

Optical manipulation allows precise control over biological matter at the cellular level, can be used to trigger interaction events, and can offer unique insights into mechanotransduction. The combination of optical manipulation with advanced microscopes adds an extra dimension to biological studies as specific aspects of processes can be started arbitrarily and followed *in toto* with fluorescent probes. With optical manipulation, the microscope becomes a truly functional tool.

Interestingly, OFTs have been remarkably under-exploited for biological studies and no use of an OFT on an advanced microscopy platform has been reported to date. The very small footprint of an OFT probe simplifies microscope integration but existing OFT designs have limited manipulation ability. In Chapter 8, an OFT probe for use with an advanced imaging platform is presented and is integrated into a commercial SIM system.

Chapter 4

Light-sheet microscopy using an Airy beam

Parts of this Chapter are adapted from the article "Light-sheet microscopy using an Airy beam" [18], published in Nature Methods (2014).

4.1 Introduction

This Chapter describes the use Airy beams for illumination in LSM. The axial resolution and FOV of an Airy light-sheet, and light-sheets generated from related transversally asymmetric beams is investigated by examining the axial modulation transfer function (MTF) of each beam. This is then described analytically for Gaussian, Bessel, and Airy beams.

A prototype system for demonstrating the use of Airy beams for LSM is described, critically evaluated, and upgraded for greater performance. These systems are used to test the theory presented through imaging of point probes and biological specimens. The phototoxicity of each light-sheet type is also experimentally evaluated.

4.2 Properties of an ideal light-sheet

As discussed in Chapter 2.3, there are two, somewhat divergent, illumination schemes under the banner of LSM. In the first, both the lateral and axial resolution is dictated by

the fluorescence detection lens and the width of the light-sheet is chosen to minimise irradiation of the sample outwith the focal volume, i.e. the width of the light-sheet is chosen to be minimal across the desired FOV but remains approximately equal to or larger than the DOF of the detection lens, $4\lambda n/\mathrm{NA}_d^2$, where NA_d is the numerical aperture of the detection lens. This scheme functions identically to epi-fluorescence microscopy but with a greatly improved signal-to-noise ratio (SNR). In the other scheme, the light-sheet may be focused to a width that is narrower than DOF, providing increased axial resolution but at the cost of a more restricted FOV due to the divergence of the focussed sheet. Here, only the latter configuration is considered, such that isotropic resolution can be achieved.

The obvious choice for an ideal light-sheet would be one which maintains a narrow width over a large FOV which is why the propagation invariant Bessel beam has been of interest in a number of high-resolution LSM studies [5, 19, 20, 59, 60, 88, 190]. However, with the aid of deconvolution this is not the only choice. Any light-sheet which forms an image that can be accurately deconvolved to yield a high resolution image of the sample will fit the criteria. Considering resolution in the spatial frequency domain, the light-sheet can yield high resolution if it supports high spatial frequencies. This is measured by the MTF, which is the absolute value of the OTF, the Fourier transform of the light-sheet PSF. Here, only the MTF in the axial direction is considered.

Propagation invariance is not a strict criteria either, any light-sheet with a cross-sectional profile that varies with propagation is still beneficial as long as the cross-sectional MTF supports high spatial frequencies at all points across the desired FOV.

The problem of the ideal light-sheet is essentially equivalent to the problem of achieving an extended DOF whilst retaining good lateral resolution which has been demonstrated using cubic phase modulations in the pupil plane of the detection lens (e.g. [191]). Cubic phase modulation of a coherent Gaussian beam yields an Airy beam [27], and are therefore a good starting point in designing a light-sheet that gives high-resolution over an extended FOV.

4.2.1 Airy beams

Much like the Bessel beam is a propagation-invariant solution in analogue of the Helmholtz equation, the Airy beam is in analogue of a dispersion-free solution of the Schrödinger equation for a free particle [27]. The electric field of an Airy beam can be expressed as:

$$E(x,z) = \mathrm{Ai}\left(\frac{x}{x_0} - \frac{z^2}{4k^2x_0^4}\right)\exp\left(i\frac{xz}{2kx_0^3} - i\frac{z^3}{12k^3x_0^6}\right) \tag{4.1}$$

where Ai is the Airy function, x is the transverse coordinate, x_0 is a characteristic transverse length, z is the propagation distance, $k = 2\pi n/\lambda$ is the wavevector where n is the refractive index [28, 29]. At the origin, $E(x,0) = \mathrm{Ai}(x/x_0)$ and, like the Bessel beam, this remains invariant upon propagation. Unlike the Bessel beam however, the Airy beam undergoes a transversal shift, or acceleration, upon free propagation [28], the main lobe of the Airy beam following a parabolic trajectory (Fig. 4.1) described by [29]:

$$x(z) = \frac{z^2}{4k^2x_0^3} \tag{4.2}$$

Perhaps the most interesting property of the Airy beam is that it can be produced in a low dimensional space. Note that equation (4.1) features only one transverse coordinate and so can be produced in a planar (2D) space, a 1+1D Airy beam [28]. In contrast, Bessel beams rely on interference of conically arranged wavevectors in a 3D space to achieve propagation invariance. The Airy solution can therefore also be applied in the temporal domain to yield non-dispersive pulses [27] and 2+1D Airy beams (Airy beams in a 3D space) can be produced by described by the separable solution:

$$\begin{aligned} E(x,y,z) &= E(x,z)\cdot E(y,z) \\ &= \mathrm{Ai}\left(\frac{x}{x_0} - \frac{z^2}{4k^2x_0^4}\right)\exp\left(i\frac{xz}{2kx_0^3} - i\frac{z^3}{12k^3x_0^6}\right) \\ &\quad\cdot \mathrm{Ai}\left(\frac{y}{y_0} - \frac{z^2}{4k^2y_0^4}\right)\exp\left(i\frac{yz}{2ky_0^3} - i\frac{z^3}{12k^3y_0^6}\right) \end{aligned} \tag{4.3}$$

The Airy beam solution in equations (4.1) and (4.3) contains infinite energy. Finite energy approximations can be described by applying an exponential apodization such

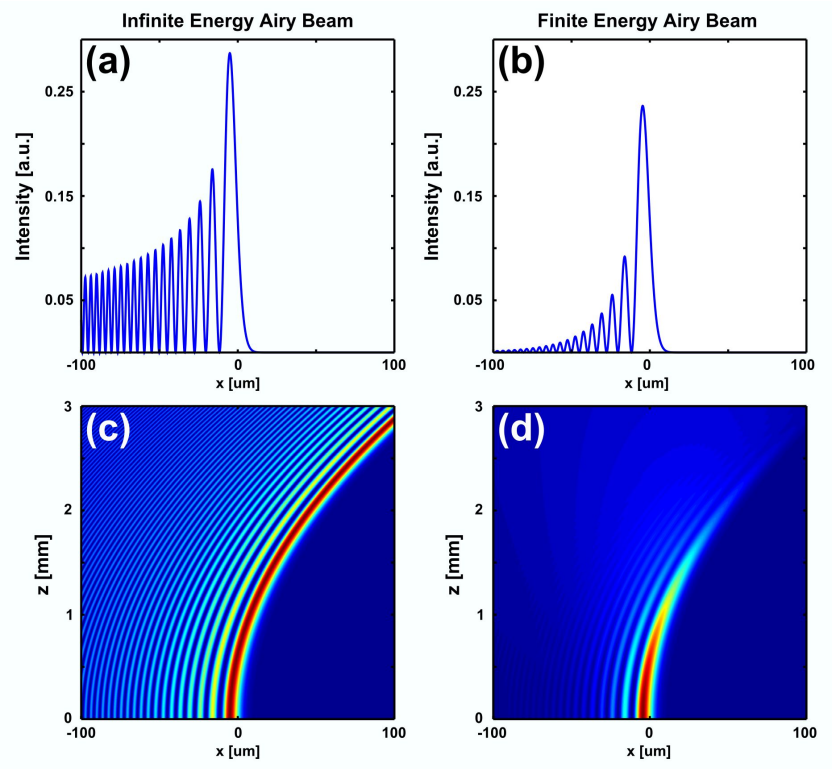

FIGURE 4.1: Intensity profiles of infinite energy (a,c; equation (4.1)) and finite energy (b,d; equation (4.4)) Airy beams. (a,b) Cross-sectional intensity profile at $z = 0$, (c,d) parabolic trajectory of the main lobe. Simulation performed with the following parameters: $\lambda = 500$nm, $n = 1$, $x_0 = 5\,\mu$m, $a = 0.1$.

that $E(x,0) = \mathrm{Ai}(x/x_0)\exp(ax/x_0)$ [28], equation (4.1) then becomes:

$$E(x,z) = \mathrm{Ai}\left(\frac{x}{x_0} - \frac{z^2}{4k^2x_0^4} + i\frac{az}{kx_0}\right)\exp\left(i\frac{xz}{2kx_0^3} - i\frac{z^3}{12k^3x_0^6} + \frac{ax}{x_0} - \frac{az^2}{2k^2x_0^4} + i\frac{a^2z}{2kx_0^2}\right) \quad (4.4)$$

where a is positive to ensure exponential decay, but $a \ll 1$ ensures the finite energy beam retains all the special properties of its infinite energy counterpart over some range [28]. Figure 4.1 shows the transverse structure at $z = 0$ and the parabolic evolution for infinite and finite energy Airy beams.

The Fourier spectrum of the Airy field (at $z = 0$) is:

$$E(k) = \exp(-ak^2)\exp(i[k^3 - 3a^2k - ia^3]/3) \quad (4.5)$$

Equation (4.5) reveals that the Fourier spectrum of the Airy beam is Gaussian, with

a cubic phase modulation in k and so can be easily generated from imparting a cubic phase modulation in the pupil plane of a lens [27, 29].

4.2.2 Parameter study of asymmetric light-sheets

The Airy beam is a specific example of a beam which does not exhibit transverse symmetry and so a parameter study was performed to explore a wide range of transversally asymmetric beams, including the Airy beam, and evaluate their suitability for high resolution LSM. Light-sheet cross-sectional intensity profiles were simulated by taking the Fourier transform of the pupil function with a defocus term applied (see Appendix C) to determine the beam shape over a propagation range. The parameters for the simulation were chosen to reflect experimental conditions for a light-sheet microscope with a spatial light modulator (SLM) that could be reconfigured to illuminate with arbitrary beam types which had previously been used to explore aberration correction in LSM [72] and is described in detail in Chapter 4.3. The relevant parameters for the study are summarised in Table 4.1. Note that both beam propagation and the optic axis of a microscope are commonly defined as the $z-$axis, in order to preserve the $z-$axis of the microscope, propagation of light-sheet illumination is herein defined along the $x-$axis.

Parameter	**Value**
Objective NA	0.42
Objective magnification	40
Objective tube lens focal length	200mm
Objective pupil function	$P(u) = \exp[2\pi i\phi(u)]$
Illumination polarisation	Circular $(P(u)\hat{\boldsymbol{u}}/\sqrt{2} + iP(u)\hat{\boldsymbol{v}}/\sqrt{2})$
Illumination λ	532nm
Sample refractive index	1.33
Sample x-range	[-300:0.1:300] μm
Sample z-range	[-50:0.1:50] μm

TABLE 4.1: Parameters used in asymmetric light-sheet parameter study.

The cylindrical pupil functions explored all have constant amplitude across the pupil but vary by a phase profile, $\phi(u)$. The pupil coordinates are normalised to $2\,\mathrm{NA}\,/\lambda$ such that $|u| = 1$ corresponds to the highest spatial frequency transmitted by the objective. The majority of phase profiles explored have the form of either equations (4.6),

naturally asymmetric (odd) single-term polynomials, or (4.7), asymmetric versions of naturally symmetric (even) single-term polynomials:

$$\phi(u) = Au^{2\gamma+1} \tag{4.6}$$

$$\phi(u) = \mathrm{sgn}(u)Au^{2\gamma} \tag{4.7}$$

where A is a scaling factor used to tune the strength of phase modulation, and γ is an integer. Light-sheets were simulated for $A = 1, 3, 7$ to allow selection of the best profiles for comparison. Some more exotic examples were also simulated. For each light-sheet profile, the axial MTF, which gives an indication of the attainable resolution after deconvolution, was determined at various positions along the beam propagation, at the typical Gaussian beam focus ($x = 0$), away from focus ($x = +25\,\mu\mathrm{m}$), and very far from focus ($x = +100\,\mu\mathrm{m}$).

The results of these simulations are shown in Figs 4.2 and 4.3. The results for all beams are compared with that of a focused beam. As all light-sheets compared contain the same distribution of spatial frequencies, they are all theoretically capable of the same resolution.

Figure 4.2 shows the results for phase profiles in the form of equation (4.6) (Fig. 4.2(b-e)) and for two phase profiles based based on the tangent and inverse tangent functions (Fig. 4.2(f-g)). Figure 4.3 shows the results for phase profiles in the form of equation (4.7) (Fig. 4.2(c,e,g)) along with their corresponding symmetric counterparts (Fig. 4.2(b,d,f)). These beams all have an intensity maximum that changes transverse coordinate as it propagates and accompanying side-lobes as a result of interference to produce such a curved trajectory. The MTF of these beams at $x = 0$ has lower support of high spatial frequencies than the focussed Gaussian but this is reversed away from focus. The support (magnitude) of the MTF at high frequencies is ultimately low valued for these beams, however, it remains non-zero and is therefore suitable for use with a deconvolution algorithm to restore an image with resolution corresponding to the highest non-zero spatial frequency present in the illuminating light-sheet [192]. In practice, noise will impose a positive threshold which the MTF must remain above in

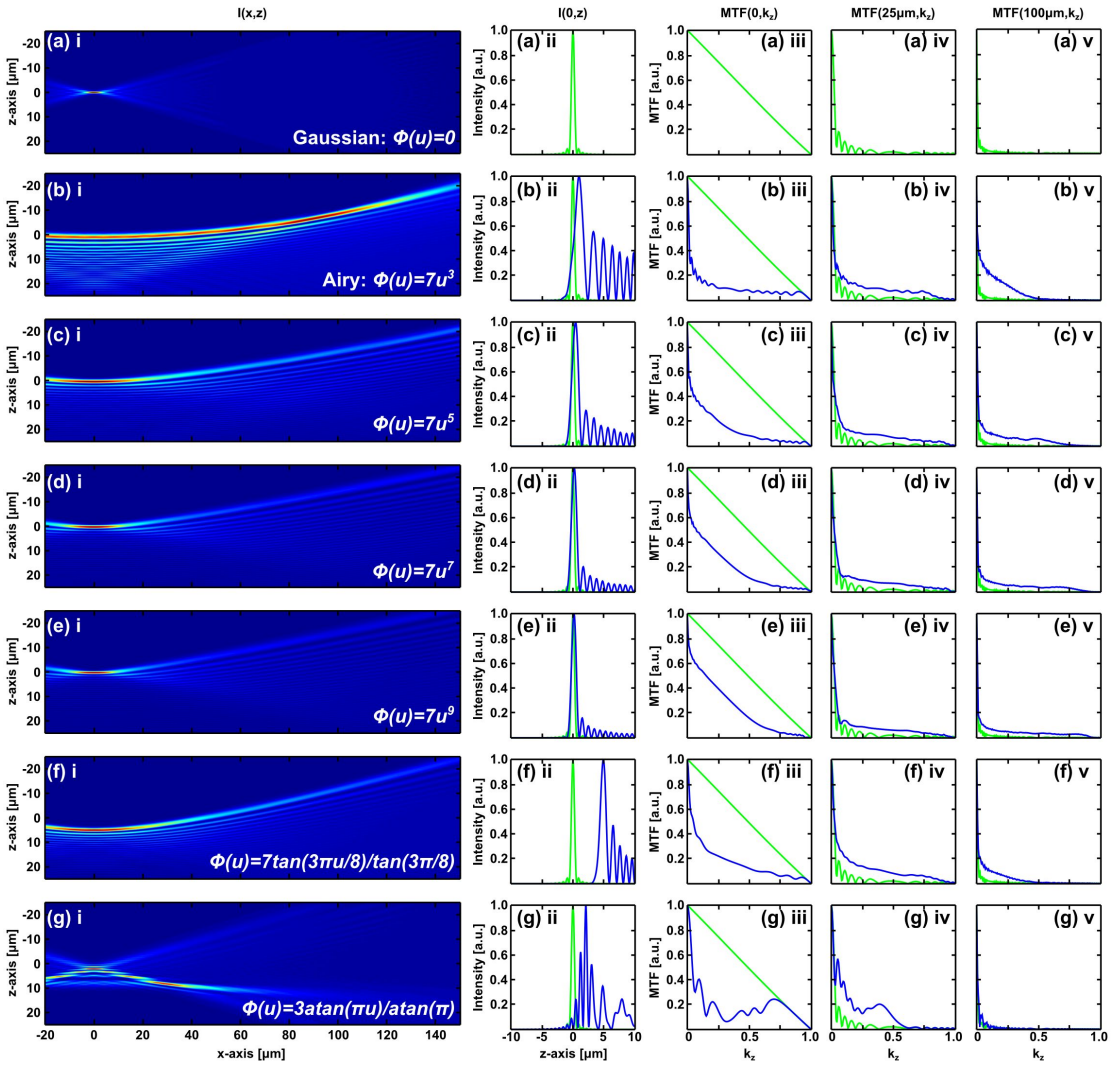

FIGURE 4.2: Theoretical $x-z$ light-sheet profile (i), axial profile at focus (ii), and axial MTF at focus (iii), $x = +25\,\mu\text{m}$ (iv), and $x = +100\,\mu\text{m}$ (v) for beams formed from selected asymmetric (b-g) cylindrical pupil functions, $P(u) = \exp[2\pi i\phi(u)]$. Results of a Gaussian light-sheet (green; a) are shown on each plot for reference.

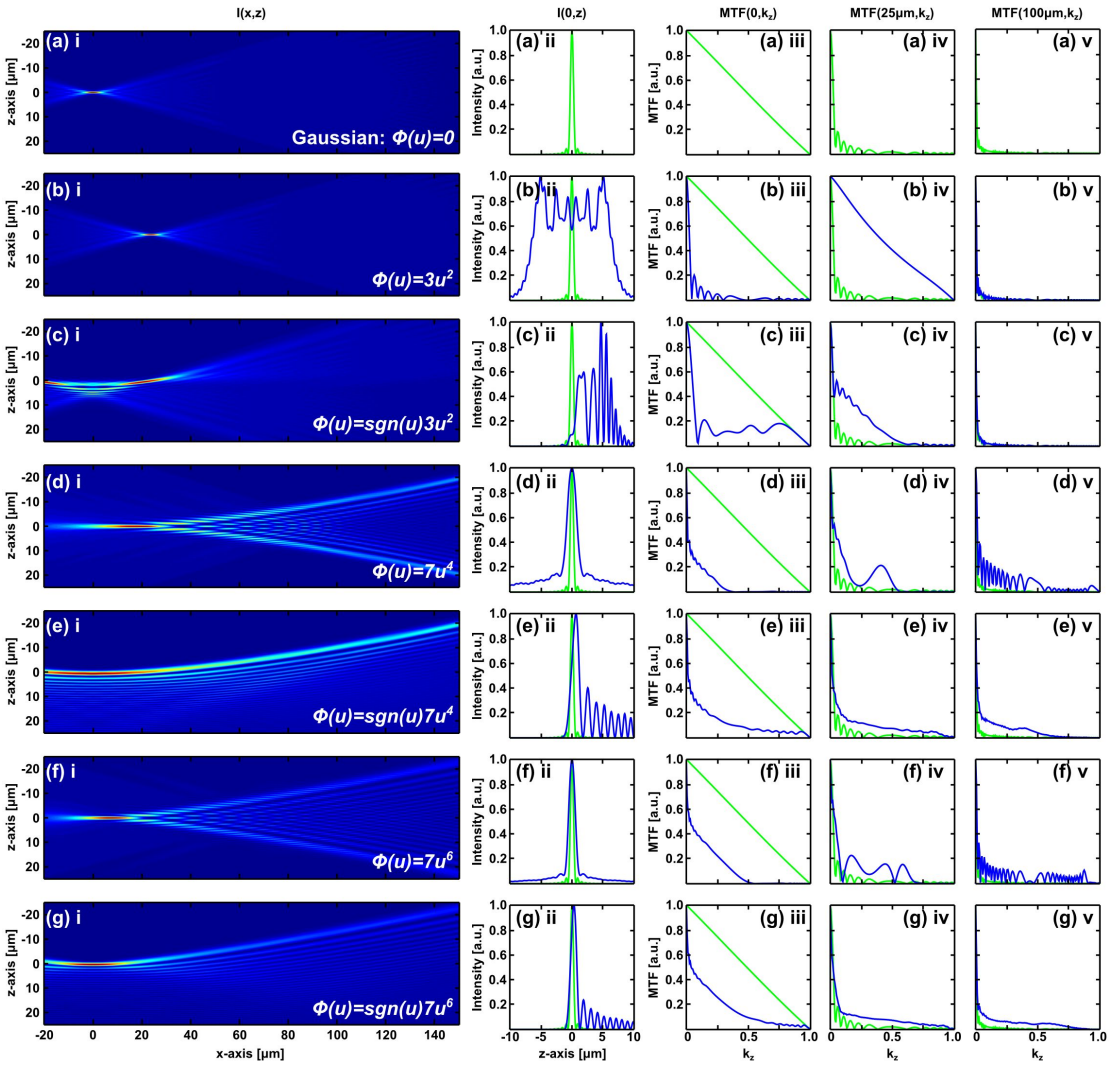

FIGURE 4.3: Theoretical $x-z$ light-sheet profile (i), axial profile at focus (ii), and axial MTF at focus (iii), $x = +25\,\mu\text{m}$ (iv), and $x = +100\,\mu\text{m}$ (v) for beams formed from selected symmetric (a,b,d,f) and asymmetric (c,e,g) cylindrical pupil functions, $P(u) = \exp[2\pi i\phi(u)]$. Results of a Gaussian light-sheet (green; a) are shown on each plot for reference.

order to enable accurate deconvolution. By definition, the MTF is normalised such that the magnitude of the zero-frequency component is unity and as such does not account for the intensity of illumination. The local light-sheet intensity will influence the local SNR which will dictate the noise-floor for the local MTF. As γ increases, the light-sheet intensity becomes more localised at $x = 0$. This can be understood by considering that for $\gamma \to \infty$, the phase profile will become flat across the majority of the pupil plane and only be modulated at the extreme edges and thus for large γ will tend towards a Gaussian beam. Therefore, the ideal light-sheet should have support of high spatial frequencies and considerable intensity over a large propagation distance. From this analysis, the Airy beam is again the optimal choice.

4.2.3 Comparison between Gaussian, Bessel, and Airy light-sheets

The previous analysis of transversally asymmetric, cylindrically focussed, light-sheets cannot include a Bessel light-sheet as no 1+1D analogue of a Bessel beam exists [28]. Bessel light-sheets must be formed from rapid 1D scanning of the 3D focussed beam in a DSLM scheme. To perform a comparison against Bessel light-sheets, the attainable axial resolution and FOV of 3D focussed Gaussian, Bessel, and Airy beams is explored analytically and by simulation.

Estimations for the axial resolution and FOV of Gaussian, Bessel, and Airy beams can be determined from considerations of the corresponding pupil functions. Derivations are given in Appendix D and summarised in Table 4.2.

The relations in Table 4.2 demonstrate the inherent trade-off that exists when using a Bessel beam for light-sheet illumination, increasing the FOV inherently reduces the resolution and *vice versa*. The trade-off with Bessel illumination is less restrictive than for Gaussian illumination, doubling $r_{z;G}$ will quarter FOV_G as this scales with NA^{-2} whereas doubling $r_{z;B}$ can be achieved simply by varying β and will only half FOV_B as this scales with β^{-1}.

From the expression for $r_{z;A}$, it would appear that super-resolution information, beyond the diffraction limit can be achieved with the Airy beam as for $\alpha < 8.33$, $r_{z;A}$ will be smaller than $\lambda/2\,\mathrm{NA}$. However, this equation is based on an approximation of the Airy MTF, for example setting $\alpha = 0$ would yield a Gaussian beam but $r_{z;A}$

Gaussian	Bessel	Airy
$P_G(u,v) = \frac{H(1-\boldsymbol{u_r})}{\sqrt{\pi}}$	$P_B(\boldsymbol{u_r}) = \frac{1}{\sqrt{\pi\beta(2-\beta)}} H(1-\boldsymbol{u_r}) \cdot H(\boldsymbol{u_r}-1+\beta)$	$P_A(u,v) = \frac{H(1-\boldsymbol{u_r})}{\sqrt{\pi}} \cdot \exp[2\pi i\alpha(u^3+v^3)]$
$MTF_G(\nu_z) = \frac{2}{\pi}\left(\arccos(\nu_z) - \nu_z\sqrt{1-\nu_z^2}\right)$	$MTF_B(\nu_z) = \frac{\beta}{\nu_z\pi\sqrt{1-\nu_z}(2-\beta)}$	$MTF_A(\nu_z) = \frac{1}{\sqrt{48\lvert\alpha\nu_z\rvert}}$
$r_{z;G} = \frac{\lambda}{1.76\,\mathrm{NA}}$	$r_{z;B} \approx \frac{0.05\pi\lambda}{\mathrm{NA}\,\beta}$	$r_{z;A} = 0.12\alpha\frac{\lambda}{2\,\mathrm{NA}}$
$FOV_G = \frac{4\lambda n}{\mathrm{NA}^2}$	$FOV_B \approx \frac{\lambda}{2n\beta}\frac{1}{1-\sqrt{1-(\mathrm{NA}/n)^2}}$	$FOV_A = \frac{6\alpha\lambda}{n}\frac{1}{1-\sqrt{1-(\mathrm{NA}/n)^2}}$

TABLE 4.2: Analytic expressions for the pupil function, axial MTF, axial resolution and field-of-view of Gaussian, Bessel, and Airy light-sheets. u and v are normalised pupil coordinates corresponding to the $z-$ and $y-$axes respectively, $\boldsymbol{u_r} = (u^2+v^2)^{1/2}$, H denotes the Heaviside step function, β is the fractional width of annulus used to generate the Bessel beam, and α is the strength of the cubic modulation.

would indicate infinite resolution, which is clearly incorrect. For $\nu_z \to 0$ or $\nu_z \to 1$ (as is the case when considering the resolution limit) the Gaussian MTF is a more valid approximation. Therefore, what is correctly inferred from $r_{z;A}$ is that the resolution achieved by an Airy beam is diffraction limited for $\alpha \leq 8.33$. For $\alpha > 8.33$, an increase in α will result in a decrease in resolution. This highlights the non-linear nature of resolution and FOV scaling with Airy light-sheets. For low values of α, there is no loss in resolution when increasing the FOV, when increasing α beyond 8.33, there is a slight reduction in resolution when the FOV is increased, and for large α, the resolution decreases inversely with the increase in FOV, the same as for the Bessel beam.

Figure 4.4 shows plots of axial resolution and FOV as a function of NA for a Gaussian and selected Bessel and Airy light-sheets, based on the equations given in Table 4.2. The α and β parameters for the Airy and Bessel light-sheets have been chosen such that there is a factor 2 difference between their FOV widths for a given NA. Light-sheets denoted Bessel5 and Bessel10 have $\beta = 5$ and $\beta = 10$ respectively, Besselβ in general. Light-sheets denoted Airy10 and Airy20 have $\alpha = 10$ and $\alpha = 20$ respectively, Airyα

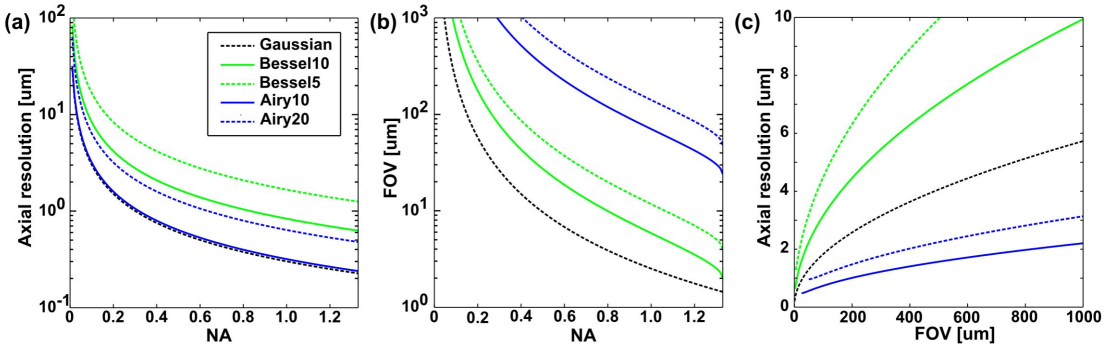

FIGURE 4.4: Analytic axial resolution and field-of-view of Gaussian, Bessel, and Airy light-sheets as given in Table 4.2. (a) Axial resolution against NA, (b) FOV width against NA, and (c) axial resolution against FOV width for selected light-sheet types. Figure adapted with permission from [18].

in general. As Fig. 4.4(c) shows, the Airy beam appears to be very suitable for high resolution light-sheet imaging over a large FOV. It is worth noting that the Bessel10 and Airy20 light-sheets yield comparable resolution but their respective fields-of-view (FOVs) differ by over an order of magnitude.

To confirm the above analytic expressions, simulations of the full 3D intensity distribution were generated for Gaussian, Bessel, and Airy beams and projected onto the y-axis to yield the DSLM light-sheet cross-section for each of the beam types. The parameters used for the simulation were the same as given in Table 4.1, the sampled $y-$range was the same as for the $z-$axis. The 2D pupil functions for the simulated beams are given in Table 4.3.

Beam type	**Pupil function**
Gaussian	1
Bessel5	$\sqrt{(u^2+v^2)} \geq 0.95$
Airy10	$\exp[2\pi i 10(u^3+v^3)]$

TABLE 4.3: Pupil functions of simulated DSLM light-sheets, shown in Fig. 4.5.

Figure 4.5 shows the simulated Gaussian, Bessel, and Airy light-sheet profiles and their corresponding axial MFT. Figures 4.5(g-i) show the MFT thresholded at 5%, the cut-off that has been used in analytic derivations as a practical noise floor, and has the analytically determined axial resolution (in terms of k_z) and FOV indicated by dashed green and solid pink lines respectively. The MTFs shown in Fig 4.5(d-i) are normalised

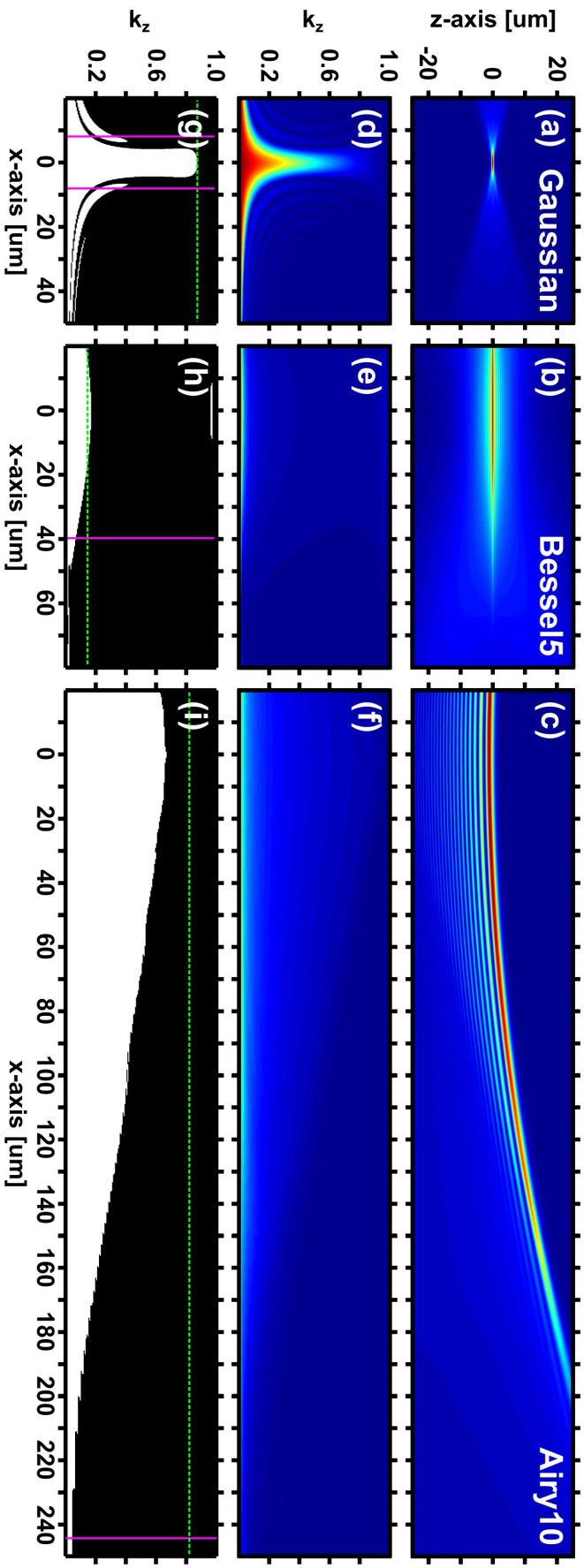

FIGURE 4.5: Simulation of axial resolution and field-of-view of Gaussian, Bessel, and Airy DSLM light-sheets. Light-sheet profiles (a-c), $MTF(x, k_z)$ (d-f), and $MTF(x, k_z)$ thresholded at 5% (g-i) for Gaussian (a,d,g), Bessel5 (b,e,h), and Airy10 (c,f,j) light-sheets respectively. Analytically predicted axial resolution (dashed green) and FOV (solid pink) are indicated in (g-i).

relative to $MTF(0, k_z)$ so as to incorporate the decay in intensity away from the focal region. Immediately apparent is that the axial resolution is not constant across the FOV, even for the propagation-invariant beam types. This implies that the edge of the FOV is also based on an arbitrary cut-off which will depend on the SNR. The main lobe of the Airy beam extends beyond the displayed axial region but remains within the simulation boundaries.

The largest deviation from the analytic expressions is the axial resolution of the Airy light-sheet. An axial resolution of 760nm is expected for an Airy10 light-sheet but the thresholded MTF only reaches maximal k_z corresponding to a resolution of $1\ \mu\mathrm{m}$. This is still significantly higher than the axial resolution of a Bessel light-sheet of equal NA and a much larger FOV than a Gaussian light-sheet of equal NA.

4.2.4 Comparison between Airy and advanced Bessel beam light-sheet techniques

As discussed in Chapter 2.3.5, Bessel beam based LSM is almost always implemented in conjunction with additional techniques to overcome the issues associated with the extended transverse structure of the Bessel beam. While these advanced Bessel light-sheet techniques are not investigated experimentally in the following sections, comparisons between these techniques and the Airy LSM technique are made below based on theoretical expectations. Comparison between techniques was based on theoretical performance of a system with parameters identical to the simulations described in Chapter 4.2 and experiments described in Chapter 4.3.

Table 4.4 lists key parameters for standard Gaussian, Bessel, and Airy light-sheets as discussed above, and also includes results for Bessel LSM implemented with confocal scanning of a line aperture (Bessel-CS) [60], and with structured illumination (Bessel-SI-OS/SR) [5, 20]. Spatiotemporal resolution and FOV is predicted from theory. The fluorescence collection efficiency is also estimated from simulations of the Gaussian, Bessel, and Airy light-sheet profiles. The collection efficiency is given by the fraction of fluorescence emitted within the DOF of the detection lens in the plane $x = 0$ and is normalised relative to a Gaussian light-sheet. The peak intensity of each light-sheet is considered as this will impact on the phototoxicity of the method, and is measured as

a fraction of the total cross-sectional intensity of the light-sheet. The normalised peak intensity is also considered, this is given by the peak intensity divided by the collection efficiency such that the normalised peak intensity compares the peak intensity required to collect the same number of emitted photons, normalised to the peak Gaussian intensity. From this, the normalised total intensity is also estimated, which is the the total irradiation at each point of the sample relative to a Gaussian light-sheet for the same number of collected photons.

Bessel light-sheets can benefit from a confocal line aperture to reject signal generated outwith the central core of the Bessel beam [60]. The Bessel beam must be scanned across the image synchronously with either a line aperture or a digital aperture, implemented by a rolling shutter on the camera. The axial resolution was estimated as the width of the Bessel core, defined as the diameter of the first minima of the Bessel function, which would be the width of the confocal line aperture. Only small differences in core width are observed for the different Bessel beams considered. All fluorescence outwith this region is rejected by the confocal slit and so the collection efficiency was estimated as the fraction of photons emitted within this region only. The temporal resolution was estimated based on the rolling shutter mode of the sCMOS camera (Hamamatsu Orca Flash 4.0). The maximum frame-rate in rolling shutter mode is half the maximum frame-rate under standard operation.

Bessel beam based LSM has also been combined with structured illumination [5, 20]. The Bessel beam is stepped along the $y-$axis in discrete steps rather than continuously scanned. For certain step intervals, the image components stemming from the Bessel side-lobes can be digitally removed, as in SIM [20, 74] (Bessel-SI-OS), from a series of 3 acquired images with the phase of the Bessel-grid translated. The necessity to acquire multiple raw image frames per image reduces the temporal resolution. The axial resolution was again estimated as the width of the Bessel core and was also used to estimate the collection efficiency. In this case, light is only rejected out-of-plane and so the collection efficiency is higher than with Bessel-CS. Additionally, SIM algorithms may be used to extract SR information from a sample [5, 99]. In the light-sheet geometry, SR can be achieved along the $y-$axis and $z-$axis with a stepped Bessel beam array (Bessel-SI-SR). Extraction of SR information requires the acquisition of 5 raw image

LS Type	$r_{x,y}$[µm]	r_z[µm]	r_t	FOV [µm]	Col. Eff.	I_{max}	Norm. I_{max}	Norm. I_{total}
Gaussian	0.72	0.72	1	16.0	1.00	1.00	1.00	1.00
Bessel10	0.72	1.99	1	39.1	0.93	0.22	0.24	1.07
Bessel5	0.72	3.98	1	78.2	0.78	0.13	0.17	1.28
Bessel2	0.72	9.95	1	195.4	0.49	0.06	0.12	2.05
Bessel1	0.72	19.89*	1	390.8	0.35	0.04	0.11	2.83
Bessel10-CS	0.72	0.98	1/2	39.1	0.19	0.19	0.98	5.14
Bessel5-CS	0.72	0.99	1/2	78.2	0.10	0.10	1.01	10.12
Bessel2-CS	0.72	1.00	1/2	195.4	0.04	0.04	0.97	24.80
Bessel1-CS	0.72	1.03	1/2	390.8	0.02	0.03	1.03	41.33
Bessel10-SI-OS	0.72	0.98	1/3	39.1	0.36	0.22	0.61	8.34
Bessel5-SI-OS	0.72	0.99	1/3	78.2	0.22	0.13	0.59	13.53
Bessel2-SI-OS	0.72	1.00	1/3	195.4	0.11	0.06	0.54	26.81
Bessel1-SI-OS	0.72	1.03	1/3	390.8	0.08	0.04	0.53	39.68
Bessel10-SI-SR	[0.72,0.42]	0.98	1/5	39.1	0.36	0.22	0.61	13.89
Bessel5-SI-SR	[0.72,0.42]	0.99	1/5	78.2	0.22	0.13	0.59	22.55
Bessel2-SI-SR	[0.72,0.42]	1.00	1/5	195.4	0.11	0.06	0.54	44.68
Bessel1-SI-SR	[0.72,0.42]	1.03	1/5	390.8	0.08	0.04	0.53	66.13
Airy5	0.72	0.72	1	234.5	0.78	0.25	0.33	1.28
Airy10	0.72	0.76	1	469.0	0.57	0.22	0.38	1.77
Airy20	0.72	1.52	1	938.0	0.45	0.19	0.42	2.20

TABLE 4.4: Parameters of advanced Bessel and Airy light-sheet techniques. Lateral resolution ($r_{x,y}$), axial resolution (r_z), temporal resolution (r_t; measured relative to Gaussian LSM), FOV, fluorescence collection efficiency (Col. Eff.), peak intensity (I_{max}), normalised peak intensity (Norm. I_{max}), and normalised total intensity (Norm. I_{total}) listed for standard Gaussian, standard Bessel, confocal scanning Bessel (Bessel-CS), optical sectioning structured illumination Bessel (Bessel-SI-OS), super-resolution structured illumination Bessel (Bessel-SI-SR), and standard Airy light-sheets.

* The axial resolution of the standard Bessel light-sheet exceeds the DOF of the detection lens and would be limited to $16\,\mu\mathrm{m}$.

frames which lowers the temporal resolution and was additionally used to weight the total intensity as the sample must be exposed multiple times per image.

Table 4.4 shows that confocal scanning and structured illumination techniques can recover high axial resolution in Bessel LSM through the rejection of the extended side lobe structure which is expected from the literature. Both Bessel-CS and Bessel-SI techniques require some additional hardware control and this necessitates a reduction in the maximum acquisition rate that can be achieved whereas Airy LSM is not hindered. The collection efficiency of Bessel-CS and Bessel-SI are very low, and decrease as the intended FOV is increased, which results in large total exposure of the sample. The total irradiance of the sample can range between 5 and 60 times greater than for a standard Gaussian light-sheet. This may be mitigated somewhat for Bessel-SI as the peak intensity (Norm. I_{max}) is much lower than for a Gaussian light-sheet [5]. Airy light-sheets give high axial resolution over a large FOV whilst maintaining high collection efficiencies, allowing simultaneous low peak and total intensities.

4.2.5 Light-sheet deconvolution algorithm

Deconvolution is a process by which knowledge of the PSF can be used to process acquired data to improve the resolution of the image [192]. The shape of the Airy light-sheet results in an image stack which is blurred and difficult to interpret (Fig. 4.6, middle row). The use of the Airy beam necessitates the use of deconvolution to yield high-resolution images [191, 192].

Image formation in fluorescence microscopy can be described generally as a convolution of the sample fluorophore distribution with the PSF of the imaging optics as in equation (2.12). In LSM, image formation in the lateral plane is described exactly the same but axially, can be described by the convolution of the sample distribution with the light-sheet cross-sectional profile (Fig. 4.6):

$$D(z) = (I_z \otimes S)(z) \tag{4.8}$$

where $D(z)$ is the recorded image, $I_z(z)$ is the axial light-sheet profile, and $S(z)$ is the sample fluorophore distribution.

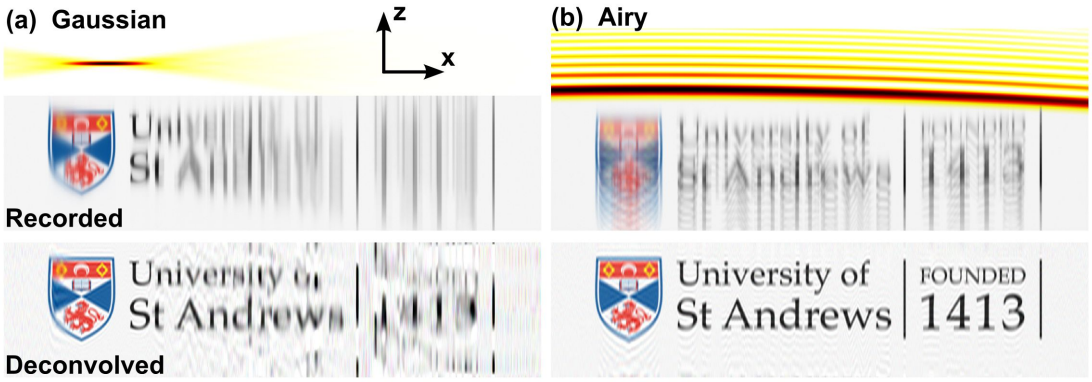

FIGURE 4.6: Simulation of light-sheet image reconstruction by Wiener deconvolution. Simulated images of University of St Andrews logo imaged by axial (z) translation through a Gaussian (a) and Airy (b) light-sheet. Only the axial image formation is simulated, lateral image formation depends solely on the detection optics and is not simulated. During imaging, zero-centred Gaussian noise was added to the image. Light-sheet cross-sectional profiles (top) and their corresponding recorded images (middle) and post-deconvolved images (bottom).

In Fourier space, equation (4.8) becomes:

$$\tilde{D}(k_z) = H(k_z)\tilde{S}(k_z) \tag{4.9}$$

where $H(k_z) = \tilde{I_z}(z)$.

As the axial profile of the light-sheet varies with propagation, this is more accurately represented as:

$$\tilde{D}(x, y, k_z) = H(x, k_z)\tilde{S}(x, y, k_z) \tag{4.10}$$

Deconvolution is the inverse process, using an estimate of the light-sheet profile, $I_z(x, z)$, and the image, $D(x, y, z)$, to recover a more accurate representation of the actual fluorophore distribution, $S(x, y, z)$. This can be naively performed by dividing by $H(x, k_z)$ in Fourier space. A more accurate and commonly used method is to use a Wiener filter [193]:

$$H_W(x, k_z) = \frac{H(x, k_z)^*}{|H(x, k_z)|^2 + SNR(k_z)^{-2}} \tag{4.11}$$

where

$$SNR(k_z) = A\frac{2\,\mathrm{NA}}{\lambda}\frac{1}{k_z} \tag{4.12}$$

The SNR is modelled as inversely proportional to k_z, normalised to the spatial frequency corresponding to the diffraction limit, $k_z = 2\,\mathrm{NA}/\lambda$, and multiplied by a scalar, A, that regulates the strength of the filter. Low A will reduce high frequency noise but will also smooth the images, lowering the axial resolution; high A will give sharper images with higher axial resolution but will exhibit more high frequency noise. $A = 5$ gave the best smoothing-noise reduction trade-off for simulations and experiments.

The deconvolved image, $\hat{S}(x, y, z)$, is therefore recovered from:

$$\hat{\tilde{S}}(x, y, k_z) = H_W(x, k_z)\tilde{D}(x, y, k_z) \tag{4.13}$$

Figure 4.6 shows that Wiener deconvolution is suitable for Airy light-sheet imaging. The light-sheets are simulated with the same parameters as in Chapter 4.2, $\alpha = 7$ for the Airy light-sheet, and deconvolved as described above. As expected, only the region near the focus of the Gaussian light-sheet is deconvolved accurately, whereas high axial resolution is achieved across the full width of the image with Airy illumination.

A MATLAB script was written to deconvolve datasets acquired with the LSM systems described in Chapter 4.3 using the Wiener filter described above.

4.3 Development of an Airy light-sheet microscope

The theory presented above was tested using an existing LSM system, shown in Fig. 4.7, referred to in this thesis as the Type-1 LSM system.

A laser beam (Coherent, Verdi, 5W, 532nm) is expanded and collimated (L_1,L_2) onto the active region of an acousto-optic deflector (AOD; Neos AOBD 45035-3) which is driven by a 20kHz triangle waveform to rapidly scan the diffracted orders along the y-axis. The first diffracted order is selected by a slit aperture and the beam from the AOD is expanded and imaged (L_3,L_4) onto a spatial light modulator (SLM; Hamamatsu LCOS X10468-04) which enables beam shaping. The beam overfills the SLM

area. Again, the first diffracted order is selected by a slit aperture and the SLM is imaged (L_5,L_6) onto back aperture of a microscope objective (MO_1; Mitutoyo 20x/0.42, working distance (w.d.) = 20mm). The beam slightly overfills the back aperture. Control of the SLM, as described in Appendix C, allows the pupil functions described in Chapter 4.2 for generation of Gaussian, Bessel, and Airy beams to be applied and easily switched between. The SLM was also used to implement an aberration correction algorithm [194] which corrected for systematic aberrations in the optical train [72]. The illumination power at the back aperture of MO_1 was typically between $30 - 300$mW.

Fluorescence is collected by a second, orthogonal objective lens (MO_2; Newport, 20x/0.40) with appropriate tube lens and fluorescence filters onto a camera (CCD; Basler piA640-210gm). A third imaging path (Fig 4.7 dashed box) consisting of an objective lens (MO_a; Mitutoyo 50x/0.55), tube lens, and camera (CCD_a, Basler piA640-210gm) was optional, but could be used to inspect the *en face* ($y - z$) light-sheet profile and aid alignment. The sample was positioned in a square-walled capillary tube and suspended between the objective lenses in air. The sample was positioned and translated through the light-sheet by an xyz nano-positioning stage (Mad City Labs, Nano-LP200).

Software for control of the system and acquisition of images was developed in LabVIEW.

4.3.1 Optimisation of microscope design for biological experiments

Results shown for the Airy light-sheet imaging proof of concept with the Type-1 LSM (shown in Chapter 4.3.4) demonstrate the potential of the method, however, there are a number of engineering challenges that must be addressed to make the Airy beam LSM suitable for biomedical imaging. The Type-1 system suffers from several issues which are discussed below and have been resolved in the Type-2 LSM (Fig. 4.8).

Inhomogeneous refractive index in optical pathways

The sample is embedded in an agarose gel, contained within a glass capillary tube, and suspended in air between the illumination and detection objective lenses. The illuminating light-sheet and the emitted fluorescence therefore undergo two refractions that are not corrected for by the objective lenses and will suffer from spherical aberration.

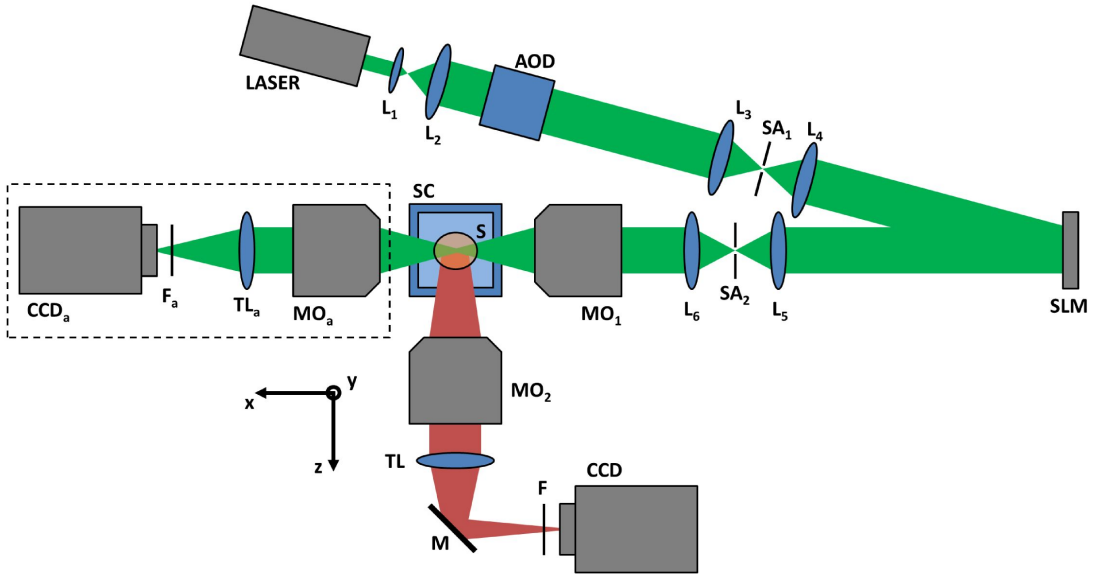

FIGURE 4.7: Schematic of the Type-1 LSM system. For clarity, only the first-diffracted orders from the AOD and SLM are shown. Dashed box indicates optional optics used to monitor the *en face* profile of the light-sheet. Lx: Lens; AOD: Acousto-optic deflector; SAx: Slit aperture; SLM: Spatial light modulator; MOx: Microscope objective lens; S: Sample; SC: Sample chamber; TLx: Tube lens; M: Mirror; F: Filter; CCDx: (EM)CCD camera.

This has the effect of elongating the light-sheet as the effective NA of the illumination is lower than intended. This effect is mirrored in the detection pathway where the lateral resolution is reduced by the same effect. This has been well characterised and is described in detail by Jahrling *et al* using geometric considerations [195]. This effect depends on the ratio of physical path lengths the light propagates through between the lens and the intended focus. The sample is scanned to acquire a volumetric image stack, therefore the focal plane of the detection lens is displaced from the plane of the light-sheet as the scan progresses. The light-sheet is unaffected by sample translations perpendicular to the beam. To counteract this focal shift, the light-sheet was holographically translated by varying the grating period on the SLM to re-align the light-sheet with the shifted focal plane but adds complexity to the acquisition process and slows acquisition as the SLM must be updated for every scan position.

A system with maximal refractive index homogeneity in the space between the objective lenses is desired. The use of water-dipping lenses immersed directly into the sample chamber is commonly used in other LSM implementations [20, 38, 49, 62, 196]

and would solve this issue. The complexity of the system would be reduced, the acquisition speed would be slightly increased, and the image quality would improve from the reduced spherical aberration.

Constrained sample choice

The use of capillary tubes for sample confinement severely limits the size of specimens which can be imaged, typically square capillary tubes with inner diameter between $200 - 500\ \mu\mathrm{m}$ were used and the square geometry of the tubing restricts the positioning of the specimen within the microscope as the walls must be perpendicular to the corresponding objective lenses. Larger samples simply will not fit in the tubing and more traditional, coverslip mounted samples may be difficult to suspend securely.

Two solutions exist, to create a fluid filled chamber around the sample, containing the objective lenses (as in, e.g., [38]), or to change the geometry of the microscope such that the sample can sit flat as in most microscope designs (as in, e.g., [20, 43, 44]). The second option was chosen for the simplicity of not designing a custom fluid filled chamber. Samples would be mounted on a glass slide on a flat sample stage, with the illumination and detection lenses both inclined at $45°$ to the horizontal in a "dual-inverted" geometry [43, 44].

Single channel acquisition

A single fixed wavelength laser for illumination limits acquisition to one wavelength channel.

This limitation is easily overcome with tunable laser sources or with laser banks containing multiple collinear sources. A fibre coupled laser bank was used to give 2 colour channels.

Revised microscope design

These considerations were used to design the Type-2 LSM system (Fig. 4.8).

Lasers (Spectra Physics argon-ion 2040E, 10W, 488nm, and Laser Quantum Finesse, 6W, 532nm) were coupled into a single-mode (SM) fibre and delivered to the microscope. The divergent beam from the fibre was collimated (L_1) and a half-waveplate and polarising beam splitter used to control the polarisation and power of the beam. The beam was expanded to overfill an SLM, the first-diffracted order of which is collected by a round aperture (RA) and imaged (L_2,L_3) onto the active area of an AOD, the

first-order beam from the AOD is collected by a slit aperture (SA) and imaged (L_4,L_5) onto the back aperture of the illumination objective (MO_1, Nikon CFI Apo 40x/0.80 DIC, w.d. = 3.5mm, water dipping). As with the Type-1 system, the SLM, AOD, and back aperture of MO_1 are mutually conjugate. A quarter-waveplate immediately before MO_1 ensures circular polarisation of the light-sheet in the sample.

Fluorescence was collected through a second objective (MO_2, Nikon CFI Apo 40x/0.80 DIC, w.d. = 3.5mm, water dipping) and through an $f = 400$mm tube lens onto an sCMOS camera (Hamamatsu, Orca Flash 4.0).

The sample was mounted as described in Chapter 4.3.2 on a glass slide and placed on an xyz nano-positioning stage. The stage could be manually moved in $x' - y'$ and manual z' movements could be achieved by raising or lowering the objective lenses. The stage was programmed to enable easy positioning of the sample in the microscope coordinates xyz and translated the sample along the $z-$axis during volumetric scanning.

No automatic laser or filter switching was implemented and the lasers were manually shuttered and filters manually changed between different colour channel acquisitions.

To replicate the performance of the Type-1 system, the illumination NA was restricted to 0.42 holographically by reducing the efficiency of the modulation to zero outwith the central region corresponding to $\mathrm{NA} = 0.42$. The detection NA was reduced to 0.4 with a variable aperture, the resulting NA was determined from resolution measurements of fluorescent point probes.

Software for control of the system and acquisition of images was developed in LabVIEW.

4.3.2 Optimisation of light-sheet microscopy sample mounting

With the use of water-dipping objective lenses, designed to be immersed in the medium surrounding the specimen, a design challenge with the Type-2 geometry is keeping the medium localised to the sample area without leaking away. This issue is further emphasised as the $45°$ angle from vertical the objective lenses sit at means their vertical working distance is very small ($< 200\,\mu\mathrm{m}$) when aligned and volumetric scans over

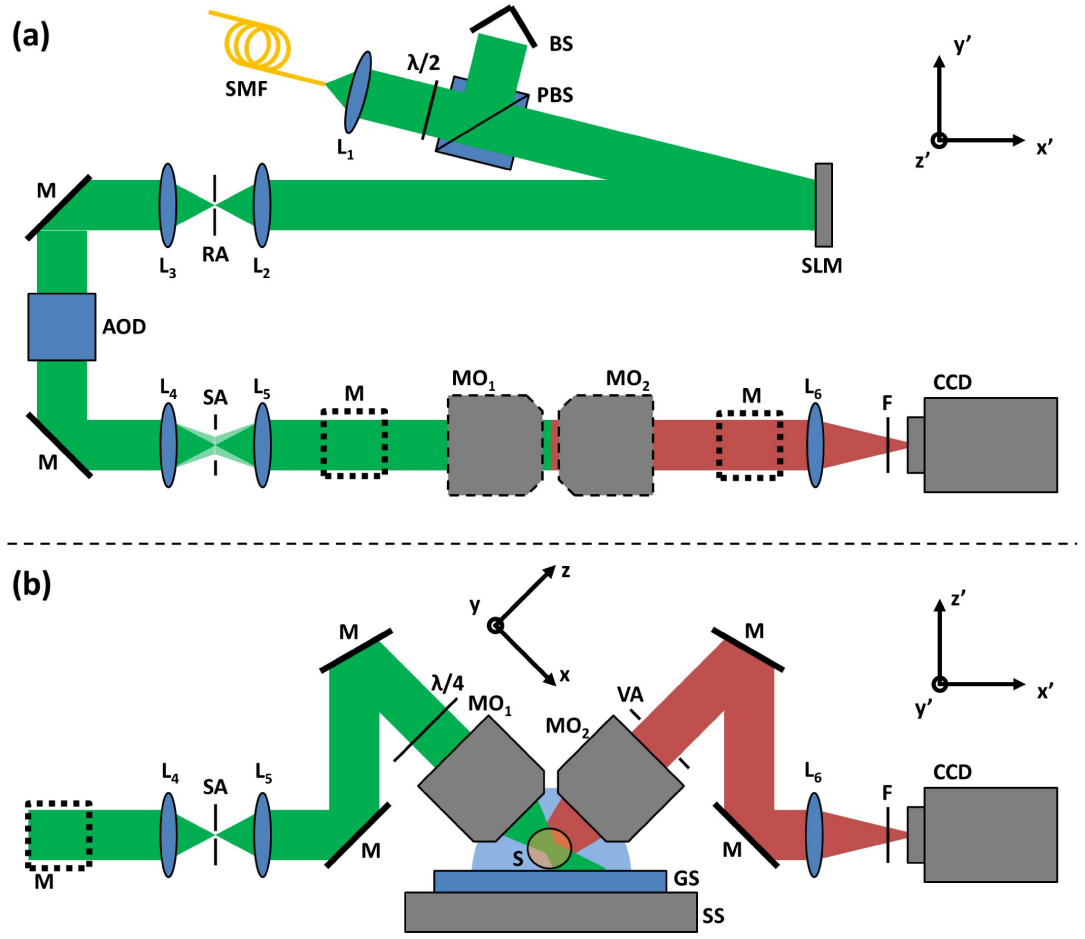

FIGURE 4.8: Schematic of the Type-2 LSM system. (a) Top-down view of the system in bench coordinates x', y'. (b) Side-on view of the system in bench coordinates, x', z', and microscope coordinates, x, z. SMF: Single-mode fibre; Lx: Lens; $\lambda/2$: Half-waveplate; PBS: Polarising beam splitter; BS: Beam stop; SLM: Spatial light modulator; RA: Round aperture; M: Mirror; AOD: Acousto-optic deflector; SA: Slit aperture; $\lambda/4$: Quarter-waveplate; MOx: Microscope objective lens; S: Sample; GS: Glass slide; SS: Sample stage; VA: Variable aperture; F: Filter; CCD: (EM)CCD camera.

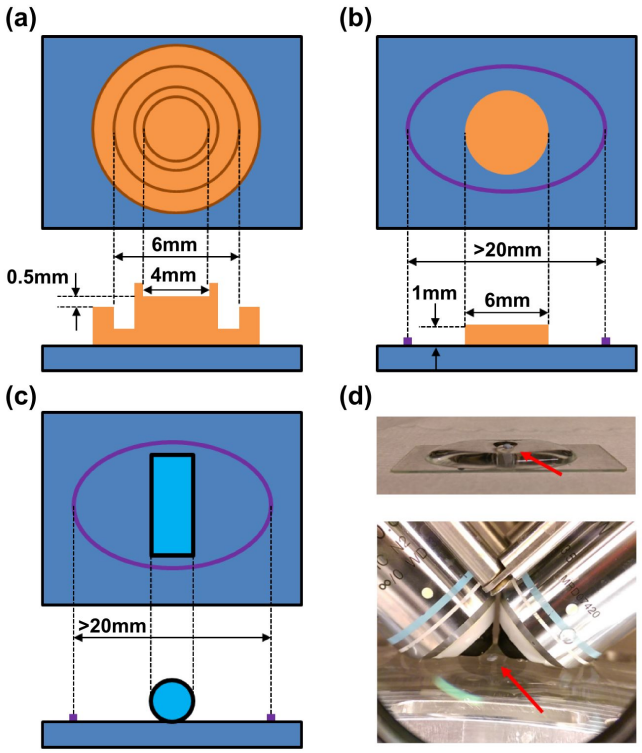

FIGURE 4.9: Various light-sheet microscopy sample mounting designs. Top down (top) and side on (bottom) schematics of (a) all PDMS (orange) multi-layer "tower-and-moat" design; (b) PDSM pedestal and drawn-on hydrophobic barrier (purple). Same design as in (b) but with a capillary tube (blue) loaded sample. The capillary tube was held in place with Blu-Tack (not shown). (d) Photos of the design in (b) alone (top) and in the microscope (bottom), red arrows indicate the location of the sample.

200 µm are desirable. Therefore, in order to avoid crashing the sample stage into the objective lenses, the sample must be raised slightly from the base of the sample mount in the region between the objective lenses.

A number of sample mounts were designed and trialled for raising the sample and containing the sample medium. These were prototyped in poly(dimethylsiloxane) (PDMS; Dow Corning Sylgard 184 Elastomer Kit), a known bio-compatible and optically clear polymer, and are shown in Fig. 4.9.

Figure 4.9(a) shows an all PDMS "tower and moat" design. A central, raised, walled pillar (the tower) contains the sample in an agaorse gel or mounted on a small (< 4mm diameter) coverslip, and a lower walled recess (the moat) provides containment for a much larger drop of water which covers the sample region and contacts with both objective lenses. The PDMS structure is secured in place on the glass slide with an

epoxy resin. While this sample mount works, it is difficult to manufacture due to the multi-level nature of the design.

A simplified approach is illustrated in Fig. 4.9(b) which utilises a pap-pen (Invitrogen, 00-8877) to draw a hydrophobic barrier for water containment directly onto the glass slide. The sample is positioned on a raised pedestal in the centre of the drawn barrier. The simplified geometry makes this a much more flexible choice as the pedestal can be cut from a single layer of PDMS (or other material) and can vary in shape to accommodate a variety of slide mounted or agarose embedded samples. Figure 4.9(c) shows the same approach but the pedestal has been replaced with a round capillary or plastic tube to accommodate tube mounted samples also.

Figure 4.9(d) shows photographs of the pedestal-based sample mount (Fig. 4.9(b)) with Blu-Tack in lieu of a sample for clarity (red arrows). The top photograph shows the position of the sample and the water confinement provided by the drawn-on hydrophobic barrier, note that the wetting angle of the water on the PDMS pedestal results in the sample remaining dry. The bottom image shows the sample sample mount positioned in the microscope. Surface tension between the water and objective lenses draws the water up, filling the space between the objectives and sample.

The sample mount shown in Fig. 4.9(b) was used for all samples with the Type-2 system unless otherwise stated.

4.3.3 Physical considerations for deconvolution

The deconvolution algorithm relies on an accurate description of the light-sheet, this could be measured experimentally but was instead simulated from experimental parameters as described in previous sections. To ensure a close match between the actual light-sheet profile and the theoretical prediction, aberration correction was implemented with the SLM as described by Čizmár, Mazilu, and Dholakia [194] to counteract systematic aberrations. This procedure was not used to correct for aberrations induced by the sample [72].

Additionally, as the deconvolution is only performed along the $z-$axis, it is critical that the expected axial PSF is well aligned with the $z-$axis and the relationship between

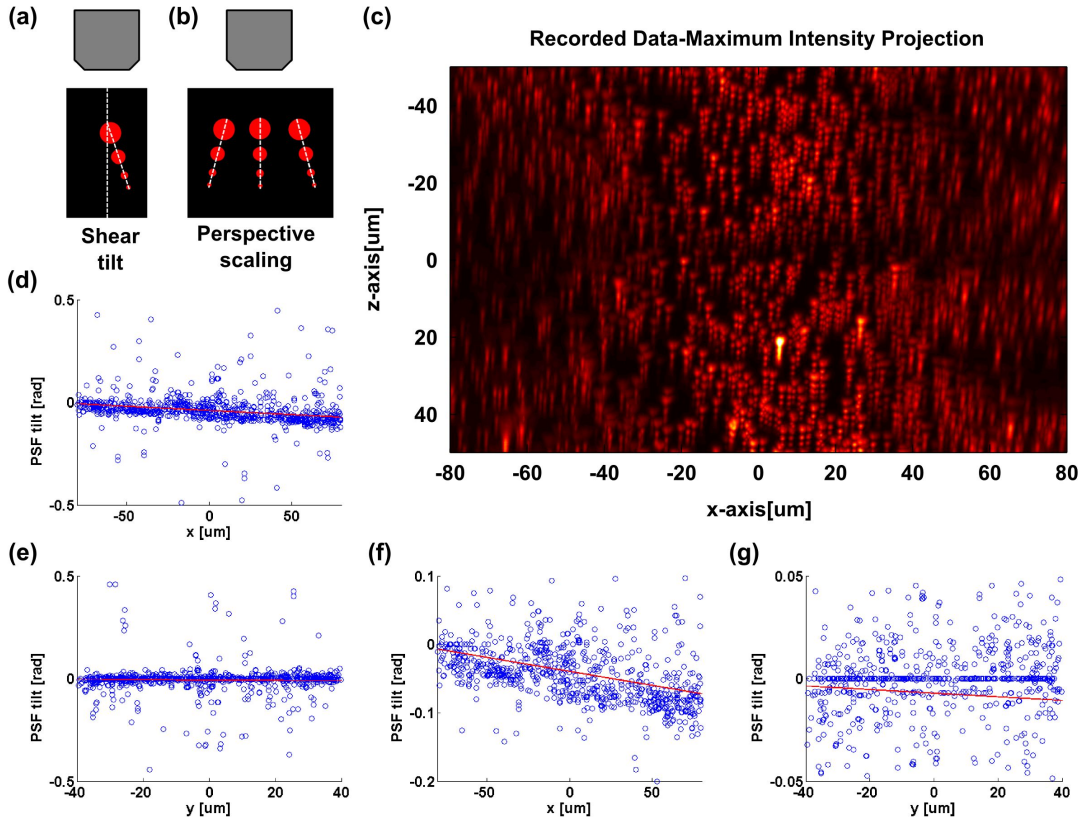

FIGURE 4.10: Geometric distortions in Type-2 light-sheet microscope. Illustrations of isolated shear tilt (a) and perspective scaling (b) effects on Airy light-sheet PSFs. (c) Maximum intensity projection ($x-z$) of example dataset showing geometric distortion from tilt and scaling. (d,e) Measured tilt (blue) and linear fit (red) of PSFs in (c) along the $x-$ and $y-$axes respectively. (f-g) Zoomed in views of (d,e).

the image and real-space coordinates are well known. Two scenarios were encountered where this does not hold true but can be corrected for computationally.

The first is quite simple, there can be a constant angle between the scan axis and the $z-$axis which results in a PSF that is tilted at an angle to the $z-$axis as illustrated in Fig. 4.10(a). This effect may also result from sample drift.

The second effect is more complex and stems from the desire for a large FOV. A microscope is only corrected to minimise aberrations over a finite FOV near is optic axis, far from the optic axis, the image is no longer fully corrected and the image plane does not remain flat. The curvature of the image plane manifests in the volumetric data as an array of PSFs that diverge from the objective lens (see Fig. 4.10(b)), so-called perspective scaling. This further implies that there is a preferential curvature of Airy

light-sheet when the parabolic trajectory of the Airy beam matches the curvature of the focal plane but this was not investigated.

Both of these effects are minor (Fig. 4.10(c)) and can be corrected digitally to enable more effective and accurate deconvolution. This is achieved by re-sampling the datacube $I(x, y, z)$ at $I(x_g, y_g, z)$, and the light-sheet PSF, $PSF(x, z)$ at $PSF(x_g, z_g)$ where:

$$x_g(z) = S_x \cdot z + (1 - P_x \cdot z) \cdot x \tag{4.14}$$

$$y_g(z) = S_y \cdot z + (1 - P_y \cdot z) \cdot y \tag{4.15}$$

where S_x and S_y are parameters describing the strength of the shear tilt in x and y respectively, and P_x and P_y describe the strength of the image plane curvature. These parameters can be easily determined by determining the local tilt (gradient) of each PSF, and fitting a linear function in x and y. The constant terms yield S_x and S_y, the linear coefficient yields P_x and P_y. A MATLAB script was written to determine these parameters from random sampling of $I(x, y, z)$. Figures 4.10(d)-(g) show the linear fits to the data shown in Fig. 4.10(c), showing 600nm red fluorescent beads, which gave $S_x = 39.4 \cdot 10^{-3}$, $S_y = 7.1 \cdot 10^{-3}$, $P_x = 408.4 \cdot 10^{-6}\,\mu\text{m}^{-1}$, and $P_y = 87.8 \cdot 10^{-6}\,\mu\text{m}^{-1}$. These values were generally stable and related mostly to the system. The parameters would need adjusted after alignment tweaks to the microscope and for some samples with large refractive index variations.

After deconvolution, the dataset was restored to the original coordinate grid, $I(x, y, z)$ to reflect the true spatial distribution within the sample.

4.3.4 Imaging of resolution probes

The resolution of the Type-1 Airy light-sheet microscope was determined experimentally by imaging small red fluorescent microspheres ($1\,\mu\text{m}$ diameter) embedded in a 1% low melting point (LMP) agarose gel inside a square walled capillary tube. Although beads much smaller than the expected resolution would be preferred, $1\,\mu\text{m}$ beads are sufficient here as it is expected that the axial resolution achieved with Gaussian and

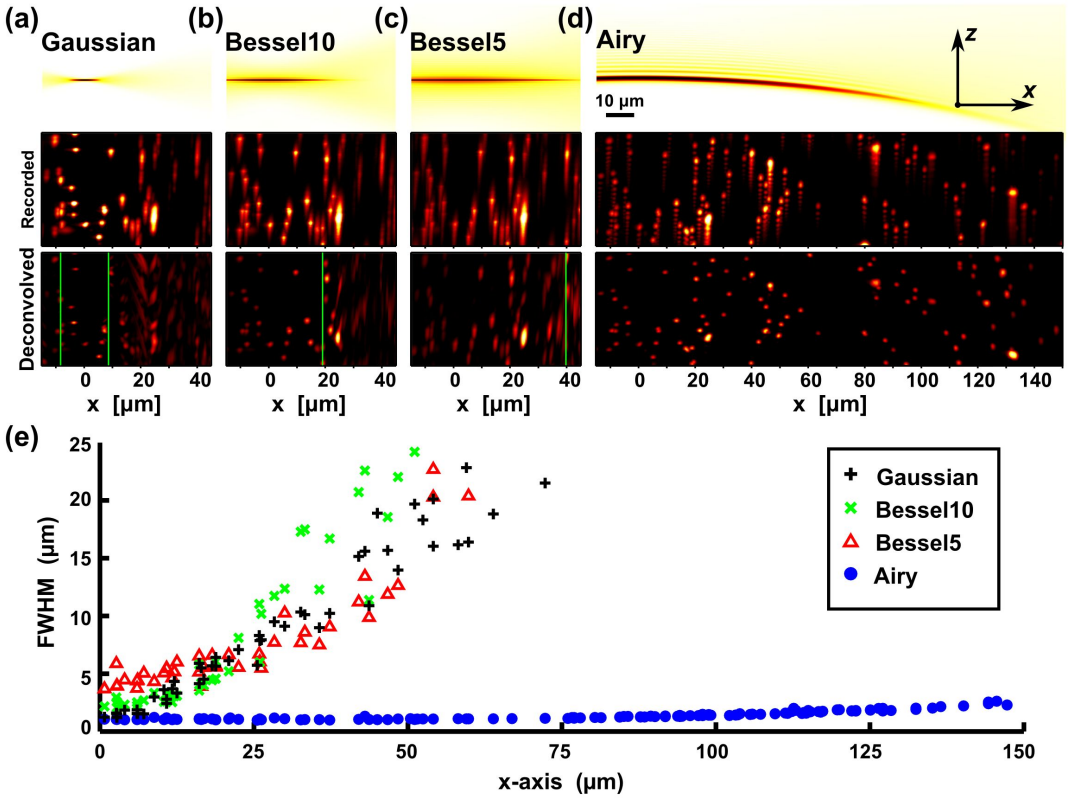

FIGURE 4.11: Axial resolution with Type-1 Airy light-sheet microscope. Theoretical light-sheets (top; inverted colour), and maximum intensity projections or recorded (middle), and deconvolved (bottom) data acquired with (a) Gaussian, (b) Bessel10, (c) Bessel5, and (d) Airy light-sheet illumination. Green lines denote the edge of the FOV as predicted from theory (FOV edge not shown for Airy as it occurs at $x = \pm 164.2\,\mu\text{m}$). (e) Plot of axial FWHM measurements across the FOV for each light-sheet type. Figure adapted with permission from [18].

Bessel light-sheets will rapidly degrade. Z-stacks were acquired with a z-plane spacing of 50nm. A laser line filter (Semrock, NF01-532-25) was used to reject scattered illumination from the acquired images.

Figures 4.11(a)-(d) show the recorded and deconvolved data of the same sample acquired with Gaussian, Bessel10, Bessel5, and Airy light-sheets. The Airy beam was formed from a cubic phase profile with $\alpha = 7$ as this was sufficient to cover the full width of the camera. Green lines mark the edge of the FOV as theoretically determined above. For the Gaussian and Bessel beams, the image quality drops dramatically approximately at the green line due to the presence of artefacts attributed to low values in the MTF beyond this point. Figure 4.11(e) plots the measured axial resolution, determined from full width at half maximum (FWHM) measurements as a function of

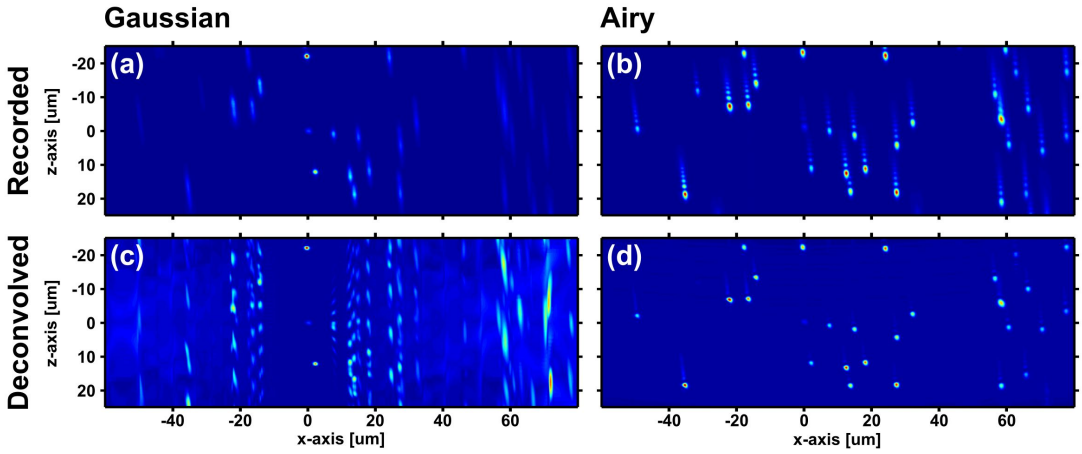

FIGURE 4.12: Imaging performance with Type-2 Airy light-sheet microscope. $x-z$ maximum intensity projections of recorded (a,b) and deconvolved (c,d) volumes with Gaussian (a,c) and Airy (b,d) light-sheet illumination.

longitudinal coordinate. At $x = 0$, the axial resolution measured correlates well with theory, showing similar resolution for Gaussian and Airy beams, a lower resolution for the Bessel10 beam, and lower again for the Bessel5 beam. The Airy beam yields the best axial resolution, maintaining resolution below $2\,\mu\mathrm{m}$ across the entire camera. As expected from theory, the reduction in resolution on propagation is slower for the Bessel5 beam than for the Bessel10 beam. The distribution of points for the Gaussian and Bessel beams is very scattered beyond $x = 25\,\mu\mathrm{m}$. This is attributed to the lower resolution in this region, resulting in lower SNR, deconvolution artefacts, and increased chance of overlapping PSFs.

The lateral resolution for all light-sheet types was also measured, although as this is solely dependent on the detection optics, and was not expected to differ. The FWHM across the FOV was measured to be $(1.9 \pm 0.3)\,\mu\mathrm{m}$ for all light-sheets. The lowered lateral resolution is attributed to spherical aberration at the capillary surface.

A similar experiment was performed using 600nm diameter red fluorescent beads to characterise the Type-2 system. Figure 4.12 shows that the Type-2 system performs similarly to the Type-1 system for Gaussian and Airy illumination. Lateral and axial FWHM was measured for all beads in the image, measuring $1.2 \pm 0.1\,\mu\mathrm{m}$ and $1.2 \pm 0.1\,\mu\mathrm{m}$ respectively for Airy illumination and showing that the system achieves isotropic resolution and is consistent with simulations in Chapter 4.2.2. The spherical

aberration that was observed with the Type-1 system has been reduced as the lateral resolution is improved.

4.3.5 Imaging thick biological specimen

To demonstrate the use of Airy beams for LSM in thick, scattering tissue, filamentous (f)-actin and nuclear material was imaged in the musculature of a tissue section from a juvenile amphioxus (*Branchiostoma lanceolatum*) (see Appendix F.1 for preparation). Volumetric images were acquired with the Type-2 system, with a $z-$plane spacing of 200nm over a $z-$range of $100\,\mu\mathrm{m}$ for each beam type. The illumination power was kept constant at approximately 0.25mW for all light-sheet types. A laser line (Semrock, NF03-488E-25) and band-pass (Semrock, FITC-BP01-Clin-25) filter combination was used to acquire the green fluorescence channel, red fluorescence was acquired using a laser line (Semrock, NF11-532-25) and band-pass (Semrock, FF01-609/54-25) filter combination.

As the Gaussian FOV is so narrow and the remainder of the image contains mostly artefacts, the recorded, rather than deconvolved, data is shown. Additionally, no image is shown for the Bessel10 light-sheet as, again, the FOV is rather limited for the sample.

Figure 4.13 shows selected 2D sections from the acquired volumes. The results are qualitatively similar to those for fluorescent beads (Chapter 4.3.4). The axial resolution of the Gaussian is good near the light-sheet focus ($x = 0$) and degrades away from this point. The Bessel5 light-sheet shows strong artefacts for $|x| > 45\,\mu\mathrm{m}$ as expected. For all light-sheet types, there is a gradual decrease in image quality and signal strength for increased propagation into the sample (large x).

The Bessel5 images exhibit a lower SNR than the Gaussian and Airy images, this is attributed to the broad cross-section of the Bessel5 light-sheet. The side-lobes of the Bessel beam impact negatively on image quality, therefore lowering the SNR for a given illumination intensity. In contrast, the Airy light-sheet uses the signal from its side-lobes constructively for image formation and so retains good SNR.

A further observation from this data is that the resolution of the Gaussian light-sheet at focus is lower than with the Airy light-sheet, as evidenced from Figs 4.13(d,l), even though they are expected to perform similarly. The reduction in axial resolution

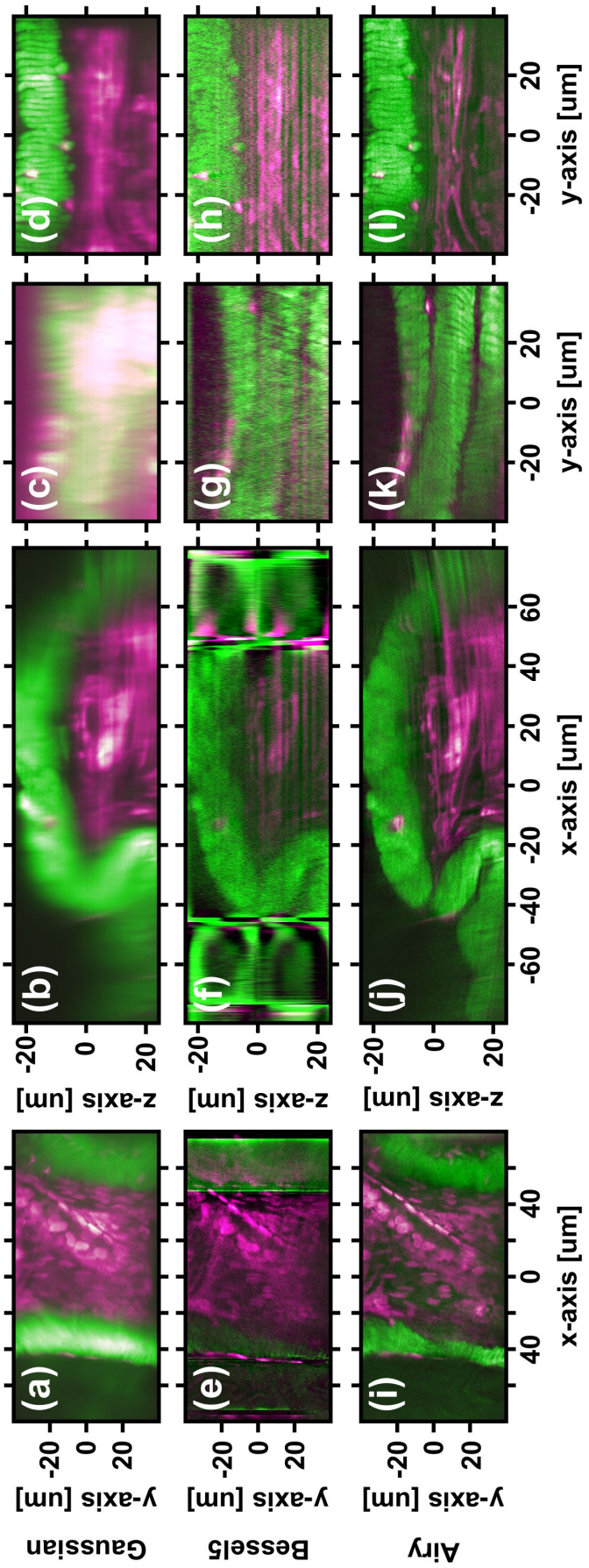

FIGURE 4.13: Light-sheet imaging of amphioxus musculature. Two-dimensional sections from volumetric scans acquired using Gaussian (a-d), Bessel5 (e-h), and Airy (i-l) light-sheets showing f-actin (green) and nuclei (magenta). (a,e,i) $x-y$ sections at $z=0$, (b,f,j) $x-z$ sections at $y=0$, (c,g,k) $y-z$ sections at $x=-40\,\mu\mathrm{m}$, and (d,h,l) at $x=0$. Figure adapted with permission from [18].

is attributed to sample induced aberrations in the Gaussian light-sheet. The Airy beam exhibits self-healing and is resistant to aberrations [27, 29] which is thought to account for the improved image quality in this case. Imaging with Gaussian and Airy light-sheets in the presence of strong aberrations will be covered in more detail in Chapter 5.

4.3.6 Photobleaching study of Gaussian, Bessel, and Airy light-sheets

As well as image quality, light induced damage to the sample must be considered for live imaging experiments. The amount of photodamage (both phototoxicity and photobleaching) depends largely on the instantaneous peak intensity of the illumination at each point in the sample [5, 55], and so photodamage is expected to be less for Bessel and Airy light-sheets due to their extended transverse structures.

This was tested experimentally by time-lapse monitoring fluorescence of Cy3-streptavidin embedded in poly(acrylamide) (PAA) gel (see Appendix F.1) over 100 volumetric scans. All light-sheets were formed by digital scanning with equal illumination power, to ensure comparability between methods. The power was intentionally higher than in imaging experiments (0.7mW) to accelerate the bleaching of fluorophores. The signal was integrated over a $10\,\mu\mathrm{m}$ thick volume centred around the point exhibiting the strongest fluorescence. This point was generally a few micrometres short of the light-sheet focus which is attributed to absorption of the light-sheet by the Cy3 dye.

Figure 4.14 shows the intensity decay over 100 volumetric scans for each of the light-sheet types discussed above. The photobleaching rates were determined by fitting with exponential functions. A single exponential was sufficient to describe the decay for both Bessel and Airy light-sheets, but a bi-exponential ($y(x) = A_1 e^{B_1} + A_2 e^{B_2}$) was needed to fit the Gaussian data. The fitted parameters are summarised in Table 4.5.

The photobleaching rates follow the expected trend. The Bessel5 and Airy light-sheets are the lowest, and are very similar.

This experiment directly characterises the effect of different light-sheet types on photobleaching, but is also indicative of phototoxicy as photobleaching can cause free radical generation and high intensity illumination has been shown to cause morphological changes in specimen development [54].

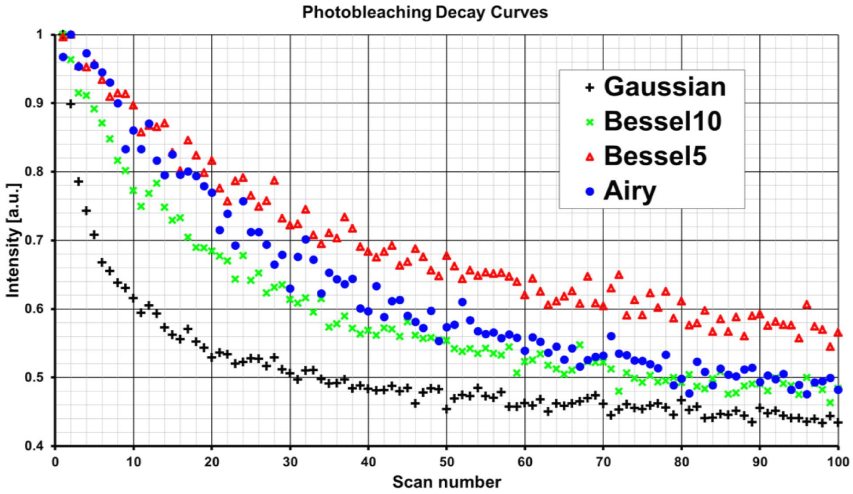

FIGURE 4.14: Photobleaching decay curves for Gaussian, Bessel, and Airy light-sheets. Normalised fluorescence signal of Cy3 with light-sheet illumination power 0.7mW over 100 volumetric scans for Gaussian (black), Bessel10 (green), Bessel5(red), and Airy (blue) light-sheets.

Light-sheet type	**PBR [scan^{-1}]**	**95% CI [scan^{-1}]**	**HL [scan]**	**95% CI [scan]**
Gaussian, 77% term	0.76 ± 0.05	$0.66 \rightarrow 0.86$	0.9	$0.8 \rightarrow 1.1$
Gaussian, 23% term	0.068 ± 0.007	$0.054 \rightarrow 0.082$	10.1	$8.4 \rightarrow 12.7$
Bessel10	0.045 ± 0.002	$0.041 \rightarrow 0.049$	15.4	$14.1 \rightarrow 16.9$
Bessel5	0.034 ± 0.002	$0.031 \rightarrow 0.038$	20.2	$18.5 \rightarrow 22.4$
Airy	0.030 ± 0.001	$0.028 \rightarrow 0.033$	22.8	$21.1 \rightarrow 24.8$

TABLE 4.5: Photobleaching decay rates for Gaussian, Bessel, and Airy light-sheets corresponding to decay curves shown in Fig. 4.14. Photobleaching rate (PBR) and half-life (HL), with corresponding 95% confidence intervals (CI) measured for Gaussian (bi-exponential), Bessel10, Bessel5, and Airy light-sheets.

4.4 Discussion and conclusions

Airy beams have been proposed as a potentially beneficial beam type for light-sheet illumination in LSM. This Chapter has investigated the use of the Airy beam, and other transversally asymmetrical beams, for light-sheet microscopy. Axial resolution and FOV are determined by observation of the MTF of each beam as a function of longitudinal coordinate, and analytic descriptions are derived for Gaussian, Bessel, and Airy beam based light-sheets. The trade-off between axial resolution and FOV is shown to be much more rewarding with Airy illumination than with Gaussian or Bessel illumination. For a given axial resolution of $1\,\mu\text{m}$, an Airy10 light-sheet covers a FOV of

$\approx 200\,\mu m$, a Gaussian light-sheet covers a FOV of $\approx 25\,\mu m$, and a Bessel10 light-sheet covers a FOV of $\approx 5\,\mu m$. High axial resolution can be recovered from Airy LSM images using a simple Wiener filter, whereas other beam types require additional hardware and image acquisition procedures to achieve high resolution [5, 20, 60]. Two designs for an Airy beam LSM are described and characterised. Experimental results on fluorescent microspheres are consistent with the developed theory, and isotropic resolution of $1.2 \pm 0.1\,\mu m$ is achieved and is consistent with simulations in Chapter 4.2.2. The Airy LSM is also used to image a muscle section of a juvenile amphioxus, demonstrating the use of this technique in a thick, turbid specimen. Time-lapse imaging of fluorescent dyes are also used to quantify the phototoxicity associated with each beam type, showing that the Airy light-sheet exhibits low phototoxicity.

The extended family of transversally asymmetric, "Airy-like", beams is a huge parameter space that could not be explored fully. However, the results indicated a trend of reducing FOV when increasing the order of the polynomial phase profile, γ, which helps to narrow the focus of the investigation. Additionally, the high-resolution FOV associated with an asymmetric 2nd-order polynomial is much lower than for the 3rd-order polynomial (Airy beam) suggesting the Airy beam is the optimal in this regard. Non-integer polynomial phase profiles, for example:

$$\phi(u) = \mathrm{sgn}(u) A u^{2.5} \tag{4.16}$$

may be an interesting point of study in future investigations.

Both simulations and analytic expressions for the performance of each beam type neglect the finite DOF of the detection objective lens which will alter and truncate the axial extent of the light-sheet and can adversely affect the light-sheet MFT. This was proven to be unnecessary for the experimental parameters used in this study but may need to be considered for extension of the Airy LSM technique to higher NA and resolution, as the DOF will be narrowed and the parabolic trajectory of the Airy beam will become more inclined. It was further observed that the image plane of the microscope curved due to aberrations in the optical train. A complete theory could include this, to optimise the orientation and strength of the cubic modulation to match the Airy

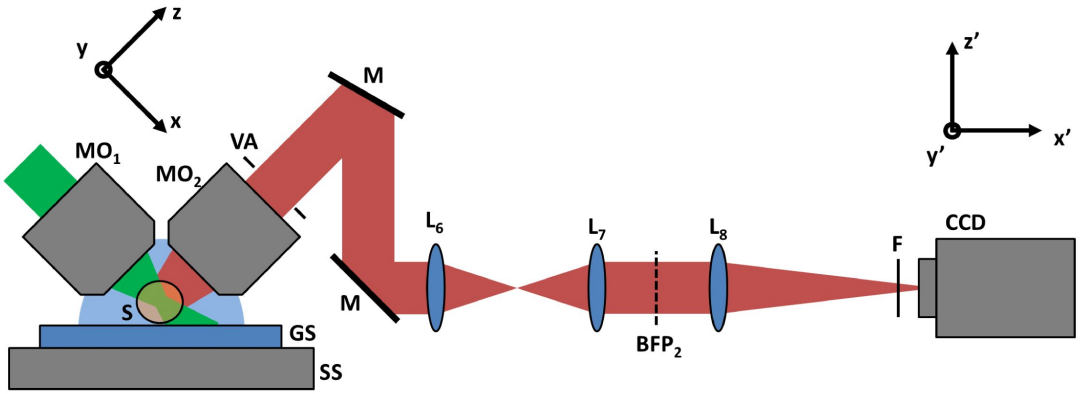

FIGURE 4.15: Schematic diagram showing modifications to the detection arm of the Type-2 LSM system to enable easier access to the back focal plane (BFP) of the detection objective lens. Additional lenses image the BFP of MO_2 and re-image the image plane onto the camera (CCD). MOx: Microscope objective lens; S: Sample; GS: Glass slide; SS: Sample stage; VA: Variable aperture; M: Mirror; Lx: Lens; BFPx: Back focal plane; F: Filter; CCD: (EM)CCD camera.

parabola with the curvature of the image plane. Furthermore, manipulation of the orientation of the image plane [69, 71] could give control over the curvature of the image plane and could be optimised to match the Airy light-sheet to maximise light-collection efficiency. Alternatively, extended-DOF techniques [191] could be implemented to obviate this limitation. The use of a cubic mask to extend the DOF of LSM has been implemented recently for the purpose of rapid volumetric image acquisition [58] and could be readily implemented into the Airy LSM system to enable ultra-wide FOV Airy LSM imaging with high resolution, or ultra-high resolution resolution Airy LSM utilising the full NA of both illumination and detection objective lenses. In preparation for this future project, the detection pathway of the Type-2 system has been modified, as shown in Fig. 4.15, to allow easier access to the back focal plane of the detection objective lens for placement of a cubic phase mask there.

Experimental data acquired with the Type-1 and Type-2 systems agrees with theory although the full extent of the Airy FOV is not observed as this exceeds the camera sensor. The magnification could be lowered to capture a larger FOV but the light-sheet height (in the $y-$axis) is limited by the deflection range of the AOD and so results in a large area of the camera sensor being unused. A scanning element with a greater scan

range should be used in future systems but the current element suffices for proof-of-concept.

Images of the amphioxus sample indicate the Airy light-sheet can achieve higher resolution than the Gaussian light-sheet in the presence of aberrations, even at focus. This was attributed to the self-healing property of propagation invariant beams [27]. A more in depth analysis is required to quantify this effect and is investigated in Chapter 5.

More advanced beam shaping in conjunction with the Airy light-sheet can also be beneficial for LSM. An Airy beam may be generated from a static phase plate rather than a reconfigurable SLM which would reduce the overall cost of the microscope. Papazoglou *et al* showed that Airy beams can be generated from the controlled aberrations induced in a beam when passed through a cylindrical lens which is tilted relative to the optic axis [197]. The use of this low-cost Airy beam generation method is explored for LSM in Chapter 6. Chapter 6 also investigates the use of attenuation compensated Airy beams [198] for delivery of Airy light-sheet illumination deeper into thick tissue and with increased uniformity.

The comparison of photobleaching rates in LSM with different light-sheet types indicates that the Airy and Bessel beams both reduce the photobleaching and therefore phototoxicity to the specimen. However, the images of the amphioxus tissue show that the Bessel light-sheet, for the same illumination power, has a lower SNR than the Airy light-sheet achieves. This is due to the side-lobes of the Bessel beam impacting negatively on image formation, whereas the side-lobes of the Airy beam contribute positively to image formation. Therefore, to achieve equal SNR in the images, the power of in the Bessel light-sheet or the camera integration time must be increased, resulting in more photodamage. The Airy light-sheet therefore exhibits the lowest phototoxicity. This could be further reduced by forming the Airy light-sheet with a cylindrical lens rather than digital scanning. This would re-introduce shadowing artefacts into the image but could be mitigated by rapid tilting of the light-sheet as described in [41].

Chapter summary

- Airy beams, in conjunction with a simple deconvolution algorithm, yield a much better trade-off between axial resolution and FOV for LSM than Gaussian or Bessel beams.
- The Airy beam appears to be the best beam in this regard within the family of transversally asymmetric 2D beams.
- The Airy LSM has been demonstrated experimentally to give axial resolution of approximately $1 - 1.5\,\mu\mathrm{m}$ over a half-FOV of over $150\,\mu\mathrm{m}$, over 15 times greater than the Gaussian LSM of equivalent resolution, which has a half-FOV of approximately $10\,\mu\mathrm{m}$.
- A study of photobleaching rates with different light-sheet types indicates that the Airy light-sheet exhibits lower phototoxicy than Gaussian or Bessel light-sheets for a given SNR in the image.
- Future investigations could exploit extended-DOF techniques or matching the light-sheet and image plane curvatures to increase the resolution, FOV, and light-collection efficiency of the imaging method.

4.5 Chapter acknowledgements

All simulations and data processing was performed by the author and Tom Vettenburg. Heather I. C. Dalgarno, the author, Tomáš Čižmar, and Tom Vettenburg designed and constructed the Type-1 LSM and performed all experiments on this system. The author designed and constructed the Type-2 LSM with assistance from Tom Vettenburg and performed all experiments on this system. Clara Coll-Lladó and David E. K. Ferrier provided and prepared amphioxus tissue sections and assisted with interpretation of the images. Carlos Penedo-Esteiro advised on aspects of the photobleaching study.

Chapter 5

Application of Airy light-sheet microscopy to imaging in turbid tissue

5.1 Introduction

The previous Chapter introduced the Airy beam as a beneficial illumination beam type for LSM, yielding good axial resolution over a large FOV, and having low phototoxicity. Imaging in a thick specimen (Chapter 4.3.5) indicated that Airy LSM may facilitate high quality imaging at greater depth into turbid tissue than traditional Gaussian LSM, owing to the self-healing and aberration resistant properties of the Airy beam [27, 29].

A recent study by Glaser, Wang, and Liu used Monte Carlo simulations to investigate imaging performance at depth in scattering tissues and concluded that, while LSM is generally limited to transparent samples, it can be applied to imaging superficial layers of highly turbid material [199]. Their study considered only LSM using Gaussian illumination and they comment that Bessel and Airy beam illumination may yield different results. Finally, Glaser, Wang, and Liu comment that there is currently no experimental investigation of LSM imaging performance, of any illumination type, in turbid tissue.

This Chapter experimentally explores the effect of beam type on the image quality and imaging depth of LSM in the presence of strong sample induced aberrations. Fixed brain sections from a mouse are imaged by Gaussian and Airy LSM prior to and after optical clearing. Fourier analysis is used to develop an image quality metric

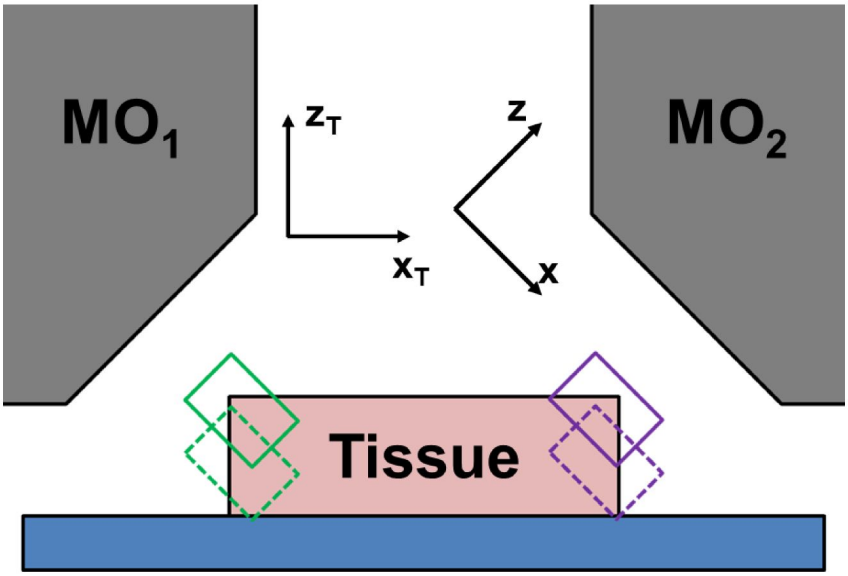

FIGURE 5.1: Schematic of imaged regions of mouse brain tissue slices. Green outlined regions have approximately constant illumination path length but fluorescence path length is dependent on tissue depth. Purple outlined regions have approximately constant fluorescence path length but illumination path length is dependent on tissue depth. $[x, y, z]$: Microscope coordinates; $[x_T, y_T, z_T]$: Sample coordinates ($y = y_T$); MO_1: illumination objective; MO_2: detection objective

for fluorescently labelled structures with heterogeneous size distributions and FWHM measurements of homogeneous, point-like resolution probes are used to quantify maximum imaging depth with each technique.

All animal experiments were reviewed and approved by the University of St Andrews Animal Ethics and Welfare Committee under Dr Javier Tello's Home Office Project License 70/7924. All *in vivo* experiments were performed by Dr Javier Tello and Ms Sanya Aggarwal only.

5.2 Comparison of image quality in non-cleared and cleared tissues

To investigate the effect of light-sheet type on image quality in turbid specimens, volumetric images were acquired throughout $400\,\mu m$ thick sections of fixed mouse brain tissue expressing mCherry, a red fluorescent protein, and fluorescent beads as resolution probes.

Volumetric scans were acquired primarily in two regions of the tissue slices. The first was at the side of the tissue nearest the illumination objective (MO_1; green boxes in Fig. 5.1). The second was on the opposite side of the tissue, nearest to the detection objective (MO_2; purple boxes in Fig. 5.1). Image quality will depend on the total optical path through the tissue; the path of the illumination to the imaged point and the path of fluorescence from that point to the detector. In most microscopy techniques, the illumination and detection share a common path but in LSM these are decoupled. By imaging regions at the tissue edge near the illumination objective, the aberrations in the illumination are minimised and the illumination path can be kept approximately constant. The dominant aberrations in this case stem from the fluorescence path, should be independent of light-sheet type, and can serve as an aberration baseline to characterise the tissue. Conversely, imaging at the side of tissue nearest the detection objective is dominated by aberrations in the illumination pathway, and may be affected by different light-sheet types.

The experiments were carried out using the Type-2 system described in Chapter 4. 2,2'-thiodiethanol (TDE) was used as a clearing agent [200] because it is water-soluble, has low viscosity, and exhibits minimal deformation of sub-cellular structures [200]. The microscope objectives used in the Type-2 system (Nikon CFI Apo 40x/0.8 DIC, w.d. = 3.5mm, water dipping) are designed for immersion in water or equivalent fluid with $n = 1.33$. The refractive index of the TDE solution can be tuned and depends on the concentration of TDE. The effectiveness of the clearing also depends on the concentration. A concentration of 47% TDE in 1x PBS was chosen, which has $n = 1.42$ and moderately clears the tissue [200]. The refractive index mismatch between water and the TDE solution will cause spherical aberration in both the illumination and detection pathways [195]. This was not accounted for in determination of the light-sheet profile for deconvolution of Airy LSM images.

5.2.1 Imaging of genetically labelled fluorescent structures in mouse brain sections

First, images were acquired in mouse brain tissue expressing mCherry in a subset of neurons. The animal had been injected with adenoassociated viral (AAV) particles (AAV1/2-Ef1a-DIO-mCherry-wPRE) prior to the experiment (see Appendix F.2 for sample preparation details). Images were acquired of the same section of tissue before and after clearing with a 47% TDE solution. In all experiments, the illumination power was kept constant at 240mW.

Figure 5.2(a,b) show $x_T - z_T$ maximum intensity projections of datasets acquired in non-cleared tissue using Gaussian and Airy ($\alpha = 7$) light-sheets. Qualitatively, Fig. 5.2(a,b) shows that Airy LSM gives a better quality image from a single imaging run as sharp features are seen across the whole FOV of the image with Airy illumination whereas the Gaussian image has spatially variant image quality. This effect has been described in depth in Chapter 4 and the aim of this study is to compare "best performance" of each imaging modality. As such, each dataset is apodized with a Gaussian function with $8\,\mu\mathrm{m}$ width along the $x-$axis and centred at the focus of the Gaussian light-sheet (Fig. 5.2(c,d)).

To further complicate the analysis, biological features within tissue typically exhibit structure across multiple length scales (Fig. 5.2(a,b)). This non-uniformity poses a challenge to assessing image quality by measurements in real-space. One alternative is perform the analysis in the spatial frequency domain. For this, a metric for image quality was developed based on the integral of the magnitude of spectral components for an image within a given spectral window. This was computed for images at different depths within the tissue, $I(x_T, y_T; z_T)$, and investigated this metric as a function of tissue depth, z_T.

The spectral magnitude within the n^{th} spectral window of an image of the $x_T - y_T$, $S_n(z_T)$, is given by:

$$S_n(z_T) = \frac{\int_{k_{r,n-1}}^{k_{r,n}} \int_0^{2\pi} |\tilde{I}(k_r, k_\theta; z_T)| k_r dk_r dk_\theta}{\int_{k_{r,n-1}}^{k_{r,n}} \int_0^{2\pi} k_r dk_r dk_\theta} \tag{5.1}$$

where $\tilde{I}(k_r, k_\theta; z_T)$ is the Fourier transform of the image plane $I(x_T, y_T; z_T)$ in cylindrical coordinates and $k_{r,n}$ is the radial spatial frequency separating spectral windows in 10% increments of the diffraction limit:

$$k_{r,n} = \frac{n}{10}\frac{2\,\mathrm{NA}}{\lambda} \tag{5.2}$$

The enhancement factor within a given spectral window is then given by the ratio between Airy and Gaussian imaging modalities:

$$EF_n(z_T) = \frac{S_n(z_T)_{Airy}}{S_n(z_T)_{Gaussian}} \tag{5.3}$$

Figure 5.2(e-n) show $S_n(z_T)$ for the apodized datasets shown in Fig. 5.2(c,d) (Gaussian: blue lines, Airy: green lines;first axis) and $EF_n(z_T)$ (red lines; second axis). This analysis is particularly robust to single-pixel noise fluctuations as the analysis is conducted only at spatial frequencies up to the diffraction limit whereas single-pixel fluctuations occur at higher spatial frequencies in properly sampled images. Figure 5.2(o) illustrates the spectral windows used to calculate $S_n(z_T)$. These plots show that the enhancement factor at low spatial frequencies is approximately unity at low spatial frequencies but steadily acquires a positive gradient with increasing spatial frequency. This shows an improvement in relative image quality and indicates that Airy LSM is more resistant to sample-induced aberrations than Gaussian LSM.

An average enhancement factor, $EF_{HF}(z_T)$, was determined by averaging over the high-frequency spectral bands between 60% and 100% of the diffraction limit (Fig. 5.2(p)). This was fitted with a linear function in z_T. The example shown in Fig. 5.2 yields a gradient of $0.06\,\mu\mathrm{m}^{-1}$. The y-intercept ($EF_{HF}(0)$) of this fit is, unexpectedly, non-unity. This indicates that even at the tissue surface, there is an improvement when using Airy illumination over Gaussian. In the presence of no aberrations, both illumination types are expected to give equal best performance. This surface enhancement is attributed to refractive index variations at the interface between the immersion medium (PBS) and the agarose gel which encapsulates the tissue section, holding it in place. This analysis was repeated across a number of different regions of tissue and in different sections from the same brain. The number of datasets (sample size) was 11.

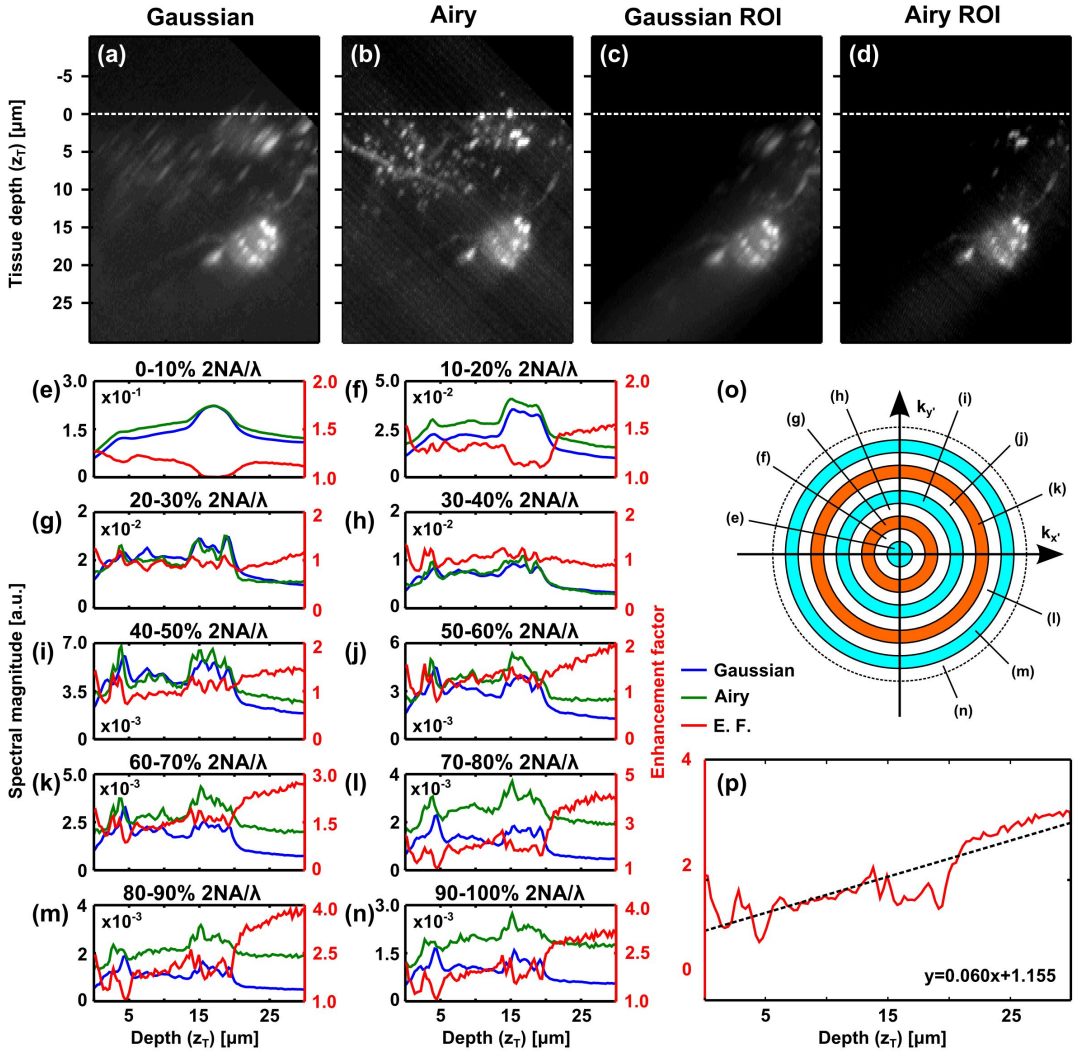

FIGURE 5.2: Fourier analysis of Gaussian and Airy LSM images in non-cleared mouse brain tissue. (a,b) Maximum intensity projections ($x_T - z_T$) of fluorescent neurons in $400\,\mu\mathrm{m}$ thick tissue slice acquired by Gaussian and Airy LSM. Dashed white lines indicate tissue surface. (c,d) Apodized version of (a,b) showing only the analysis region, around Gaussian beam focus. (e,n) Plots of spectral magnitude, $S_n(z_T)$, versus tissue depth for Gaussian (blue) and Airy (green) light-sheet illumination within selected spectral windows. $EF_n(z_T)$ (red; second axis) is also plotted. (o) Illustration of spectral windows used to segment the data for plots (e-n). The dashed circle corresponds to the diffraction limit, a spatial frequency of $2\,\mathrm{NA}/\lambda$. (p) The average enhancement factor over high-frequency spectral bands, $EF_{HF}(z_T)$, $(60 - 100\%2\,\mathrm{NA}/\lambda$; plots (k-n)). Dashed line in (p) shows a linear fit to the data, equation shown on plot.

As the enhancement of image quality with Airy LSM appears to be linked to the aberration resistance of the illumination beam, optical clearing was used as a method to vary the optical properties and aberrations of the tissue to test this hypothesis. A 47% TDE solution was used to clear the tissue sections and was also used as the immersion medium for the cleared tissue sections when imaging. The clearing process reduced the aberrations of the tissue. Images were acquired in similar regions as those imaged before clearing. The sample size was 9.

The average linear fit parameters (mean $\pm$ standard deviation) for $EF_{HF}(z_T)$ in non-cleared and cleared tissue are shown in Table 5.1. No trend was observed in the behaviour between datasets acquired at the sides of tissue nearest to the illumination or detection objective lenses and this factor was neglected from the analysis. There is a five-fold reduction in the gradient of $EF_{HF}(z_T)$ in cleared tissue. The reduction in enhancement factor when facing reduced aberrations is indicative of the effect being linked to the aberration resistance of the Airy beam. The y-intercept is slightly higher in cleared tissue than in non-cleared tissue. This is attributed to additional aberrations caused at the objective lens/imaging buffer interface as the microscope objective is optimised for immersion in water ($n = 1.33$), not the TDE solution ($n = 1.42 \pm 0.01$ [200]).

Tissue Type	**Gradient (μm^{-1})**	**y-intercept**
Non-cleared	0.04 ± 0.02	1.2 ± 0.2
Cleared	0.008 ± 0.007	1.6 ± 0.4

TABLE 5.1: Linear fit parameters of $EF_{HF}(z_T)$ in non-cleared and cleared mouse brain tissue. Sample size was 11 for non-cleared tissue, 9 for cleared tissue.

Due to the reduced aberrations in the cleared tissue, data could be collected from much greater depths within the tissue section. Figure 5.3(a,b) shows composite images acquired using Gaussian and Airy LSM at 3 different depths within the tissue. Regions of interest were apodized around Gaussian beam focus (Fig. 5.3(c-h)) and the above analysis was performed. The average high-frequency enhancement factor, $EF_{HF}(z_T)$, is plotted in Fig. 5.3(i-k). The example in Fig. 5.3 is representative of 4 out of 5 multi-depth composite datasets. The gradient of $EF_{HF}(z_T)$ increases with increasing depth into tissue. This is to be expected, as aberrations are cumulative and should increase

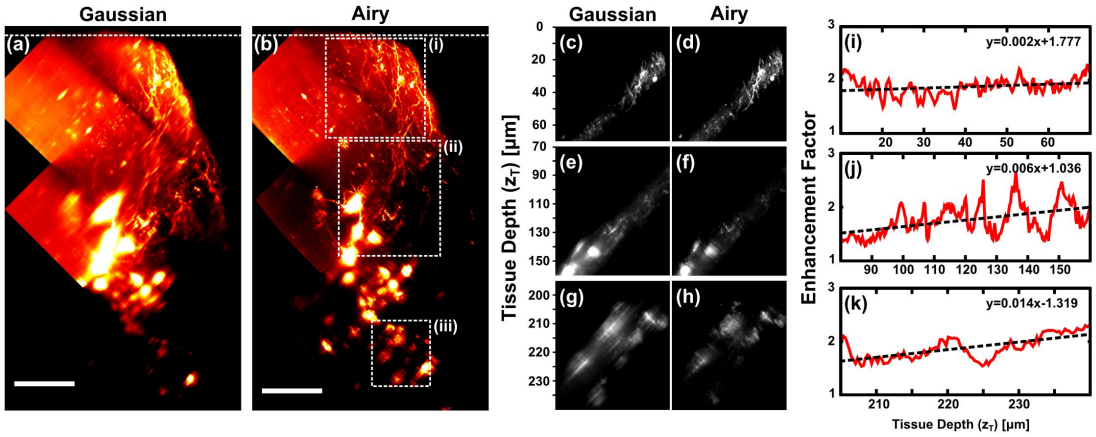

FIGURE 5.3: a,b) Maximum intensity projections ($x_T - z_T$ view) of fluorescent neurons in $400\,\mu\text{m}$ thick, cleared mouse brain tissue slice acquired using GLSM (a) and ALSM (b). Composite images of 3 datasets at different tissue depths. Dashed white lines indicate tissue surface. (c-h) Cropped regions of (a,b) within dashed boxes (i-iii) apodized to only show the region around Gaussian beam focus. (i-k) High-frequency enhancement factor, $EF_{HF}(z_T)$ within dashed boxes (i-iii). Scale bar in (a,b): $50\,\mu\text{m}$. Dashed lines in (i-k) are linear fits to the data, equations shown on each plot.

with depth. The variation in slope with depth also highlights that a simple linear model is a not sufficient to capture the full complex behaviour through an entire tissue section, although over small subsections a linear model is appropriate and was sufficient in most cases encountered in this study.

5.2.2 Imaging of resolution probes in mouse brain sections

Another method to quantify the effect of light-sheet type on image quality in turbid specimens is to use point-like resolution probes which control for effects caused by inhomogeneous feature size. Mouse brain tissue slices with resolution probes distributed throughout were imaged. The animal was injected with 600nm diameter red fluorescent beads (see Appendix F.2 for sample preparation details). Images were again acquired on the same section of tissue before and after clearing with a 47% TDE solution. Experimental parameters were kept the same as in Chapter 5.2.1, except the microscope had been upgraded as shown in Fig. 4.15, this increased the FOV by 2 times along the $x-$axis but otherwise did not affect the microscope performance.

Figure 5.4 shows $x - z$ maximum intensity projections of initial datasets acquired using Gaussian and Airy ($\alpha = 7$) light-sheets before and after clearing.

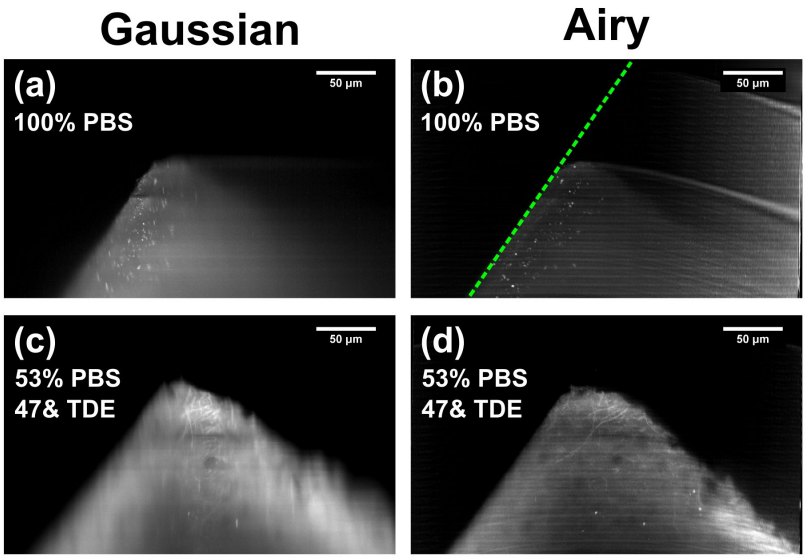

FIGURE 5.4: Initial resolution probe comparison between Gaussian and Airy LSM in mouse brain tissue slice injected with fluorescent beads. $x-z$ maximum intensity projections of datasets for Gaussian (a,c) and Airy (b,d) illumination before (a,b), and after (c,d) clearing with 47% TDE in 1x PBS. Light-sheet illumination is incident from left and fluorescence collection is from top. Datasets are acquired at tissue surface. Dashed green line in (b) indicates the orientation of the tissue surface. Scale bars: $50\ \mu\mathrm{m}$.

Figures 5.4(a-d) show images from a region of tissue near the detection objective acquired with Gaussian and Airy light-sheets, before and after clearing respectively. There are very few beads observed in the tissue after clearing. This was attributed to diffusion of the beads out of the tissue during the clearing process. The beads are not bound in place by any antigen-antibody link and the clearing process involves immersing the sample for several hours in multiple solutions at $37°$C under continuous agitation. Additional imaging experiments ruled out dissolution of the polystyrene beads into the TDE solvent.

Figures 5.5 show images of cleared tissue acquired at a depth approximately $400\ \mu\mathrm{m}$ below those in Fig 5.4(c,d). Again, no beads are present, but autofluorescence reveals the limits of the tissue showing the bottom of the tissue slice. Without beads or other features to accurately stitch images of different height together, the exact thickness of the tissue cannot be quantified. This shows that images may be acquired at least $400\ \mu\mathrm{m}$ into the cleared tissue, even if the resolution attainable at this depth is unknown.

Image quality was determined as a function of depth by manually taking FWHM

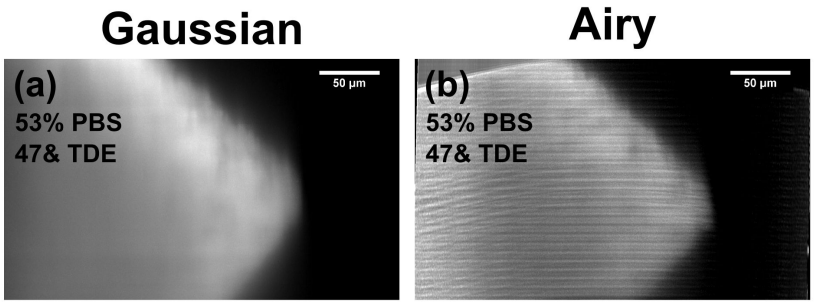

FIGURE 5.5: Initial resolution probe comparison between Gaussian and Airy LSM in cleared mouse brain tissue slice injected with fluorescent beads. $x-z$ maximum intensity projections of datasets for Gaussian (a) and Airy (b) illumination at the bottom of the $400\ \mu\mathrm{m}$ thick tissue section.

measurements of lateral and axial resolution for each light-sheet type in tissue before and after clearing. Figure 5.6 shows results from the datasets shown in Fig. 5.4(a,b). The plots show that lateral resolution remains fairly constant (approximately $1-1.5\ \mu\mathrm{m}$) for both beam types up to about $40\ \mu\mathrm{m}$ depth, it would appear that the resolution degrades beyond $z_T = 40\ \mu\mathrm{m}$ but there are few datapoints to verify this. There is more variation in the axial resolution of the Gaussian light-sheet with depth (Fig. 5.6(b)), this is to be expected as the axial resolution is spatially variant along the $x-$axis. The axial resolution of the Airy light-sheet remains consistently low for at all tissue depths measured.

Figure 5.7 shows equivalent results in cleared tissue, measured from Fig 5.4(c,d). Due to the lack of beads in this sample, trends in the data are not as obvious. Figure 5.7(a) shows that the distribution of lateral resolution is approximately the same as in non-cleared tissue although these measurements are made at greater depths. Axial resolution of the Airy light-sheet (Fig. 5.7(b)) shows results consistent with Fig. 5.6(b), the axial resolution remains low but steadily increases with increasing depth. There is not sufficient evidence to comment on the axial resolution of the Gaussian light-sheet as a function of tissue depth.

To improve the accuracy of these results, and to increase the number of resolution probes in the cleared tissue sections, an additional injection was performed on the cleared tissue section. The injection was performed on cleared tissue with the same parameters as for the bead-injection into live mice (see Appendix F.2). The newly injected

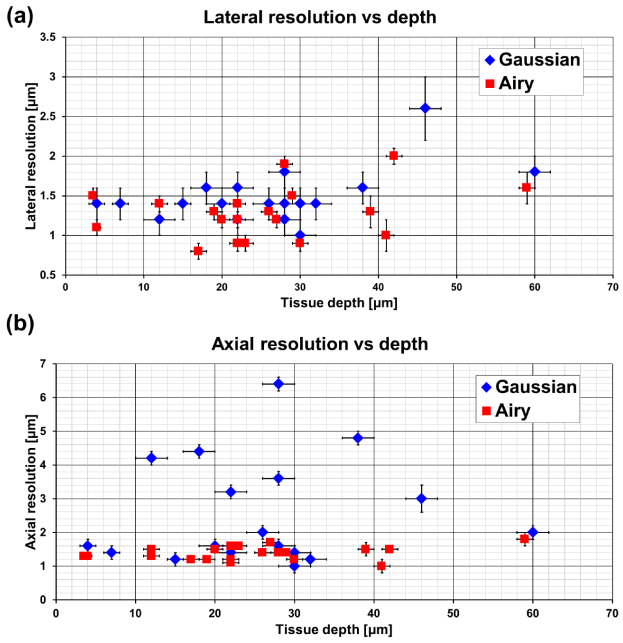

FIGURE 5.6: Resolution measurements in non-cleared tissue. 20 beads were measured in the Gaussian dataset and approximately corresponding beads were measured in the Airy dataset. Lateral (a) and axial (b) FWHM measurements as a function of tissue depth for resolution probes imaged with Gaussian (blue; Fig. 5.4(a)) and Airy (red; Fig. 5.4(b)) light-sheet illumination before clearing. Error bars show standard error.

beads were localised within the tissue and so the tissue section was cut through the injection site, and the tissue section oriented such that the beads were in the side of the tissue closest to the detection objective.

Figure 5.8(a,b) shows maximum intensity projections of LSM images of resolution probes in cleared tissue where the beads have been injected post-clearing. A spot finding algorithm was implemented to find all beads within the size range $(0.6 - 4.0\,\mu\mathrm{m})$ and fit 1D Gaussian functions along the lateral (x) and axial (Z) directions. The FWHM of the detected beam widths are plotted in Fig. 5.8(c,d). 86 distinct beads were detected in the Gaussian image, 257 were detected in the Airy image. Linear fits of lateral and axial FWHM as a function of tissue depth are also plotted. The linear fit parameters are given in Table 5.2.

As the beads are located on the side of the tissue closest to the detection objective, aberrations in the detection pathway should be minimal and constant for both beam

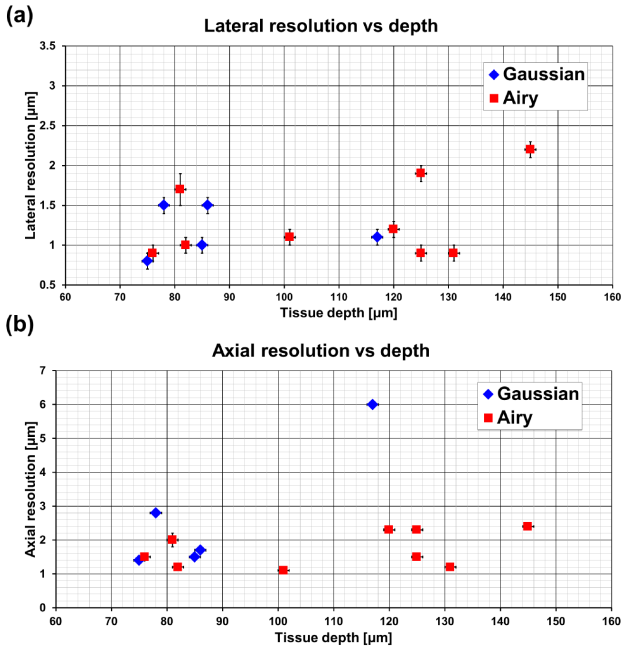

FIGURE 5.7: Resolution measurements in cleared tissue. All visible beads in the image were measured, 5 in the Gaussian dataset, 9 in the Airy dataset. Lateral (a) and axial (b) FWHM measurements as a function of tissue depth for resolution probes imaged with Gaussian (blue; Fig. 5.4(c)) and Airy (red; Fig. 5.4(d)) light-sheet illumination after clearing with 47% TDE in 1x PBS. Error bars show standard error.

types. Figures 5.8(c,d) show that the lateral resolution of both illumination types is approximately equal which agrees with this statement. The gradient of axial resolution is also approximately equal for both illumination types. This is not quite as expected but can be explained by the limitations of the spot finding algorithm. The range specified for the spot finding has a maximum value so it does not find overlapping beads. The axial resolution of the Gaussian light-sheet is spatially variant and increases rapidly away from beam focus and can exceed the upper limit for the algorithm very easily. These low-resolution regions are neglected by the algorithm, artificially boosting the apparent resolution of the Gaussian illumination. Additionally, the rapid increase in axial PSF also greatly increases the chance of overlap between two adjacent beads. Therefore, even before the axial PSF exceeds the algorithm's size range, beads will be rejected due to overlap and their combined with being greater than the limit. This is seen in the number of beads which are detected by the algorithm. Only about a third of all beads detected in the Airy image are detected in the Gaussian image despite being

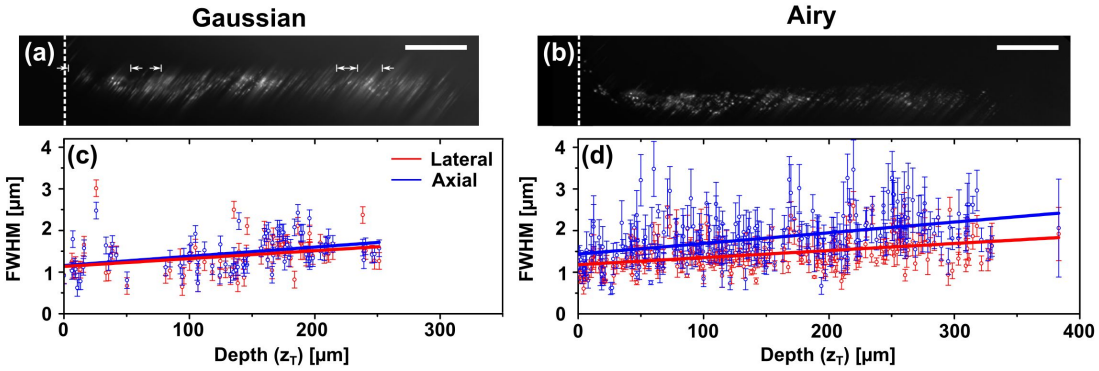

FIGURE 5.8: Maximum intensity projections ($x_T - y_T$ view) of mouse brain tissue injected with red fluorescent microspheres (600nm diameter) post-clearing. Gaussian (a) and Airy illumination (b) is shown. Tissue surface is indicated by dashed white line. (c,d) FWHM measurements of lateral (red) and axial (blue) bead sizes. Solid lines indicate a linear fit to the FWHM measurements as a function of tissue depth. Scale bar in (a,b): $50\,\mu\text{m}$.

the same sample. Due to the spatially variant axial PSF of the Gaussian light-sheet, beads are only detected in distinct regions of the image, highlighted by arrows in Fig. 5.8(a), and also observed by empty or sparse regions at corresponding positions in Fig. 5.8(c).

Finally, Fig 5.8(c,d) shows that Airy illumination allows images to be recovered from greater depths within the tissue section. The deepest observable feature in the Gaussian image was at $z_T = 251 \pm 1$ below the tissue surface whereas the deepest observable feature in the Airy image was at $z_T = 383 \pm 1$. This is approximately 50% ($125\,\mu\text{m}$) deeper and may be underestimated as the depth of the tissue section is approximately $400\,\mu\text{m}$.

Beam Type	Fit Orientation	FWHM at surface (μm)	Gradient FWHM vs Depth
Airy	Lateral	1.18 ±0.04	0.0017 ±0.0002
	Axial	1.44 ±0.06	0.0026 ±0.0003
Gaussian	Lateral	1.1 ±0.1	0.0019 ±0.0006
	Axial	1.16 ±0.09	0.0022 ±0.0006

TABLE 5.2: Linear fits to the plot of FWHM vs depth in Figure 5.8(c,d)

5.3 Discussion and conclusions

This Chapter has investigated the effect of illumination beam type on the image quality at depth within turbid samples. This study was performed in mouse brain tissue slices expressing mCherry in a subset of hypothalamic neurons, and wild-type samples injected with fluorescent resolution markers. Both samples were imaged prior to, and after, optical clearing with a 47% TDE solution. Image quality in both non-cleared and cleared tissue is qualitatively higher for Airy light-sheet illumination, this is attributed to the spatially variant axial resolution of the Gaussian light-sheet and not in itself a figure of merit to be characterised in this study as this has already been demonstrated in Chapter 4 to apply in all samples. A number of methods are used to analyse the images acquired. First, a novel method based on the spatial Fourier content within a given spectral window is used to analyse image quality irrespective of feature size. Secondly, FWHM measurements of homogeneous resolution probes are used to quantify maximum imaging depth within tissue. The results of these analyses show an enhancement in image quality when using Airy LSM over Gaussian LSM in samples with strong aberrations. The average linear fit indicates the average enhancement in non-cleared mouse brain tissue at $50\,\mu\mathrm{m}$ depth is 3.2 times. This enhancement is shown to be linked to the degree of aberrations and the enhancement factor decreases in optically cleared tissue, where aberrations are reduced. This is further validated by imaging at different depths within a thick cleared tissue slice. With increasing depth, the gradient of enhancement factor increases, showing a stronger enhancement in the presence of stronger cumulative aberrations at greater depth. The maximum imaging depth achievable with Airy LSM was also found to be 50% ($125\,\mu\mathrm{m}$) greater than with Gaussian LSM.

An unexpected observation was the disappearance of resolution probes after the clearing process. The polystyrene beads were shown not to dissolve in the TDE solution and so the great reduction in bead numbers is attributed to diffusion out of the tissue during the clearing process. This was overcome by injecting beads into the tissue post-clearing but remains a mystery. Future studies could make use of fluorescent beads coated with antibodies targeted to specific structures within the tissue.

An assumption used in this study is that the light-sheet profile is unaffected by the refractive index change between PBS and the 47% TDE solution. The objective lenses (Nikon CFI Apo 40x/0.8 DIC, w.d. = 3.5mm, water dipping) are designed for use in water or equivalent fluids with $n = 1.33$. The 47% TDE solution has a refractive index of approximately 1.42 [200] and will cause spherical aberration of the light-sheet. The results of Fig. 5.6, Fig. 5.7, and Fig. 5.8 indicate that any spherical aberration has a very small effect on the imaging performance of the microscope but the effect on light-sheet shape could explain the curved stripe artefacts present in Fig. 5.4(b,d). Given the increased refractive index of the imaging medium oil immersion objective lenses may be more suitable for future studies involving optical clearing. This would potentially allow more optimal concentrations of clearing solution, as 47% TDE in PBS was chosen to trade off optical clearing potential against aberration caused by refractive index mismatch.

Chapter summary

- Non-cleared and cleared mouse brain tissue slices can be used as a medium for investigation of light-sheet illumination shape on image quality in turbid specimens.
- Airy LSM achieves higher contrast than Gaussian LSM when imaging in turbid tissue (3.2 times higher contrast at $50\,\mu\mathrm{m}$ depth, gradient: $0.04\,\mu\mathrm{m}^{-1}$).
- Optical clearing is a useful tool to tune the aberrations of tissue sections for more detailed analysis.
- The enhancement observed with Airy LSM is linked to aberration resistance of the Airy beam.
- Airy LSM achieves 50% greater depth penetration than Gaussian LSM.

5.4 Chapter acknowledgements

Javier Tello designed experimental conditions for tissue preparation. Mouse brain slices were prepared by Javier Tello and Sanya Aggarwal, who performed all *in vivo* experiments, tissue sectioning, and tissue clearing. The author designed and performed all imaging experiments with the assistance of Kaley McCluskey and Javier Tello. Kaley McCluskey performed the automated FWHM analysis. All other analysis was performed by the author.

Chapter 6

Advanced beam shaping strategies for Airy light-sheet microscopy

Parts of this Chapter are adapted from the article "A compact Airy beam light sheet microscope with a tilted cylindrical lens" [201], published in Biomedical Optics Express (2014).

6.1 Introduction

Building on the work laid out in Chapter 4, this Chapter now looks at two separate advanced beam shaping strategies to enhance Airy beam based LSM.

The first technique investigates an ultra-low cost method for the generation of Airy beams in order to realise a compact and low-cost microscope based on the Airy light-sheet principle. This method involves tilting a cylindrical lens to induce the appropriate aberrations to impart an approximately cubic phase profile of the beam. Simulations are used to quantify the aberrations and the performance of the system is evaluated experimentally.

The second technique goes beyond the standard Airy beam, exploiting so-called attenuation-compensating [198] or loss-proof [202] Airy beams to counteract losses from absorption in thick specimens and recover homogeneous illumination at depth without relying on multiple illumination angles as in mSPIM (e.g. [41, 62, 64]). The method is investigated through analysis of simulated MTFs with the aim of future implementation on the Type-2 LSM system.

6.2 Development of a compact and low-cost Airy light-sheet microscope based on a tilted cylindrical lens

The Airy beam LSM described in Chapter 4 may be beneficial for biomedical imaging, but its intended users may find the advanced optical concepts and the use of SLMs daunting. Additionally, the cost of such advanced equipment is substantial, an SLM will easily consume several thousand pounds of an equipment budget. As such, this technique may only ever be used by a small group of collaborators with access to the original microscope. In contrast, the OpenSPIM design, an open source light-sheet design, can potentially be constructed in full for less than £15k [196]. In order to widen accessibility and use of the Airy LSM technique, the equipment must be made as simple and as low-cost as possible.

Custom made phase plates allow a static beam shape to be controlled but each plate can still be costly (approx. £2k). This Chapter investigates the use of a tilted cylindrical lens to generate the necessary phase profile for Airy light-sheet generation. The cylindrical lens is a low cost element (<£100) and can easily be incorporated into the OpenSPIM system for a low-cost and compact Airy LSM.

Modifications required to convert an OpenSPIM system are discussed, the quality of Airy light-sheet that may be produced by a tilted cylindrical lens is investigated by simulations, and image quality is experimentally determined.

6.2.1 Generation of Airy beams by harnessing low order aberrations

The generation of Airy beams from aberrations induced in a Gaussian beam when passed through a series of cylindrical lenses appropriately offset laterally and angularly from the optic axis was initially proposed by Papazoglou *et al* [197] for the generation of high intensity Airy beams across a wide range of wavelengths. Airy beams can be generated with an SLM, as in Chapter 4, but rapidly varying phase profiles, as are required near the edge of the pupil plane for high $\alpha-$value Airy beams, cannot be accurately produced, and SLMs can be sensitive to damage from high intensity illumination at short wavelengths. Fixed phase-plates can be manufactured to produce Airy beams that may withstand high intensity, short wavelength irradiation but cannot be

used to tune the $\alpha-$value. The section below summarises the work by Papazoglou *et al* in generation of tunable Airy beams with tilted cylindrical lenses [197].

One model for characterisation of aberrations resulting from an optical system is the Seidel wave aberration [197, 203]. For a single spherical lens, the Seidel wave aberrations, $\phi^{(4)}$, are given by:

$$\begin{aligned}\phi^{(4)}(r_0,\rho,\theta) = &-\frac{1}{4}B\rho^4 - \frac{1}{2}(2C\cos^2(\theta)+D)r_0^2\rho^2 \\ &+ Er_0^3\rho\cos(\theta) + Fr_0\rho^3\cos(\theta)\end{aligned} \tag{6.1}$$

where r_0 is the object (or beam) radius, ρ and θ are the radial and azimuthal coordinates at the exit pupil, and B, C, D, E, and F are the coefficients of spherical aberration, astigmatism, field curvature, distortion, and coma aberration respectively.

As an Airy beam can exist in a 2D space, spherical lenses are overly complicated for Airy beam generation and a cylindrical lens will suffice. For a cylindrical lens, equation (6.1) simplifies to:

$$\phi^{(4)}(u_0,u) = -\frac{1}{4}Bu^4 - \frac{1}{2}(2C+D)u_0^2u^2 + Eu_0^3u + Fu_0u^3 \tag{6.2}$$

where u_o is the object height (or beam width), and u is the transverse coordinate at the normal cylindrical axis of the lens.

From equation (6.2) is is clear that the coma term creates a purely cubic phase modulation to an incident light field. This is hard to isolate from the other aberrations when a single lens is used. However, this can be achieved by addition of a second cylindrical lens of opposite power in such a way as to minimise all but the coma term [197, 203]. A 1D cubic modulation (1+1D Airy beam) can be formed from the lens pair shown in Fig. 6.1(a). To create a 2D cubic modulation (2+1D Airy beam), two orthogonally oriented lens pairs can be used, as shown in Fig. 6.1(b). The amplitude of the cubic modulation can be tuned by changing the tilt angle of the first lens in each pair [197].

6.2.2 Integration of tilted lens into a compact light-sheet microscope

A compact LSM, based on the OpenSPIM design [196], was constructed as the base for the compact Airy LSM. This base system, referred to as the Type-3 system is shown in

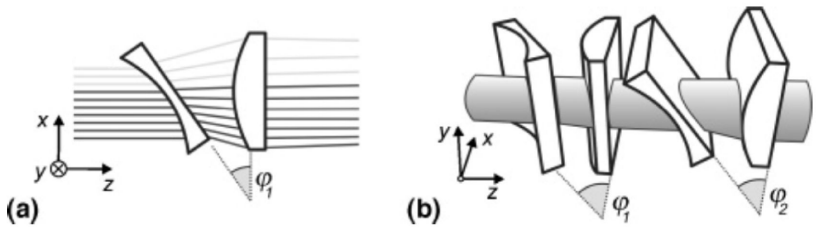

FIGURE 6.1: Generation of 1+1D and 2+1D Airy beams by cylindrical lens pairs. (a) A pair of lenses offset by an angle, ϕ_1, imparts a 1D cubic modulation on the beam along the $x-$axis. (b) A series of orthogonally positioned lens pairs offset by angles ϕ_1 and ϕ_2 respectively imparts a 2D cubic modulation along the $x-$ and $y-$axes of the beam. Figure used with permission from [197].

Fig. 6.2 and described below.

A laser (Laser Quantum, Finesse, 6W, 532nm) was coupled via a SM fibre into the microscope and collimated by lens L1. The beam width is controlled by an adjustable slit (AS; Thorlabs, VA100/M) which controls the effective NA of the light-sheet. A cylindrical lens (CL; Thorlabs, LJ1695RM-A) focuses the beam into a horizontal line on the mirror (M). A beam expansion telescope (L2,L3) then images this line onto the back aperture of the illumination objective (MO_1; Olympus, UMPLFLN 10x/0.3, water dipping) which creates a vertically oriented ($x-y$ plane) light-sheet in the specimen chamber (SC). Fluorescence is collected from the light-sheet plane by a second microscope objective (MO_2; Nikon CFI Apo 40x/0.80 DIC, w.d. = 3.5mm, water dipping) and $f = 200mm$ tube lens (TL) onto a camera (CCD; Basler, piA640-210gm). A laser line filter (Semrock, NF01-532-25) was used to reject scattered illumination from the image. The sample was suspended within the water filled sample chamber in an agarose gel extruded from a syringe tube and moved using a xyz linear stage (Newport, M-562-XYZ) with manual actuators for $x-$ and $y-$axes, and a motorised actuator for the $z-$axis to enable accurate volumetric acquisition.

To enable Airy light-sheet illumination with the Type-3 system, a cylindrical lens pair could be added between the adjustable slit and the existing cylindrical lens. This would increase the overall size of the microscope as some components would have to be moved back to accommodate the new optics.

To reduce the footprint of the compact Airy LSM, the roles of the second cylindrical lens in the lens pair, for minimisation of additional aberrations, and the existing

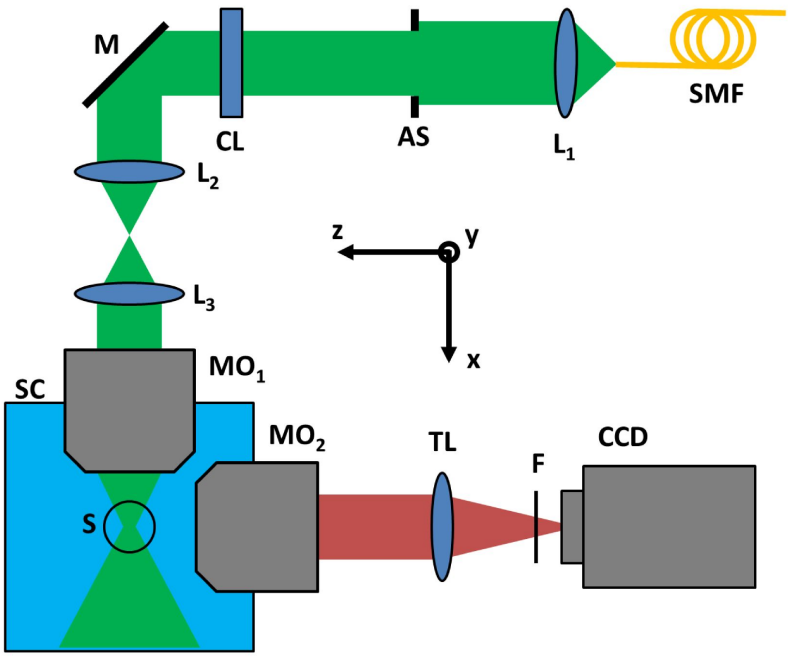

FIGURE 6.2: Schematic of the base system for the Type-3 light-sheet microscope. SMF: Single-mode fibre; Lx: (spherical) Lens;AS: Adjustable slit; CL: Cylindrical lens; M: Mirror; MOx: Microscope objective lens; TL: Tube lens; F: Filter; CCD: (EM)CCD camera; SC: Sample chamber; S: Sample.

cylindrical lens, for light-sheet formation, were combined and performed by a spherical lens. The initial phase profile containing the cubic modulation is still generated by a cylindrical lens that is tilted off-axis. This cylindrical-spherical lens pair design reduces the overall footprint of the device. The Type-3 system with Airy illumination capability is shown in Fig. 6.3

The only difference from the base system (Fig. 6.2) is the orientation of the cylindrical lens, which has been rotated by 90° in the transverse plane of the beam, and then tilted at an angle, θ, relative to the lateral plane to achieve a cubic phase modulation, and the addition of a spherical lens (L_4) immediately after the cylindrical lens which is used to minimise non-cubic aberrations and form a light-sheet with the correct orientation.

The entire optical system has a small footprint, the whole microscope fits within an volume of $35\text{cm} \times 35\text{cm} \times 10\text{cm}$. This is mainly limited by the bulky sample stage which is positioned to the left of the sample chamber as the system is shown in Fig. 6.3 and could be reduced by use of a smaller stage positioned in the space between

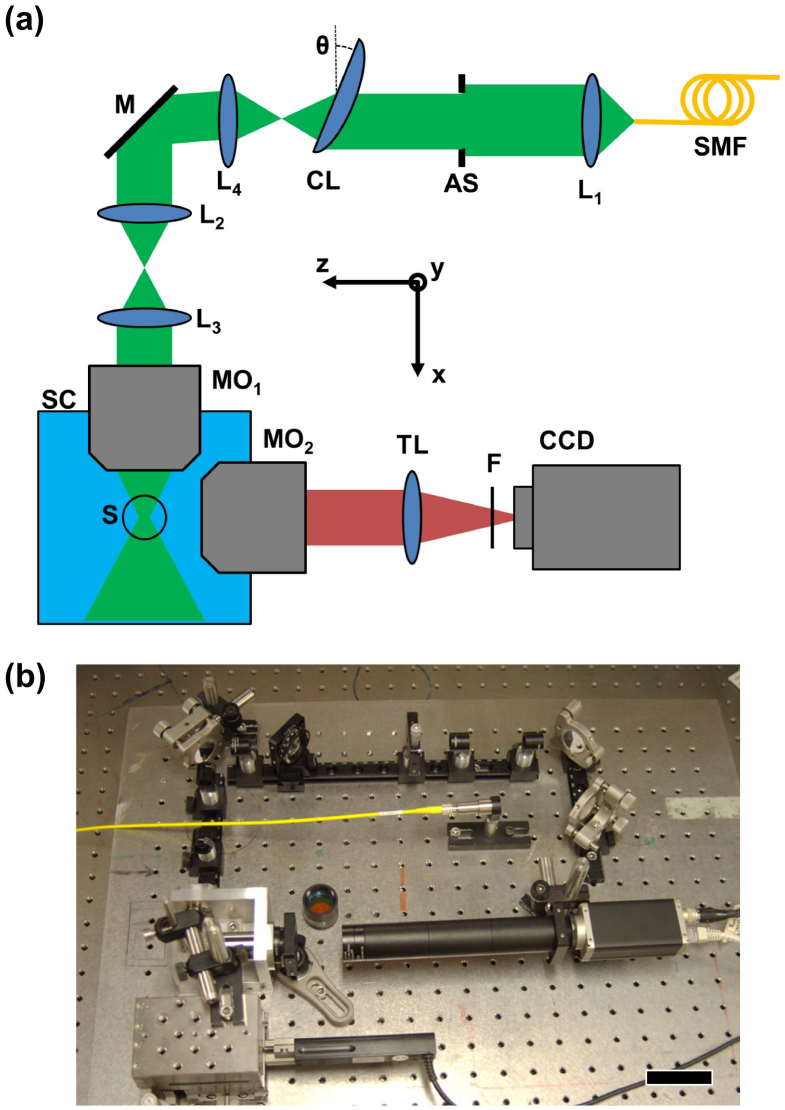

FIGURE 6.3: (a) Schematic of the Type-3 light-sheet microscope. The beam passes through one half of a cylindrical lens (CL) tilted at an angle, θ, to the optic axis. A spherical lens, L_4, is placed after CL to minimise beam aberrations and correctly orient the light-sheet. The sample stage (not shown) is positioned to the left of SC. SMF: Single-mode fibre; Lx: (spherical) Lens;AS: Adjustable slit; CL: (tilted) Cylindrical lens; M: Mirror; MOx: Microscope objective lens; TL: Tube lens; F: Filter; CCD: (EM)CCD camera; SC: Sample chamber; S: Sample. (b) Photograph of Type-3 light-sheet microscope. Scale bar in (b): approximately 5cm.

illumination and detection optics.

6.2.3 Simulation of aberrations from single tilted cylindrical lens

The expected phase modulation from tilting the cylindrical lens (Thorlabs, LJ1695RM-A) was determined from ray tracing simulations in Zemax using the model supplied for the lens. It is only necessary to simulate behaviour across the normal cylindrical axis of the lens. An array of 100 monochromatic rays was used for the simulation, uniformly spaced over a 5mm section of the lens, from the centre of the lens extending out towards the edge, as shown in Fig. 6.4(a). The simulation was performed for a number of commonly used fluorophore excitation wavelengths across the visible spectrum. The lateral shift (Fig. 6.4(b)) of the beam and back focal length (Fig. 6.4(c)) were determined from the convergence of rays. The optical path length of each ray was used to determine the wavefront aberrations at the focus. A cubic polynomial was fitted to the wavefront to determine the $\alpha-$value for Airy beam generation (Fig. 6.4(d)), and the residual aberrations quantify the magnitude of higher order aberrations (Fig. 6.4(e)) .

Figure 6.4 shows that the aberrations induced by tilting the angle of the lens are largely linear (lateral offset) and quadratic (defocus) phase polynomials. The resulting beam therefore needs refocused and laterally adjusted. This is achieved in the Type-3 system (Fig. 6.3) using lens, L_4, and mirror, M. The inter-lens spacing between CL and L_4 is set such that the beam is collimated onto mirror M and the angle of the mirror is adjusted to ensure the light-sheet remains co-aligned with the focal plane of the detection optics.

The cubic modulation (Fig. 6.4(d)) varies rapidly for $35° < \theta < 60°$, yielding $\alpha-$values from $4 - 15$ for $40° < \theta < 45°$ which are appropriate for high-resolution LSM (see Chapter 4.2). Over this angle range, the residual aberrations are minimal.

Additionally, the polynomial phase terms are remarkably wavelength independent, most importantly the lateral and focal shifts, which would mean no adjustment of the microscope would be required when switching between multiple illumination wavelengths. The $\alpha-$value exhibits the strongest wavelength dependence, this must be considered when performing deconvolution of data acquired with different illumination

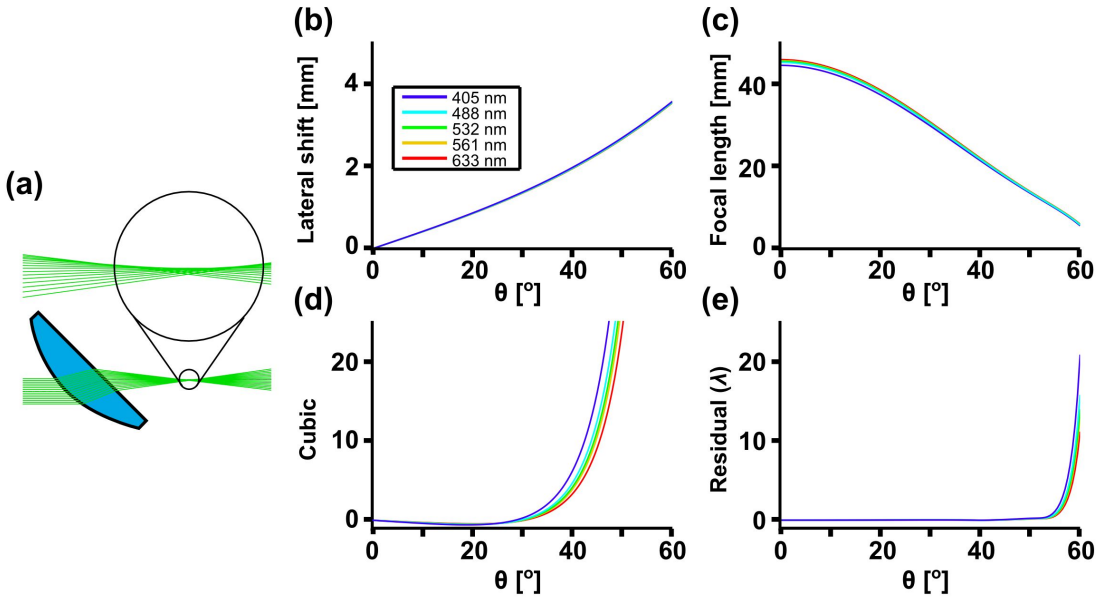

FIGURE 6.4: Wavefront analysis of beam through tilted cylindrical lens. Results of ray tracing simulation of monochromatic beam propagation through tilted cylindrical lens (a). (b) Linear wavefront aberration (beam tilt) against lens tilt angle, θ. (c) Quadratic wavefront aberration (defocus, focal shift) versus tilt angle. (d) Cubic wavefront aberration (coma, Airy) versus tilt angle. (e) Residual (quartic & quintic) wavefront aberration versus tilt angle. A number of common illumination wavelengths across the visible spectrum are simulated. Trace colours are matched to the wavelength. Figure adapted with permission from [201].

wavelengths, but again does not require physical recalibration of the microscope optics.

The cylindrical lens in the Type-3 system was set at $40°$, giving an expected cubic modulation of $\alpha = 4.13$ for $\lambda = 532$nm illumination.

6.2.4 Assessment of image quality

Before use, the system must be calibrated as the light-sheet profile is unknown. This was measured by placing a small mirror in the sample chamber oriented at $45°$ to both objective lenses which permitted imaging of the light-sheet profile. The mirror was scanned axially and the resulting light-sheet cross-sectional profile is shown in Fig. 6.5(a) and 6.5(b). This profile resembles an Airy beam but shows significant deviations, however, an exact Airy profile is not the requirement for high axial resolution. The recorded profile could, in principle, be used to construct the Wiener filter, $H_W(x, k_z)$, but if the recorded image extended beyond the range of the recorded light-sheet profile

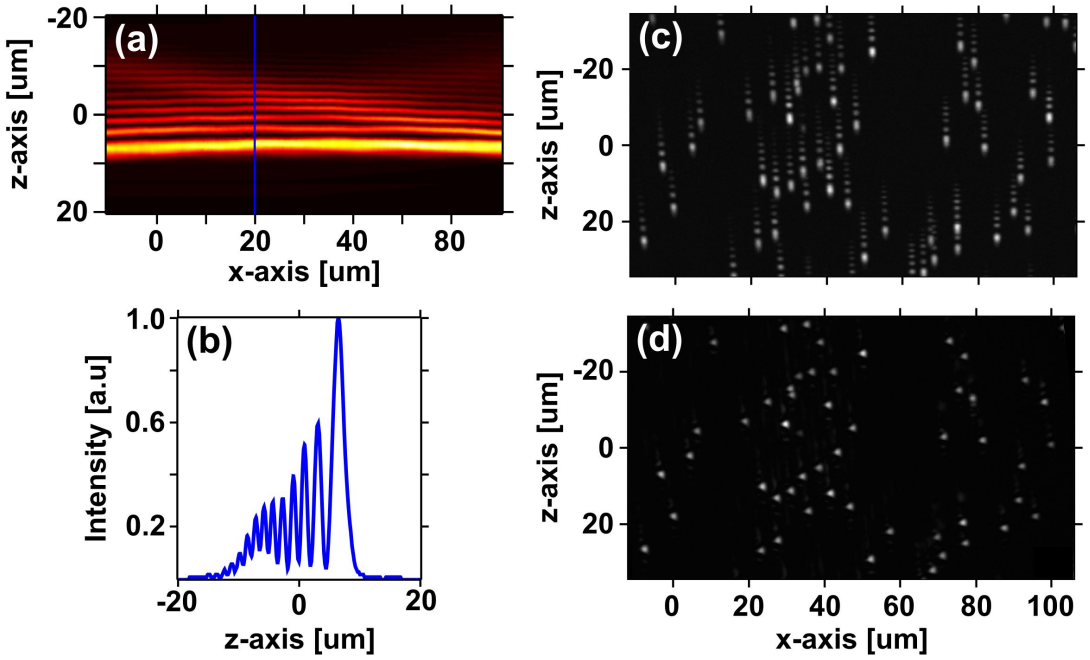

FIGURE 6.5: Imaging performance with the Type-3 Airy light-sheet microscope. (a) Experimentally measured Airy light-sheet cross-sectional ($x-z$) beam profile. (b) Axial profile of Airy light-sheet at $x = 20\,\mu m$ showing similarity with, and deviation from, an Airy profile. $x-z$ maximum intensity profiles of recorded (c) and deconvolved (d) volumes acquired using the light-sheet in (a). Figure adapted with permission from [201].

(along the $x-$axis), deconvolution would not be possible in those regions. As the mirror placement and orientation can have a significant positional error, the experimental light-sheet profile was used to fit a model for the pupil function. This allows calculation of the Wiener filter outwith the recorded region. The model for the pupil function included phase modulations up to fifth order and amplitude modulations up to third order to account for the phase distortions and non-uniform illumination given by:

$$\begin{aligned} P_{fit}(u) =& [A_0 + A_1 u + A_2 u^2 + A_3 u^3] \\ & \cdot \exp(2\pi i[\phi_3 u^3 + \phi_4 u^4 + \phi_5 u^5]) \end{aligned} \tag{6.3}$$

where u is the normalised pupil coordinate.

Linear and quadratic phase polynomials are not included in the model as these are adjusted with lens, L_4, and mirror, M. The coefficients determined for the model fitting the profile in Fig. 6.5 are listed in Table 6.1.

Coefficient	A_0	A_1	A_2	A_3	ϕ_3	ϕ_4	ϕ_5
Value	0.5	0.6	-0.5	0.4	7.8	1.65	2.9

TABLE 6.1: Parameters of fitted pupil function for Type-3 light-sheet microscope. Coefficients of $x^{th}-$order amplitude (A_x) and phase (ϕ_x) polynomials used in fitting the light-sheet profile for a tilted cylindrical lens.

Image quality was demonstrated by acquiring volumetric images of 600nm red fluorescent microspheres, embedded in 1% LMP agarose, and partially extruded from a syringe suspended in the water-immersed sample chamber. Volumetric scans were acquired with a $z-$plane spacing of 185nm. Figure 6.5(c) shows a $(x-z)$ maximum intensity projection of a recorded volume revealing an axial PSF similar to those observed in Chapter 4 for a pure Airy light-sheet. Slight geometric distortions are also observed and corrected for as previously described. Figure 6.5(d) shows the same projection after deconvolution. The axial resolution was measured to be approximately $1.9\,\mu\text{m}$ across the FOV. Direct comparison could not be made against a Gaussian light-sheet as this would require reconfiguration of the microscope. A Gaussian light-sheet with the same NA would produce a light-sheet of $1.4\,\mu\text{m}$ thickness but only over a FOV of approximately $20\,\mu\text{m}$.

Image performance in a thick specimen was demonstrated by imaging musculature in a zebrafish (*Danio rerio*) larva (see Appendix F.3 for sample preparation). Figure 6.6 shows selected regions of the image volume. Figures 6.6(a) and 6.6(b) show characteristic shadowing artefacts common to cylindrical lens LSM implementations. Figure 6.6(a) shows the variation in cross-sectional area of the individual muscle fibres. Figures 6.6(c) and 6.6(d) show disc-like structures (sarcomeres) within each fibre can be resolved. Part of the V-shaped intermuscular septa (diagonal line in Fig. 6.6(c) and 6.6(d)) is also visible in the images.

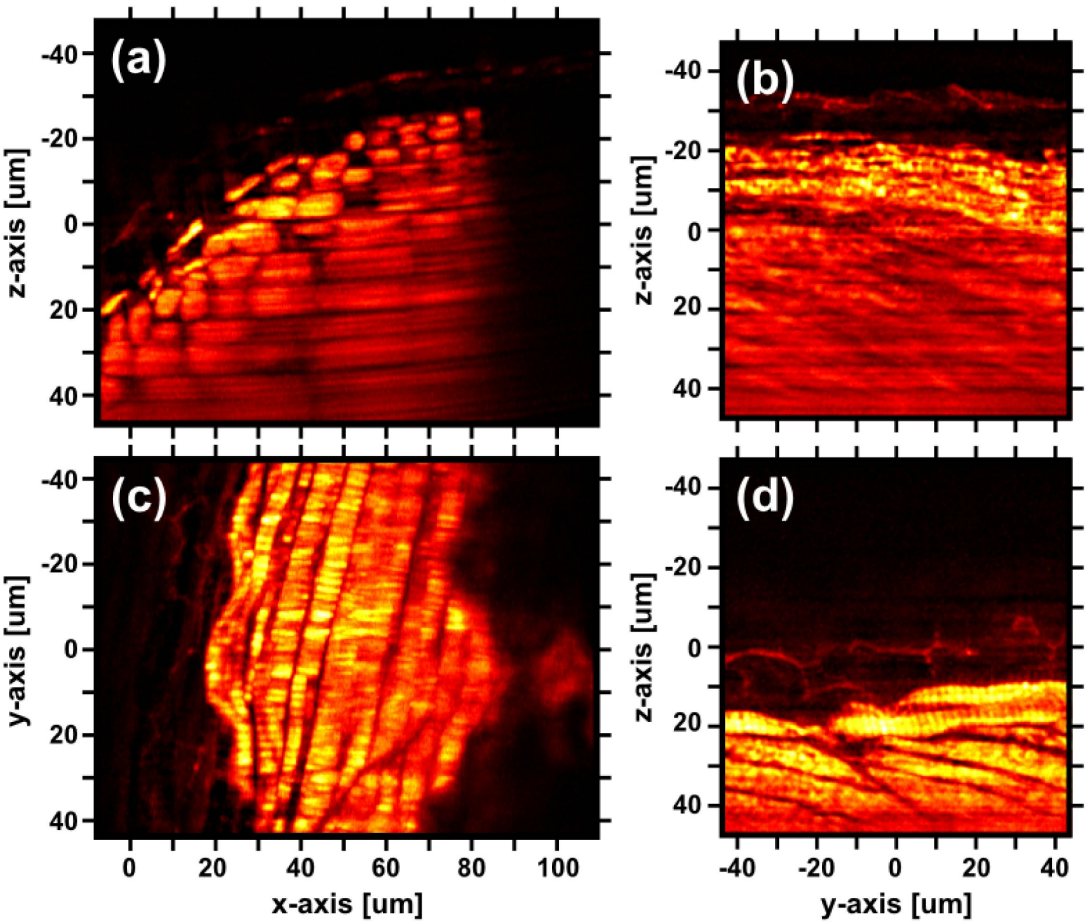

FIGURE 6.6: Airy light-sheet imaging of zebrafish musculature with the Type-3 system. Maximum intensity projections of selected regions from a volumetric scan showing f-actin in the musculature of a zebrafish larva. (a) $x-z$ projection centred at $y = -40\,\mu\text{m}$. (b) $x-y$ projection centred at $z = -10\,\mu\text{m}$. $y-z$ projections centred at $x = 10\,\mu\text{m}$ (c) and $x = 45\,\mu\text{m}$ (d). The thickness of each prjected section is $7.4\,\mu\text{m}$. Figure adapted with permission from [201].

6.3 Attenuation-compensated Airy light-sheets for improved illumination uniformity at depth with a single illumination lens

Attenuation of the light-sheet limits the imaging depth that can be achieved within thick samples and also reduces the uniformity of light-sheet illumination across the FOV. This issue has been overcome by the use of multi-view reconstruction techniques

as discussed in Chapter 2.3.5, but these techniques necessitate an additional illumination pathway entering the sample from the opposite side of the FOV which can limit sample choice. For example, a 2 objective LSM system could conceivably be used for *in vivo* imaging of an exposed mouse brain, however this would be impossible using a 3 objective (2 illumination pathways) setup. Other multi-view methods involve rotating the sample and acquiring images from different views, again there are scenarios where this becomes difficult or impossible. Multi-view techniques also have intrinsically lower temporal resolution and increased photodamage as multiple sample exposures are required per image. Multi-photon excitation LSM can penetrate deeper into tissue but greatly increases system cost and limits fluorophore choice. Samples may be optically cleared to decrease sample attenuation, as discussed in Chapter 5, but this precludes live imaging.

Ideally, an imaging method would work in the single-photon excitation regime, utilise only one illumination pathway, one sample exposure, and be compatible with living specimens.

Attenuation-compensation of Airy beams is a beam shaping technique which has been demonstrated to overcome beam attenuation in absorbing media [198]. The technique is investigated for use in LSM for increasing imaging depth and uniformity of illumination. Beam propagation simulations and analysis of the axial MTF are used to characterise the performance of attenuation-compensated Airy light-sheets.

6.3.1 Attenuation-compensated Airy beams

All beams experience an exponential decay of intensity upon propagation through an absorbing medium. The Airy beam may be modified to counteract this intensity decay over a finite range. The following section summarises the approach of Preciado, Dholakia, and Mazilu to create attenuation-compensated Airy beams [198].

The spatial Fourier spectrum of a 1+1D (infinite energy) Airy beam propagating through a linearly absorbing medium can be approximated as:

$$\tilde{E}(k_x, z) \approx \exp\left(\frac{ik_x^2 z}{2nk_0 - iC_{abs}} - ink_0 z - \frac{C_{abs} z}{2}\right) \exp\left(\frac{ix_0^3 k_x^3}{3}\right) \tag{6.4}$$

where k_x is the spatial frequency of the transverse coordinate, x, z is the longitudinal coordinate, $k_0 = 2\pi/\lambda$ is the vacuum wavevector, and n and C_{abs} are the refractive index and absorption coefficient or the absorbing medium respectively.

The Fourier transform of (6.4) yields the propagation of the Airy field in the absorbing medium:

$$E(x,z) = \mathrm{Ai}\left(\frac{x}{x_0} - \frac{z^2}{4z_0^2}\right)\exp\left(-\frac{C_{abs}z}{2}\right)\exp\left(i\left[\frac{z^3}{12z_0^3} - \frac{z_0 z}{x_0^2} - \frac{xz}{2x_0 z_0}\right]\right) \tag{6.5}$$

where $z_0 = nk_0x_0^2$.

The middle term, $\exp(-C_{abs}z/2)$, characterises the decay of the field upon propagation. As this stems from a real exponential term in the Fourier spectrum of the beam, it can be accounted for by introducing another exponential, $\exp(-b_0k_x)$ which results in the field equation:

$$\begin{aligned} E(x,z) = \mathrm{Ai}&\left(\frac{x}{x_0} - \frac{z^2}{4z_0^2} + \frac{ib_0}{x_0}\right)\exp\left(-\frac{C_{abs}z}{2} + \frac{zb_0}{2x_0z_0}\right) \\ &\exp\left(i\left[\frac{z^3}{12z_0^3} - \frac{z_0z}{x_0^2} - \frac{xz}{2x_0z_0}\right]\right) \end{aligned} \tag{6.6}$$

The total intensity loss due to absorption, C'_{abs}, is now given by:

$$C'_{abs} = C_{abs} - \frac{b_0}{x_0 z_0} \tag{6.7}$$

For $b_0 = x_0z_0C_{abs}$, the beam will completely counteract attenuation and the intensity of the main lobe will propagate without decay, as if in free-space. In free-space, $b_0 \neq 0$ will result in a beam where the intensity of the main lobe increases or decreases with propagation.

This treatment can be extended to 2+1D Airy beams, where the overall compensation is the sum of the compensation along each individual axis:

$$C'_{abs} = C_{abs} - \frac{b_{0x}}{x_0z_0} - \frac{b_{0y}}{y_0z_0} \tag{6.8}$$

Attenuation-compensation is essentially the application of an amplitude mask in the pupil plane which weights each spectral component based on the path length of

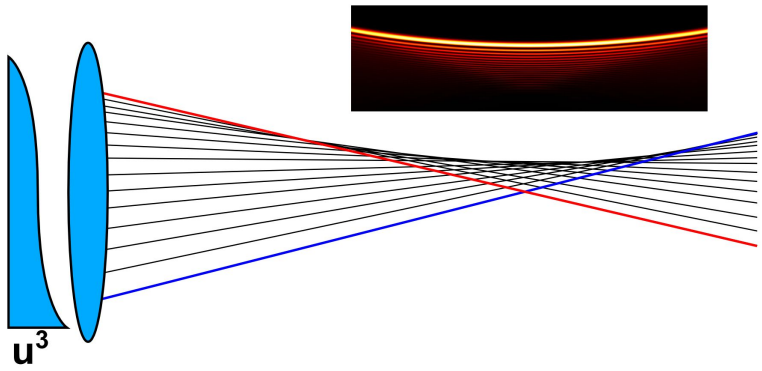

FIGURE 6.7: Ray optics representation of an Airy beam with a short-focussing (red) and long-focusing (blue) ray highlighted. The rays trace out a parabolic trajectory. Inset shows the corresponding Airy beam intensity profile.

that component before it contributes to the main lobe of the beam. This is illustrated in Fig. 6.7. This shows a ray optics representation of an Airy beam, the rays trace out the characteristic parabolic trajectory of the Airy beam. The red ray, from the top of the aperture, contributes to the Airy profile in the region nearest the lens, the blue ray, from the bottom of the aperture, contributes to the Airy profile furthest from the lens. Therefore attenuation-compensation is achieved by amplification of the rays, increasing exponentially from red to blue rays.

The compensating term, $\exp(-b_0 k_x)$, can easily be applied to the Fourier spectrum on the beam with a digital micromirror device (DMD), SLM or other beam shaping device. These devices cannot provide gain to the beam and therefore cannot alone compensate for absorption. Instead, these devices introduce loss in the spectral components which contribute to the main lobe at shorter propagation distances. This gives the appearance of a beam which does not decay but the overall power in the beam is reduced. The intensity of the beam at the end of the attenuation-compensated region is equal to the intensity of the same beam without compensation. Gain is provided by increasing the laser power of the beam incident on the beam shaping device.

Attenuation-compensation is not a technique specific to the Airy field and can, in principle, be applied to any other propagation-invariant beam type. Control of the axial propagation characteristics has been demonstrated for Bessel beams [204] and Airy-like, self-accelerating beams with a circular trajectory [202].

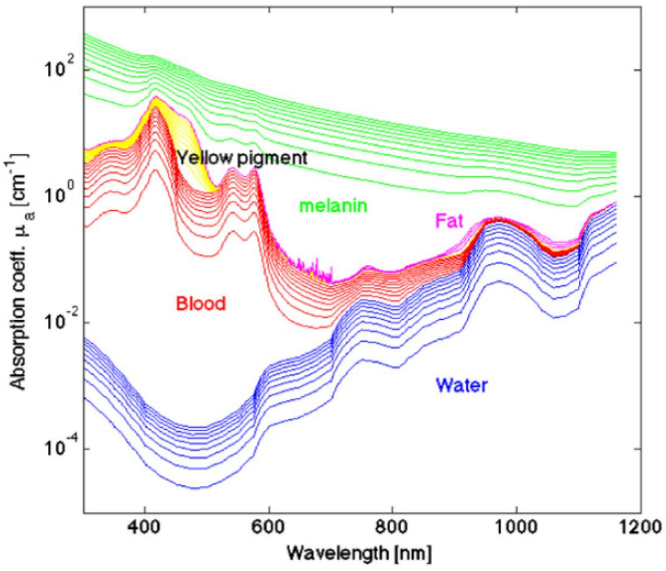

FIGURE 6.8: Absorption coefficients of biological tissue components. Water (blue), blood (red), fat (magenta), yellow pigment (yellow), and melanin (green), shown in a variety of biologically relevant concentrations. Figure used with permission from [205] ©Institute of Physics and Engineering in Medicine. Reproduced by permission of IOP Publishing. All rights reserved.

6.3.2 Generation of an attenuation-compensated Airy light-sheet

Attenuation-compensated Airy light-sheets were simulated in 2D as described in Chapter 4. Attenuation was introduced by multiplication of the free-space light-sheet profile by an exponential term, $\exp(-C_{abs}x)$. Figures 6.9(a) and 6.9(b) show the propagation of an Airy7 light-sheet in free space and in absorbing media ($C_{abs} = 100\text{cm}^{-1}$) respectively.

Absorption in biological tissue varies greatly depending on the type of tissue. Jacques gives a comprehensive review of scattering and absorption coefficients for biological tissues [205]. Figure6.8 shows absorption coefficients for the major tissue components which contribute to scattering. $C_{abs} = 100\text{cm}^{-1}$ was chosen as the absorption coefficient for this study as it represents the upper end of the range found in biological tissue.

As attenuation is effectively an exponential weighting of spatial frequencies, the pupil function no longer has an amplitude resembling a top-hat function, at one side of the aperture, the field amplitude will be low, at the other however, the amplitude

will be increasing sharply and then decay to zero rapidly due to the finite extend of the pupil, a so-called hard aperture. This sharp spike causes unwanted intensity modulations along the lobes of the light-sheet profile (see Fig. 6.9(e)). This issue was overcome by implementing a soft-aperture with an 8-th order super-Gaussian apodization [198].

The pupil must now extend beyond $\mathrm{NA} = 0.42$ (as was previously used in LSM simulations) to accommodate the soft-aperture. The hard-aperture was therefore increased to $\mathrm{NA} = 0.6$ which is still within the maximum NA offered by the objectives in the Type-2 system and compatible with future experimentation. The normalisation of the pupil plane sets $|u| = 1$ to correspond to the maximum NA, this necessitated an increase in $\alpha-$value such that the strength of the cubic modulation was consistent with that of an Airy7 beam with $\mathrm{NA} = 0.42$. The resulting pupil function is described by:

$$P(u) = A \exp[2\pi i \alpha u^3] \exp[-(1.3\sqrt{2}u)^8] \exp[\sigma(u-1)] \tag{6.9}$$

where u is normalised such that $|u| = 1$ corresponds to $\mathrm{NA} = 0.6$. the first exponential term describes the cubic modulation for Airy beam generation, the second term is the super-Gaussian apodization function, and the third term is the attenuation compensating term with compensation parameter, σ, which is b_0 expressed in normalised pupil coordinates. An additional scaling factor, A, is used to keep the amplitude of the pupil function between 0 and 1.

Figures 6.9(b), 6.9(d), and 6.9(f) show a soft-apertured Airy light-sheet ($\alpha = 21$) equivalent to the hard-apertured Airy7 light-sheet. Figure 6.9(f) shows that there are fewer distorting ripples in the light-sheet profile than with a hard aperture. However, the intensity of the main lobe in Fig. 6.9(b) indicates that the FOV of the soft-apertured beam is slightly shorter than with a hard aperture. This is expected as the spatial frequencies corresponding to the extremes of the FOV have been attenuated by the super-Gaussian apodization and is also expected to lower the attainable axial resolution.

The scaling factor, A, was determined such that the maximum pupil magnitude for any light-sheet was 1, and that all light-sheets have a comparable intensity at the start of the propagation-invariant region. Figure 6.10 shows normalised pupil functions for selected compensation factors. Their normalisation factors and relative total powers

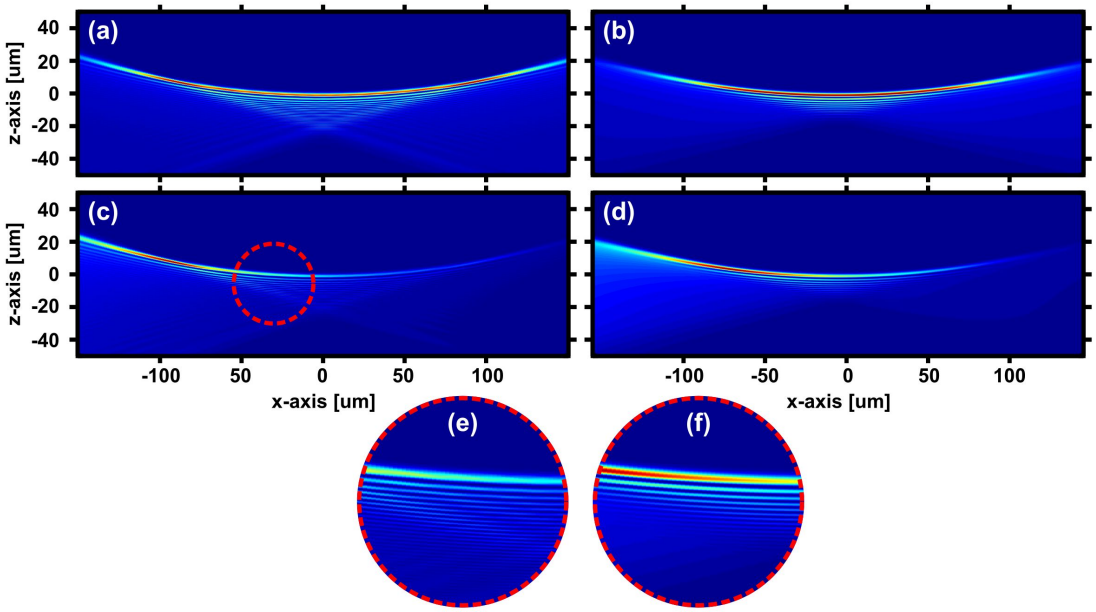

FIGURE 6.9: Simulations showing the effect of hard and soft apertures on attenuated Airy light-sheet. Propagation of hard-apertured (a,c) and soft-apertured (b,d) Airy light-sheets in free-space (a,b) and in an absorbing medium (c,d). (e,f) Zoomed-in view of the circled area in (c) and corresponding area in (d) respectively.

$\boldsymbol{\sigma}$	0	0.25	0.5	1	2
$\boldsymbol{A}$	0.19	0.28	0.40	0.81	3.61
$\frac{\int\lvert\boldsymbol{P(u;\sigma)}\rvert\boldsymbol{du}}{\int\lvert\boldsymbol{P(u;0)}\rvert\boldsymbol{du}}$	1	1.09	1.23	1.59	3.02

TABLE 6.2: Parameters of normalised pupil functions for attenuation-compensated light-sheets shown in Fig. 6.10. σ: Compensation parameter; A normalisation factor; $\int|P(u;\sigma)|du/\int|P(u;0)|du$: Normalised power in light-sheet relative to $\sigma = 0$.

are given in Table 6.2.

Table 6.2 shows that by using attenuation-compensation, more power, and therefore intensity, can be targeted to greater depth within a sample. For $\sigma = 1$, 59% more power is delivered by the light-sheet than when no compensation is used.

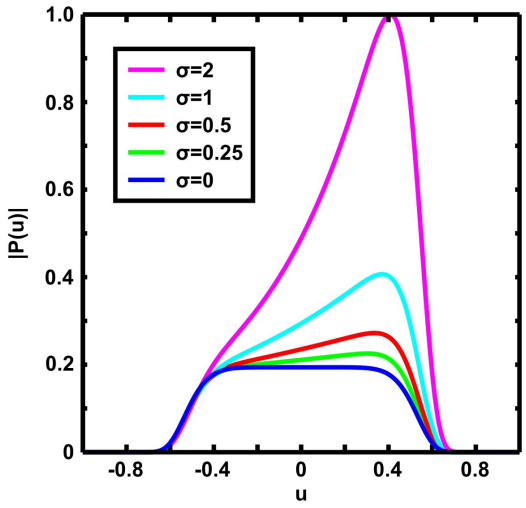

FIGURE 6.10: Normalised pupil functions for attenuation-compensated light-sheets. Magnitude, $|P(u)|$, of pupil functions for Airy light-sheets with compensation factors, $\sigma = 0.25, 0.5, 1,$ and 2.

6.3.3 Theoretical imaging performance of an attenuation compensated Airy light-sheet

The expected imaging performance of attenuation-compensated Airy light-sheets in absorbing media was assessed through analysis of the axial MTF. $x-z$ light-sheet profiles were simulated as described in Chapter 6.3.2 with $\alpha = 21$ and $C_{abs} = 100\text{cm}^{-1}$. Figure 6.11 shows the light-sheet profile, peak transverse intensity, and 5% thresholded MTF for selected compensation coefficients. The spatial frequency, k_z is normalised to $2\,\text{NA}\,/\lambda$, where $\text{NA} = 0.42$ is used for comparison with the results of Chapter 4 and to be consistent with the soft aperture pupil function. The MTF was normalised such that its peak magnitude was unity, the additional power delivered by the compensated light-sheet was accounted for by additionally scaling the MTF by $A(\sigma)/A(0)$, the ratio of the pupil normalisation factors for the compensated and non-compensated light-sheets.

The light-sheet profile with no compensation, propagating in free space is shown in Fig. 6.11(a) and is used as a baseline for comparison. The 5% MTF threshold is similar to that shown for the Airy10 ($\text{NA} = 0.42$) light-sheet shown in Fig. 4.5 and peaks at $k_z = 0.66$, corresponding to an axial resolution of approximately $1\,\mu\text{m}$, the same as achieved experimentally in Chapter 4. The light-sheet maintains a peak intensity

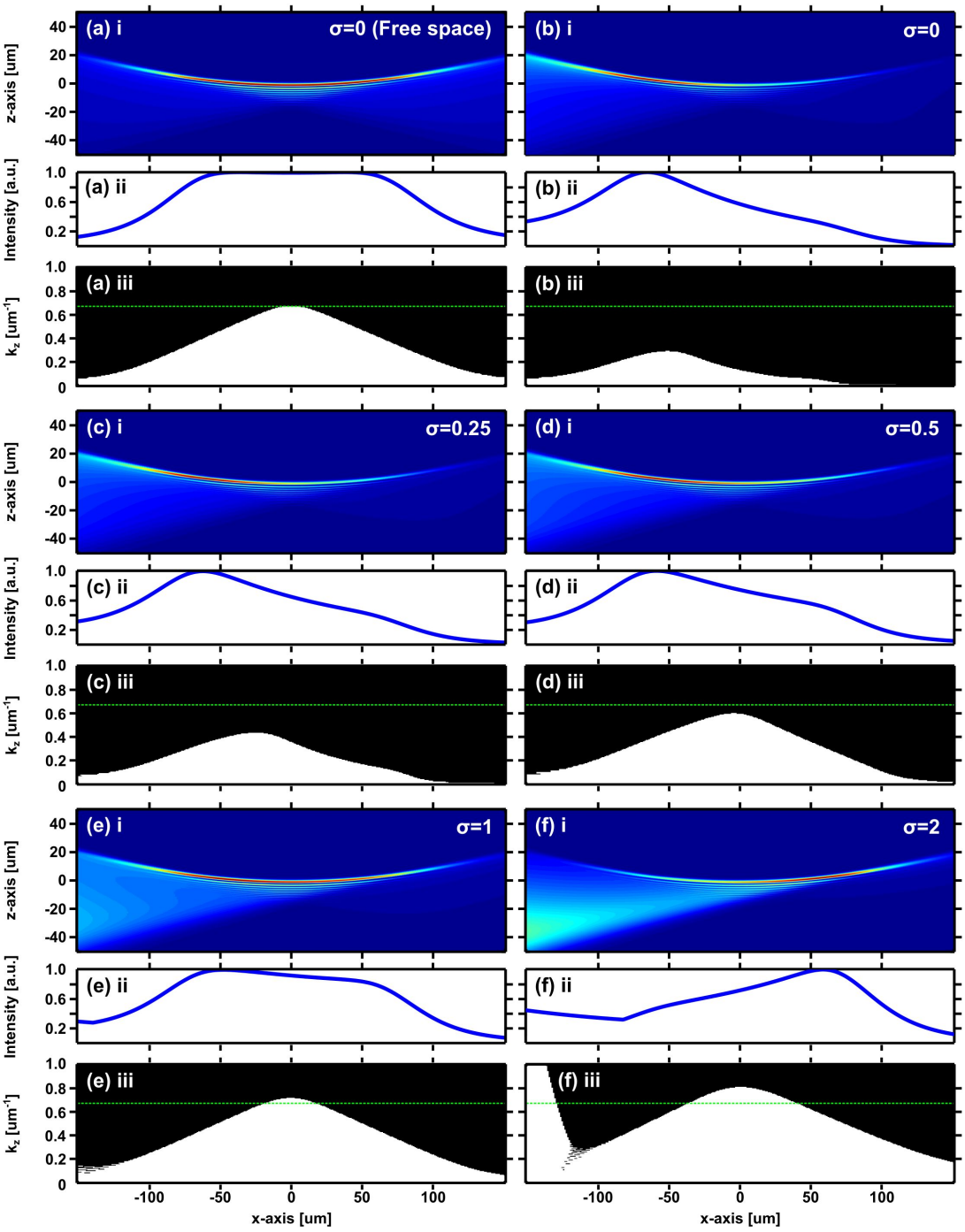

FIGURE 6.11: Simulated profiles and modulation transfer functions of attenuation-compensated Airy light-sheets. Light-sheet $x - z$ cross-sectional profiles (i), peak transverse intensity (ii), and intensity normalised MTFs thresholded at 5% for attenuation compensated Airy light-sheets in an absorbing medium with absorption coefficient, $C_{abs} = 100\text{cm}^{-1}$. (a) $\sigma = 0$ (no compensation) in free-space, (b) $\sigma = 0$, (c) $\sigma = 0.25$, (d) $\sigma = 0.5$, (e) $\sigma = 1$, and (f) $\sigma = 2$. (b-e) show under-compensation, whereas (f) shows an over-compensated case. Green dashed lines indicate the axial resolution achieved in free space with no compensation.

(intensity of the main lobe) that is constant over approximately $100\,\mu\mathrm{m}$, after which it begins to decay. Attenuation of this light sheet (Fig. 6.11(b)) causes a shift of the MTF 5% threshold to lower spatial frequencies and peaks at lower x. The longitudinal peak intensity profile decays as expected, giving non-uniform illumination.

Including a compensation factor reverses this trend. Figures 6.11(c) and 6.11(d) show under-compensated cases, but the longitudinal peak intensity profile becomes more homogeneous with increasing σ and the MTF trends back towards the free space scenario, increasing the spatial frequency of the 5% threshold and shifting the peak back to $x = 0$.

Figure 6.11(e) shows an under-compensated case which is close to completely nullifying the attenuation of the medium. The longitudinal peak intensity profile is almost flat within the central region and the thresholded MTF very closely resembles the case shown in Fig. 6.11(a). Interestingly, the peak spatial frequency exceeds that of the free-space case. This may be due to high amplification of the high spatial frequencies at one side of the pupil or may be an artefact of the analysis. Additionally, another deviation is observed for low x, showing a slight rise in the MTF threshold.

Figure 6.11(f) shows the case of over-compensation. The longitudinal peak intensity profile is inhomogeneous but increases on propagation instead of decreasing. There is a kink in the peak intensity profile at approximately $x = -80\,\mu\mathrm{m}$ which is attributed to the intensity of the intensity of the side-lobe section of the light-sheet exceeding the intensity of the main lobe. The thresholded MTF peaks in the centre as expected and peaks at an even higher spatial frequency than in Fig. Figure 6.11(e). The low x artefact is also greatly increased, suggesting a link between this and the peak intensity kink.

6.4 Discussion and conclusions

This Chapter has explored the use of advanced beam shaping concepts in Airy LSM. Tilted cylindrical lenses have been investigated as ultra low-cost elements for Airy light-sheet generation. Simulations have shown that a rather high quality Airy light-sheet can be generated by controlled tilting of a cylindrical lens. The other distortions

to the light-sheet are $1^{st}-$ and $2^{nd}-$order phase polynomials (tilt and defocus respectively) which can be adjusted for through careful microscope design (Type-3 LSM system). Ray tracing simulations also show that even a simple singlet lens has a behaviour that is remarkably wavelength independent. Experimental validation reveals that the aberrations are more complex than indicated by ray tracing simulations but are still suitable for high axial resolution imaging over an extended FOV and result in a PSF that resembles the characteristic PSF on an Airy light-sheet. Images of resolution probes indicate an axial resolution of $1.9\,\mu\mathrm{m}$ is achieved over a FOV of approximately $120\,\mu\mathrm{m}$. Direct experimental comparison between beam types is not possible with the Type-3 system but the FOV is estimated to be at least 6 times larger than the equivalent Gaussian light-sheet. This is lower than the improvement over a Gaussian light-sheet that is achieved with the SLM based Type-1 and Type-2 systems but is limited by the FOV of the camera sensor, the resolution of the Airy light-sheet beyond the camera sensor is unknown.

Ray tracing simulations indicate that aberrations are limited to $1^{st}-$, $2^{nd}-$, and $3^{rd}-$order polynomials for a wide range of tilt angles. The typical $\alpha-$values for Airy light-sheet imaging can be achieved within this tilt range. $1^{st}-$ and $2^{nd}-$order polynomials can be adjusted for in a calibration phase prior to imaging and are remarkably independent of wavelength, making the technique suitable for multi-colour acquisition.

The compact and low-cost Type-3 Airy LSM presented here is rather robust in construction as it based on the popular OpenSPIM design [196]. The microscope is portable, occupying a $35\mathrm{cm} \times 35\mathrm{cm} \times 10\mathrm{cm}$ volume, and could be easily transported for increased accessibility to end users. A more sensitive camera would be preferable to improve the quality of image and allow imaging of weakly fluorescent samples. The system presented utilised a fibre coupled laser source which is large with respect to the microscope but this could be replaced with a small laser source on the optical breadboard of the microscope as in [196]. Further additional equipment is minimal as all hardware can be controlled via a PC through μManager [206, 207]. The Wiener deconvolution algorithm used with this system is relatively simple and does not require sophisticated computer hardware to function. The algorithm has been implemented on a

domestic laptop with 8 Gigabytes (GB) and can process 4GB datasets in approximately 5 minutes. This keeps the overall footprint low as no large equipment is required to accompany the microscope.

Experimental results do not agree perfectly with simulations as the experimental light-sheet profile has significant deviations from a true Airy light-sheet. This can be modelled and an accurate light-sheet profile was determined and allowed accurate Wiener deconvolution. A more Airy-like light-sheet profile may be generated through additional spatial filtering of the laser beam incident on the titled cylindrical lens, or by use of additional elements to minimise non-cubic phaser aberrations from the tilted lens. This approach would increase the cost and complexity of the microscope and is not necessary. A strict Airy profile is not a requirement for high axial resolution over a large FOV in LSM. Image quality may also be aided by a more accurate model of the light-sheet profile or by an iterative deconvolution algorithm that does not require precise knowledge of the light-sheet profile. Both these approaches retain optical simplicity but increase the computational workload.

Attenuation-compensation techniques have recently been demonstrated for several families of self-accelerating beam [202], including the Airy beam [198], and could be complimentary for LSM with an Airy beam. The second part of this Chapter has used simulations to investigate the use of attenuation-compensated light-sheets to improve the uniformity of illumination in a single-illumination approach, not requiring multiple illumining light-sheets or multiple sample exposures as commonly used [41, 45, 62, 64]. A soft-aperture is used for apodization in the pupil plane to remove beam artefacts stemming from sharp discontinuities in the pupil and absorption of the light-sheet. Consideration is given to the normalisation of the light-sheet pupils with varying degrees of attenuation-compensation to allow direct comparison between light-sheets, this analysis also quantifies the additional power that may be delivered into the sample by a compensated light-sheet without increasing the peak intensity. Finally, image performance is characterised by analysis of simulated MTFs with varying degrees of attenuation-compensation. This revealed that an Airy light-sheet with compensation factor matched to the sample absorption coefficient could potentially yield illumination

which is homogeneous and uniform throughout the FOV and give the same axial resolution as the equivalent non-compensated Airy light-sheet propagating in free space.

The thresholded MTF plots shown in Fig. 6.11 raise questions regarding the normalisation of the MTF as it would appear that attenuation-compensated beams in absorbing media can potentially yield resolution in excess of their non-compensated counterparts in free-space. This may well be the case as the pupil functions (Fig. 6.10 of compensated light-sheets do extend to marginally higher u than those of a non-compensated light-sheet. As observed in the case of slight under-compensation of the absorption (Fig. 6.11(e)), the increase in axial resolution is minimal. This effect may be linked to the high-frequency artefact in the MTF for low x, which is believed to stem from the high intensity of the side-lobe region of the Airy light-sheet relative to its main lobe. This suggests there will be a maximum compensation factor, and therefore maximum attenuation which may be overcome by this technique. Further investigation into these aspects is required.

An alternative approach to the image quality obtained by attenuation-compensated light-sheets might be to leave the MTF normalised as standard, and instead introduce a spatially variant SNR into the Wiener filter. This may mitigate the effect of the high frequency artefact observed in the MTF for low x, which may be caused by the amplification of MTF by the pupil normalisation factors. In this case, equation (4.12) would become:

$$SNR(x, k_z) = AA_I(x)\frac{2\,\mathrm{NA}}{\lambda}\frac{1}{k_z} \tag{6.10}$$

where $A_I(x)$ is an additional, spatially variant scaling factor, dependent on the transverse light-sheet intensity.

Experimental validation is the next step for this project. The exponential amplitude modulation can be easily implemented using the SLM in the Type-2 system and the deconvolution algorithm requires only small changes to implement scaling of the OTF. A challenge for experimental validation may be finding suitable samples in which to test the technique. An initial test should focus on ideal samples with minimal scattering and quantified absorption, dyes with strong absorption at the laser wavelength

will generally exhibit some level of fluorescence which may result in a spatially variant background in the image. Care should be taken to spectrally separate this from the desired signal from resolution probes and careful selection of filters. In biological samples, strong absorption is rarely observed in isolation and scattering will also affect the imaging process. Experimentation will also be required to investigate the effect of scattering on attenuation-compensated light-sheet imaging.

LSM with multi-photon excitation is much less affected by scattering than single-photon excitation LSM due to the longer wavelength of the illumination [205]. However, the absorption coefficient of water increases at longer wavelengths [208] and, as the 2PE signal scales with the square of the intensity, absorption of the illuminating light-sheet may be even more detrimental in the multi-photon regime than for single-photon excitation. Use of attenuation-compensation of in 2PE-LSM can counteract this, provided enough power can be delivered in the compensated light-sheet to achieve sufficient 2PE fluorescence signal.

Although attenuation-compensation has been investigated to overcome the effects of absorption, leading to an exponential compensating term, other shapes of compensating filter may have uses in LSM. The compensation filter may allow isolated imaging of a small region over a limited $x-$axis range by using a filter that peaks at a certain position in the pupil plane. This would be particularly useful for long term imaging of photosensitive samples. An initial large volume scan could be performed and from this, a region of interest (ROI) could be selected. The compensation filter could then be used to minimise the light-sheet intensity outside this ROI, reducing the photodamage to the specimen. This would require no mechanical adjustment of the microscope. Investigation of the limits of this filtering method, such as how narrow can the ROI be made, and what impact does this have on the axial resolution, would be required.

Just as low cost elements have been used for generation of Airy light-sheets by manipulation of phase, low cost and compact implementations of attenuation-compensation may be possible with readily available optics, albeit with a more limited choice of amplitude functions. For example, the pupil function of an Airy light-sheet

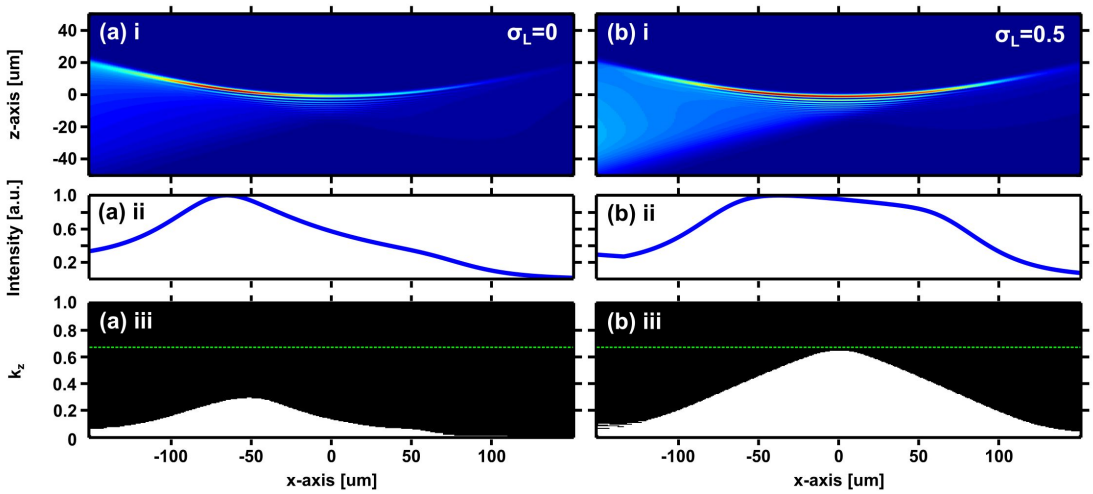

FIGURE 6.12: Simulated profiles and modulation transfer functions of Airy light-sheets with linear attenuation-compensation. Light-sheet $x-z$ cross-sectional profiles (i), peak transverse intensity (ii), and intensity normalised MTFs thresholded at 5% for attenuation compensated Airy light-sheets in an absorbing medium with absorption coefficient, $C_{abs} = 100\text{cm}^{-1}$. (a) $\sigma_L = 0$ (no compensation), (b) $\sigma_L = 0.5$. Green dashed lines indicate the axial resolution achieved in free space with no compensation.

after passing through a linear neutral density (ND) filter is given by:

$$P(u) = A\exp[2\pi i\alpha u^3]\exp[-(1.3\sqrt{2}u)^8]\sigma_L(u+1) \tag{6.11}$$

where σ_L is the linear compensation factor.

This pupil function yields a light-sheet in an absorbing medium ($C_{abs} = 100\text{cm}^{-1}$) as shown in Fig. 6.12 for $\sigma_L = 0.5$.

Figure 6.12 shows that even a linear compensating term could potentially be used to effectively counteract attenuation of the light-sheet.

This study has only investigated the use of attenuation-compensation for light-sheets formed by cylindrical focusing. In a DSLM the scanned light-sheet is formed from 1D scanning of a beam formed by a 2D pupil function, $P(u,v)$. As the light sheet is integrated along the $y-$axis in the sample, essentially any pupil function along v can be used without affecting the integrated light-sheet profile. If a 2D Airy beam is used, attenuation-compensation may also be applied along the $v-$axis. This does not

alter the light-sheet profile as the intensity is integrated. However, this does potentially allow new schemes to reduce the instantaneous peak intensity at any given point in the sample. For low x, the light-sheet profile in an attenuating medium reaches its maximum value, for large x, the peak intensity is low, the instantaneous peak intensity of the scanned beam matches this trend. If compensation is applied along v the total intensity in a transverse plane at low x will have increased, increasing the overall intensity of the light-sheet profile but without increasing the instantaneous peak intensity of the scanned beam, potentially allowing an increased SNR without increasing photodamage.

Chapter summary

- Advanced beam shaping strategies can be used to compliment the Airy LSM technique.
- A compact, low cost, and portable Airy LSM can be constructed by adding a tilted cylindrical lens to an existing LSM system.
- Such a tilted lens based LSM was demonstrated, giving axial resolution of approximately $1.9\,\mu\mathrm{m}$ over a FOV of $120\,\mu\mathrm{m}$, over 6 times greater than the equivalent Gaussian light-sheet.
- Attenuation-compensated Airy beams have been shown, in simulations, to enable light-sheet imaging at greater depths (approximately $100\,\mu\mathrm{m}$ deeper in x) into absorbing tissue, recovering the performance of the equivalent non-compensated Airy light-sheet in free-space.
- Future investigations will experimentally investigate the use of attenuation-compensated Airy light-sheets and there are many directions, such as ROI targeted imaging, multi-photon excitation LSM, investigation into other forms of compensating pupil functions, and reduced photodamage DSLM implementations, that this work may take.

6.5 Chapter acknowledgements

Simulations of the imparted phase profile when tilting a cylindrical lens were performed by Zhengyi Yang and Tom Vettenburg. The compact LSM was designed and constructed by Martynas Prokopas and modified for Airy illumination by Zhengyi Yang, the author, and Tom Vettenburg. Zhengyi Yang, Tom Vettenburg, and the author performed all experiments and data analysis. Clara Coll-Lladó and David E. K. Ferrier provided and prepared zebrafish larvae and assisted with interpretation of the images.

Simulations and theory for the attenuation-compensated Airy light-sheet were developed by the author with assistance from Miguel A. Preciado. Analysis of results was performed by the author.

Chapter 7

Structured illumination microscopy for diagnosis of nephrotic disease

Parts of this chapter are adapted from the article "Visualization of podocyte substructure with structured illumination microscopy (SIM): a new approach to nephrotic disease" [209] published in Biomedical Optics Express.

7.1 Introduction

Nephrotic syndrome is a catch-all term for a group of debilitating and sometimes lethal diseases in which normal kidney function is disrupted and its ability to retain proteins in the blood while filtering smaller molecules into the urine is lost. Within the kidney, the ultrastructure of the glomerulus (described in detail by Mundel and Reiser [210] and summarised below) is of key diagnostic importance. The ultrastructural features of interest are at or below the diffraction limit for light microscopy; foot processes have a diameter of between $250 - 700$nm [211] and filtration slit diaphragms between them have a width of approximately 40nm [212]. As such, visualisation of these structures and diagnosis of nephrotic disease relies on electron microscopy (EM).

Diagnosis by transmission electron microscopy (TEM) suffers from a limited FOV ($<$10 x 10 μm^2) of very thin sections of tissue (approximately $100m$m), requires costly equipment and specially trained technicians to prepare samples, and is time consuming; routinely taking up to a week for the preparation, imaging, and analysis of a sample. With the recent advent of SR optical microscopy visualisation of these structures by optical microscopy may be feasible. An optical technique could make use of much

more accessible immunofluorescent staining protocols for sample preparation, and enable visualisation of larger and thicker tissue sections.

Confocal microscopy has been used to visualise the glomerular ultrastructure in transgenically fluorescent mouse models where a small subset of glomerular cells exhibit fluorescence [213, 214] but cannot sufficiently resolve individual ultrastructural features when globally stained with exogenous dyes [214]. STORM has been applied to related structures within the glomerulus [215]. This promising study, which correlates the structures observed by STORM and TEM, is not directly applicable to routine diagnosis as STORM requires additional sample preparations for modulation of fluorophores, limits fluorophore choice, and cannot capture the full 3D nature of the ultrastucture over a sufficient volume of tissue. Recently, STED microscopy has also been used to image an optically cleared glomerulus [216], yielding approximately 50nm isotropic resolution throughout. This technique is also not directly applicable for diagnosis due to the extended (> 20 days) optical clearing procedure used [216].

SIM gives only a modest improvement of resolution, breaking the diffraction limit by a factor 2, but this may be sufficient to resolve the necessary ultrastuctural details with standard immunofluorescence preparations and could enable 3D views of thick tissue sections by its optical sectioning ability. This chapter describes the proof of concept experiment exploring the use of 3D-SIM for the visualisation of nephrotic disease.

7.2 Nephrotic disease

The primary symptom of nephrotic disease is elevated protein content in urine caused by disruption to normal kidney function and failure to retain these proteins in the blood. Normally, protein loss through urine (proteinuria) for a healthy person does not exceed 150mg/day [210], and anything above this is considered indicative of kidney disease. Interestingly, after exercise, proteinuria can increase transiently for $24-48$ hours with rates up to 10g/day observed for particularly high-intensity exercise, such as a marathon [210, 217]. This transient, and perfectly healthy, renal response indicates that proteinuria, while heavily correlated with nephrotic disease, is not in itself causative of kidney failure [210].

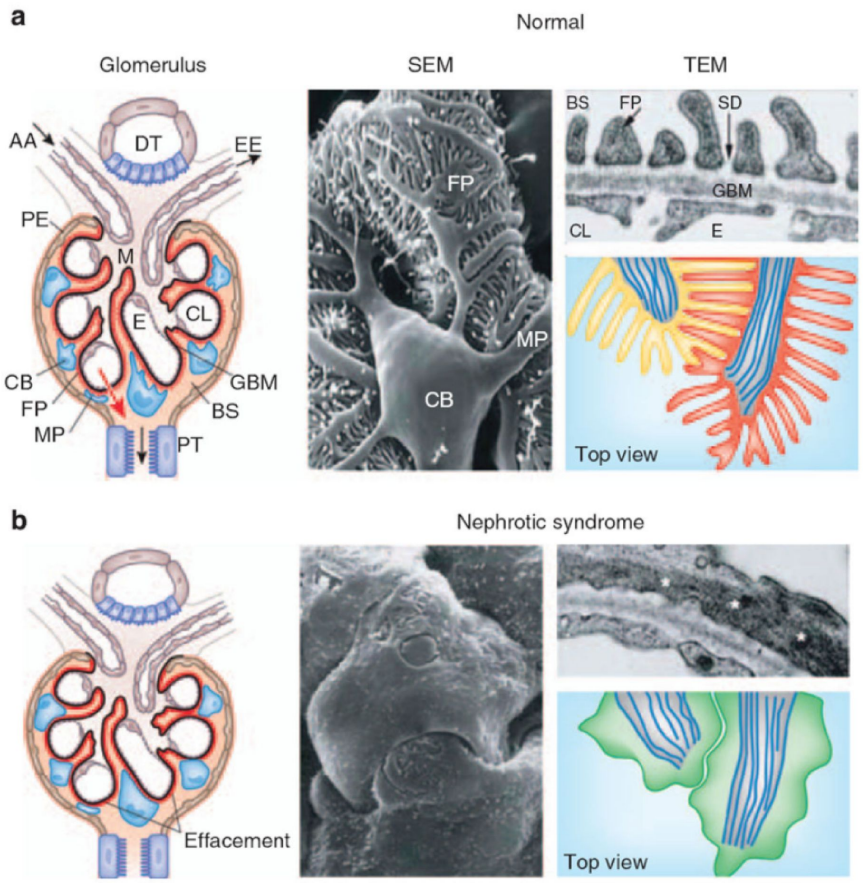

FIGURE 7.1: Normal and diseased podocyte structure. (a) Normal podocyte structure. Left: schematic representation of the glomerulus. Podocytes (blue) cover the outer surface of the GBM (black) and connect to it at multiple locations (FPs; red). Middle: Scanning electron microscopy (SEM) image of a podocyte on the GMB showing the dense and complex podocyte morphology. Right: TEM image of glomerular filtration barrier cross section (top) and tangential schematic (bottom). (b) Podocyte structure in nephrotic disease. Left: Podocytes (blue) no longer connect to the GMB at multiple discrete points as effacement of foot processes occurs. Middle: SEM image showing loss of the tight interdigitating podocyte substructue. Right: Cross sectional TEM image (top) and tangential schematic (bottom) of the glomerular filtration barrier with nephrotic disease. AA: afferent arteriole, BS: Bowman's space, CB: cell body (podocyte), CL: capilary lumen, DT: distal tubule, E: glomerular endothelial cell, EE: efferent arteriole, FP: foot process, GBM: glomerular basement membrane, M: mesangial cell, MP: major process (pedicel), PT: proximal tubule, SD: slit diaphragm. Figure used with permission from [210].

Within the kidney, one subsystem is of particular interest in relation to nephrotic disease, the glomerulus (Fig. 7.1). Each kidney contains approximately $1 - 1.2$ million glomeruli, which are multicellular filtration apparatus. Derived from the latin, *glomus* meaning "ball of yarn", the glomerulus is a tightly coiled ball of interconnected capillaries. The podocyte, one of three cell types constituting the glomerulus, covers the surface of glomeruluar capillaries (Fig. 7.1(a)). Podocytes have cytoplasmic extensions, pedicels, emanating from their cell body which branch and terminate in small projections of between $250 - 700$nm diameter [211], called foot processes (FPs). Pedicels and FPs or adjacent podocytes connect in a tightly interdigitated arrangement and attach to the underlying glomerular basement membrane (GBM) by thin filtration slits, anchoring the capillaries in place and completing the filtration barrier [210]. This barrier is incredibly efficient at filtering macromolecules (proteins) based on size and charge. Effacement (loss) of this highly ordered podocyte substructure (Fig. 7.1(b)) results in protein leakage and is the major structural change associated with nephrotic disease [210].

The model of filtration occurring primarily at the glomerular membrane, was challenged by *in vivo* 2-photon microscopy of fluorescently labelled albumin throughout a rat kidney which observed 50 times the expected albumin leakage through the GBM than expected [218]. This claim was later refuted and accounted for by experimental artefacts [17, 219], highlighting the need to consider limitations of the imaging system when carrying out experiments.

The diagnostic features of the primary causes of nephrotic syndrome are summarised below.

Minimal change disease

Minimal change disease is the most common cause of nephrotic syndrome in children and is so called because, by traditional light microscopy, glomerular ultrastructure appears normal. Diagnosis requires observation by EM and reveals a high degree of effacement of podocyte FPs [220, 221].

Membranous nephropathy

Membranous nephropathy is characterised by intermediate podoctye FP effacement

and thickening of the GBM throughout the glomerulus when observed by EM. Diagnosis by light microscopy is possible through immunostaining of immunoglobulin G and C3 which reveal granular deposits [220, 221].

Focal segmental glomerulosclerosis

Focal segmental glomerulosclerosis is characterised by sclerosis (hardening) and hyalinosis (amorphous, glassy appearance) of segments of glomeruli revealed by EM, although not all glomeruli are affected. Deposits of immunoglobulin M and C3 can be observed by light microscopy through immunostaining [220–222].

7.3 Structured illumination microscopy of renal biopsies

In order to test the ability of 3D-SIM to resolve podocyte substructure, a fluorescent probe was tagged to podocin, a protein which localises to the outer edge of FPs [223]. The predicted image was anticipated to show a curvilinear outline of FPs similar to FP profiles observed by TEM. Additionally, with pathological diagnosis in mind, sample preparation was restricted to using only standard immunofluorescence equipment and reagents which would typically be found in a surgical pathology laboratory.

Kidney tissue used in this study was excess tissue from patient biopsies taken for diagnosis of kidney disease, no tissue was obtained primarily for research. The research usage of this tissue was approved by the Montefiore-Einstein Institutional Review Board (docket #2014-3678). Three tissue sections were of normal (healthy) biopsies, three were diagnosed as minimal change disease, and two were diagnosed as membranous nephropathy. The tissue was frozen in O.C.T.^{TM} tissue mounting media (Sakura Finetek, 4583) immediately following biopsy. The tissue was prepared for imaging by SIM and TEM as described in Appendix F.4.

Samples were imaged using a commercial structured illumination microscope (Nikon, N-SIM on Eclipse Ti base unit) with both epi-fluorescence and 3D-SIM imaging modalities. Epi-fluorescence images were acquired at 20x (Nikon, Plan Fluor 20x Ph1 DLL) or 100x magnification (Nikon, Plan Apo TIRF 100x Oil DIC H N2) with FITC filter sets, and imaged onto an electron multiplied charge coupled device (EMCCD;

Andor, iXon+). 3D-SIM images were acquired at 100x only, with 488nm laser illumination and a specialist N-SIM filter block for green emission. 3D images (z-stacks) were acquired with a plane separation of 120nm. 3D volumes through the entire thickness of the tissue, over the field-of-view (approximately 30 x 30 μm^2), were acquired in approximately 5 minutes.

For comparison with SIM images, TEM images of kidney biopsies were taken as part of routine diagnosis processed by standard EM preparation and imaging methods [224]. TEM samples were imaged with a JEOL 1400 TEM equipped with a side-mounted CCD (GATAN, 785 ES1000W) at magnifications between $1000 - 20000$x.

Figures 7.2(a) and (b) show epi-fluorescence images of a normal tissue section at 20x and 100x magnification respectively. These show that the FITC-podocin staining does localise along the capillary walls, and is therefore valid for this study. At 100x, evidence of podocyte substructure is observed but contrast is very low. Figure 7.2(c) shows the maximum intensity projection of a 3D-SIM z-stack of the same region as in Fig. 7.2(b). The contrast enhancement and increased resolution makes the highly detailed substructure immediately visible. Tightly packed, coiled structures are indicative of interdigitating foot processes, and comparison of SIM and TEM images (Figs 7.2(d-g)) at the same magnification confirms this. The diameter of FPs as determined from 3D-SIM images is $300 - 600\,\mu m$ compared to EM measurements of $250 - 400\,\mu m$. This difference may be due to differences in sample preparation and imaging; with EM, the podocyte substructure is directly observed whereas with SIM, the podocyte substructure is indirectly imaged with a fluorescent marker bound to the edge of the FP.

Figures 7.3(a) and (b) show 20x and 100x magnification epi-fluorescence images of a diseased tissue section diagnosed with minimal change disease. Comparison with Figs 7.2(a) and (b) shows no obvious difference. Perhaps there is less granularity in the substructure in the tangential (*en face*) view (T) for minimal change disease than for normal tissue at 100x magnification, but this is very subjective. Figure 7.3(c) shows a maximum intensity projection of a 3D-SIM z-stack of the the same region as in Fig. 7.3(b), revealing similar structures as in Fig. 7.2(c) but with some marked differences. The coiled structures are more sparse, show less interlinking, and have more shallow

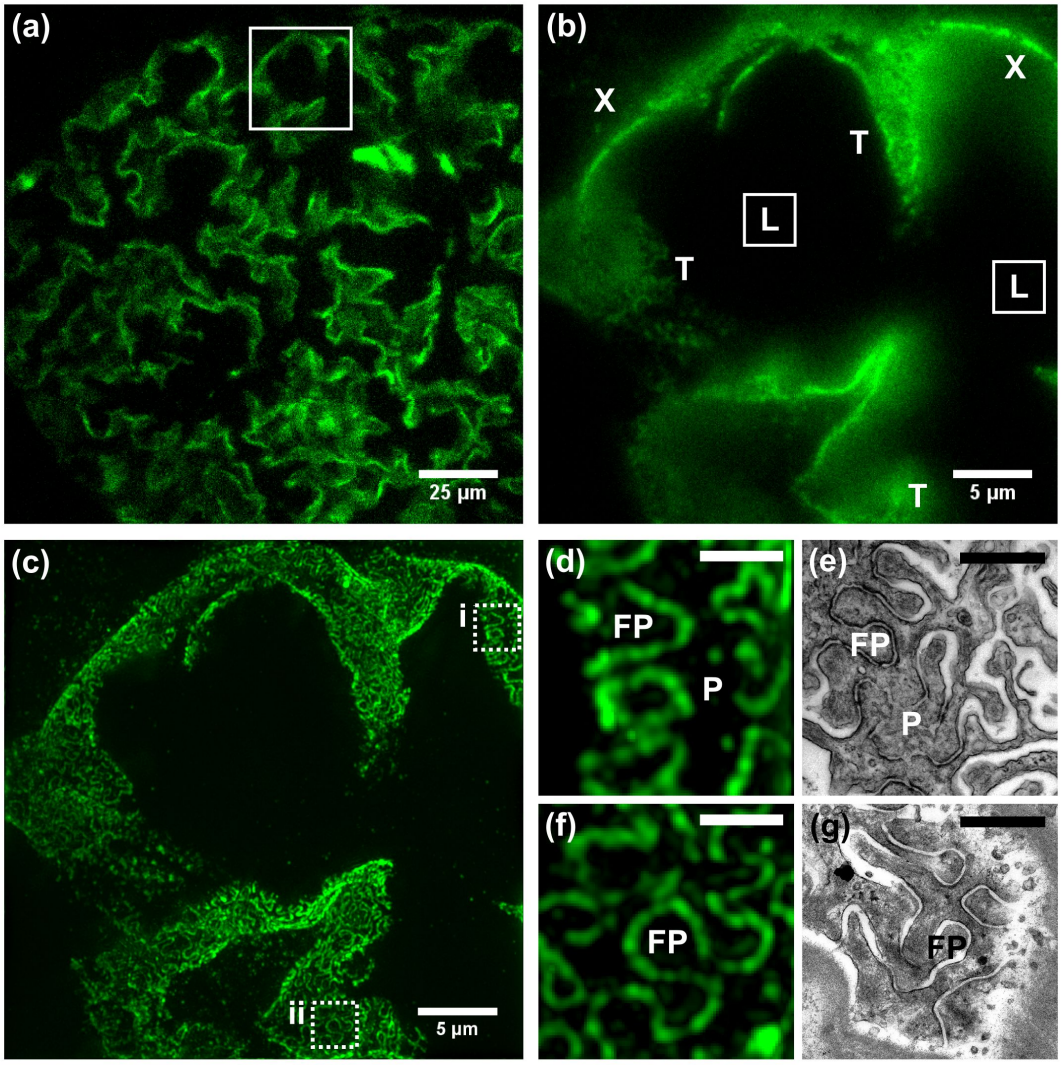

FIGURE 7.2: Images of normal podocyte substructure. (a) 20x epi-fluorescence image of glomerulus. (b) 100x epi-fluorescence image of white box in (a). (c) Maximum intensity projection of 3D-SIM images of same region as in (b). (d, f) Enlarged images of regions i and ii from (c) respectively. (e, g) TEM images showing similar podocyte substructure as (d, f) respectively. L: capillary lumen, P: podocyte, FP: foot process, T: regions showing tangential (*en face*) views of podocyte substructure, X: regions showing cross-sectional view of podocyte substructure. Scale bar in (d-g): 1 µm. Figure adapted with permission from [209].

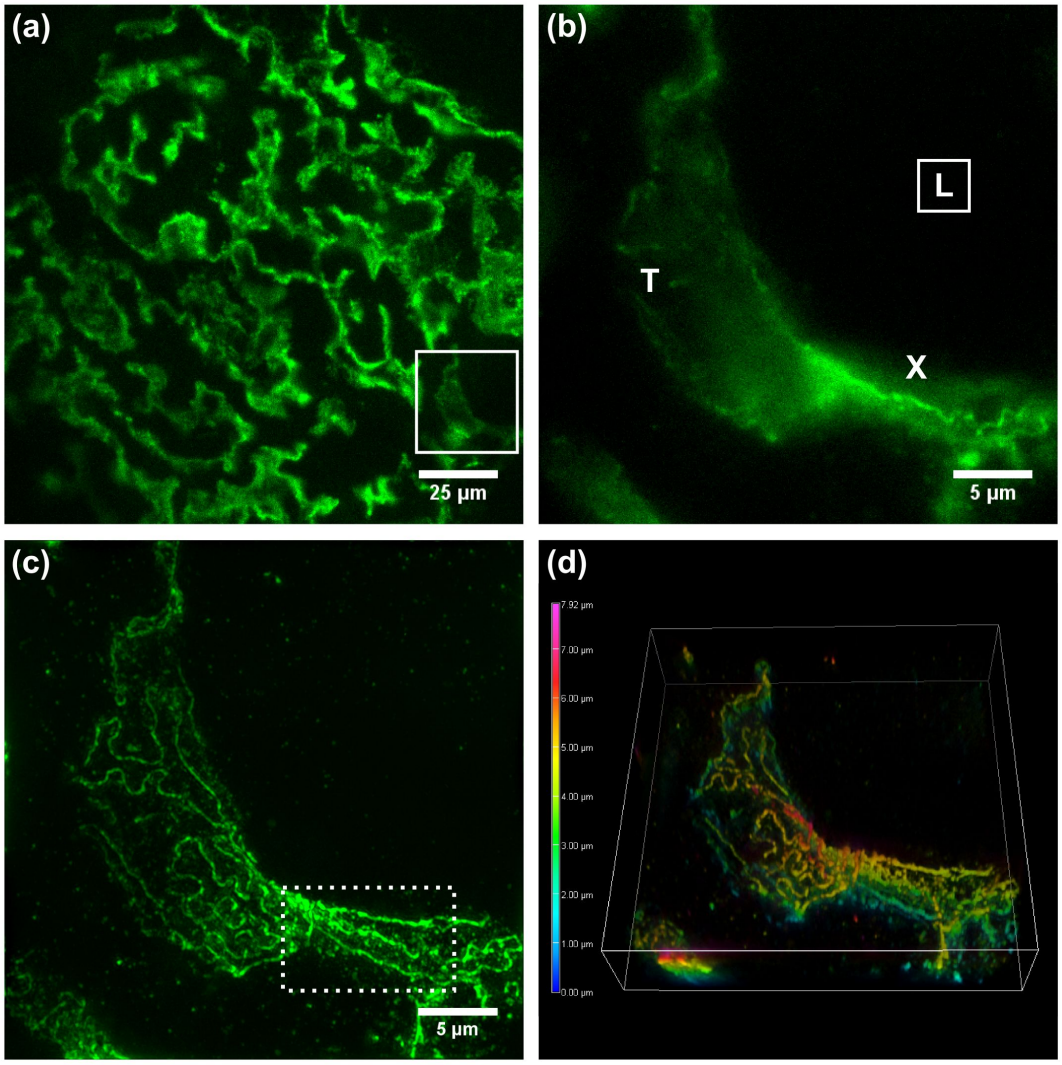

FIGURE 7.3: Images of podocyte substructure in minimal change disease biopsy. (a) 20x epi-fluorescence image of glomerulus. (b) 100x epi-fluorescence image of white box in (a). (c) Maximum intensity projection of 3D-SIM images of same region as in (b). The dashed white box highlights long, relatively straight features observed in diseased biopsies only which are not observed by TEM. (d) $z-$depth coded volume rendering of the same data as (c). L: capillary lumen, T: regions showing tangential (*en face*) views of podocyte substructure, X: regions showing cross-sectional view of podocyte substructure. Figure adapted with permission from [209].

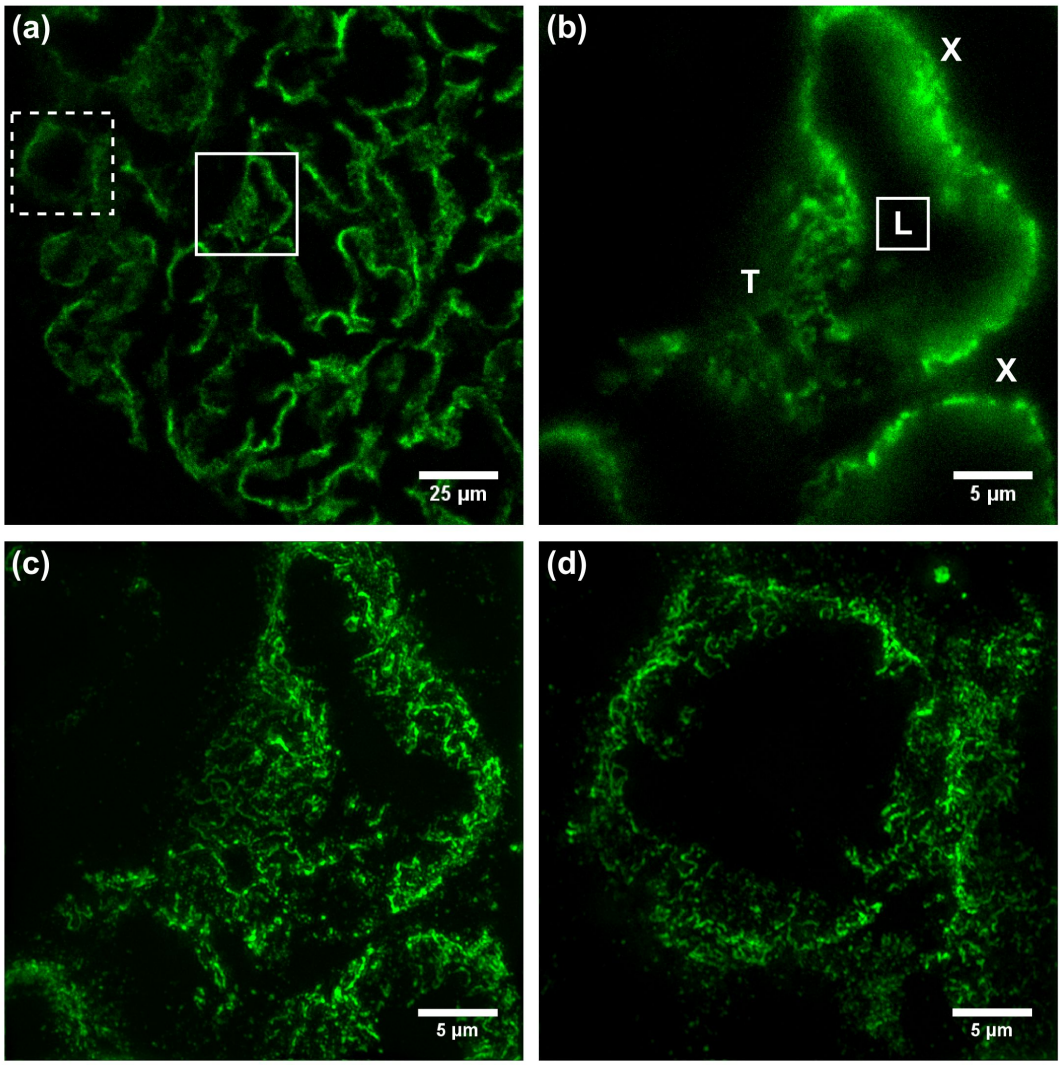

FIGURE 7.4: Images of podocyte substructure in membranous nephropathy biopsy. (a) 20x epi-fluorescence image of glomerulus. (b) 100x epi-fluorescence image of solid white box in (a). (c) Maximum intensity projection of 3D-SIM images of same region as in (b). (d) Maximum intensity projection of 3D-SIM images of dashed white box in (a). L: capillary lumen, T: regions showing tangential (*en face*) views of podocyte substructure, X: regions showing cross-sectional view of podocyte substructure.

curvature. The extreme case of this is observed in the lower right corner of Fig. 7.3(c) (see dashed box) where three almost parallel lines are observed. These are attributed to almost complete effacement of the substructure as the outline of the tightly interdigitating structure effectively unravels. There is no direct analogue of this observation in TEM images of effacement. This is because sections for TEM are sliced to a thickness of approximately 100nm and the likelihood of an effaced foot process lying within the plane of the section over any significant distance is effectively zero. The 3D nature of the podocyte substructure is emphasised in Fig. 7.3(d) which shows a volume rendering of the same data as Fig. 7.3(c) with a $z-$depth coded colourmap. The tissue extends from approximately $1.5\,\mu\mathrm{m}$ to $6.5\,\mu\mathrm{m}$ depth which is consistent with the $5\,\mu\mathrm{m}$ section thickness indicating the tissue is well preserved. Even FPs which are observed relatively *en face* have a $z-$depth variation of approximately $2\,\mu\mathrm{m}$, highlighting the 3D curvilinear nature of the podocyte substructure.

Figures 7.4(a) and (b) show 20x and 100x magnification epi-fluorescence images of a diseased tissue section diagnosed with membranous nephropathy. Again, comparison with normal tissue (Figs 7.2(a) and (b)) or minimal change disease (Figs 7.3(a) and (b)) is very subjective. Figure 7.4(c) shows a maximum intensity projection of a 3D-SIM z-stack of the same region as in Fig. 7.4(b) and Fig. 7.4(d) shows the maximum intensity projection of a 3D-SIM z-stack of the dashed box in Fig. 7.4(a). SIM images of membranous nephropathy specimens showed a more fractured substructure. The density of substructural features was lower than for normal tissue but higher than for minimal change disease indicating an moderate degree of effacement. Whereas the interlinked outline of many FPs can be traced continuously in the images of normal and minimal change disease samples, with tissue exhibiting membranous nephropathy outlines of FPs tended to be isolated and fragmented.

For easier comparison, Fig. 7.5 displays 3D-SIM images of normal and diseased tissue side-by-side. Figure 7.5(a) shows a full FOV maximum intensity projection of a 3D-SIM z-stack for healthy tissue and Fig. 7.5(b) shows a similar image for tissue diagnosed with minimal change disease. Again, the structural differences are quickly and easily identified, with normal tissue showing tightly packed, interlocking structures whereas minimal change disease exhibits structure which is less dense and with slower

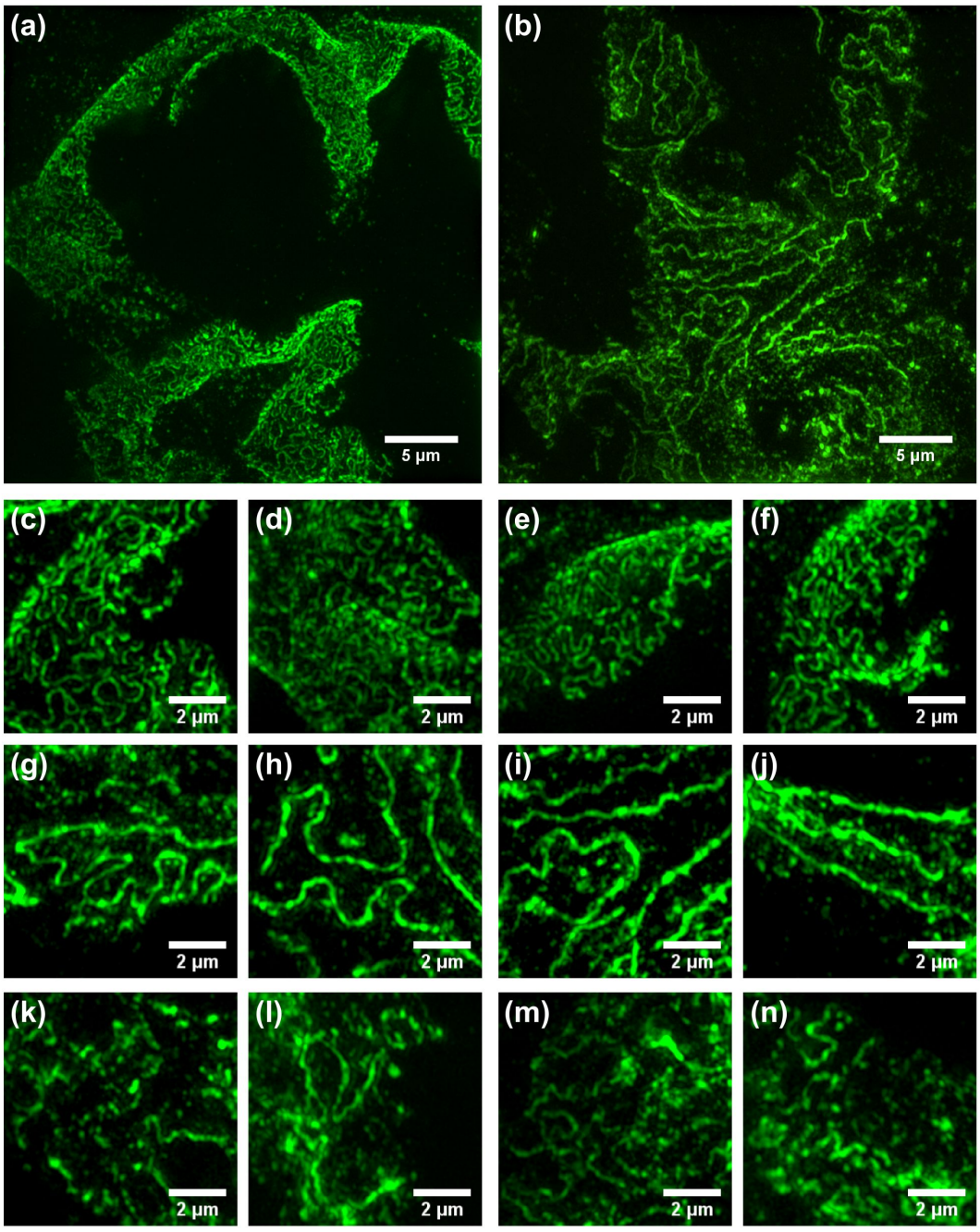

FIGURE 7.5: Comparison of SIM images of podocyte substructure in normal and diseased biopsies. All images shown are maximum intensity projections of 3D-SIM z-stacks. (a,b) Full FoV images of normal and minimal change disease podocyte substructure respectively. (c-f) Enlarged regions from various normal tissue sections. (g-j) Enlarged regions from various minimal change disease tissue sections. (k-n) Enlarged regions from various membranous nephropathy tissue sections.

curvature. The extreme case of infinitely slow curvature (i.e a straight line) is also readily observed in Fig. 7.5(b). Figures 7.5(c-f) show enlarged sections of SIM images of normal podocyte substructure, Figs 7.5(g-j) show similar regions of podocyte substructure in minimal change disease, and Figs 7.5(k-n) show similar regions in membranous nephropathy. These images further emphasise the morphological differences between the three states of tissue: normal tissue exhibits densely packed FPs in a tightly interlocking structure; minimal change disease reveals a much sparser pattern, with similar features observed, but enlarged, and also the presence of outlines with minimal curvature; and membranous nephropathy shows FP structures of intermediate size and sparsity, although the outlines are more discontinuous and the outlines of adjacent FPs do not link up.

7.4 Discussion and conclusions

This chapter has demonstrated the potential use of SIM in clinical applications traditionally requiring EM imaging for diagnosis by applying 3D-SIM to the visualisation of ultrastructural changes in nephrotic disease. Healthy podocyte substructure as visualised by 3D-SIM and TEM is compared to confirm that SIM can indeed resolve important diagnostic features and the changes in this substructure are investigated for two diseased states; minimal change disease and membranous nephropathy.

3D-SIM images of normal glomerular tissue revealed a complex network of interdigitated FPs as expected, minimal change disease samples showed enlarged and sparse FPs as expected from EM analysis and in agreement with a high degree of effacement, membranous nephropathy samples showed FPs of intermediate size and a moderate level of effacement. These images agree well with current understanding of the podocyte substructure and TEM images of these diseases, supporting the use of SIM for diagnosis of nephrotic disease. The primary difference between SIM and TEM images is that the measured widths of FPs are larger, $300 - 600\,\mu\mathrm{m}$ by 3D-SIM compared to $250 - 400\,\mu\mathrm{m}$ by TEM. This difference may be due to shrinkage of tissue when preparing samples for TEM or because of the exact location of the fluorescent

podocin marker attached to the FP, and different widths may be measured using different proteins for visualisation. Gundersen *et al* [211] presented a statistical method to determine the true width of FPs based on the measurement obtained from a thin tissue section taken at an arbitrary angle relative to the FP; as 3D-SIM images can build up a 3D model of the podocyte substructure and can be arbitrarily rotated, SIM may be able to obtain more accurate measurements of FP width than EM, however, it would be expected that the widths obtained by SIM should be smaller than for EM in this case.

A number of TEM images are required to support a diagnosis, and volumetric information must be mentally visualised by the pathologist from multiple images taken from different planes of the tissue. The ability to optically section the tissue by 3D-SIM enables volumetric data to be acquired trivially through the full thickness of the tissue slice. Coupled with the FoV of the SIM microscope, which is approximately 50 times larger than for TEM, a single 3D-SIM dataset of a $5\,\mu\mathrm{m}$ thick sample can contain the equivalent of 2500 TEM images, and diagnosis can be performed almost at a glance from this incredibly information-rich dataset. Furthermore, SIM images of minimal change disease also revealed long, approximately parallel lines of FP outlines which are attributed to fully effaced FPs although these are not observed with TEM due to the thin tissue sections imaged by TEM suggesting 3D-SIM may also be highly useful in basic science investigations into nephrotic disease and could enable highly functional microanatomy studies.

Only standard immunofluorescence staining protocols were used to prepare tissue sections for SIM imaging, all of which would be standard equipment in a surgical pathology lab. The protocols are relatively quick and simple, taking only a few hours, and are already performed as standard in the preparation of kidney biopsies. In contrast, standard TEM preparations require specially trained technicians and are involved, taking 1 to 2 days. Time can also be saved in the image acquisition and analysis stages with SIM. Z-stacks can be acquired rapidly and can be reconstructed in 3D with minimal computational strain; a single z-stack through the entire thickness of the tissue can be acquired within 5 minutes and visualised in 3D in real time. This greatly reduces the cognitive strain on the pathologist from mentally visualising the 3D substructure

from a large number of TEM images and can reduce diagnosis time. With TEM, diagnosis will routinely take between 1 day and 1 week, whereas with SIM, diagnosis could be achieved potentially only a few hours after the biopsy is taken. This potentially dramatic reduction in diagnosis time also has a social advantage, as the patient would spend less time worrying about the results of their biopsy.

SIM is a relatively expensive technology but this can be partially attributed to its relatively recent commercialisation and it is assumed that the cost of the microscope itself will reduce over time. In contrast electron microscopes are equally expensive despite being a well established technique. EM incurs additional high costs due to the specialist training and consumables required to prepare samples for EM. SIM is compatible with standard immunofluorescence preparation protocols, requiring much less training than EM and utilising consumables that are already standard use for pathological analysis. The speed with which diagnosis by SIM can be achieved could greatly reduce the number of labour-hours per diagnosis and with it, the cost per diagnosis. Although diagnosis by SIM would require substantial investment to set up, it would appear to be a much more economically sustainable technique for routine diagnosis of nephrotic disease.

Though EM still provides far superior resolution, SR microscopy techniques are closing the gap between these imaging modalities. This study has exploited a modest, but essential, resolution enhancement beyond the diffraction limit which already provides substantial evidence for the benefits of optical pathology by SIM as detailed in this Chapter. By making use of recent advances in NL-SIM (such as [102]), this technique could apply to an even wider range of ultrastructural studies.

Further investigation, involving larger patient numbers and examples of all nephrotic diseases, is required to provide solid evidence to validate the use of SIM for diagnosis of nephrotic disease. This may be complimented by development of compact, low cost, and portable SIM which can be taken into pathology labs as was demonstrated for Airy LSM in Chapter 6.2.

Future innovation could focus on automated diagnosis by machine vision image analysis. This could potentially be implemented by analysis of Fourier content of images, as the FPs in diseased samples were larger than in healthy tissue. Successful

implementation of automated analysis would reduce the workload on the pathologist, and increase the diagnostic throughput.

A long-term direction would be to combine SIM with Airy LSM (Chapter 4), as has been done with other LSM techniques [20, 59, 76, 78, 102], and exploit this for high-throughput diagnostic imaging.

Chapter summary

- SIM can be used to visualise diagnostically relevant podocyte ultrastructure.
- Standard immunofluorescence staining of podocin reveals FP outlines and correlates well with features observed by EM.
- SIM images were used to differentiate between healthy, membranous nephropathy, and minimal change disease tissues.
- SIM potentially offers large financial and time savings over EM for use in medical diagnosis.

7.5 Chapter acknowledgements

Renal tissue sections were prepared for imaging by Wa Chen and Joseph Albanese (Montefiore surgical pathology Translational Research Laboratory). SIM imaging of the renal tissue sections was performed by the author and Elaine C. Campbell with the assistance of James Pullman and Frances E. Goff. James Pullman correlated visible structures in the SIM images with EM images. James Pullman and the author interpreted the SIM images.

Chapter 8

Integrated optical trapping and microscopy

Parts of this chapter are adapted from the article "Development of a graded index microlens based fiber optical trap and its characterization using principal component analysis" [225] published in Biomedical Optics Express (2015).

8.1 Introduction

Previous chapters have discussed advances in imaging technologies and the imaging studies they have enabled, the focus of this chapter shifts to address the issue of how to make the microscope a more functional tool. Optical manipulation is a powerful tool for biophotonics which allows microscopic events to be triggered at will. An optical microscope with optical manipulation capability elevates the user from a simple observer to the director of a microscopic scene where cells can be positioned at will. Such microscopy platforms exist [161, 163, 164, 169, 170] but require complex optical systems and are difficult to reconfigure to perform additional imaging modalities. Optical fibre trapping (OFT) provides a flexible and low cost optical manipulation solution but OFT probes have a low manipulation length and produce generally weak traps so they have been under-exploited in combination with advanced microscopy techniques.

An ideal tool to add functionality to a microscopy platform would be a strong OFT probe with a long ($> 50\,\mu\mathrm{m}$) manipulation length, which could be easily attached to multiple microscopy platforms with minimal modification to either the OFT probe or

the microscope. Such a system is presented in Chapter 8.2 and incorporated into a commercial SR microscope. When considering the best microscopy platform to combine with optical manipulation, the spatial and temporal resolution of the microscope must be compared to the motion of particles held within the trap. Particles held within a weak trap ($0.1\text{pN}\,\mu\text{m}^{-1}\text{mW}^{-1}$) can oscillate within the trap by approximately $\pm$200nm [226]. SR methods such as SIM or STORM compute super-resolved images from a number of sequentially acquired images, thus if the trapped particle undergoes movement which is significant relative to the resolution of the microscope during the acquisition period for one super-resolved image, the image will contain artefacts or appear blurred and will not achieve the desired resolution. For these reasons, the OFT probe is combined with SIM. Although SIM only provides a modest resolution enhancement (2 times), it is one of the fastest super-resolution techniques and provides one of the best trade-offs between spatial and temporal resolution for combination with optical trapping.

This Chapter describes the development of a compact OFT probe based on a GRIN micro-objective lens, its characterisation, and its use in biomedical imaging experiments.

8.2 Development and characterisation of an optical fibre trap based on a graded index microlens

To produce an OFT probe with a high NA and long manipulation length, a hybrid system consisting of an optical fibre combined with miniaturised macro-optics was developed. The limitation of short manipulation length with OFTs stems from geometric considerations of the fibre size and the high angled rays required for tight focusing. By utilising a GRIN micro-objective lens, a single, commercially available, miniaturised optical component for focussing the light emitted by an optical fibre, an ultra-facile OFT probe is achieved. The OFT probe has a long manipulation length which can be easily integrated into inverted microscopy platforms that can enable advanced functional biology experiments.

8.2.1 Design of the optical fibre trapping system

The experimental set-up is shown in Figure 8.1. The OFT probe consists of a commercially available GRIN micro-objective lens (Fig. 8.1(a), GRINtech, GT-MO-080-018-810) mounted at the distal end of a single-mode (SM) optical fibre (Thorlabs, 780HP-CUSTOM, NA: 0.13, design wavelength: $780-960$nm, SMA-SMA connectored) and held in place, a distance of $200\,\mu\mathrm{m}$ from the fibre facet, by a custom made SMA adapter as shown in the insert of Fig. 8.1(c).

A laser beam (TuiOptics, TA 100, λ: 785nm, maximum output power: 300mW) was coupled into the SM fibre via lens, L (Thorlabs, F220SMA-780), as shown in Fig. 8.1(b). Two mirrors provide sufficient degrees of freedom to optimise the coupling efficiency into the SM fibre. A variable neutral density (ND) filter (Thorlabs, NDC-50C-2-B) allowed continuous tuning of the laser power in the range $3-300$mW. At the distal fibre facet, the laser beam diverges and is collected and focussed by the GRIN lens. The GRIN micro-objective has a cross section of 1.4mm diameter and a length of 7mm and is composed of two GRIN lenses of 1mm diameter, followed by a high-NA, 1mm diameter plano-convex lens. Figure 8.1(a) shows the ray optics propagation through the GRIN lens, of rays from a point $200\,\mu\mathrm{m}$ away from the lens. The refractive index of the two GRIN lenses are tuned to minimise the spherical aberration induced by the plano-convex lens. The GRIN micro-objective is capped with a $120\,\mu\mathrm{m}$ thick BK7 coverslip and the optical elements are fixed in place within a stainless steel sheath. The specified NA of 0.8 is only achieved when the light entering the GRIN lens diverges with a light cone corresponding to an NA 0.18. The SM fibre used in this system has an NA of 0.13 so the beam focussed through the GRIN lens has an NA of 0.58. This focus is formed approximately $200\,\mu\mathrm{m}$ from the distal facet of the GRIN microlens which enables optical manipulation with a large manipulation length. The coupling efficiency through the combined SM fibre and GRIN lens system was $(37\pm1)\%$.

Theoretical values for the lateral and axial beam widths are $1.35\,\mu\mathrm{m}$ and $4.67\,\mu\mathrm{m}$ respectively. This was determined experimentally by acquiring an image stack, with z-plane spacing of $0.5\,\mu\mathrm{m}$, around the beam focus of the trapping probe using a 0.8 NA, 60X objective lens (Nikon, CFI 60X) and imaging onto an electron multiplied charge

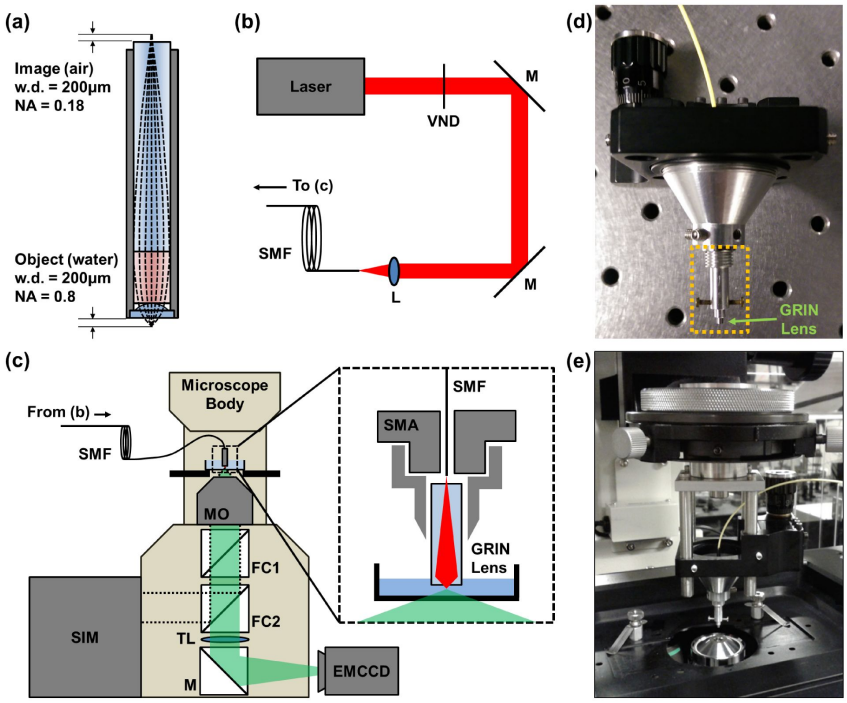

FIGURE 8.1: Schematic of GRIN lens OFT system. (a) Schematic of the GRIN microlens, dashed lines show ray optics propagation through the microlens. (b) Schematic of laser coupling into the proximal fibre facet. (c) Shows the fibre probe mounted on an inverted microscope with structured illumination capability. Insert shows detail of the probe head. (d) Photograph of the probe head, outlining the fibre-GRIN lens area in orange and the GRIN lens (green arrow). The probe is further mounted on a z-axis micrometer positioning stage (black). (f) Photograph of the probe fully mounted on the condenser mount of an inverted microscope. VND: variable neutral density filter, M: mirror, L: Lens, SMF: single-mode fibre, MO: microscope objective, FCx: filter cubes, TL: tube lens, EMCCD: electron multiplied charge coupled device, SIM: structured illumination microscopy illumination unit, SMA: SMA fibre connector. Figures (a) and (c) adapted with permission from [225].

coupled device (EMCCD, Andor, iXon+). The optic axis of the beam was found to be offset from the optic axis of the microscope by $10°$. This was corrected for and intensity profiles were taken through the focus along the major Cartesian directions. Full width at half maximum (FWHM) values gave lateral beam widths along the $x-$ and $y-$axes of $(1.3 \pm 0.1)\,\mu\text{m}$ and $(1.9 \pm 0.1)\,\mu\text{m}$ respectively and an axial beam width of $(6.4 \pm 0.1)\,\mu\text{m}$. Since the publication of [225] this data has been revisited, the rotation performed with a sub-pixel interpolation method, and beam widths fitted with a Gaussian model. Intensity profiles taken through beam focus using this method are shown in Fig. 8.2 and lateral beam widths were found to be $0.83\,\mu\text{m}$ and $1.33\,\mu\text{m}$ along the

x- and y-axes respectively and an axial beam width of $6.17\,\mu\mathrm{m}$. A physical tilt of $10°$ would be visible by eye but this is not observed, therefore the beam tilt is attributed to a small misalignment between the SM fibre tip and the GRIN lens. The lateral width of the beam along the x-axis is smaller than expected given the NA of the SM fibre but reasonable for a lens with 0.8 NA which suggests the divergence angle of the SM fibre is greater than specified. The asymmetry in the $x - y$ plane is also attributed to aberrations resulting from the misalignment of the SM fibre tip and the GRIN lens.

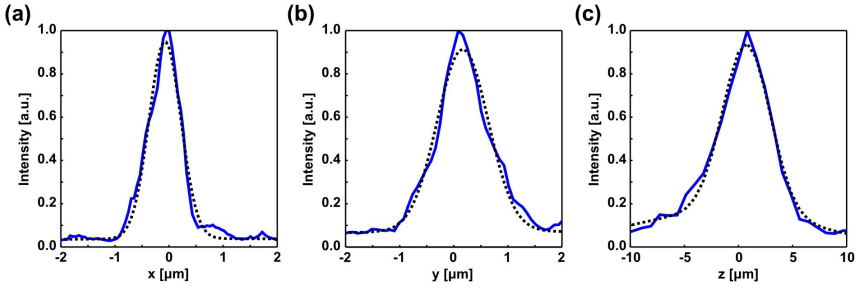

FIGURE 8.2: Beam profiles for GRIN lens OFT. Normalised intensity profiles through the beam focus along the (a) x-, (b) y-, and (c) z-axes (solid blue). Intensity profiles were fitted with a Gaussian model (dashed black).

8.2.2 Integration with a commercial microscope

The GRIN lens fibre probe was mounted on an inverted microscope with structured illumination capability (Nikon, N-SIM on Eclipse Ti base unit) as shown in Fig. 8.1(c) using an adapter attached to the microscope mount traditionally reserved for a condenser lens when using brightfield illumination (see Fig. 8.1(e)). The probe could be positioned using the xyz positioning screws for the condenser lens mount, additional fine z-positioning was provided by a z-axis micrometer positioning stage (Thorlabs, SM1Z) to match the trapping plane with the image plane of the microscope. The placement of the probe effectively disables the brightfield capability of the microscope.

Epi-fluorescence illumination was provided from the top tier of microscope ports and directed into the sample by appropriate choice of filters in filter cube 1 (Fig. 8.1(c)) and the microscope objective lens. Fluorescence was collected from the sample by the objective lens and imaged by a tube lens onto an EMCCD (Andor, iXon+). Structured illumination was delivered into the sample from the bottom tier of microscope ports

and filters in filter cube 2 (Fig. 8.1(c)). The 2D or 3D periodic illumination is generated by a diffraction grating in the SIM illumination unit and imaged into the sample by the microscope objective. Whereas epi-fluorescence illumination can be used with any microscope objective, the SIM mode is only compatible with a particular objective lens (Nikon, CFI Apo TIRF 100X Oil). The only modification to the microscope required for use with the trapping probe is the addition of a short-pass filter to protect the camera from the high intensity of the trapping beam (Semrock, FF01-650/SP-25). This additional filter was mounted in whichever filter cube was not required by the imaging modality of interest. The orientation of the filter is such that it lies in the plane transverse to beam propagation, minimising aberrations in the imaging pathway. A fast CCD camera (Basler, piA640-210gm) was mounted in a secondary microscope camera port and was used for characterisation of the probe.

8.2.3 Characterisation of the optical fibre trap

While the probe may be readily attached to a number of different microscope platforms, characterisation of the probe was still performed on the N-SIM platform despite its lack of brightfield imaging modality. The reasoning for this was to include a full description of the system, including mechanical noise (e.g. vibrations) resulting from the mounting of the probe on the microscope, in the analysis. If another microscope was used for calibration, the degree of mechanical noise could significantly alter the trap stiffness and give misleading indications of the probe performance in conjunction with the N-SIM platform.

The N-SIM platform is a specialist fluorescence microscope but fluorescent particles should not be used for characterisation of optical traps as the absorption and emission from the particle is an additional light-matter interaction which can affect the results [227]. Additionally, the trap laser, in combination with a poor short-pass filter for direct viewing of the beam, is a poor choice for observation of the trapped particle as the beam is tightly focussed and so it is very difficult to find beads for trapping. Two illumination schemes were trialled as shown in Fig. 8.3. The first scheme used a laser (Elforlight DL-10-6, 532nm), coupled into the sample through the optical fibre and GRIN lens, using a long-pass dichroic mirror (Thorlabs DMLP605R, 605nm cut-off) to merge with the

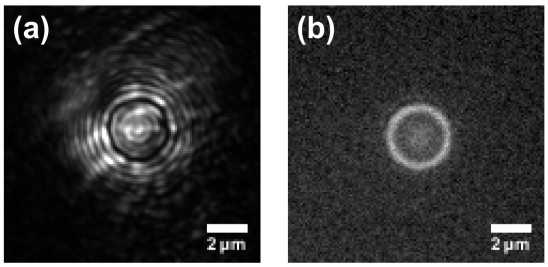

FIGURE 8.3: Illumination scheme for optical fibre trap characterisation. Example images of trapped $3\,\mu\mathrm{m}$ diameter polystyrene bead illuminated with (a) fibre delivered laser illumination, and (b) white light reflection. (b) gives the most uniform background but has lower contrast between the bead and background. Scale bars: $2\,\mu\mathrm{m}$.

trap beam path. Although the fibre has SM-operation at 785nm, at 532nm it supports multiple modes and the illumination is not uniform over the image (Fig. 8.3(a)). Additionally, the illumination only covers a limited area near to the trap focus, making it difficult to find beads in spare samples. The second scheme was a reflection imaging scheme, using the Mercury lamp illumination source for epi-fluorescence imaging with only a 50:50 beam splitting mirror in filter cube 1, to enable imaging of non-fluorescent samples. This scheme gives much more uniform illumination (Fig. 8.3(b)) and covers the entire FOV of the camera. The images acquired with this reflection imaging scheme have low contrast between the signal and background (the image in Fig. 8.3(b) has been scaled). This is attributed to a strong reflection from the GRIN lens which contributes a large background signal to the image. The reflection imaging scheme was used for characterisation of the optical fibre trap.

Images of trapped particles were acquired with a 60X objective lens (Nikon, CFI 60X) and the fast CCD camera. The region of interest (ROI) of the camera was cropped to 60x60 pixels which adequately contained an image of a single trapped microsphere and facilitated acquisition rates of up to 400Hz. Movies of 100s duration were recorded for polystyrene microspheres of $(3.00 \pm 0.02)\,\mu\mathrm{m}$ (Polysciences Inc., 64060) and $(4.17 \pm 0.03)\,\mu\mathrm{m}$ (Polysciences Inc., 64070) diameter in optically-flat glass-bottom dishes (World Precision Instruments (WPI), FD3510-100) at 400Hz, with an integration time per frame of 400μs, for a range of trap beam powers. Temperature control was implemented by isolating the microscope body from the rest of the laboratory inside a large perspex box, in order to keep the microscope stage as a constant (25.6 ± 0.2)°C

throughout the experiment.

Trap stiffness for the probe was to be determined by the power spectral density method detailed in Chapter 3.3 but additional image processing was required before accurate particle tracking could be performed on the movies. This is a consequence of the reflection imaging scheme utilised here to enable trap characterisation. The image formed on the camera has a large background level resulting from the reflection of the illumination from the output facet of the trapping probe, and the signal from microspheres contains two components, one from the initial reflection of illumination by the microspheres and the second from the transmission through the microspheres of illumination reflected from the probe. The result is an image with very low contrast and a movie with a lot of stochastic noise. Figure 8.4(a) shows a typical frame from a movie of a trapped $3\,\mu\mathrm{m}$ diameter trapped bead with 60mW trap beam power.

Traditionally, image processing, such as low- or high-pass filtering and thresholding, must be laboriously fine-tuned to suit each particular experimental apparatus and filter out specific noise which is unique to that system. Such a process is subjective and can only be tested on a small subset of the movie frames, to manually determine a processing method that works for all 10000+ frames acquired in an experiment is intractable, and so a substandard filtering method, which will create some errors in the tracking data, is used. Manual determination of optimal image filters and their parameters for the low-contrast movies acquired resulted in spurious tracking with many obvious errors. To aid in the processing of the movies, an adaptive filter based on principal component analysis (PCA) was implemented to remove stochastic noise. The adaptive nature of the filter circumvents the user, reducing the impact of subjective decisions in the filtering process.

Adaptive image filter based on principal component analysis

The adaptive image filtering procedure is outlined in Fig. 8.4(b-d). The first few principal components (PCs) of the original movie are determined in the spatial domain, taking into account all the frames for a movie of a trapped bead with a certain trap beam power. The spatial PCs describe major variations between individual frames of a movie and are similar to the eigenfaces used for facial recognition [228]. The first few PCs are associated with a degree of freedom of the particle. In the example in Fig.

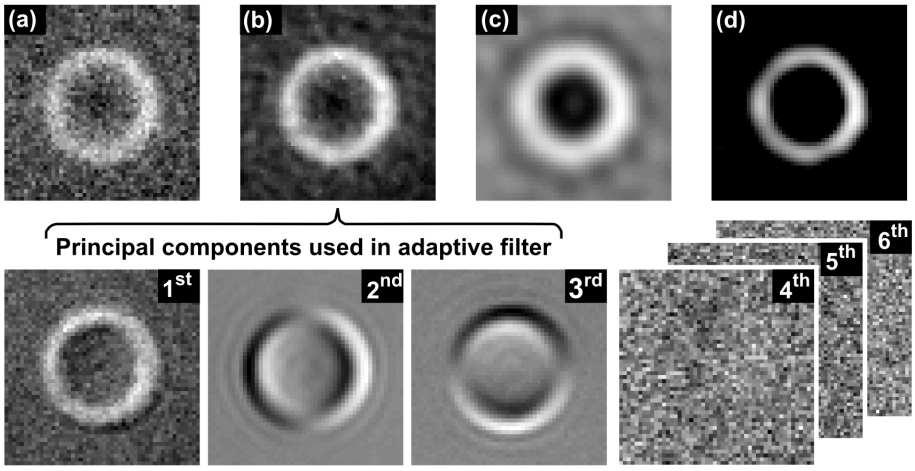

FIGURE 8.4: Representation of PCA based adaptive image filter applied to a typical movie of a trapped bead ($3\,\mu\mathrm{m}$ diameter) with 60mW trap beam power. (a) shows a single frame from the original movie. (b) shows the same frame after being processed by the adaptive filter. The bottom row shows the first six PCs for the movie. Only the first three PCs contain information on the motion of the particle and are retained by the filter, the 4^{th} and higher PCs in this example contain only random noise. (c) A spatial band-pass filter is then applied to the filtered frame to remove dead pixels and other stationary noise features. (d) Finally, a minimum-value threshold is applied to the image, this image is then used to determine the bead position. Figure adapted with permission from [225].

8.4, the first PC is akin to the mean image of the bead and gives the positional offset of the bead, the next two PCs relate to motion in the $x-y$ plane, yielding differential images of the particles x- and y-motion respectively. In Fig. 8.4, the higher order PCs (4^{th} and higher) contain no structure, relate only to random image fluctuations, and do not give any relevant information on the motion of the particle. Reconstructing the movie without these irrelevant PCs yields a movie which still contains all of the particle motion, but with significantly reduced stochastic noise (see Fig. 8.4(b)). This process is outlined mathematically in Appendix E. The filtered images are free of inter-frame, stochastic noise while retaining the particle motion. The number of PCs used to reconstruct each movie contained $(95 \pm 2)\%$ of all the variations (defined as the the sum of retained projection coefficients: $\sum_{k=1}^{k_{max}} c_k^i$; see Appendix E) and typically only the first three PCs were retained (as in the example shown in Fig. 8.4). Occasionally some structure was observed in higher order PCs which can be attributed to small asymmetries of the trapped particle or motion that is not described accurately by a

linear model. In these situations, more PCs were retained as required but in all special cases, the first three PCs still described $(91 \pm 1)\%$ of all the variations.

The only user specified parameter of the PCA filtering method is the number of PCs to retain, k_{max}, although, as the example case shows, this is generally a simple choice. The adaptive nature of the filter will adjust to systems with more complex motion or different imaging conditions rather than requiring an entirely new set of filtering criteria. The adaptive filter does not remove stationary objects from the images however, and an additional band-pass filter was required to remove these (Fig. 8.4(c)). After adaptive filtering, the choice of band-pass parameters becomes trivial. The frames were then thresholded (Fig. 8.4(d)) to facilitate centre-of-mass (COM) tracking which was performed using a cross-correlation based sub-pixel image registration method [229]. Typical cross-correlation algorithms compute the cross-correlation in the centre of a zero padded Fourier space, and then perform an inverse Fourier transform to determine the translation between the 2 images. If the image has dimensions $M \times N$ and the accuracy is desired to within $1/\kappa$ of a pixel, the size of the Fourier space must be $\kappa M \times \kappa N$ and the inverse fast Fourier transform becomes very computationally intensive, taking both a long time and requiring a large amount of memory. Briefly, the method developed by Guizar-Sicairos *et al* [229] uses an inverse fast Fourier transform as described above with $\kappa = 1$ as a starting point before using a discrete Fourier transform centred around the initial guess to improve the accuracy in a fast and memory efficient way. The discrete Fourier transform step can be run iteratively until the desired accuracy is achieved, however, noise will place a limit on the maximum accuracy.

To validate the use of the adaptive filter in the context of particle tracking, tracking was performed on fixed particles of known position. Particles were immobilised on a glass coverslip and were moved along known trajectories using a nanopositioning stage (Physik Instrumente (PI), P-733.3DD) and were imaged under conditions as close as possible to that of the trapped particle imaging. The standard deviation of the difference between the tracked particle position and the actual position of the particle was 12nm, verifying the use of the adaptive filter for particle tracking.

Trap stiffness determination by power spectral density

The traces of the particle were Fourier transformed then norm squared and divided

by the total acquisition time (100s) to yield the power spectra. The theoretical power spectrum (equation (3.15)) was modified to account for motion blur and aliasing due to the low bandwidth of the camera as:

$$S(f) = \prod_{n=-3}^{3} \frac{k_B T}{\pi^2 \gamma (f_c^2 + f^2)} \operatorname{sinc}(W f_n)^2 \tag{8.1}$$

where W is the integration time of the camera and $f_n = f + n f_{sample}$, $f_{sample} = 400\text{Hz}$ is the camera framerate or sampling frequency [156, 158, 226]. Faxen's correction was included in γ as described in equation (3.13) where the bead height is $z = r + s$. Trapping occurred in very close proximity to the bottom of the sample chamber and s was estimated to be $(0.25 \pm 0.2)\,\mu\text{m}$. The large uncertainty in s originated from the low contrast of the images used for trap calibration. Windowing (averaging) of the data, as is typical for power spectrum analysis [156], is problematic at low frequencies and so cannot be used with optical traps with a low corner frequency as is expected in the case of an OFT. Instead, an exponential distribution of the data is assumed and a maximum likelihood estimation is used to determine the corner frequency, f_c, from the raw, non-averaged experimentally measured power spectrum, $S_{meas}(f)$. This is expressed as:

$$\max\left(\prod_{i=1}^{N}\left[\frac{1}{S(f,f_c)}\exp\left(\frac{S_{meas}(f)}{S(f,f_c)}\right)\right]\right) \tag{8.2}$$

where the product is over N exponentially distributed data points from $S(f)$ [226].

The trap stiffness, including the dependence of the trapping beam power, was determined to be $k_{trap;[x,3\,\mu\text{m}]} = (0.63 \pm 0.01)\text{pN}\,\mu\text{m}^{-1}\text{mW}^{-1}$ and $k_{trap;[y,3\,\mu\text{m}]} = (0.522 \pm 0.006)\text{pN}\,\mu\text{m}^{-1}\text{mW}^{-1}$ for the x- and y-axes respectively for $3.00\,\mu\text{m}$ diameter polystyrene microspheres, and $k_{trap;[x,4\,\mu\text{m}]} = (0.39 \pm 0.01)\text{pN}\,\mu\text{m}^{-1}\text{mW}^{-1}$ and $k_{trap;[y,4\,\mu\text{m}]} = (0.35 \pm 0.01)\text{pN}\,\mu\text{m}^{-1}\text{mW}^{-1}$ for the x- and y-axes respectively for $4.17\,\mu\text{m}$ diameter polystyrene microspheres. Figure 8.5 shows plots of the trap stiffness or force constant, k_{trap}, along the x-axis only.

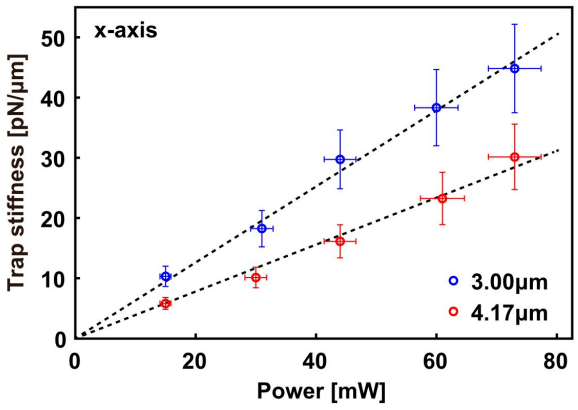

FIGURE 8.5: Plot of trap stiffness versus optical power along the x-axis for the GRIN lens based OFT. Figure adapted with permission from [225].

8.3 Application of optical fibre trap for imaging of dynamic biological processes

As mentioned in Chapter 3.5, single beam OFTs have been significantly under-used for biological applications and often do not go beyond proof-of-principle optical manipulation demonstrations. The OFT probe described in Chapter 8.2 was developed for precisely this purpose and is immediately applicable to a number of biological studies. To demonstrate this, the GRIN lens trapping probe was exploited in two biological studies; optically mediating the formation of an immunological synapse and observing subsequent calcium signalling activity using epi-fluorescence imaging, and, as a proof-of-concept experiment, imaging the cilia of C3H10T-1/2 cells in SR by SIM while being held optically.

8.3.1 Induction of an immunological synapse

The cell-cell interactions of cells in the immune system is a dynamic and complex process, featuring remodelling on all length scales from whole cell, to molecular distributions and as such, is an ideal target system for advanced microscopy methods. Traditional methods to observe IS formation are hindered by lack of spatio-temporal control of the sample, IS formation cannot be triggered at will and a sample of many such events must be observed from which the temporal evolution of the process is inferred

(see, for example, [230]). Studies which have attempted to increase the frequency of observed IS interactions, and therefore the likelihood of observing the full temporal evolution of such events, have included "carpet-bombing" of T-cells with antibody coated microspheres which mimic other immune cells [231] and plating T-cells directly onto antibody coated substrates such that all T-cells are sampled [232–234].

In a 2D cell culture, IS connections are formed in the $x-z$ plane rather than the lateral ($x-y$) plane and imaging of the synapse suffers due to the reduced axial resolution of most microscopes. The approach of exploiting a substrate to form the synapse aligns the IS in the lateral plane to exploit the higher lateral resolution of the microscope and also enabled super-resolution imaging of the IS by SIM [234] but does not sufficiently recapitulate the 3D *in vivo* nature of IS formation.

Optical manipulation offers excellent spatio-temporal control and can be used to trigger a specific interaction event, allowing the full temporal evolution of a single IS *in toto* [142, 143]. Additionally, optical tweezers allow further manipulation of the sample in three dimensions and can be used to orient the IS within the lateral image plane by lifting one cell on top of the other [142]. Integration of optical manipulation into an advanced microscope platform could enable combination of these techniques and facilitate super-resolution imaging of the IS in a biologically relevant environment. The OFT probe presented in Chapter 8.2 is an important step towards this goal despite only being able of 2D trapping.

The immunological synapse

An immunological synapse (IS) is the interaction between a T-cell and an antigen presenting cell (APC) and is responsible for regulation of the immune system. APCs capture antigenic peptides from their surrounding environment and process these into a format which can be read by the T-cell. The T-cell probes the APC surface membrane for peptides and interrogates them. If a peptide is determined to be pathogenic the T-cell can become cytotoxic to kill the now pathogenic APC directly or release cytokines, molecules which attract specialised pathogen-killing cells [235].

More specifically, an IS is the highly stable, highly ordered interface between the T-cell and APC. Activation of the IS occurs when the T-cell receptor (TCR) recognises an antigenic peptide presented on a major histocompatibility complex (MHC) of the APC

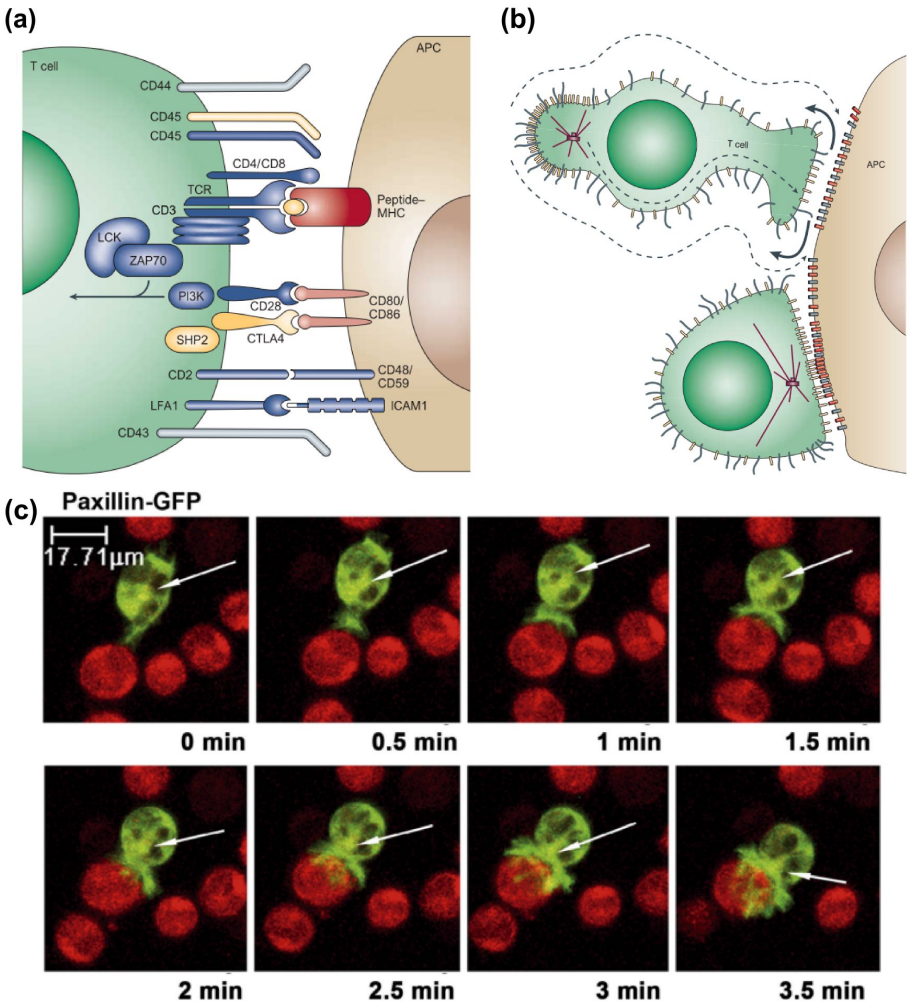

FIGURE 8.6: Overview of the structure of a mature IS and morphological changes during formation. (a) Schematic view of IS cross-section showing a selection of key signalling molecules involved in T-cell recognition. Shown are the stimulatory antigenic peptide-MHC molecule (red), co-stimulatory molecules (blue), inhibitory molecules (yellow), and non-contributing molecules (grey). The arrows indicate signal convergence leading to T-cell activation from the TCR-peptide-MHC and CD28/CD80 channels. (b) Change in T-cell morphology from before (top) and after (bottom) initial IS formation. The MTOC (purple) moves into close proximity of the IS, the contact area between the T-cell and APC increases. Membrane proteins and cell-surface molecules reorganise, TCR (yellow) and stimulatory (red) molecules are recruited to the IS while non-stimulatory (grey) are excluded. (c) Time series of confocal microscopy sequence showing cytoskeletal remodelling during IS formation between Jurkat cells overexpressing paxillin-GFP (green) and SEE-pulsed Raji APCs labelled with CMCTR cell tracker (red). Arrows show the location of the MTOC. Figures (a,b) used with permission from [235], (c) used with permission from [230].

[235]. It has been shown that activation rarely occurs solely through TCR-peptide-MHC coupling alone, due to the sparse nature of peptide-MHC complexes across the surface area of the APC and the sampling of the APC surface membrane by the T-cell, and generally requires the presence of co-stimulatory molecules which provide amplification of the TCR signal and provide sustained signalling [231]. Figure 8.6(a) shows a schematic picture of the key molecules involved in IS formation. Upon initial formation of an IS, the T-cell stops migrating and undergoes a rapid and drastic remodelling procedure to secure its connection to the APC [235]. Intracellular calcium signalling occurs almost instantly and increases rapidly, remaining stable for up to 24 hours depending of the T-cell type [235]. Global polarisation of the T-cell also occurs, with the microtubule organising centre (MTOC) relocating to be in close proximity of the IS through microtubule reorganisation (Fig. 8.6(c)), which also brings the golgi close to the APC for secretion of toxic lytic granules into the APC or cytokines into the surrounding environment [230]. Polarisation of the T-cell occurs over several to tens of minutes [235]. Figure 8.6(d) shows selected images from a timelapse confocal video microscopy sequence of remodelling of the T-cell cytoskeleton (green) during IS formation [230].

Optically mediated immunological synapse formation

Selective formation of an immunological synapse was triggered in B3Z cells, a murine hybridoma cell line, by contact with a polystyrene bead conjugated to mouse antibodies; anti-CD3, which bypasses the B3Z T-cell receptor (TCR) mechanism and directly activates the T-cell [138, 143], and anti-CD28, a co-factor which sustains synapse activity [231, 236]. Synaptic activity was detected by monitoring calcium signalling within the T-cell. B3Z cells and antibody coated beads were prepared as described in Appendix F.5.

The pre-loaded B3Z cells were then plated out into an optical-flat glass-bottom dish (WPI, FD3510-100) and 10μL of the antibody coated bead solution added. Over time, both the cells and beads adhered to the bottom surface of the dish and could not be trapped; beads adhered much more readily than cells and so the OFT probe was used to pick up cells and hold them in contact with adherent and immobilised beads. A single cell was positioned in contact with a single antibody coated bead and held during

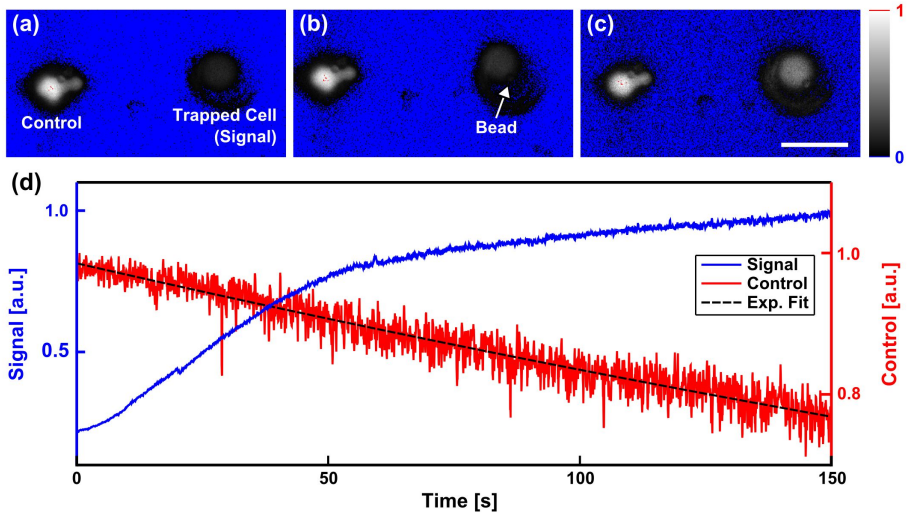

FIGURE 8.7: Calcium imaging of optically mediated immunological synapse formation. Selected movie frame (a-c) show a trapped T-cell (Signal) positioned to trigger IS formation with an antibody coated bead. Frames show the trapped cell (a) before, (b) shortly after, and (c) much after initial contact with the bead. Scale bar in (c) is $10\,\mu\text{m}$. Another cell in the field-of-view (Control) is used to correct for photobleaching. (d) Graph showing the increase in fluorescence from the trapped cell, thereby indicating IS formation. Control was fitted with an exponential curve (Exp. Fit) to confirm its decrease can be attributed to photobleaching. Figure adapted with permission from [225].

each experiment. Epi-fluorescence imaging was performed with a fluorescein isothiocyanate (FITC, green) filter set (Nikon, 49002 ET-GFP) and a 60X objective lens (Nikon, CFI 60X). Images were acquired of a single plane aligned with both the trap focus and the B3Z cells with 50ms intervals. Figures 8.7(a-c) show selected frames from a movie of IS formation. A T-cell to the right of the FOV is trapped and moved towards an antibody coated bead immobilised on the surface of the dish (Fig. 8.7(a), bead cannot be observed in this frame). Shortly after contact with the bead, the fluorescence within the trapped cell increases (Fig. 8.7(b)), and after prolonged contact the signal continues to increase (Fig. 8.7(c)). In Fig. 8.7(c) the fluorescence is so strong that the shadow of the bead is observed and the GRIN lens is partially illuminated, manifesting as a halo around the cell. Another cell, to the left of the FOV, fluoresces strongly throughout the movie which is attributed to formation of an IS with a bead which settled in close proximity to the cell several minutes before the movie was recorded. The signal from this cell was used to correct for photobleaching decay in the signal from the trapped

cell. Figure 8.7(d) shows plots of the fluorescent signal from the trapped cell (Signal) and the control cell (Control).

8.3.2 Controlling the orientation of cilia in mesenchymal stem cells

The methods by which cells signal and communicate with each other and their surroundings is an important area of study [237]. Cell signalling by mechanotransduction, signalling through force interactions, is a mechanism that is poorly understood, and yet recent studies have shown this to be a crucial process [238, 239]. In order to accurately measure this phenomena, minute forces must be precisely applied whilst intracellular signalling activity is monitored. Optical manipulation can be used to apply such precise, localised forces and SIM can provide accurate information on the morphology of cells in response to such forces with sufficient temporal resolution.

Signalling activity and differentiation in the mesenchymal stem cell (MSC) cell line, C3H10T-1/2, is believed to be triggered by mechanical stimulation of cilia [240]. The GRIN OFT probe was used to optically trap a cilium, changing its orientation relative to the cell body, and 3D-SIM was used to, very accurately, track the orientation of the cilium.

SIM excels at observing high frequency spatial information but is prone to producing artefacts in reconstructions of diffuse images with no high frequency structures. Signalling activity would be preferentially monitored by epi-fluorescence imaging, as this signal is diffuse throughout the cell, but it is not possible to acquire images in both SIM and epi-fluorescence modalities with the commercial microscope used for this study. As such, cell signalling activity was not measured, but would be crucial in developing this study further.

C3H10T-1/2 cells, provided my Mohammed Arastoo, were transfected to express Smo-yellow fluorescent protein (Smo-YFP) in cilia by Mohammed Arastoo, plated up in a glass bottom dish (WPI, FD3510-100) and allowed to adhere to the bottom surface prior to the experiment.

3D-SIM z-stacks of Smo-YFP C3H10T-1/2 cells (Fig. 8.8(a)) were acquired every 2.5 minutes (figs 8.8(b-e)) using 488nm laser illumination and green filter sets. For the first 2 volumes, the cilium is unbounded and the optical trap was turned on just before $t = 5$

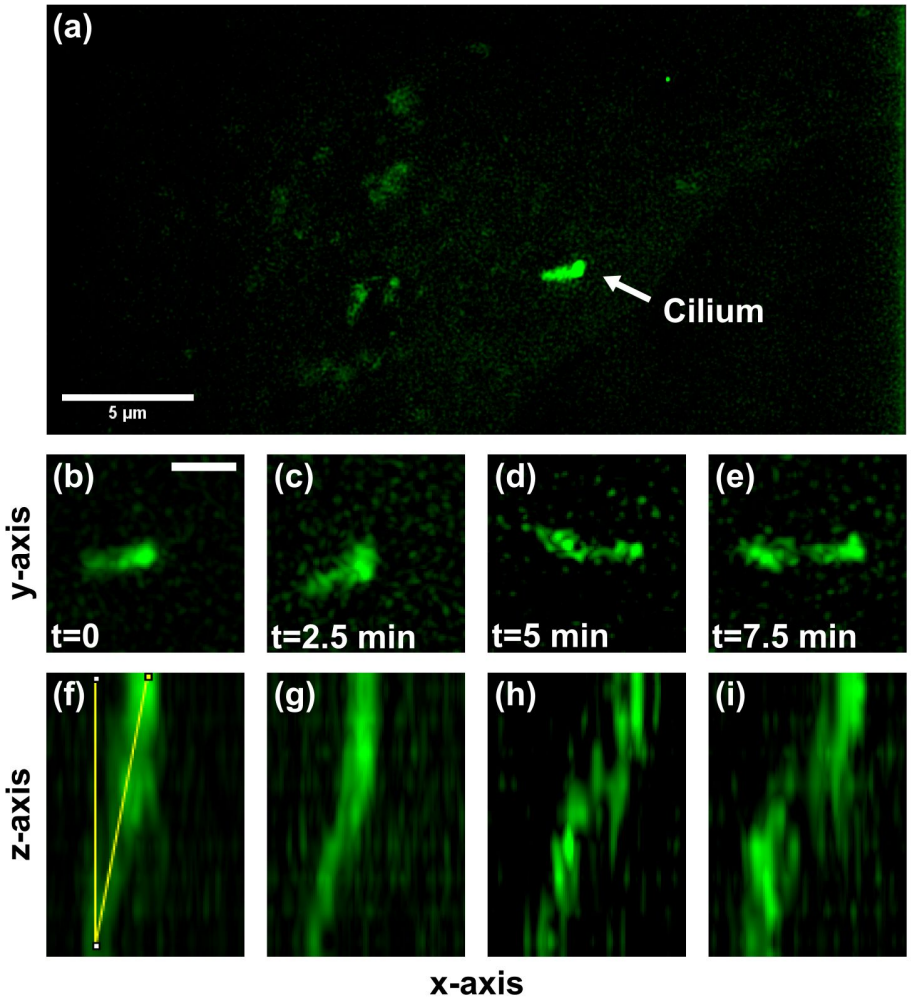

FIGURE 8.8: SIM imaging of optically manipulated cilium. (a) Maximum intensity projection of 3D-SIM z-stack of C3H10T-1/2 cell showing cilium. (b-e) Time series of enlarged region around the cilium at 2.5 minute intervals. (f-i) xz maximum intensity projections of the same time points in (b-e) respectively. The cilium is unbound at $t = 0$ and the optical trap is turned on just before $t = 5$ min. The angle of the cilium relative to the $z-$axis in the $xz-$plane was measured (as shown in (f)) for each time point. The look-up-tables in each image have been adjusted such that each image has a similar intensity range. Scale bar in (b): $1\,\mu\mathrm{m}$, applies to images (b-i).

minutes. The optical trap is focused immediately right of the cilium, which connects to the cell body at its left side. The orientation of the cilium, relative to the $z-$axis was determined from $x-z$ maximum intensity projections (Figs 8.8(f-i)). Before the trap was turned on, the angle of the cilium was $37.8°$ and $41.4°$ at $t = 0$ and $t = 2.5$ minutes respectively. After the trap was turned on the angle was $55.2°$ and $54.6°$ at $t = 5$ minutes and $t = 7.5$ minutes respectively. The increase in angle after the trap is turned on indicates the cilium is influenced by the optical trap and drawn towards it. The distribution of angles after the trap is turned on is lower than before, which is further evidence that the trap constrains the cilium and can be used to accurately manipulate this small subcellular component.

8.4 Discussion and conclusions

This chapter has demonstrated the development of an OFT probe based on a GRIN micro-objective lens which can be readily incorporated into commercial microscopy platforms. The probe is characterised through measurement of the trapping beam focal spot size and determination of the trap stiffness, k_{trap}, by the power spectral density method for 2 sizes of polystyrene bead. To aid with particle tracking for trap stiffness determination, an adaptive image filter based of PCA was implemented for removal of stochastic noise. The OFT probe is incorporated onto a commercial inverted microscope with epi-fluorescence and SIM imaging capability. Use of the OFT probe in conjunction with both these techniques is demonstrated through the controlled induction of an IS between a B3Z cell and an antibody coated polystyrene bead and by the optomechanical control of cilia in C3H10T-1/2 cells.

The GRIN lens based single-beam OFT is a remarkably simple modification which avoids the drawbacks traditionally associated with OFT probes, such as short manipulation length and low NA, through combination with a miniaturised objective lens. The measured trap beam profile gives results that are in agreement with theoretical predictions for the micro-objective lens but indicate some aberrations due to misalignment of the fibre with the GRIN lens. This issue can be avoided by careful refinement of the SMA adapter which holds the GRIN lens in place at the fibre tip. Alignment problems

may also be solved by more complex launch mechanisms to couple light into the GRIN lens, such as an adjustable SMA mount, use of a SM fibre bundle to allow selection of the best fibre position, or complex beam shaping through a MM fibre [189] and may even enable 3D trapping (tweezing). Such techniques may also allow generation of multiple simultaneous traps and trapping with non-Gaussian light modes.

Characterisation of the OFT probe yielded power dependent trap stiffness values between $0.35 - 0.63\text{pN}\,\mu\text{m}^{-1}\text{mW}^{-1}$ with $3.00\,\mu\text{m}$ and $4.17\,\mu\text{m}$ diameter polystyrene beads. Trap stiffness values reported in the literature for other OFT approaches with similar sized beads are varied, $0.035\text{pN}\,\mu\text{m}^{-1}\text{mW}^{-1}$ ($7\,\mu\text{m}$ diameter polystyrene beads) [178], $0.053\text{pN}\,\mu\text{m}^{-1}\text{mW}^{-1}$ ($2\,\mu\text{m}$ diameter polystyrene beads) [179], and $0.22\text{pN}\,\mu\text{m}^{-1}\text{mW}^{-1}$ ($2\,\mu\text{m}$ diameter polystyrene beads) [181] are some examples. The GRIN lens OFT presented in Chapter 8.2 is at the upper end of this range, improving on some designs by over an order of magnitude. Direct comparison with GRIN-MM-OFTs [180, 187, 188] could not be performed as these were characterised using the hydrodynamic-drag method which breaks the linearity of the trap and k_{trap} is no longer a valid figure of merit for these probes.

The adaptive filter based on PCA is a power tool which can be applied to trap stiffness determination and, more generally, particle tracking. The adaptive nature of the filter will adapt to changes in experimental conditions such as noise level, particle size and shape, and the particle motion. The filter greatly reduces stochastic noise but has difficulty in removing static features, a more detailed analysis of the filter performance over a wide range of imaging conditions is required to determine under what conditions such a filter is most beneficial. Although the filter is based on PCA, not all the standard steps for PCA are followed. Typically, the data is mean-centred before determination of the covariance matrix (C_{ij}, equation (E.1)) [241]. This results in the first PC being closely related to the mean (i.e. how the movie differs from a sequence of empty frames) and so multiple PCs and their corresponding eigenvalues are required to reconstruct the image before particle tracking can be performed. Reconstruction of the image reintroduces static noise contained in the mean image (first PC) whereas the relative positional information (the second and third PCs in the case of the example given in Fig. 8.4) are smooth images containing virtually no stochastic or static noise.

The second and third PCs contain all the information relevant to particle position and it may be possible to extract the position directly from the eigenvalues of these PCs rather than simply use this technique to filter the image. This would represent a great compression of data as each video frame would be reduced to two variables, relating to the x- and y-coordinates of the particle. This method could enable characterisation of multiple optical traps simultaneously as the independent motions of different particles would appear as different PCs of the same covariance matrix whereas traditional centre-of-mass techniques must be performed on images of isolated particles to ensure accuracy. Additionally, coupled motion resulting from inter-particle forces between particles in adjacent traps may manifest as higher order PCs which could be isolated from independent motions for more detailed studies.

Formation of an IS between a B3Z T-cell hybridoma and an antibody coated bead was demonstrated using the GRIN lens OFT probe and monitored by epi-fluorescence microscopy. This is, to the author's knowledge, the first demonstration of a single-beam OFT being combined with an advanced microscopy platform, and the first demonstration of a functional biological experiment performed with a single-beam OFT. Calcium imaging was performed to monitor the signalling of the T-cell and infer synapse activity although T-cell shape in Fig. 8.7(a-c) remains fairly constant and spherical which indicates no remodelling of the T-cell which would normally be expected. This was backed up by further experiments in which optical induction of ISs as described in Chapter 8.3.1 was repeated with either labelled plasma membranes (and therefore subsequently, intra-cellular vesicles), stained using a wheat germ agglutinin conjugate of Alexa Fluor 555 (Life Technologies, W32464), or microtubes, stained using Tubulin Tracker Green (Life Technologies, Oregon Green 488 taxol, bis-acetate, T35075), which both also failed to show intracellular remodelling of the T-cell. This may be due to the model system used for this experiment. B3Z cells are a hybridoma cell line which often exhibit non-physiological behaviour [235] which may explain why calcium signalling is observed without remodelling. To improve the physiological accuracy of future experiments, primary T-cells obtained from peripheral blood samples could be used [235, 242].

SIM imaging of optically trapped subcellular organelles was demonstrated by observing the optomechanical control of cilia in C3H10T-1/2 cells by the GRIN lens OFT probe. This study is a proof-of-concept demonstration, showing the potential use of OFT probes in combination with SR microscopy and is a first step towards all optical stimulation and monitoring of mechanotransduction in MSCs. This experiment is hampered by several factors. The desired signal readout will be calcium monitoring which is ill-suited for SIM. As epi-fluorescence and SIM modalities cannot be combined within the same experimental sequence with the apparatus used in this study, validation and quantification of the movement of cilia by the optical trap will have to be performed by SIM before acquiring epi-fluorescence images of calcium levels while "blindly" manipulating the cilium. This sequential study would necessitate the experiment to be repeated many times to develop robust statistics. Additionally, the imaging suffers from low SNR and rapid photobleaching, which limits repetition of the experiment of the same cell, as observed by the increasing noise as the time series progresses (Figs 8.8(b-i) and the presence of reconstruction artefacts at later time points. This originates from the use of YFP for labelling cilia, as it has a relatively low excitation cross-section for the excitation lasers available to the SIM and its emission does not match well with the SIM emission filters either. These issues make experimental repeatability a challenge, and it is still to be confirmed if the trap does influence the cilia. This observed behaviour could be due to natural motion. Thermal effects may also play a role, although it could be expected that heating caused by laser irradiation would increase thermal motion and therefore increase the variance in cilium angle whereas the opposite is observed, which is indicative of optical trapping. Identifying a more suitable fluorescent tag for cilia is vital for continuation of this study, enabling long term monitoring of cilium position and increasing the accuracy and quantity of measurements.

The lack of multiple simultaneous traps also limits the biological studies that can be performed. Even the addition of a second trap would enable cell stretching experiments. To realise this, a system that combines miniatured optics with more traditional beam steering methods should be utilised. A dual-trap system, based on the design by

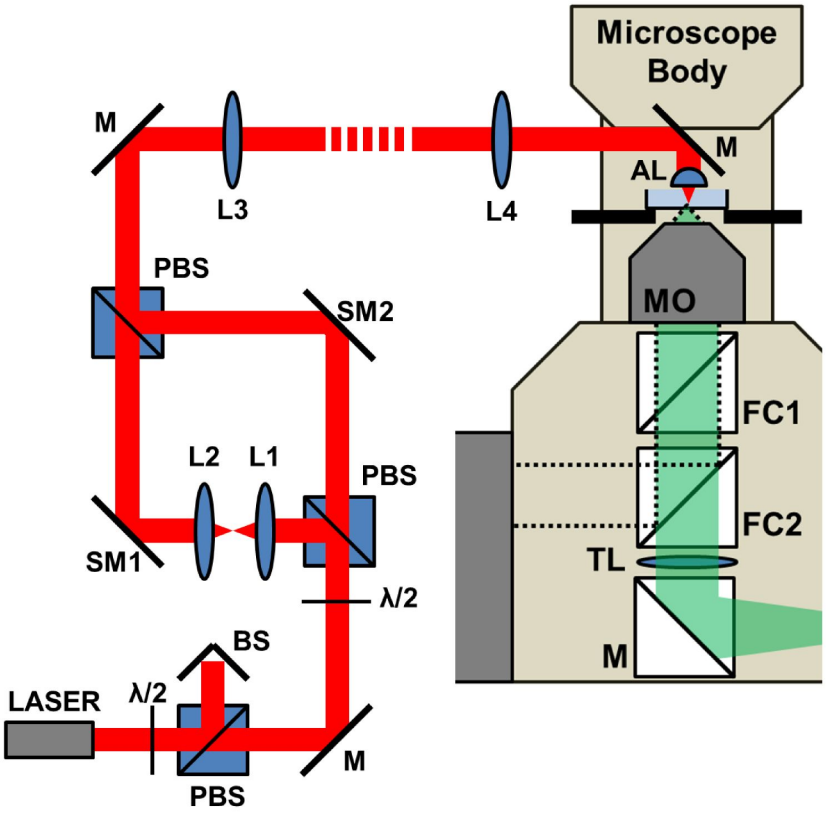

FIGURE 8.9: Schematic of aspheric lens based dual-optical trap system. $\lambda/2$: Half-waveplate; PBS: Polarising beam splitter; BS: Beam stop; M: Mirror; Lx: Lens; SMx: Steering mirror; AL: Aspheric lens; MO: Microscope objective; FCx: Filter cube; TL: Tube lens.

Fällman and Axner [162], was designed with a compact aspheric lens (AMS technologies, 355330B-00-MT) measuring 6.33mm in diameter, with an effective focal length of 3.1mm, and NA of 0.77. The system, currently under construction, is shown in Fig. 8.9.

A collimated laser beam (IPG Lasers YLR-10-1064-LP-SF, 1070nm, 10W) is passed through a half-waveplate and polarising beam splitter (PBS) allowing control over the beam power. The beam is then split by another PBS with the split ratio determined by the input polarisation which is controlled by a second half-waveplate. Each beam is reflected from a steering mirror (SMx) before being recombined and the beams are directed into the sample through an aspheric lens. Each steering mirror is conjugate to the back focal plane of the aspheric lens, enabling precise movement of each trap within the sample. Additionally, a 1:1 telescope (L1 and L2) in one beam path allows axial translation of one trap by adjusting the axial position of L1. This trap design provides two

optical traps which can be independently positioned in the lateral microscope plane and can be arbitrarily positioned relative to each other in 3D. Motorised control of SM1, SM2, or both would enable use of the system for quantitative cell stretching studies.

Chapter summary

- An OFT probe based on a GRIN micro-objective lens has been presented and characterised.
- The OFT probe enables 2D trapping with a long manipulation length ($200\,\mu\mathrm{m}$) and has a trap stiffness measured between $0.35 - 0.63\mathrm{pN}\,\mu\mathrm{m}^{-1}\mathrm{mW}^{-1}$.
- A PCA image filter was used to extract particle motion from low contrast images of trapped microspheres.
- The OFT probe was integrated into a commercial SIM microscope and used to perform fluorescence and SIM studies observing IS formation and manipulation of cilia.

8.5 Chapter acknowledgements

The GRIN microlens based OFT probe was designed by Anisha Kubasik-Thayil and constructed by the author with Claire A. Mitchell. Data for characterisation of the OFT probe was acquired by the author with Claire A. Mitchell and processed by Martin V. G. Kristensen. The PCA image filtering method was developed by Michael Mazilu and Martin V. G. Kristensen and validated by the author. IS induction experiments were performed by the author with Claire A. Mitchell and Elaine C. Campbell, B3Z cells for this study were gifted by Prof. Nilabh Shastri (University of California, Berkeley, CA) and prepared for imaging by the author with Elaine C. Campbell. Experiments on cilliated C3H10T-1/2 cells were performed by the author with Mohammed Arastoo and Samantha J. Pitt, C3H10T-1/2 cells for this study were prepared by Mohammed Arastoo, the author performed all analysis for this study.

Chapter 9

Conclusions and future work

9.1 Summary

This Thesis has demonstrated several cases where optical beam shaping and optical manipulation can be applied to enhance biomedical microscopy techniques. The key novel aspects that have been addressed in this Thesis are:

- Theoretical, analytic, and experimental description of Airy beams for light-sheet illumination to yield high axial resolution over an large field-of-view (Chapter 4).
- Analysis of the effect of light-sheet beam type on image quality within highly turbid tissues (Chapter 5).
- Demonstration of Airy light-sheet generation with controlled aberrations from simple optical elements to realise an ultra low-cost Airy light-sheet microscope (Chapter 6.2).
- Theoretical and analytical description of attenuation-compensated Airy beams for use in light-sheet microscopy to increase illumination uniformity across the field-of-view, increase imaging depth, and recover high axial resolution (Chapter 6.3).
- Use of structured illumination microscopy for the visualisation of sub-cellular features relevant for the diagnosis of nephrotic disease (Chapter 7).
- Development and characterisation of a GRIN lens based fibre optical trap and application to biomedical studies (Chapter 8).

This Thesis began with the question: What are the roles of optical techniques in modern microscopy? Optical techniques offer relatively high spatiotemporal resolution, can be applied *in vivo*, and can be minimally toxic, making it the technique of choice for the imaging of living specimens. Beam shaping has been shown to extend the possibilities of optical microscopy and can be used to tailor a microscopy technique for a given task. Chapter 2 discussed a range of optical techniques for volumetric imaging of large specimens and for super-resolution imaging, weighing the advantages, disadvantages, and limitations of each technique before selecting one optimal technique for each task. Light-sheet microscopy was selected as the technique for further investigation for large volumetric imaging due to its high contrast, rapid acquisition speed, and low phototoxicity, and structured illumination was selected as the most suitable super-resolution method for live imaging due to its high temporal resolution. Chapter 3 introduced optical manipulation as a sterile and accurate method for controlling biological forces at the cellular level. Optical manipulation is identified as a technique that can add functionality in microscopy as the user can interact with, rather than simply observe, the sample.

Chapter 4 focused on a detailed theoretical, analytical, and experimental description of the use of Airy beams for light-sheet illumination. Beam shaping has been used previously to enhance light-sheet microscopy and the Airy light-sheet microscopy technique is compared against other state-of-the-art implementations. The Airy light-sheet gives a much more favourable trade-off between axial resolution and observable field-of-view than Gaussian and Bessel beam based light-sheet microscopy. Although advanced Bessel beam light-sheet techniques can recover comparably high axial resolution over an equally large field-of-view, this is achieved with low collection efficiencies and increased irradiation of sample which may cause additional photodamage. In contrast, the Airy light-sheet microscope achieves high collection efficiencies and maintains low sample irradiance. Experimental demonstration of the Airy light-sheet microscope achieves axial resolution of approximately $1 - 1.5\,\mu\mathrm{m}$ over a half-field-of-view of over $150\,\mu\mathrm{m}$, over 15 times greater than a Gaussian light-sheet microscope of equivalent axial resolution. A study of photobleaching rates with different light-sheet types confirms the low phototoxicity of the Airy light-sheet microscope.

The Airy light-sheet microscope is further characterised in Chapter 5 which focused on quantifying image quality at depth within turbid tissue and making comparison between images acquired using Gaussian and Airy light-sheet microscopy. Brain tissue sections from mice were imaged prior to, and after, clearing with a TDE solution. A novel image quality metric was developed based on Fourier analysis of images acquired at different depths within the tissue and showed that Airy illumination yielded a depth-dependent enhancement with a gradient of $0.04\,\mu\mathrm{m}^{-1}$, increasing with greater depth into the tissue. This enhancement was shown to be dependent on the aberrations of the sample, yielding a stronger enhancement with stronger aberrations. The maximum imaging depth with Airy light-sheet microscopy was also shown to be greater than with Gaussian light-sheet microscopy by approximately 50%.

Chapter 6 investigated advanced beam shaping strategies to compliment the Airy light-sheet microscopy method. Control of optical aberrations from tilting a cylindrical lens was demonstrated to realise a compact, low-cost, and portable Airy light-sheet microscope with similar performance as the system developed in Chapter 4. This low cost system achieves an axial resolution of approximately $1.9\,\mu\mathrm{m}$ over a field-of-view of $120\,\mu\mathrm{m}$, at least 6 times greater than the equivalent Gaussian light-sheet microscope. Use of attenuation-compensating Airy beams is also investigated through theory and simulations. It is shown that attenuation-compensated Airy light-sheets could penetrate approximately $100\,\mu\mathrm{m}$ deeper into absorbing tissue whilst retaining the performance of their non-compensated counterparts in free-space. Initial studies show that attenuation-compensated Airy light-sheets may be particularly useful for multi-photon excitation light-sheet microscopy in absorbing tissue, and for selective imaging of specific regions-of-interest in photosensitive samples.

The focus shifted from volumetric imaging techniques to super-resolution imaging in Chapter 7, which investigated the use of structured illumination microscopy for the visualisation of sub-cellular structures relevant to the diagnosis of nephrotic disease. The ultrastructure of podocyte foot processes from healthy patients was imaged by structured illumination microscopy and features correlated with current diagnostic electron microscopy images. Comparison of healthy and diseased (minimal change

disease and membranous nephropathy) tissues revealed ultrastructural changes consistent with the current understanding of these diseases and supported the use of structured illumination for the diagnosis of nephrotic disease. Structured illumination microscopy is a relatively fast and low cost technique compared to electron microscopy and the associated potential time and financial savings are discussed.

Chapter 8 explored how integration of optical manipulation can be beneficial, and add depth to studies, in advanced biomedical microscopy. The first part of this Chapter focused on the development of a compact and flexible optical fibre trap based on a GRIN micro-objective lens and its characterisation. The optical fibre trap is characterised by the power spectral density method, using an image filter based on principal component analysis to increase the signal-to-noise ratio. Power dependent trap stiffness values were measured between $0.35-0.63$pN μm^{-1}mW^{-1}, consistent with the upper end of values reported for optical fibre traps in the literature. The optical fibre trap was then integrated into a commercial structured illumination microscope and use of the probe in biomedical studies was demonstrated by proof-of-concept studies; inducing immunosynaptic connections between B3Z cells and antibody coated polystyrene microspheres and optomechanical control of cilia in C3H10T-1/2 cells.

9.2 Future work

The work detailed in this Thesis demonstrates steps towards the realisation of powerful optical microscopy techniques adopted in the biomedical sciences. A number of interesting directions exist for further study. Short term goals, as have been discussed in each Chapter, are summarised below and longer term future directions are discussed.

Chapter 4: Light-sheet microscopy using an Airy beam

- Investigation of other optimal pupil functions, including non-integer asymmetric polynomial phase functions, for light-sheet microscopy.
- Incorporation of extended depth-of-focus techniques in the detection pathway to enable ultra-wide field-of-view or ultra-high resolution Airy light-sheet microscopy.

Chapter 5: Application of Airy light-sheet microscopy to imaging in turbid tissue

- Repeat studies using oil immersion optics.
- Investigate the complex non-linear behaviour of the enhancement factor over large depth ranges.

Chapter 6: Advanced beam shaping strategies for Airy light-sheet microscopy

- Experimental investigation of attenuation-compensated Airy light-sheets in absorbing media.

Chapter 7: Structured illumination microscopy for diagnosis of nephrotic disease

- Repeat study using a larger number of patients and disease types.
- Development of a compact, low cost, and portable structured illumination microscope to increase accessibility of the technique by pathologists and other end-users.

Chapter 8: Integrated optical trapping and microscopy

- Further development and characterisation of an aspheric lens based optical trap/tweezers system for integration into advanced microscopy platforms.

In the longer-term, there are many directions future work may take.

Investigations into light-sheet microscopy may continue to refine the Airy light-sheet concept, integrating additional advanced beam shaping techniques such as attenuation-compensation for realising greater imaging depth and image uniformity, or structured illumination to increase the resolution of the technique. An interesting avenue for further exploration would be the development of a system where the image plane is purposely deformed, introducing a controlled curvature that can be tuned to match the curvature of the Airy light-sheet. The idea of using imperfect optics and disordered media to improve imaging techniques is one that is gaining interest [23, 194, 201, 243] and will feature in future innovation in microscopy.

Although the Airy beam has been demonstrated as a relatively optimal beam type for light-sheet illumination, further study is required to prove this definitively or to

find an even better beam type. Airy light-sheet microscopy necessitates the use of deconvolution to recover a high resolution image, other beam types could avoid this post-processing step or combination with different acquisition or processing methods may lead to new imaging techniques. Development of new imaging techniques inherently involves a trade-off between imaging parameters, spatiaotemporal resolution, field-of-view, phototoxicity, and many techniques can optimise one or a few of these at the cost of others. The Airy light-sheet microscope has a very favourable trade-off and achieves good performance in all parameters mentioned above. The use of new beam types for light-sheet illumination should seek to further improve the cost of the trade-off globally.

Innovation in super-resolution techniques could take the form of finding new applications for existing techniques. All super-resolution microscopy techniques are relatively new and have only recently been commercialised. Biomedical end users may be reluctant to invest in such techniques until they have been proven to have a practical benefit over other techniques. Use of structured illumination for disease diagnosis (as has been shown in Chapter 7 for nephrotic disease and by Westmoreland *et al* for blood disorders [244]) demonstrates the practicality of the method. This practicality must be further demonstrated in studies with larger sample sizes and in a number of different fields to encourage wide adoption of the technique.

The spatial resolution of structured illumination microscopy may be improved by use of non-linearities in photo-switchable fluorophores. The stability and brightness of such fluorophores with improvements in camera technology have made non-linear structured illumination a viable technique for live imaging. Separately, Fourier ptychographic algorithms have been demonstrate which can fundamentally increase the temporal resolution of structured illumination. Such techniques are complimentary and warrant investigation.

Optical manipulation in microscopy has shown to be greatly beneficial for a number of studies [138–144], but the complexity of systems combining advanced microscopy and advanced optical manipulation techniques can be daunting to many end users wishing to replicate the technique. Fibre base optical manipulation greatly simplifies

the design of an optical manipulation system and can be easily incorporated into existing microscopy platforms. Future work in this area will investigate compact and fibre based optical manipulation that can achieve three-dimensional trapping, simultaneous trapping of multiple objects, and trapping with non-Gaussian beams. These systems will rely on miniaturised optics and careful design of systematic aberrations.

Perhaps the direction with the most potential for impact, is the combination of light-sheet microscopy, structured illumination, and optical manipulation. Each of these techniques have been studied in relative isolation in this Thesis, but are complimentary to each other and further work will investigate integration of various techniques for superior imaging techniques. Light-sheet microscopy has been combined with structured illumination to achieve higher resolution, optical sectioning ability, lower phototoxicity, and faster imaging than each technique can achieve alone [20, 59, 76, 78, 102]. Light-sheet microscopy and optical manipulation has also been combined for control and imaging of specimens in a more natural environment [165]. The combination of structured illumination microscopy and optical manipulation has been touched upon in this Thesis (Chapter 8).

9.3 Concluding remarks

This Thesis has addressed the use of beam shaping in microscopy for several applications, targeting volumetric microscopy, super-resolution microscopy, and combination of microscopy with optical manipulation. All techniques discussed have the potential to be used for long-term imaging of biological specimens. In moving forward, all imaging techniques must address the challenges of live imaging and not overlook phototoxicity as a parameter of microscope design. Beam shaping has played a central role in all of the techniques discussed, and will continue to be pivotal in future advancements and pushing back the limits of microscopy and, in general, photonics.

Bibliography

[1] Shu, X., Lev-Ram, V., Deerinck, T. J., Qi, Y., Ramko, E. B., Davidson, M. W., Jin, Y., Ellisman, M. H., and Tsien, R. Y. "A genetically encoded tag for correlated light and electron microscopy of intact cells, tissues, and organisms." In: *PLoS biology* 9.4 (Apr. 2011), e1001041. DOI: 10.1371/journal.pbio.1001041.

[2] Martell, J. D., Deerinck, T. J., Sancak, Y., Poulos, T. L., Mootha, V. K., Sosinsky, G. E., Ellisman, M. H., and Ting, A. Y. "Engineered ascorbate peroxidase as a genetically encoded reporter for electron microscopy." In: *Nature biotechnology* 30.11 (Nov. 2012), pp. 1143–8. DOI: 10.1038/nbt.2375.

[3] Tsien, R. Y. "New Molecular Tools for Light and Electron Microscopy". In: *Microscopy and Microanalysis* 21.S2 (Aug. 2015), pp. 40–41. DOI: 10.1017/S1431927615014567.

[4] Hübner, W., McNerney, G. P., Chen, P., Dale, B. M., Gordon, R. E., Chuang, F. Y. S., Li, X.-D., Asmuth, D. M., Huser, T., and Chen, B. K. "Quantitative 3D video microscopy of HIV transfer across T cell virological synapses." In: *Science (New York, N.Y.)* 323.5922 (Mar. 2009), pp. 1743–7. DOI: 10.1126/science.1167525.

[5] Gao, L., Shao, L., Higgins, C. D., Poulton, J. S., Peifer, M., Davidson, M. W., Wu, X. F., Goldstein, B., and Betzig, E. "Noninvasive Imaging beyond the Diffraction Limit of 3D Dynamics in Thickly Fluorescent Specimens". In: *Cell* 151.6 (2012), pp. 1370–1385. DOI: DOI10.1016/j.cell.2012.10.008.

[6] Ahrens, M. B., Orger, M. B., Robson, D. N., Li, J. M., and Keller, P. J. "Whole-brain functional imaging at cellular resolution using light-sheet microscopy." In: *Nature methods* 10.5 (May 2013), pp. 413–20. DOI: 10.1038/nmeth.2434.

[7] Prevedel, R., Yoon, Y.-G., Hoffmann, M., Pak, N., Wetzstein, G., Kato, S., Schrödel, T., Raskar, R., Zimmer, M., Boyden, E. S., and Vaziri, A. "Simultaneous whole-animal 3D imaging of neuronal activity using light-field microscopy." In: *Nature methods* 11.7 (July 2014), pp. 727–30. DOI: 10.1038/nmeth.2964.

[8] Hecht, E. "Modern Optics: Lasers and Other Topics". In: *Optics*. 4th Edition. Addison Wesly, 2002. Chap. 13, pp. 581–648.

[9] Heintzmann, R. and Ficz, G. "Breaking the resolution limit in light microscopy." In: *Briefings in functional genomics & proteomics* 5.4 (Dec. 2006), pp. 289–301. DOI: 10.1093/bfgp/ell036.

[10] Inoué, S. "Foundations of Confocal Scanned Imaging in Light Microscopy". In: *Handbook of Biological Confocal Microscopy*. 3rd Edition. Springer Science & Business Media, 2010. Chap. 1, pp. 1–19.

[11] Hecht, E. "Diffraction". In: *Optics*. 4th Edition. Addison Wesley, 2002. Chap. 10, pp. 443–518.

[12] Campagnola, P. "Second harmonic generation imaging microscopy: applications to diseases diagnostics." In: *Analytical chemistry* 83.9 (May 2011), pp. 3224–31. DOI: 10.1021/ac1032325.

[13] Theodossiou, T. A., Thrasivoulou, C., Ekwobi, C., and Becker, D. L. "Second harmonic generation confocal microscopy of collagen type I from rat tendon cryosections." In: *Biophysical journal* 91.12 (Dec. 2006), pp. 4665–77. DOI: 10.1529/biophysj.106.093740.

[14] Débarre, D., Supatto, W., Pena, A.-M., Fabre, A., Tordjmann, T., Combettes, L., Schanne-Klein, M.-C., and Beaurepaire, E. "Imaging lipid bodies in cells and tissues using third-harmonic generation microscopy." In: *Nature methods* 3.1 (Jan. 2006), pp. 47–53. DOI: 10.1038/nmeth813.

[15] Denk, W., Strickler, J. H., and Webb, W. W. "2-Photon Laser Scanning Fluorescence Microscopy". In: *Science* 248.4951 (1990), pp. 73–76. DOI: DOI10.1126/science.2321027.

[16] Denk, W. "Two-photon excitation in functional biological imaging." In: *Journal of biomedical optics* 1.3 (July 1996), pp. 296–304. DOI: 10.1117/12.242945.

[17] Peti-Peterdi, J. "Independent two-photon measurements of albumin GSC give low values." In: *American journal of physiology. Renal physiology* 296.6 (June 2009), F1255–7. DOI: 10.1152/ajprenal.00144.2009.

[18] Vettenburg, T., Dalgarno, H. I. C., Nylk, J., Coll-Lladó, C., Ferrier, D. E. K., Cizmár, T., Gunn-Moore, F. J., and Dholakia, K. "Light-sheet microscopy using an Airy beam." In: *Nature methods* 11.5 (2014), pp. 541–4.

[19] Fahrbach, F. O. and Rohrbach, A. "A line scanned light-sheet microscope with phase shaped self-reconstructing beams". In: *Optics Express* 18.23 (2010), pp. 24229–24244.

[20] Planchon, T. A., Gao, L., Milkie, D. E., Davidson, M. W., Galbraith, J. A., Galbraith, C. G., and Betzig, E. "Rapid three-dimensional isotropic imaging of living cells using Bessel beam plane illumination". In: *Nature Methods* 8.5 (2011), pp. 417–423. DOI: Doi10.1038/Nmeth.1586.

[21] Blatter, C., Grajciar, B., Eigenwillig, C. M., Wieser, W., Biedermann, B. R., Huber, R., and Leitgeb, R. A. "Extended focus high-speed swept source OCT with self-reconstructive illumination." In: *Optics express* 19.13 (June 2011), pp. 12141–55. DOI: 10.1364/OE.19.012141.

[22] Hell, S. W. and Wichmann, J. "Breaking the Diffraction Resolution Limit by Stimulated-Emission - Stimulated-Emission-Depletion Fluorescence Microscopy". In: *Optics Letters* 19.11 (1994), pp. 780–782. DOI: Doi10.1364/Ol.19.000780.

[23] Cizmár, T. and Dholakia, K. "Exploiting multimode waveguides for pure fibre-based imaging." In: *Nature communications* 3 (Jan. 2012), p. 1027. DOI: 10.1038/ncomms2024.

[24] Svelto, O. "Ray and Wave Propagation through Optical Media". In: *Principles of Lasers*. 4th Edition. Plenum Press, 1998. Chap. 4, pp. 129–160.

[25] Durnin, J. "Exact solutions for nondiffracting beams. I. The scalar theory". In: *Journal of the Optical Society of America A* 4.4 (Apr. 1987), p. 651. DOI: 10.1364/JOSAA.4.000651.

[26] McGloin, D. and Dholakia, K. "Bessel beams : diffraction in a new light". In: *Contemporary Physics* 46, 1 (2005), pp. 15–28. DOI: 10.1080/00107510420002752 59.

[27] Siviloglou, G. A., Broky, J., Dogariu, A., and Christodoulides, D. N. "Observation of Accelerating Airy Beams". In: *Physical Review Letters* 99.21 (Nov. 2007), p. 213901. DOI: 10.1103/PhysRevLett.99.213901.

[28] Siviloglou, G. A. and Christodoulides, D. N. "Accelerating finite energy Airy beams". In: *Optics Letters* 32.8 (Mar. 2007), p. 979. DOI: 10.1364/OL.32.000979.

[29] Baumgartl, J., Mazilu, M., and Dholakia, K. "Optically mediated particle clearing using Airy wavepackets". In: *Nature Photonics* 2.11 (Sept. 2008), pp. 675–678. DOI: 10.1038/nphoton.2008.201.

[30] Tsien, R. Y. "The green fluorescent protein." In: *Annual review of biochemistry* 67 (Jan. 1998), pp. 509–44. DOI: 10.1146/annurev.biochem.67.1.509.

[31] Stepanenko, O. V., Verkhusha, V. V., Kuznetsova, I. M., Uversky, V. N., and Turoverov, K. K. "Fluorescent proteins as biomarkers and biosensors: throwing color lights on molecular and cellular processes." In: *Current protein & peptide science* 9.4 (Aug. 2008), pp. 338–69.

[32] Gustafsson, M. G. L., Shao, L., Carlton, P. M., Wang, C. J. R., Golubovskaya, I. N., Cande, W. Z., Agard, D. A., and Sedat, J. W. "Three-dimensional resolution doubling in wide-field fluorescence microscopy by structured illumination". In: *Biophysical Journal* 94.12 (2008), pp. 4957–4970. DOI: DOI10.1529/biophysj.107.120345.

[33] Goodman, J. W. *Introduction to Fourier Optics*. 3rd Editio. Roberts & Company Publishers, 2005.

[34] Huisken, J. and Stainier, D. Y. R. "Selective plane illumination microscopy techniques in developmental biology". In: *Development* 136.12 (2009), pp. 1963–1975. DOI: Doi10.1242/Dev.022426.

[35] Hewlett, S. J. and Wilson, T. "Resolution enhancement in three-dimensional confocal microscopy". In: *Machine Vision and Applications* 4.4 (Sept. 1991), pp. 233–242. DOI: 10.1007/BF01815300.

[36] Toomre, D. and Pawley, James, B. "Disk-scanning Confocal Microscopy". In: *Handbook of Biological Confocal Microscopy*. 3rd Edition. Springer Science & Business Media, 2010. Chap. 10, pp. 221–237.

[37] Ruzin, S. and Aaron, H. "http://microscopy.berkeley.edu/courses/tlm/2P/index.html". In: (last accessed: 15/06/2016).

[38] Huisken, J., Swoger, J., Del Bene, F., Wittbrodt, J., and Stelzer, E. H. K. "Optical sectioning deep inside live embryos by selective plane illumination microscopy." In: *Science (New York, N.Y.)* 305.5686 (Aug. 2004), pp. 1007–9. DOI: 10.1126/science.1100035.

[39] Santi, P. A. "Light sheet fluorescence microscopy: a review." In: *The journal of histochemistry and cytochemistry : official journal of the Histochemistry Society* 59.2 (Feb. 2011), pp. 129–38. DOI: 10.1369/0022155410394857.

[40] Keller, P. J., Schmidt, A. D., Wittbrodt, J., and Stelzer, E. H. K. "Reconstruction of Zebrafish Early Embryonic Development by Scanned Light Sheet Microscopy". In: *Science* 322.5904 (2008), pp. 1065–1069. DOI: DOI10.1126/science.1162493.

[41] Huisken, J. and Stainier, D. Y. R. "Even fluorescence excitation by multidirectional selective plane illumination microscopy (mSPIM)". In: *Optics Letters* 32.17 (Sept. 2007), p. 2608. DOI: 10.1364/OL.32.002608.

[42] Stelzer, E. H. and Lindek, S. "Fundamental reduction of the observation volume in far-field light microscopy by detection orthogonal to the illumination axis: confocal theta microscopy". In: *Optics Communications* 111.5-6 (Oct. 1994), pp. 536–547. DOI: 10.1016/0030-4018(94)90533-9.

[43] Wu, Y., Wawrzusin, P., Senseney, J., Fischer, R. S., Christensen, R., Santella, A., York, A. G., Winter, P. W., Waterman, C. M., Bao, Z., Colón-Ramos, D. A., McAuliffe, M., and Shroff, H. "Spatially isotropic four-dimensional imaging

with dual-view plane illumination microscopy." In: *Nature biotechnology* 31.11 (Nov. 2013), pp. 1032–8. DOI: 10.1038/nbt.2713.

[44] Kumar, A., Wu, Y., Christensen, R., Chandris, P., Gandler, W., McCreedy, E., Bokinsky, A., Colón-Ramos, D. A., Bao, Z., McAuliffe, M., Rondeau, G., and Shroff, H. "Dual-view plane illumination microscopy for rapid and spatially isotropic imaging." In: *Nature protocols* 9.11 (Nov. 2014), pp. 2555–73. DOI: 10.1038/nprot.2014.172.

[45] Schmid, B., Shah, G., Scherf, N., Weber, M., Thierbach, K., Campos, C. P., Roeder, I., Aanstad, P., and Huisken, J. "High-speed panoramic light-sheet microscopy reveals global endodermal cell dynamics." In: *Nature communications* 4 (Jan. 2013), p. 2207. DOI: 10.1038/ncomms3207.

[46] Chen, B.-C., Legant, W. R., Wang, K., Shao, L., Milkie, D. E., Davidson, M. W., Janetopoulos, C., Wu, X. S., Hammer, J. A., Liu, Z., English, B. P., Mimori-Kiyosue, Y., Romero, D. P., Ritter, A. T., Lippincott-Schwartz, J., Fritz-Laylin, L., Mullins, R. D., Mitchell, D. M., Bembenek, J. N., Reymann, A.-C., Bohme, R., Grill, S. W., Wang, J. T., Seydoux, G., Tulu, U. S., Kiehart, D. P., and Betzig, E. "Lattice light-sheet microscopy: Imaging molecules to embryos at high spatiotemporal resolution". In: *Science* 346.6208 (Oct. 2014), pp. 1257998–1257998. DOI: 10.1126/science.1257998.

[47] Zanacchi, F. C., Lavagnino, Z., Donnorso, M. P., Del Bue, A., Furia, L., Faretta, M., and Diaspro, A. "Live-cell 3D super-resolution imaging in thick biological samples". In: *Nature Methods* 8.12 (2011), pp. 1047–+. DOI: Doi10.1038/Nmeth.1744.

[48] Zanacchi, F. C., Lavagnino, Z., Faretta, M., Furia, L., and Diaspro, A. "Light-sheet confined super-resolution using two-photon photoactivation." In: *PloS one* 8.7 (Jan. 2013), e67667. DOI: 10.1371/journal.pone.0067667.

[49] Swoger, J., Muzzopappa, M., Lopez-Schier, H., and Sharpe, J. "4D retrospective lineage tracing using SPIM for zebrafish organogenesis studies". In: *Journal of Biophotonics* 4.1-2 (2011), pp. 122–134. DOI: DOI10.1002/jbio.201000087.

[50] Levoy, M., Ng, R., Adams, A., Footer, M., and Horowitz, M. "Light field microscopy". In: *ACM SIGGRAPH 2006 Papers on - SIGGRAPH '06*. Vol. 25. 3. New York, New York, USA: ACM Press, July 2006, p. 924. DOI: 10.1145/1179352.1141976.

[51] Okoshi, T. *Three Dimensional Imaging Techniques*. New York: Academic Press, 1976.

[52] Levoy, M., Zhang, Z., and McDowall, I. "Recording and controlling the 4D light field in a microscope using microlens arrays." In: *Journal of microscopy* 235.2 (Aug. 2009), pp. 144–62. DOI: 10.1111/j.1365-2818.2009.03195.x.

[53] Lin, X., Wu, J., Zheng, G., and Dai, Q. "Camera array based light field microscopy." In: *Biomedical optics express* 6.9 (Sept. 2015), pp. 3179–89. DOI: 10.1364/BOE.6.003179.

[54] Jemielita, M., Taormina, M. J., Delaurier, A., Kimmel, C. B., and Parthasarathy, R. "Comparing phototoxicity during the development of a zebrafish craniofacial bone using confocal and light sheet fluorescence microscopy techniques." In: *Journal of biophotonics* 6.11-12 (Dec. 2013), pp. 920–8. DOI: 10.1002/jbio.201200144.

[55] Reynaud, E. G., Krzic, U., Greger, K., and Stelzer, E. H. K. "Light sheet-based fluorescence microscopy: more dimensions, more photons, and less photodamage." In: *HFSP journal* 2.5 (Oct. 2008), pp. 266–75. DOI: 10.2976/1.2974980.

[56] Medeiros, G. de, Norlin, N., Gunther, S., Albert, M., Panavaite, L., Fiuza, U.-M., Peri, F., Hiiragi, T., Krzic, U., and Hufnagel, L. "Confocal multiview light-sheet microscopy." In: *Nature communications* 6 (Jan. 2015), p. 8881. DOI: 10.1038/ncomms9881.

[57] Fahrbach, F. O., Voigt, F. F., Schmid, B., Helmchen, F., and Huisken, J. "Rapid 3D light-sheet microscopy with a tunable lens." In: *Optics express* 21.18 (Sept. 2013), pp. 21010–26. DOI: 10.1364/OE.21.021010.

[58] Olarte, O. E., Andilla, J., Artigas, D., and Loza-Alvarez, P. "Decoupled illumination detection in light sheet microscopy for fast volumetric imaging". In: *Optica* 2.8 (Aug. 2015), p. 702. DOI: 10.1364/OPTICA.2.000702.

[59] Zhao, M., Zhang, H., Li, Y., Ashok, A., Liang, R., Zhou, W., and Peng, L. "Cellular imaging of deep organ using two-photon Bessel light-sheet nonlinear structured illumination microscopy." In: *Biomedical optics express* 5.5 (May 2014), pp. 1296–308. DOI: 10.1364/BOE.5.001296.

[60] Fahrbach, F. O. and Rohrbach, A. "Propagation stability of self-reconstructing Bessel beams enables contrast-enhanced imaging in thick media". In: *Nature Communications* 3 (2012). DOI: Artn632Doi10.1038/Ncomms1646.

[61] Silvestri, L., Bria, A., Sacconi, L., Iannello, G., and Pavone, F. S. "Confocal light sheet microscopy: micron-scale neuroanatomy of the entire mouse brain". In: *Optics Express* 20.18 (2012), pp. 20582–20598.

[62] Krzic, U., Gunther, S., Saunders, T. E., Streichan, S. J., and Hufnagel, L. "Multiview light-sheet microscope for rapid in toto imaging." In: *Nature methods* 9.7 (July 2012), pp. 730–3. DOI: 10.1038/nmeth.2064.

[63] Preibisch, S., Amat, F., Stamataki, E., Sarov, M., Singer, R. H., Myers, E., and Tomancak, P. "Efficient Bayesian-based multiview deconvolution." In: *Nature methods* 11.6 (June 2014), pp. 645–8. DOI: 10.1038/nmeth.2929.

[64] Tomer, R., Khairy, K., Amat, F., and Keller, P. J. "Quantitative high-speed imaging of entire developing embryos with simultaneous multiview light-sheet microscopy". In: *Nature Methods* 9.7 (2012), 755–U181. DOI: Doi10.1038/Nmeth.2062.

[65] Preibisch, S., Saalfeld, S., Schindelin, J., and Tomancak, P. "Software for bead-based registration of selective plane illumination microscopy data." In: *Nature methods* 7.6 (June 2010), pp. 418–9. DOI: 10.1038/nmeth0610-418.

[66] Barman, I., Tan, K. M., and Singh, G. P. "Optical sectioning using single-plane-illumination Raman imaging". In: *Journal of Raman Spectroscopy* 41.10 (2010), pp. 1099–1101. DOI: Doi10.1002/Jrs.2785.

[67] Jahr, W., Schmid, B., Schmied, C., Fahrbach, F. O., and Huisken, J. "Hyperspectral light sheet microscopy." In: *Nature communications* 6 (Jan. 2015), p. 7990. DOI: 10.1038/ncomms8990.

[68] Rocha-Mendoza, I., Licea-Rodriguez, J., Marro, M., Olarte, O. E., Plata-Sanchez, M., and Loza-Alvarez, P. "Rapid spontaneous Raman light sheet microscopy using cw-lasers and tunable filters." In: *Biomedical optics express* 6.9 (Sept. 2015), pp. 3449–61. DOI: 10.1364/BOE.6.003449.

[69] Bouchard, M. B., Voleti, V., Mendes, C. S., Lacefield, C., Grueber, W. B., Mann, R. S., Bruno, R. M., and Hillman, E. M. C. "Swept confocally-aligned planar excitation (SCAPE) microscopy for high speed volumetric imaging of behaving organisms." In: *Nature photonics* 9.2 (Feb. 2015), pp. 113–119. DOI: 10.1038/nphoton.2014.323.

[70] Tokunaga, M., Imamoto, N., and Sakata-Sogawa, K. "Highly inclined thin illumination enables clear single-molecule imaging in cells." In: *Nature methods* 5.2 (Feb. 2008), pp. 159–61. DOI: 10.1038/nmeth1171.

[71] Dunsby, C. "Optically sectioned imaging by oblique plane microscopy". In: *Optics Express* 16.25 (Nov. 2008), p. 20306. DOI: 10.1364/OE.16.020306.

[72] Dalgarno, H. I. C., Cizmár, T., Vettenburg, T., Nylk, J., Gunn-Moore, F. J., and Dholakia, K. "Wavefront corrected light sheet microscopy in turbid media". In: *Applied Physics Letters* 100.19 (2012).

[73] Bourgenot, C., Saunter, C. D., Taylor, J. M., Girkin, J. M., and Love, G. D. "3D adaptive optics in a light sheet microscope." In: *Optics express* 20.12 (June 2012), pp. 13252–61. DOI: 10.1364/OE.20.013252.

[74] Neil, M. A. A., Jukaitis, R., and Wilson, T. "Method of obtaining optical sectioning by using structured light in a conventional microscope". In: *Optics Letters* 22.24 (1997), pp. 1905–1907. DOI: Doi10.1364/Ol.22.001905.

[75] Lei, M. and Zumbusch, A. "Structured light sheet fluorescence microscopy based on four beam interference". In: *Optics Express* 18.18 (2010), pp. 19232–19241.

[76] Breuninger, T., Greger, K., and Stelzer, E. H. K. "Lateral modulation boosts image quality in single plane illumination fluorescence microscopy". In: *Optics Letters* 32.13 (June 2007), p. 1938. DOI: 10.1364/OL.32.001938.

[77] Mertz, J. and Kim, J. "Scanning light-sheet microscopy in the whole mouse brain with HiLo background rejection." In: *Journal of biomedical optics* 15.1 (Jan. 2010), p. 016027. DOI: 10.1117/1.3324890.

[78] Mertz, J. "Optical sectioning microscopy with planar or structured illumination." In: *Nature methods* 8.10 (Jan. 2011), pp. 811–9. DOI: 10.1038/nmeth.1709.

[79] Schröter, T. J., Johnson, S. B., John, K., and Santi, P. A. "Scanning thin-sheet laser imaging microscopy (sTSLIM) with structured illumination and HiLo background rejection." In: *Biomedical optics express* 3.1 (Jan. 2012), pp. 170–7. DOI: 10.1364/BOE.3.000170.

[80] Friedrich, M., Gan, Q., Ermolayev, V., and Harms, G. S. "STED-SPIM: Stimulated Emission Depletion Improves Sheet Illumination Microscopy Resolution". In: *Biophysical Journal* 100.8 (Apr. 2011), pp. L43–L45. DOI: 10.1016/j.bpj.2010.12.3748.

[81] Scheul, T., Wang, I., and Vial, J.-C. "STED-SPIM made simple." In: *Optics express* 22.25 (Dec. 2014), pp. 30852–64. DOI: 10.1364/OE.22.030852.

[82] Hell, S. W. "Far-field optical nanoscopy." In: *Science (New York, N.Y.)* 316.5828 (May 2007), pp. 1153–8. DOI: 10.1126/science.1137395.

[83] Zhang, P., Goodwin, P. M., and Werner, J. H. "Fast, super resolution imaging via Bessel-beam stimulated emission depletion microscopy." In: *Optics express* 22.10 (May 2014), pp. 12398–409. DOI: 10.1364/OE.22.012398.

[84] Thaning, A., Jaroszewicz, Z., and Friberg, A. T. "Diffractive axicons in oblique illumination: analysis and experiments and comparison with elliptical axicons". In: *Applied Optics* 42.1 (Jan. 2003), p. 9. DOI: 10.1364/AO.42.000009.

[85] Bin, Z. and Zhu, L. "Diffraction property of an axicon in oblique illumination". In: *Applied Optics* 37.13 (May 1998), p. 2563. DOI: 10.1364/AO.37.002563.

[86] Tanaka, T. and Yamamoto, S. "Comparison of aberration between axicon and lens". In: *Optics Communications* 184.1-4 (Oct. 2000), pp. 113–118. DOI: 10.1016/S0030-4018(00)00963-9.

[87] Olarte, O. E., Licea-Rodriguez, J., Palero, J. A., Gualda, E. J., Artigas, D., Mayer, J., Swoger, J., Sharpe, J., Rocha-Mendoza, I., Rangel-Rojo, R., and Loza-Alvarez, P. "Image formation by linear and nonlinear digital scanned light-sheet fluorescence microscopy with Gaussian and Bessel beam profiles." In: *Biomedical optics express* 3.7 (July 2012), pp. 1492–505. DOI: 10.1364/BOE.3.001492.

[88] Fahrbach, F. O., Gurchenkov, V., Alessandri, K., Nassoy, P., and Rohrbach, A. "Light-sheet microscopy in thick media using scanned Bessel beams and two-photon fluorescence excitation." In: *Optics express* 21.11 (June 2013), pp. 13824–39. DOI: 10.1364/OE.21.013824.

[89] Gao, L., Zhu, L., Li, C., and Wang, L. V. "Nonlinear light-sheet fluorescence microscopy by photobleaching imprinting." In: *Journal of the Royal Society, Interface / the Royal Society* 11.93 (Apr. 2014), p. 20130851. DOI: 10.1098/rsif.2013.0851.

[90] Bewersdorf, J., Egner, A., and Hell, S. W. "4Pi Microscopy". In: *Handbook of Biological Confocal Microscopy*. 3rd Edition. Springer Science & Business Media, 2010. Chap. 30, pp. 561–570.

[91] Gugel, H., Bewersdorf, J., Jakobs, S., Engelhardt, J., Storz, R., and Hell, S. W. "Cooperative 4Pi excitation and detection yields sevenfold sharper optical sections in live-cell microscopy". In: *Biophysical Journal* 87.6 (Dec. 2004), pp. 4146–4152. DOI: 10.1529/biophysj.104.045815.

[92] Willig, K. I., Harke, B., Medda, R., and Hell, S. W. "STED microscopy with continuous wave beams". In: *Nature Methods* 4.11 (2007), pp. 915–918. DOI: Doi10.1038/Nmeth1108.

[93] Osseforth, C., Moffitt, J. R., Schermelleh, L., and Michaelis, J. "Simultaneous dual-color 3D STED microscopy." In: *Optics express* 22.6 (Mar. 2014), pp. 7028–39. DOI: 10.1364/OE.22.007028.

[94] Arlt, J. and Padgett, M. J. "Generation of a beam with a dark focus surrounded by regions of higher intensity: the optical bottle beam". In: *Optics Letters* 25.4 (Feb. 2000), p. 191. DOI: 10.1364/OL.25.000191.

[95] Wildanger, D., Patton, B. R., Schill, H., Marseglia, L., Hadden, J. P., Knauer, S., Schönle, A., Rarity, J. G., O'Brien, J. L., Hell, S. W., and Smith, J. M. "Solid immersion facilitates fluorescence microscopy with nanometer resolution and sub-ångström emitter localization." In: *Advanced materials (Deerfield Beach, Fla.)* 24.44 (Nov. 2012), OP309–13. DOI: 10.1002/adma.201203033.

[96] Wildanger, D., Rittweger, E., Kastrup, L., and Hell, S. W. "STED microscopy with a supercontinuum laser source". In: *Optics Express* 16.13 (2008), pp. 9614–9621. DOI: Doi10.1364/Oe.16.009614.

[97] Chmyrov, A., Keller, J., Grotjohann, T., Ratz, M., D'Este, E., Jakobs, S., Eggeling, C., and Hell, S. W. "Nanoscopy with more than 100,000 'doughnuts'." In: *Nature methods* 10.8 (Aug. 2013), pp. 737–40. DOI: 10.1038/nmeth.2556.

[98] Bergermann, F., Alber, L., Sahl, S. J., Engelhardt, J., and Hell, S. W. "2000-fold parallelized dual-color STED fluorescence nanoscopy." In: *Optics express* 23.1 (Jan. 2015), pp. 211–23. DOI: 10.1364/OE.23.000211.

[99] Gustafsson, M. G. L. "Surpassing the lateral resolution limit by a factor of two using structured illumination microscopy". In: *Journal of Microscopy-Oxford* 198 (2000), pp. 82–87. DOI: DOI10.1046/j.1365-2818.2000.00710.x.

[100] Gustafsson, M. G. L. "Nonlinear structured-illumination microscopy: Wide-field fluorescence imaging with theoretically unlimited resolution". In: *Proceedings of the National Academy of Sciences of the United States of America* 102.37 (2005), pp. 13081–13086. DOI: DOI10.1073/pnas.0406877102.

[101] Heintzmann, R., Jovin, T. M., and Cremer, C. "Saturated patterned excitation microscopy: a concept for optical resolution improvement". In: *Journal of the Optical Society of America A* 19.8 (Aug. 2002), p. 1599. DOI: 10.1364/JOSAA.19.001599.

[102] Li, D., Shao, L., Chen, B.-C., Zhang, X., Zhang, M., Moses, B., Milkie, D. E., Beach, J. R., Hammer, J. A., Pasham, M., Kirchhausen, T., Baird, M. A., Davidson, M. W., Xu, P., and Betzig, E. "Extended-resolution structured illumination imaging of endocytic and cytoskeletal dynamics". In: *Science* 349.6251 (Aug. 2015), aab3500–aab3500. DOI: 10.1126/science.aab3500.

[103] Hirvonen, L., Mandula, O., Wicker, K., and Heintzmann, R. "Structured illumination microscopy using photoswitchable fluorescent proteins". In: *Three-Dimensional and Multidimensional Microscopy: Image Acquisition and Processing Xv* 6861 (2008), pp. L8610–L8610. DOI: Doi10.1117/12.763021.

[104] Rego, E. H., Shao, L., Macklin, J. J., Winoto, L., Johansson, G. A., Kamps-Hughes, N., Davidson, M. W., and Gustafsson, M. G. L. "Nonlinear structured-illumination microscopy with a photoswitchable protein reveals cellular structures at 50-nm resolution." In: *Proceedings of the National Academy of Sciences of the United States of America* 109.3 (Jan. 2012), E135–43. DOI: 10.1073/pnas.1107547108.

[105] Betzig, E., Patterson, G. H., Sougrat, R., Lindwasser, O. W., Olenych, S., Bonifacino, J. S., Davidson, M. W., Lippincott-Schwartz, J., and Hess, H. F. "Imaging intracellular fluorescent proteins at nanometer resolution." In: *Science (New York, N.Y.)* 313.5793 (Sept. 2006), pp. 1642–5. DOI: 10.1126/science.1127344.

[106] Churchman, L. S., Okten, Z., Rock, R. S., Dawson, J. F., and Spudich, J. A. "Single molecule high-resolution colocalization of Cy3 and Cy5 attached to macromolecules measures intramolecular distances through time." In: *Proceedings of the National Academy of Sciences of the United States of America* 102.5 (Feb. 2005), pp. 1419–23. DOI: 10.1073/pnas.0409487102.

[107] Lidke, K. A., Rieger, B., Jovin, T. M., and Heintzmann, R. "Superresolution by localization of quantum dots using blinking statistics". In: *Optics Express* 13.18 (Sept. 2005), p. 7052. DOI: 10.1364/OPEX.13.007052.

[108] Patterson, G. H. and Lippincott-Schwartz, J. "A photoactivatable GFP for selective photolabeling of proteins and cells." In: *Science (New York, N.Y.)* 297.5588 (Sept. 2002), pp. 1873–7. DOI: 10.1126/science.1074952.

[109] Ando, R., Hama, H., Yamamoto-Hino, M., Mizuno, H., and Miyawaki, A. "An optical marker based on the UV-induced green-to-red photoconversion of a fluorescent protein". In: *Proceedings of the National Academy of Sciences* 99.20 (Sept. 2002), pp. 12651–12656. DOI: 10.1073/pnas.202320599.

[110] Hess, S. T., Girirajan, T. P. K., and Mason, M. D. "Ultra-high resolution imaging by fluorescence photoactivation localization microscopy." In: *Biophysical journal* 91.11 (Dec. 2006), pp. 4258–72. DOI: 10.1529/biophysj.106.091116.

[111] Bates, M., Blosser, T. R., and Zhuang, X. "Short-range spectroscopic ruler based on a single-molecule optical switch." In: *Physical review letters* 94.10 (Mar. 2005), p. 108101. DOI: 10.1103/PhysRevLett.94.108101.

[112] Rust, M. J., Bates, M., and Zhuang, X. W. "Sub-diffraction-limit imaging by stochastic optical reconstruction microscopy (STORM)". In: *Nature Methods* 3.10 (2006), pp. 793–795. DOI: Doi10.1038/Nmeth929.

[113] Olivier, N., Keller, D., Rajan, V. S., Gönczy, P., and Manley, S. "Simple buffers for 3D STORM microscopy." In: *Biomedical optics express* 4.6 (June 2013), pp. 885–99. DOI: 10.1364/BOE.4.000885.

[114] Pohl, D. W., Denk, W., and Lanz, M. "Optical stethoscopy: Image recording with resolution $\lambda/20$". In: *Applied Physics Letters* 44.7 (Apr. 1984), p. 651. DOI: 10.1063/1.94865.

[115] Betzig, E., Lewis, A., Harootunian, A., Isaacson, M., and Kratschmer, E. "Near Field Scanning Optical Microscopy (NSOM): Development and Biophysical Applications." In: *Biophysical journal* 49.1 (Jan. 1986), pp. 269–79. DOI: 10.1016/S0006-3495(86)83640-2.

[116] Lewis, A., Isaacson, M., Harootunian, A., and Muray, A. "Development of a 500 Å spatial resolution light microscope". In: *Ultramicroscopy* 13.3 (Jan. 1984), pp. 227–231. DOI: 10.1016/0304-3991(84)90201-8.

[117] Oshikane, Y., Kataoka, T., Okuda, M., Hara, S., Inoue, H., and Nakano, M. "Observation of nanostructure by scanning near-field optical microscope with small sphere probe". In: *Science and Technology of Advanced Materials* 8.3 (Apr. 2007), pp. 181–185. DOI: 10.1016/j.stam.2007.02.013.

[118] Hofmann, M., Eggeling, C., Jakobs, S., and Hell, S. W. "Breaking the diffraction barrier in fluorescence microscopy at low light intensities by using reversibly photoswitchable proteins". In: *Proceedings of the National Academy of Sciences of*

the United States of America 102.49 (2005), pp. 17565–17569. DOI: DOI10.1073/pnas.0506010102.

[119] Rust, M. J., Bates, M., and Zhuang, X. "Sub-diffraction-limit imaging by stochastic optical reconstruction microscopy (STORM)." In: *Nature methods* 3.10 (Oct. 2006), pp. 793–5. DOI: 10.1038/nmeth929.

[120] Huang, B., Wang, W., Bates, M., and Zhuang, X. "Three-dimensional super-resolution imaging by stochastic optical reconstruction microscopy." In: *Science (New York, N.Y.)* 319.5864 (Feb. 2008), pp. 810–3. DOI: 10.1126/science.1153529.

[121] Fernández-Suárez, M. and Ting, A. Y. "Fluorescent probes for super-resolution imaging in living cells." In: *Nature reviews. Molecular cell biology* 9.12 (Dec. 2008), pp. 929–43. DOI: 10.1038/nrm2531.

[122] Patterson, G. H. and Piston, D. W. "Photobleaching in Two-Photon Excitation Microscopy". In: *Biophysical Journal* 78.4 (Apr. 2000), pp. 2159–2162. DOI: 10.1016/S0006-3495(00)76762-2.

[123] Wolf, S., Supatto, W., Debrégeas, G., Mahou, P., Kruglik, S. G., Sintes, J.-M., Beaurepaire, E., and Candelier, R. "Whole-brain functional imaging with two-photon light-sheet microscopy." In: *Nature methods* 12.5 (May 2015), pp. 379–80. DOI: 10.1038/nmeth.3371.

[124] Dholakia, K., Reece, P., and Gu, M. "Optical micromanipulation." In: *Chemical Society reviews* 37.1 (Jan. 2008), pp. 42–55. DOI: 10.1039/b512471a.

[125] Nichols, E. F. and Hull, G. F. "A Preliminary Communication on the Pressure of Heat and Light Radiation". In: *Physical Review (Series I)* 13.5 (Nov. 1901), pp. 307–320. DOI: 10.1103/PhysRevSeriesI.13.307.

[126] Nichols, E. F. and Hull, G. F. "The Pressure Due to Radiation. (Second Paper.)" In: *Physical Review (Series I)* 17.1 (July 1903), pp. 26–50. DOI: 10.1103/PhysRevSeriesI.17.26.

[127] Beth, R. A. "Mechanical Detection and Measurement of the Angular Momentum of Light". In: *Physical Review* 50.2 (July 1936), pp. 115–125. DOI: 10.1103/PhysRev.50.115.

[128] Ashkin, A. "Acceleration and Trapping of Particles by Radiation Pressure". In: *Physical Review Letters* 24.4 (1970), pp. 156–&. DOI: DOI10 . 1103 / PhysRevLett.24.156.

[129] Ashkin, A., Dziedzic, J. M., Bjorkholm, J. E., and Chu, S. "Observation of a single-beam gradient force optical trap for dielectric particles". In: *Optics Letters* 11.5 (May 1986), p. 288. DOI: 10.1364/OL.11.000288.

[130] Visscher, K., Gross, S., and Block, S. "Construction of multiple-beam optical traps with nanometer-resolution position sensing". In: *IEEE Journal of Selected Topics in Quantum Electronics* 2.4 (1996), pp. 1066–1076. DOI: 10.1109/2944.577338.

[131] Sasaki, K., Koshioka, M., Misawa, H., Kitamura, N., and Masuhara, H. "Laser-Scanning Micromanipulation and Spatial Patterning of Fine Particles". In: *Japanese Journal of Applied Physics* 30.Part 2, No. 5B (May 1991), pp. L907–L909. DOI: 10.1143/JJAP.30.L907.

[132] Chowdhury, A., Ackerson, B. J., and Clark, N. A. "Laser-Induced Freezing". In: *Physical Review Letters* 55.8 (Aug. 1985), pp. 833–836. DOI: 10 . 1103 / PhysRevLett.55.833.

[133] Curtis, J. E., Koss, B. A., and Grier, D. G. "Dynamic holographic optical tweezers". In: *Optics Communications* 207.1-6 (June 2002), pp. 169–175. DOI: 10.1016/S0030-4018(02)01524-9.

[134] McLeod, J. H. "The Axicon: A New Type of Optical Element". In: *Journal of the Optical Society of America* 44.8 (Aug. 1954), p. 592. DOI: 10.1364/JOSA.44.000592.

[135] Allen, L., Beijersbergen, M. W., Spreeuw, R. J. C., and Woerdman, J. P. "Orbital angular momentum of light and the transformation of Laguerre-Gaussian laser modes". In: *Physical Review A* 45.11 (June 1992), pp. 8185–8189. DOI: 10.1103/PhysRevA.45.8185.

[136] He, H., Friese, M., Heckenberg, N., and Rubinsztein-Dunlop, H. "Direct observation of transfer of angular momentum to absorptive particles from a

laser beam with a phase singularity." In: *Physical review letters* 75.5 (July 1995), pp. 826–829.

[137] Cizmár, T., Garcés-Chávez, V., Dholakia, K., and Zemánek, P. "Optical conveyor belt for delivery of submicron objects". In: *Applied Physics Letters* 86.17 (Apr. 2005), p. 174101. DOI: 10.1063/1.1915543.

[138] Tam, J. M., Castro, C. E., Heath, R. J. W., Cardenas, M. L., Xavier, R. J., Lang, M. J., and Vyas, J. M. "Control and Manipulation of Pathogens with an Optical Trap for Live Cell Imaging of Intercellular Interactions". In: *PLoS ONE* 5.12 (Dec. 2010). Ed. by Poh, L. N. F., e15215. DOI: 10.1371/journal.pone.0015215.

[139] Kress, H., Stelzer, E. H. K., Griffiths, G., and Rohrbach, A. "Control of relative radiation pressure in optical traps: Application to phagocytic membrane binding studies". In: *Physical Review E* 71.6 (June 2005), p. 061927. DOI: 10.1103/PhysRevE.71.061927.

[140] Kress, H., Stelzer, E. H. K., Holzer, D., Buss, F., Griffiths, G., and Rohrbach, A. "Filopodia act as phagocytic tentacles and pull with discrete steps and a load-dependent velocity." In: *Proceedings of the National Academy of Sciences of the United States of America* 104.28 (July 2007), pp. 11633–8. DOI: 10.1073/pnas.0702449104.

[141] McNerney, G. P., Hübner, W., Chen, B. K., and Huser, T. "Manipulating CD4+ T cells by optical tweezers for the initiation of cell-cell transfer of HIV-1." In: *Journal of biophotonics* 3.4 (Apr. 2010), pp. 216–23. DOI: 10.1002/jbio.200900102.

[142] Oddos, S., Dunsby, C., Purbhoo, M. A., Chauveau, A., Owen, D. M., Neil, M. A. A., Davis, D. M., and French, P. M. W. "High-speed high-resolution imaging of intercellular immune synapses using optical tweezers." In: *Biophysical journal* 95.10 (Nov. 2008), pp. L66–8. DOI: 10.1529/biophysj.108.143198.

[143] Wei, X., Tromberg, B. J., and Cahalan, M. D. "Mapping the sensitivity of T cells with an optical trap: polarity and minimal number of receptors for Ca(2+) signaling." In: *Proceedings of the National Academy of Sciences of the United States of America* 96.15 (July 1999), pp. 8471–6.

[144] Mirsaidov, U., Scrimgeour, J., Timp, W., Beck, K., Mir, M., Matsudaira, P., and Timp, G. "Live cell lithography: using optical tweezers to create synthetic tissue." In: *Lab on a chip* 8.12 (Dec. 2008), pp. 2174–81. DOI: 10.1039/b807987k.

[145] Neuman, K. C. and Nagy, A. "Single-molecule force spectroscopy: optical tweezers, magnetic tweezers and atomic force microscopy." In: *Nature methods* 5.6 (June 2008), pp. 491–505. DOI: 10.1038/nmeth.1218.

[146] Ranjit, G., Atherton, D. P., Stutz, J. H., Cunningham, M., and Geraci, A. A. "Attonewton force detection using microspheres in a dual-beam optical trap in high vacuum". In: *Physical Review A* 91.5 (May 2015), p. 051805. DOI: 10.1103/PhysRevA.91.051805.

[147] Block, S. M., Goldstein, L. S., and Schnapp, B. J. "Bead movement by single kinesin molecules studied with optical tweezers." In: *Nature* 348.6299 (Nov. 1990), pp. 348–52. DOI: 10.1038/348348a0.

[148] Svoboda, K. and Block, S. M. "Biological applications of optical forces." In: *Annual review of biophysics and biomolecular structure* 23 (Jan. 1994), pp. 247–85. DOI: 10.1146/annurev.bb.23.060194.001335.

[149] Gennerich, A., Carter, A. P., Reck-Peterson, S. L., and Vale, R. D. "Force-induced bidirectional stepping of cytoplasmic dynein." In: *Cell* 131.5 (Nov. 2007), pp. 952–65. DOI: 10.1016/j.cell.2007.10.016.

[150] Kerssemakers, J. W. J., Munteanu, E. L., Laan, L., Noetzel, T. L., Janson, M. E., and Dogterom, M. "Assembly dynamics of microtubules at molecular resolution." In: *Nature* 442.7103 (Aug. 2006), pp. 709–12. DOI: 10.1038/nature04928.

[151] Footer, M. J., Kerssemakers, J. W. J., Theriot, J. A., and Dogterom, M. "Direct measurement of force generation by actin filament polymerization using an optical trap." In: *Proceedings of the National Academy of Sciences of the United States of America* 104.7 (Feb. 2007), pp. 2181–6. DOI: 10.1073/pnas.0607052104.

[152] Ashkin, A. "Forces of a single-beam gradient laser trap on a dielectric sphere in the ray optics regime." In: *Biophysical journal* 61.2 (Feb. 1992), pp. 569–82. DOI: 10.1016/S0006-3495(92)81860-X.

[153] Hulst, H. C. van de. *Light Scattering by Small Particles*. New York: Dover Press, 1981.

[154] Gahagan, K. T. and Swartzlander, G. A. "Trapping of low-index microparticles in an optical vortex". In: *Journal of the Optical Society of America B* 15.2 (Feb. 1998), p. 524. DOI: 10.1364/JOSAB.15.000524.

[155] Gahagan, K. T. and Swartzlander, Jr., G. A. "Simultaneous trapping of low-index and high-index microparticles observed with an optical-vortex trap". In: *Journal of the Optical Society of America B* 16.4 (Apr. 1999), p. 533. DOI: 10.1364/JOSAB.16.000533.

[156] Berg-Sørensen, K. and Flyvbjerg, H. "Power spectrum analysis for optical tweezers". In: *Review of Scientific Instruments* 75.3 (Feb. 2004), p. 594. DOI: 10.1063/1.1645654.

[157] Perkins, T. "Optical traps for single molecule biophysics: a primer". In: *Laser & Photonics Review* 3.1-2 (Feb. 2009), pp. 203–220. DOI: 10.1002/lpor.200810014.

[158] Wong, W. P. and Halvorsen, K. "The effect of integration time on fluctuation measurements: calibrating an optical trap in the presence of motion blur". In: *Optics Express* 14.25 (Dec. 2006), p. 12517. DOI: 10.1364/OE.14.012517.

[159] Press, W. H., Teukolsky, S. A., Vetterling, W. T., and Flannery, B. P. *Numerical Recipies in C, The Art of Scientific Computing*. 2nd Editio. New York: Cambridge University Press, 1992.

[160] Seol, Y., Carpenter, A. E., and Perkins, T. T. "Gold nanoparticles: enhanced optical trapping and sensitivity coupled with significant heating". In: *Optics Letters* 31.16 (July 2006), p. 2429. DOI: 10.1364/OL.31.002429.

[161] Hoffmann, A., Meyer zu Hörste, G., Pilarczyk, G., Monajembashi, S., Uhl, V., and Greulich, K. "Optical tweezers for confocal microscopy". In: *Applied Physics B* 71.5 (Apr. 2000), pp. 747–753. DOI: 10.1007/s003400000454.

[162] Fällman, E. and Axner, O. "Design for fully steerable dual-trap optical tweezers". In: *Applied Optics* 36.10 (Apr. 1997), p. 2107. DOI: 10.1364/AO.36.002107.

[163] Goksör, M., Enger, J., and Hanstorp, D. "Optical Manipulation in Combination with Multiphoton Microscopy for Single-Cell Studies". In: *Applied Optics* 43.25 (Sept. 2004), p. 4831. DOI: 10.1364/AO.43.004831.

[164] Heller, I., Sitters, G., Broekmans, O. D., Farge, G., Menges, C., Wende, W., Hell, S. W., Peterman, E. J. G., and Wuite, G. J. L. "STED nanoscopy combined with optical tweezers reveals protein dynamics on densely covered DNA." In: *Nature methods* 10.9 (Sept. 2013), pp. 910–6. DOI: 10.1038/nmeth.2599.

[165] Yang, Z., Piksarv, P., Ferrier, D. E., Gunn-Moore, F. J., and Dholakia, K. "Macro-optical trapping for sample confinement in light sheet microscopy". In: *Biomedical Optics Express* 6.8 (July 2015), p. 2778. DOI: 10.1364/BOE.6.002778.

[166] Thalhammer, G., Steiger, R., Bernet, S., and Ritsch-Marte, M. "Optical macro-tweezers : trapping of highly motile micro-organisms". In: *Journal of Optics* 13, Numb 4 (2011), p. 44024.

[167] Zwick, S., Haist, T., Miyamoto, Y., He, L., Warber, M., Hermerschmidt, A., and Osten, W. "Holographic twin traps". In: *Journal of Optics a-Pure and Applied Optics* 11.3 (2009). DOI: Artn034011Doi10.1088/1464-4258/11/3/034011.

[168] Liesener, J., Reicherter, M., Haist, T., and Tiziani, H. "Multi-functional optical tweezers using computer-generated holograms". In: *Optics Communications* 185.1-3 (Nov. 2000), pp. 77–82. DOI: 10.1016/S0030-4018(00)00990-1.

[169] Spesyvtsev, R., Rendall, H. A., and Dholakia, K. "Wide-field three-dimensional optical imaging using temporal focusing for holographically trapped microparticles". In: *Optics Letters* 40.21 (Oct. 2015), p. 4847. DOI: 10.1364/OL.40.004847.

[170] Yevnin, M., Kasimov, D., Gluckman, Y., Ebenstein, Y., and Roichman, Y. "Independent and simultaneous three-dimensional optical trapping and imaging." In: *Biomedical optics express* 4.10 (Jan. 2013), pp. 2087–94. DOI: 10.1364/BOE.4.002087.

[171] Constable, A., Kim, J., Mervis, J., Zarinetchi, F., and Prentiss, M. "Demonstration of a Fiberoptic Light-Force Trap". In: *Optics Letters* 18.21 (1993), pp. 1867–1869. DOI: Doi10.1364/Ol.18.001867.

[172] Guck, J., Ananthakrishnan, R., Mahmood, H., Moon, T. J., Cunningham, C. C., and Käs, J. "The optical stretcher: a novel laser tool to micromanipulate cells." In: *Biophysical journal* 81.2 (Aug. 2001), pp. 767–84. DOI: 10.1016/S0006-3495(01)75740-2.

[173] Black, B. J. and Mohanty, S. K. "Fiber-optic spanner". In: *Optics Letters* 37.24 (Dec. 2012), p. 5030. DOI: 10.1364/OL.37.005030.

[174] Kolb, T., Albert, S., Haug, M., and Whyte, G. "Dynamically reconfigurable fibre optical spanner". In: *Lab Chip* 14.6 (Mar. 2014), pp. 1186–1190. DOI: 10.1039/C3LC51277K.

[175] Liu, Z., Guo, C., Yang, J., and Yuan, L. "Tapered fiber optical tweezers for microscopic particle trapping: fabrication and application". In: *Optics Express* 14.25 (Dec. 2006), p. 12510. DOI: 10.1364/OE.14.012510.

[176] Liu, Y. and Yu, M. "Investigation of inclined dual-fiber optical tweezers for 3D manipulation and force sensing". In: *Optics Express* 17.16 (July 2009), p. 13624. DOI: 10.1364/OE.17.013624.

[177] Berthelot, J., Aimovi, S. S., Juan, M. L., Kreuzer, M. P., Renger, J., and Quidant, R. "Three-dimensional manipulation with scanning near-field optical nanotweezers." In: *Nature nanotechnology* 9.4 (Apr. 2014), pp. 295–9. DOI: 10.1038/nnano.2014.24.

[178] Liberale, C., Cojoc, G., Bragheri, F., Minzioni, P., Perozziello, G., La Rocca, R., Ferrara, L., Rajamanickam, V., Di Fabrizio, E., and Cristiani, I. "Integrated microfluidic device for single-cell trapping and spectroscopy". In: *Scientific Reports* 3 (Feb. 2013), p. 1258. DOI: 10.1038/srep01258.

[179] Mohanty, S. K., Mohanty, K. S., and Berns, M. W. "Organization of microscale objects using a microfabricated optical fiber". In: *Optics Letters* 33.18 (Sept. 2008), p. 2155. DOI: 10.1364/OL.33.002155.

[180] Gong, Y., Zhang, C., Liu, Q.-F., Wu, Y., Wu, H., Rao, Y., and Peng, G.-D. "Optofluidic tunable manipulation of microparticles by integrating graded-index fiber taper with a microcavity". In: *Optics Express* 23.3 (Feb. 2015), p. 3762. DOI: 10.1364/OE.23.003762.

[181] Mohanty, S. K., Mohanty, K. S., and Berns, M. W. "Manipulation of mammalian cells using a single-fiber optical microbeam." In: *Journal of biomedical optics* 13.5 (Jan. 2008), p. 054049. DOI: 10.1117/1.2983663.

[182] Mohanty, K. S., Liberale, C., Mohanty, S. K., and Degiorgio, V. "In depth fiber optic trapping of low-index microscopic objects". In: *Applied Physics Letters* 92.15 (Apr. 2008), p. 151113. DOI: 10.1063/1.2908216.

[183] Liberale, C., Minzioni, P., Bragheri, F., De Angelis, F., Di Fabrizio, E., and Cristiani, I. "Miniaturized all-fibre probe for three-dimensional optical trapping and manipulation". In: *Nature Photonics* 1.12 (Nov. 2007), pp. 723–727. DOI: 10.1038/nphoton.2007.230.

[184] Bragheri, F., Minzioni, P., Liberale, C., Di Fabrizio, E., and Cristiani, I. "Design and optimization of a reflection-based fiber-optic tweezers." In: *Optics express* 16.22 (Oct. 2008), pp. 17647–53.

[185] Liu, Y., Stief, F., and Yu, M. "Subwavelength optical trapping with a fiber-based surface plasmonic lens." In: *Optics letters* 38.5 (Mar. 2013), pp. 721–3. DOI: 10.1364/OL.38.000721.

[186] Hu, Z., Wang, J., and Liang, J. "Manipulation and arrangement of biological and dielectric particles by a lensed fiber probe." In: *Optics express* 12.17 (Aug. 2004), pp. 4123–8.

[187] Gong, Y., Ye, A.-Y., Wu, Y., Rao, Y.-J., Yao, Y., and Xiao, S. "Graded-index fiber tip optical tweezers: numerical simulation and trapping experiment." In: *Optics express* 21.13 (July 2013), pp. 16181–90. DOI: 10.1364/OE.21.016181.

[188] Gong, Y., Huang, W., Liu, Q.-F., Wu, Y., Rao, Y., Peng, G.-D., Lang, J., and Zhang, K. "Graded-index optical fiber tweezers with long manipulation length." In: *Optics express* 22.21 (Oct. 2014), pp. 25267–76. DOI: 10.1364/OE.22.025267.

[189] Cizmár, T. and Dholakia, K. "Shaping the light transmission through a multimode optical fibre: complex transformation analysis and applications in biophotonics." In: *Optics express* 19.20 (Sept. 2011), pp. 18871–84. DOI: 10.1364/OE.19.018871.

[190] Gao, L., Shao, L., Chen, B.-C., and Betzig, E. "3D live fluorescence imaging of cellular dynamics using Bessel beam plane illumination microscopy." In: *Nature protocols* 9.5 (May 2014), pp. 1083–101. DOI: 10.1038/nprot.2014.087.

[191] Dowski, E. R. and Cathey, W. T. "Extended depth of field through wave-front coding." In: *Applied optics* 34.11 (Apr. 1995), pp. 1859–66. DOI: 10.1364/AO.34.001859.

[192] McNally, J. G., Karpova, T., Cooper, J., and Conchello, J. A. "Three-dimensional imaging by deconvolution microscopy." In: *Methods (San Diego, Calif.)* 19.3 (Nov. 1999), pp. 373–85. DOI: 10.1006/meth.1999.0873.

[193] Gonzalez, R. C. and Woods, R. E. "Image Restoration". In: *Digital Image Processing*. 3rd Edition. Prentice Hall, 2007. Chap. 5, pp. 311–393.

[194] Cizmár, T., Mazilu, M., and Dholakia, K. "In situ wavefront correction and its application to micromanipulation". In: *Nature Photonics* 4.6 (2010), pp. 388–394. DOI: Doi10.1038/Nphoton.2010.85.

[195] Jährling, N., Becker, K., Kramer, E. R., and Dodt, H.-U. "3D-Visualization of nerve fiber bundles by ultramicroscopy". In: *Medical Laser Application* 23.4 (Nov. 2008), pp. 209–215. DOI: 10.1016/j.mla.2008.06.001.

[196] Pitrone, P. G., Schindelin, J., Stuyvenberg, L., Preibisch, S., Weber, M., Eliceiri, K. W., Huisken, J., and Tomancak, P. "OpenSPIM: an open-access light-sheet microscopy platform." In: *Nature methods* 10.7 (July 2013), pp. 598–9. DOI: 10.1038/nmeth.2507.

[197] Papazoglou, D. G., Suntsov, S., Abdollahpour, D., and Tzortzakis, S. "Tunable intense Airy beams and tailored femtosecond laser filaments". In: *Physical Review A* 81.6 (June 2010), p. 061807. DOI: 10.1103/PhysRevA.81.061807.

[198] Preciado, M. A., Dholakia, K., and Mazilu, M. "Generation of attenuation-compensating Airy beams". In: *Optics letters* 39.16 (Aug. 2014), pp. 4950–3. DOI: 10.1364/OL.39.004950.

[199] Glaser, A. K., Wang, Y., and Liu, J. T. "Assessing the imaging performance of light sheet microscopies in highly scattering tissues". In: *Biomedical Optics Express* 7.2 (Jan. 2016), p. 454. DOI: 10.1364/BOE.7.000454.

[200] Costantini, I., Ghobril, J.-P., Di Giovanna, A. P., Allegra Mascaro, A. L., Silvestri, L., Müllenbroich, M. C., Onofri, L., Conti, V., Vanzi, F., Sacconi, L., Guerrini, R., Markram, H., Iannello, G., and Pavone, F. S. "A versatile clearing agent for multi-modal brain imaging." In: *Scientific reports* 5 (Jan. 2015), p. 9808. DOI: 10.1038/srep09808.

[201] Yang, Z., Prokopas, M., Nylk, J., Coll-Lladó, C., Gunn-Moore, F. J., Ferrier, D. E. K., Vettenburg, T., and Dholakia, K. "A compact Airy beam light sheet microscope with a tilted cylindrical lens." In: *Biomedical optics express* 5.10 (Oct. 2014), pp. 3434–42. DOI: 10.1364/BOE.5.003434.

[202] Schley, R., Kaminer, I., Greenfield, E., Bekenstein, R., Lumer, Y., and Segev, M. "Loss-proof self-accelerating beams and their use in non-paraxial manipulation of particles' trajectories." In: *Nature communications* 5 (Jan. 2014), p. 5189. DOI: 10.1038/ncomms6189.

[203] Born, M. and Wolf, E. "Geometrical theory of aberrations". In: *Principles of Optics*. 7th Edition. Cambridge University Press, 1999. Chap. 5, pp. 228–260.

[204] Cizmár, T. and Dholakia, K. "Tunable Bessel light modes: engineering the axial propagation." In: *Optics express* 17.18 (Aug. 2009), pp. 15558–70. DOI: 10.1364/OE.17.015558.

[205] Jacques, S. "Optical properties of biological tissues: a review". In: *Physics in medicine and biology* 58.311 (June 2013), R37–61. DOI: 10.1088/0031-9155/58/11/R37.

[206] Edelstein, A., Amodaj, N., Hoover, K., Vale, R., and Stuurman, N. "Computer control of microscopes using ţManager." In: *Current protocols in molecular biology / edited by Frederick M. Ausubel ... [et al.]* Chapter 14 (Oct. 2010), Unit14.20. DOI: 10.1002/0471142727.mb1420s92.

[207] Edelstein, A. D., Tsuchida, M. A., Amodaj, N., Pinkard, H., Vale, R. D., and Stuurman, N. "Advanced methods of microscope control using μManager software." In: *Journal of biological methods* 1.2 (Jan. 2014), e10. DOI: 10.14440/jbm.2014.36.

[208] Pegau, W. S., Gray, D., and Zaneveld, J. R. V. "Absorption and attenuation of visible and near-infrared light in water: dependence on temperature and salinity". In: *Applied Optics* 36.24 (Aug. 1997), p. 6035. DOI: 10.1364/AO.36.006035.

[209] Pullman, J. M., Nylk, J., Campbell, E. C., Gunn-Moore, F. J., Prystowsky, M. B., and Dholakia, K. "Visualization of podocyte substructure with structured illumination microscopy (SIM): a new approach to nephrotic disease". In: *Biomedical Optics Express* 7.2 (Jan. 2016), p. 302. DOI: 10.1364/BOE.7.000302.

[210] Mundel, P. and Reiser, J. "Proteinuria: an enzymatic disease of the podocyte?" In: *Kidney international* 77.7 (Apr. 2010), pp. 571–80. DOI: 10.1038/ki.2009.424.

[211] Gundersen, H. J., Seefeldt, T., and Østerby, R. "Glomerular epithelial foot processes in normal man and rats. Distribution of true width and its intra- and inter-individual variation." In: *Cell and tissue research* 205.1 (Jan. 1980), pp. 147–55.

[212] Rodewald, R. and Karnovsky, M. J. "Porous substructure of the glomerular slit diaphragm in the rat and mouse." In: *The Journal of cell biology* 60.2 (Feb. 1974), pp. 423–33.

[213] Grgic, I., Brooks, C. R., Hofmeister, A. F., Bijol, V., Bonventre, J. V., and Humphreys, B. D. "Imaging of podocyte foot processes by fluorescence microscopy." In: *Journal of the American Society of Nephrology : JASN* 23.5 (May 2012), pp. 785–91. DOI: 10.1681/ASN.2011100988.

[214] Höhne, M., Ising, C., Hagmann, H., Völker, L. A., Brähler, S., Schermer, B., Brinkkoetter, P. T., and Benzing, T. "Light microscopic visualization of podocyte ultrastructure demonstrates oscillating glomerular contractions." In: *The American journal of pathology* 182.2 (Feb. 2013), pp. 332–8. DOI: 10.1016/j.ajpath.2012.11.002.

[215] Suleiman, H., Zhang, L., Roth, R., Heuser, J. E., Miner, J. H., Shaw, A. S., and Dani, A. "Nanoscale protein architecture of the kidney glomerular basement membrane." In: *eLife* 2 (Jan. 2013), e01149. DOI: 10.7554/eLife.01149.

[216] Unnersjö-Jess, D., Scott, L., Blom, H., and Brismar, H. "Super-resolution stimulated emission depletion imaging of slit diaphragm proteins in optically cleared kidney tissue". In: *Kidney International* (Oct. 2015). DOI: 10.1038/ki.2015.308.

[217] Bellinghieri, G., Savica, V., and Santoro, D. "Renal alterations during exercise." In: *Journal of renal nutrition : the official journal of the Council on Renal Nutrition of the National Kidney Foundation* 18.1 (Jan. 2008), pp. 158–64. DOI: 10.1053/j.jrn.2007.10.031.

[218] Russo, L. M., Sandoval, R. M., McKee, M., Osicka, T. M., Collins, A. B., Brown, D., Molitoris, B. A., and Comper, W. D. "The normal kidney filters nephrotic levels of albumin retrieved by proximal tubule cells: retrieval is disrupted in nephrotic states." In: *Kidney international* 71.6 (Mar. 2007), pp. 504–13. DOI: 10.1038/sj.ki.5002041.

[219] Tanner, G. A. "Glomerular sieving coefficient of serum albumin in the rat: a two-photon microscopy study." In: *American journal of physiology. Renal physiology* 296.6 (June 2009), F1258–65. DOI: 10.1152/ajprenal.90638.2008.

[220] Kodner, C. "Nephrotic Syndrome in Adults: Diagnosis and Management - American Family Physician". In: *American Family Physician* 80.10 (2009), pp. 1129–1134.

[221] Karnarth, B. M. and Keddis, M. T. "The nephrotic syndrome". In: *Hopital Physician* 43.10 (2007), pp. 25–30.

[222] Orth, S. R. and Ritz, E. "The nephrotic syndrome." In: *The New England journal of medicine* 338.17 (Apr. 1998), pp. 1202–11. DOI: 10.1056/NEJM199804233381707.

[223] Roselli, S., Gribouval, O., Boute, N., Sich, M., Benessy, F., Attié, T., Gubler, M.-C., and Antignac, C. "Podocin localizes in the kidney to the slit diaphragm area." In: *The American journal of pathology* 160.1 (Jan. 2002), pp. 131–9. DOI: 10.1016/S0002-9440(10)64357-X.

[224] Bozzola, J. J. and Russel, L. D. "Specimen Preparation for Transmission Electron Microscopy". In: *Electron Microscopy: Principles and Techniques for Biologists*. 2nd Edition. Jones and Bartlett Publishers, 1999. Chap. 2, pp. 16–47.

[225] Nylk, J., Kristensen, M. V. G., Mazilu, M., Thayil, A. K., Mitchell, C. A., Campbell, E. C., Powis, S. J., Gunn-Moore, F. J., and Dholakia, K. "Development of a graded index microlens based fiber optical trap and its characterization using principal component analysis." In: *Biomedical optics express* 6.4 (Apr. 2015), pp. 1512–9. DOI: 10.1364/BOE.6.001512.

[226] Lindballe, T. B., Kristensen, M. V., Kylling, A. P., Palima, D. Z., Glüuckstad, J., Keiding, S. R., and Stapelfeldt, H. "Three-dimensional imaging and force characterization of multiple trapped particles in low NA counterpropagating optical traps". In: *Journal of the European Optical Society: Rapid Publications* 6 (Dec. 2011), p. 11057. DOI: 10.2971/jeos.2011.11057.

[227] Shane, J. C., Mazilu, M., Lee, W. M., and Dholakia, K. "Effect of pulse temporal shape on optical trapping and impulse transfer using ultrashort pulsed lasers." In: *Optics express* 18.7 (Mar. 2010), pp. 7554–68. DOI: 10.1364/OE.18.007554.

[228] Turk, M. and Pentland, A. "Eigenfaces for recognition." In: *Journal of cognitive neuroscience* 3.1 (Jan. 1991), pp. 71–86. DOI: 10.1162/jocn.1991.3.1.71.

[229] Guizar-Sicairos, M., Thurman, S. T., and Fienup, J. R. "Efficient subpixel image registration algorithms". In: *Optics Letters* 33.2 (Jan. 2008), p. 156. DOI: 10.1364/OL.33.000156.

[230] Martín-Cófreces, N. B., Robles-Valero, J., Cabrero, J. R., Mittelbrunn, M., Gordón-Alonso, M., Sung, C.-H., Alarcón, B., Vázquez, J., and Sánchez-Madrid, F. "MTOC translocation modulates IS formation and controls sustained T cell signaling." In: *The Journal of cell biology* 182.5 (Sept. 2008), pp. 951–62. DOI: 10.1083/jcb.200801014.

[231] Wülfing, C. and Davis, M. M. "A receptor/cytoskeletal movement triggered by costimulation during T cell activation." In: *Science (New York, N.Y.)* 282.5397 (Dec. 1998), pp. 2266–9.

[232] Grakoui, A. "The Immunological Synapse: A Molecular Machine Controlling T Cell Activation". In: *Science* 285.5425 (July 1999), pp. 221–227. DOI: 10.1126/science.285.5425.221.

[233] Groves, J. T. and Dustin, M. L. "Supported planar bilayers in studies on immune cell adhesion and communication." In: *Journal of immunological methods* 278.1-2 (July 2003), pp. 19–32.

[234] Brown, A. C. N., Oddos, S., Dobbie, I. M., Alakoskela, J.-M., Parton, R. M., Eissmann, P., Neil, M. A. A., Dunsby, C., French, P. M. W., Davis, I., and Davis, D. M. "Remodelling of Cortical Actin Where Lytic Granules Dock at Natural Killer Cell Immune Synapses Revealed by Super-Resolution Microscopy". In: *PLoS Biology* 9.9 (Sept. 2011). Ed. by Marrack, P., e1001152. DOI: 10.1371/journal.pbio.1001152.

[235] Huppa, J. B. and Davis, M. M. "T-cell-antigen recognition and the immunological synapse." In: *Nature reviews. Immunology* 3.12 (Dec. 2003), pp. 973–83. DOI: 10.1038/nri1245.

[236] June, C. H., Bluestone, J. A., Nadler, L. M., and Thompson, C. B. "The B7 and CD28 receptor families." In: *Immunology today* 15.7 (July 1994), pp. 321–31. DOI: 10.1016/0167-5699(94)90080-9.

[237] Albertson, B., Bray, D., Hopkin, K., Johnson, A., Lewis, J., Raff, M., Roberts, K., and Walter, P. "Cell Communication". In: *Essential Cell Biology*. 3rd Edition. Garland Science, 2010. Chap. 16, pp. 531–570.

[238] Na, S., Collin, O., Chowdhury, F., Tay, B., Ouyang, M., Wang, Y., and Wang, N. "Rapid signal transduction in living cells is a unique feature of mechanotransduction". In: *Proceedings of the National Academy of Sciences* 105.18 (May 2008), pp. 6626–6631. DOI: 10.1073/pnas.0711704105.

[239] Liedert, A., Kaspar, D., Blakytny, R., Claes, L., and Ignatius, A. "Signal transduction pathways involved in mechanotransduction in bone cells". In: *Biochemical and Biophysical Research Communications* 349.1 (Oct. 2006), pp. 1–5. DOI: 10.1016/j.bbrc.2006.07.214.

[240] Tummala, P., Arnsdorf, E. J., and Jacobs, C. R. "The Role of Primary Cilia in Mesenchymal Stem Cell Differentiation: A Pivotal Switch in Guiding Lineage Commitment." In: *Cellular and molecular bioengineering* 3.3 (Sept. 2010), pp. 207–212. DOI: 10.1007/s12195-010-0127-x.

[241] Bro, R. and Smilde, A. K. "Principal component analysis". In: *Analytical Methods* 6.9 (Apr. 2014), p. 2812. DOI: 10.1039/c3ay41907j.

[242] Raulf-Heimsoth, M. "T cell - primary culture from peripheral blood." In: *Methods in molecular medicine* 138 (Jan. 2008), pp. 17–30. DOI: 10.1007/978-1-59745-366-0_2.

[243] Vellekoop, I. M., Lagendijk, A., and Mosk, A. P. "Exploiting disorder for perfect focusing". In: *Nature Photonics* 4.5 (Feb. 2010), pp. 320–322. DOI: 10.1038/nphoton.2010.3.

[244] Westmoreland, D., Shaw, M., Grimes, W., Metcalf, D. J., Burden, J. J., Gomez, K., Knight, A. E., and Cutler, D. F. "Super-resolution microscopy as a potential approach to platelet granule disorder diagnosis." In: *Journal of thrombosis and haemostasis : JTH* (Jan. 2016). DOI: 10.1111/jth.13269.

[245] Neil, M. A. A., Juskaitis, R., and Wilson, T. "Real time 3D fluorescence microscopy by two beam interference illumination". In: *Optics Communications* 153.1-3 (1998), pp. 1–4. DOI: Doi10.1016/S0030-4018(98)00210-7.

[246] Lukosz, W. and Marchand, M. "Optischen Abbildung Unter Überschreitung der Beugungsbedingten Auflösungsgrenze". In: *Optica Acta* 10.3 (1963), pp. 241–255.

[247] Morgenstern, B. and Paris, D. P. "Optical Bandwidth Extension in Two Dimensions Beyond the Classical Limit". In: *Journal of the Optical Society of America* 54.10 (Oct. 1964), pp. 1282–1283. DOI: 10.1364/JOSA.54.001282.

[248] Hecht, E. "Interference". In: *Optics*. 4th Edition. Addison Wesley, 2002. Chap. 9, pp. 385–442.

[249] Karadaglic, D. and Wilson, T. "Image formation in structured illumination wide-field fluorescence microscopy". In: *Micron* 39.7 (2008), pp. 808–818. DOI: DOI10.1016/j.micron.2008.01.017.

[250] Wilson, T. and Sheppard, C. J. R. "Image Formation in Scanning Microscopes". In: *Theory and practice of scanning optical microscopy*. London: Academic Press Inc., 1984. Chap. 3, pp. 37–78.

[251] Bailey, B., Krishnamurthi, V., Farkas, D. L., Taylor, D. L., and Lanni, F. "Three-dimensional imaging of biological specimens with standing wave fluorescence microscopy". In: *IS&T/SPIE 1994 International Symposium on Electronic Imaging: Science and Technology*. Ed. by Cogswell, C. J. and Carlsson, K. International Society for Optics and Photonics, Apr. 1994, pp. 208–213. DOI: 10.1117/12.172101.

[252] Orieux, F., Sepulveda, E., Loriette, V., Dubertret, B., and Olivo-Marin, J.-C. "Bayesian estimation for optimized structured illumination microscopy." In: *IEEE transactions on image processing : a publication of the IEEE Signal Processing Society* 21.2 (Feb. 2012), pp. 601–14. DOI: 10.1109/TIP.2011.2162741.

[253] Dong, S., Liao, J., Guo, K., Bian, L., Suo, J., and Zheng, G. "Resolution doubling with a reduced number of image acquisitions." In: *Biomedical optics express* 6.8 (Aug. 2015), pp. 2946–52. DOI: 10.1364/BOE.6.002946.

[254] Gustafsson, M. G. L., Agard, D. a., and Sedat, J. W. "I5M: 3D widefield light microscopy with better than 100 nm axial resolution". In: *Journal of Microscopy* 195.1 (1999), pp. 10–16. DOI: 10.1046/j.1365-2818.1999.00576.x.

[255] Shao, L., Isaac, B., Uzawa, S., Agard, D. A., Sedat, J. W., and Gustafsson, M. G. L. "I5S: wide-field light microscopy with 100-nm-scale resolution in three dimensions." In: *Biophysical journal* 94.12 (June 2008), pp. 4971–83. DOI: 10.1529/biophysj.107.120352.

[256] Isobe, K., Takeda, T., Mochizuki, K., Song, Q., Suda, A., Kannari, F., Kawano, H., Kumagai, A., Miyawaki, A., and Midorikawa, K. "Enhancement of lateral resolution and optical sectioning capability of two-photon fluorescence microscopy by combining temporal-focusing with structured illumination." In: *Biomedical optics express* 4.11 (Jan. 2013), pp. 2396–410. DOI: 10.1364/BOE.4.002396.

[257] Cheng, L.-C., Lien, C.-H., Da Sie, Y., Hu, Y. Y., Lin, C.-Y., Chien, F.-C., Xu, C., Dong, C. Y., and Chen, S.-J. "Nonlinear structured-illumination enhanced temporal focusing multiphoton excitation microscopy with a digital micromirror device." In: *Biomedical optics express* 5.8 (Aug. 2014), pp. 2526–36. DOI: 10.1364/BOE.5.002526.

Appendix A

Extended theory underpinning structured illumination microscopy

This Appendix details the physical mechanisms underpinning the SIM technique in the linear regime. Non-linear SIM is also briefly discussed.

SIM is a technique where the illumination takes the form of a one- or two-dimensional periodic pattern consisting of a few discrete Fourier components. Typically this pattern is formed from 2- [245] or 3-beam interference [32]. Such a technique was originally developed to provide optical sectioning in a widefield microscope [74] but it was later shown that the same technique could yield improved resolution two times beyond the diffraction limit in the lateral plane [99], and then extended to include the axial direction [32]. Though the concept of extending the optical bandwidth by patterned illumination has been known for nearly 40 years at the time [246, 247].

A.1 Optical sectioning by structured illumination microscopy

Image formation in a fluorescence microscope can be described by:

$$D(r) = (H \otimes [SI])(r) \tag{A.1}$$

where $\otimes$ is the convolution operator, $D(r)$ is the resulting image intensity, $H(r)$ is the point-spread-function (PSF) of the imaging system, $S(r)$ is the fluorophore distribution within the sample, $I(r)$ is the illumination intensity within the sample, and, for simplicity, r is a one-dimensional vector in the lateral plane of the microscope [32]. $S(r) \cdot I(r)$

is the emission intensity from the sample, for uniform illumination, $I(r)$ is unity, which is the case for a standard fluorescence microscope.

When the illumination takes the form of a periodic modulation:

$$I(r) = 1 + \mu \cos(\nu r + \phi) \tag{A.2}$$

where μ is the modulation depth, ν is the frequency of the grating, and ϕ is an arbitrary phase offset. This form of illumination can be produced from the interference of two plane waves [245] and is analogous to Young's double slit experiment [248]. The image then becomes:

$$D(r) = D_0(r) + \frac{\mu}{2} e^{i\phi} D_\nu(r) + \frac{\mu}{2} e^{-i\phi} D_{-\nu}(r) \tag{A.3}$$

where $D_0(r)$, $D_\nu(r)$, and $D_{-\nu}(r)$ are given by:

$$D_0(r) = (H \otimes S)(r) \tag{A.4}$$

$$D_\nu(r) = (H \otimes [e^{i\nu r} S])(r) \tag{A.5}$$

$$D_{-\nu}(r) = D_\nu^*(r) \tag{A.6}$$

$D_0(r)$ is the image obtained with uniform illumination, the case of a standard fluorescence microscope. $D_\nu(r)$ and $D_{-\nu}(r)$ are images formed from the interaction of the object with the periodic illumination. If $D_0(r)$ could be removed from the image, and the grid pattern removed from the remaining image, a true optically sectioned image would be achieved, described by:

$$D_{sect}(r) = [D_\nu(r)^2 + D_{-\nu}(r)^2]^{1/2} \tag{A.7}$$

$D_{sect}(r)$ can be extracted from $D(r)$ if multiple images are acquired with different phase offsets, ϕ. Considering the phase offset explicitly as a variable of the image:

$$D(r) \equiv D(r, \phi) \tag{A.8}$$

then for 3 images acquired with phase offsets equidistantly spaced over one period of the illumination modulation:

$$D_1(r, \phi) = D(r, \frac{2\pi}{3}) \tag{A.9}$$

$$D_2(r, \phi) = D(r, \frac{4\pi}{3}) \tag{A.10}$$

$$D_3(r, \phi) = D(r, 2\pi) \tag{A.11}$$

From the above expressions $D_{sect}(r)$ can be determined from:

$$D_{sect}(r) = |D_1(r) + e^{i\frac{2\pi}{3}} D_2(r) + e^{i\frac{4\pi}{3}} D_3(r)| \tag{A.12}$$

in a manner equivalent to homodyne detection [74, 249], however this method requires that μ, ϕ, and ν are known or estimated. Alternatively, the sectioned image may be determined from the sum of squared differences between the three images [74, 249]:

$$D_{sect}(r) = [(D_1(r) - D_2(r))^2 + (D_2(r) - D_3(r))^2 + (D_3(r) - D_1(r))^2]^{1/2} \tag{A.13}$$

which does not require knowledge of μ, ϕ, and ν.

The acquisition of the three images, $D_1(r)$, $D_2(r)$, and $D_3(r)$, serve to translate the illumination grating such that all regions of the sample are maximally illuminated in at least one of the images. To use a simple analogy, SIM plays "spot the difference" with these images. The periodic illumination is only well focused in a single plane, and only in this plane will the sample distribution contain this modulation and change with the phase offset, ϕ. In axially offset planes, the periodic illumination will defocus

and become uniform for all values of ϕ. The in-focus information will be different in each of the images whereas the out-of-focus signal will be a constant, unmodulated, background. Equations (A.12) and (A.13) perform this comparison and reject out-of-focus signal from the image.

It is also worth noting that the case of uniform illumination can also be recovered by [74]:

$$D_0(r) = \frac{1}{3}[D_1(r) + D_2(r) + D_3(r)] \tag{A.14}$$

To assess the optical sectioning ability of the SIM technique, consider the image of a thin fluorescent layer, $S(r) = 1$. From equation (A.3), the Fourier transform of the image, $\tilde{D}(r)$ is:

$$\tilde{D}(k_r) = \tilde{D}_0(k_r) + \frac{\mu}{2}e^{i\phi}\tilde{D}_\nu(k_r) + \frac{\mu}{2}e^{-i\phi}\tilde{D}_{-\nu}(k_r) \tag{A.15}$$

where $\tilde{D}_0(k_r)$, $\tilde{D}_0(k_r)$, and $\tilde{D}_{-\nu}(k_r)$ are given by:

$$\tilde{D}_0(k_r) = O(k_r)\tilde{S}(k_r) \tag{A.16}$$

$$\tilde{D}_\nu(k_r) = O(k_r)\tilde{S}(k_r - \nu) \tag{A.17}$$

$$\tilde{D}_{-\nu}(k_r) = O(k_r)\tilde{S}(k_r + \nu) \tag{A.18}$$

where $O(k_r)$, the optical transfer function (OTF), is the Fourier transform of the PSF, $H(r)$.

For the thin fluorescent layer, $\tilde{S}(k_r)$ becomes a delta function, therefore:

$$\tilde{D}_\nu(k_r) = O(k_r - \nu) \tag{A.19}$$

The optical sectioning ability of the periodic illumination is then related to the axial response of the OTF at the modulation frequency, ν. Including the axial behaviour,

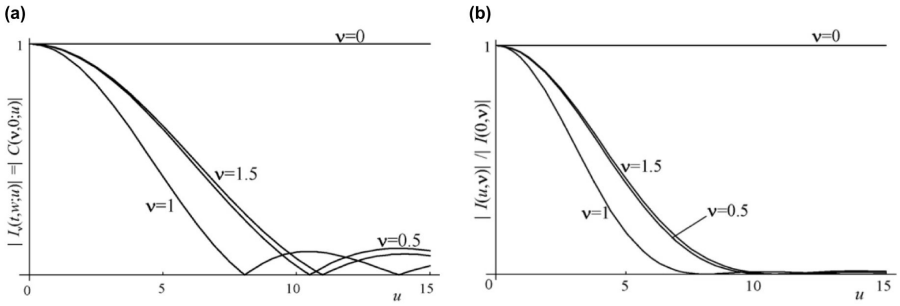

FIGURE A.1: Dependence of optical sectioning ability of structured illumination on the frequency of the illuminating pattern, ν. Plots of optical sectioning ability, $|O(k_t, k_w, u)| = |O(\nu, 0, u)| \equiv |C(\nu, 0, u)| \equiv |I(u, \nu)|/|I(0, \nu)|$ against defocus, u, for selected values of ν, for the cases of periodic illumination generated by (a) two-beam interference, and (b) imaging of a physical grating into the sample. Figure used with permission from [249].

equation(A.19) becomes:

$$|\tilde{D}_\nu(k_r), z| \approx |O(\nu, z)| \tag{A.20}$$

It is clear that the SIM technique will give the greatest optical sectioning when the grating frequency, ν, is such that the MTF in equation (A.20) decays most rapidly with z. Figure A.1 shows the axial response of the OTF for selected values of ν. In composing Fig. A.1, Karadidaglić and Wilson have extended the relations to three dimensions where $\boldsymbol{k_r} = (k_x^2 + k_y^2)^{1/2}$, and k_x, k_y, and z, and have been expressed in optical coordinates, k_t, k_w, and u, with the following relation to real-space coordinates:

$$(t, w) = \frac{2\pi}{\lambda}(x, y) n \sin(\theta) \tag{A.21}$$

$$u = \frac{8\pi}{\lambda} z \sin(\theta/2)^2 \tag{A.22}$$

where λ is the wavelength of the illumination, and for simplicity, the increase in wavelength of the emitted fluorescence has been neglected, and $n \sin(\theta)$ is the numerical aperture (NA) of the imaging system. In this notation, the diffraction limit corresponds to any point on the circle $(k_t^2 + k_w^2)^{1/2} = 2$. It is found that the strongest optical sectioning occurs when $\nu = 1$, corresponding to a frequency exactly half of the diffraction

limit. Figure A.1 highlights a difference between methods of generation of periodic illumination which have thus far been neglected in this derivation. When a periodic illumination is formed in the sample by imaging a physical grating, the image of the grating is itself, also subject to blurring with axial defocus away from the image plane. This additional imaging step is similar to the "double imaging" that occurs in confocal microscopy where a point illumination source is imaged into the sample and is then imaged onto the detector [250] and results in squaring of the PSF. The plots in Fig. A.1(b) are the squares of the corresponding plots in Fig. A.1(a), showing that SIM implemented with a physical grating can achieve improved optical sectioning over SIM implemented with two-beam interference, however this grating must accurately be translated in $2\pi/3$ steps to acquire the necessary images to compute the optically sectioned image which may be easier to achieve with interferometric techniques.

A.2 Resolution doubling by linear structured illumination microscopy

The use of patterned illumination can also improve the resolution of an image. Gustafsson realised that this form of illumination encodes high-frequency information, normally inaccessible to the microscope, on lower frequency information which is retained in the image through the phenomenon of Moiré fringes [99], as shown in Fig. A.2(a). This method is particularly beneficial in comparison to confocal microscopy because the resolution enhancement is achieved without rejecting any signal emitted by the sample. In this section, the mechanism underpinning this resolution enhancement is discussed in both the lateral and axial directions. SIM exploiting an illumination that is periodic only in the lateral plane will be referred to as 2D-SIM, whereas SIM that makes use of periodicity in both the lateral and axial directions simultaneously will be referred to as 3D-SIM.

Lateral resolution enhancement

Staying with the illumination scheme presented in Appendix A.1, lateral resolution enhancement can be gained using this form of periodic illumination as was first demonstrated by Gustafsson [99].

Revisiting equation (A.15), rewriting it here in full and extending the lateral axis to a two-dimensional (2D) plane, it becomes:

$$\tilde{D}(\boldsymbol{k_r}) = O(\boldsymbol{k_r})[\tilde{S}(\boldsymbol{k_r}) + \frac{\mu}{2}e^{i\phi}\tilde{S}(\boldsymbol{k_r} - \boldsymbol{\nu}) + \frac{\mu}{2}e^{-i\phi}\tilde{S}(\boldsymbol{k_r} + \boldsymbol{\nu})] \tag{A.23}$$

Equation (A.23) contains three separate components, two of which contain the Fourier spectrum of the sample, $\tilde{S}(\boldsymbol{k_r})$, but shifted by $\pm\boldsymbol{\nu}$. The shifted components enable the microscope to acquire spatial frequencies which are normally outwith the support of the OTF (Fig. A.2(c)). These additional higher frequencies are not directly observed, instead they manifest as Moiré fringes [99], a lower frequency pattern generated from the beating of the grating frequency, $\boldsymbol{\nu}$, with the spatial frequencies of the object as is demonstrated in Fig. A.2(a). If the three spectral regions of the image can be separated and restored to their correct location in the Fourier spectrum of the image, then the resulting image will contain higher resolution information than the OTF can normally yield. The resolution enhancement can be characterised simply by the enhancement factor:

$$C_{res}(|\boldsymbol{\nu}|) = 1 + \frac{|\boldsymbol{\nu}|}{|\boldsymbol{k_{r,max}}|} \tag{A.24}$$

where $|\boldsymbol{k_{r,max}}|$ is the maximum spatial frequency supported by the OTF. $C_{res}(0) = 1$ corresponds to no enhancement beyond the traditional case.

In contrast to the optical sectioning capability of 2D-SIM, the resolution enhancement factor is maximal when $\boldsymbol{\nu}$ is maximal. As the grating must be delivered into the sample by traditional optics (typically the same objective lens as is used for detection), the grating is subject to diffraction, therefore $|\boldsymbol{\nu_{max}}| = |\boldsymbol{k_{r,max}}|$, resulting in a resolution enhancement of two times beyond the diffraction limit [99].

In order to achieve a super-resolution image, each spectral region, which overlap in the recorded images, must be separated and restored to its true location in Fourier space. This can be achieved from matrix arithmetic if multiple images are acquired with different phase offsets [251]. As 3 spectral regions must be recovered, 3 phase-shifted images are required. The sequence of images, equations (A.9) - (A.11) are a suitable sequence for this purpose [99]. More recently, Baysian estimation [252] and incoherent

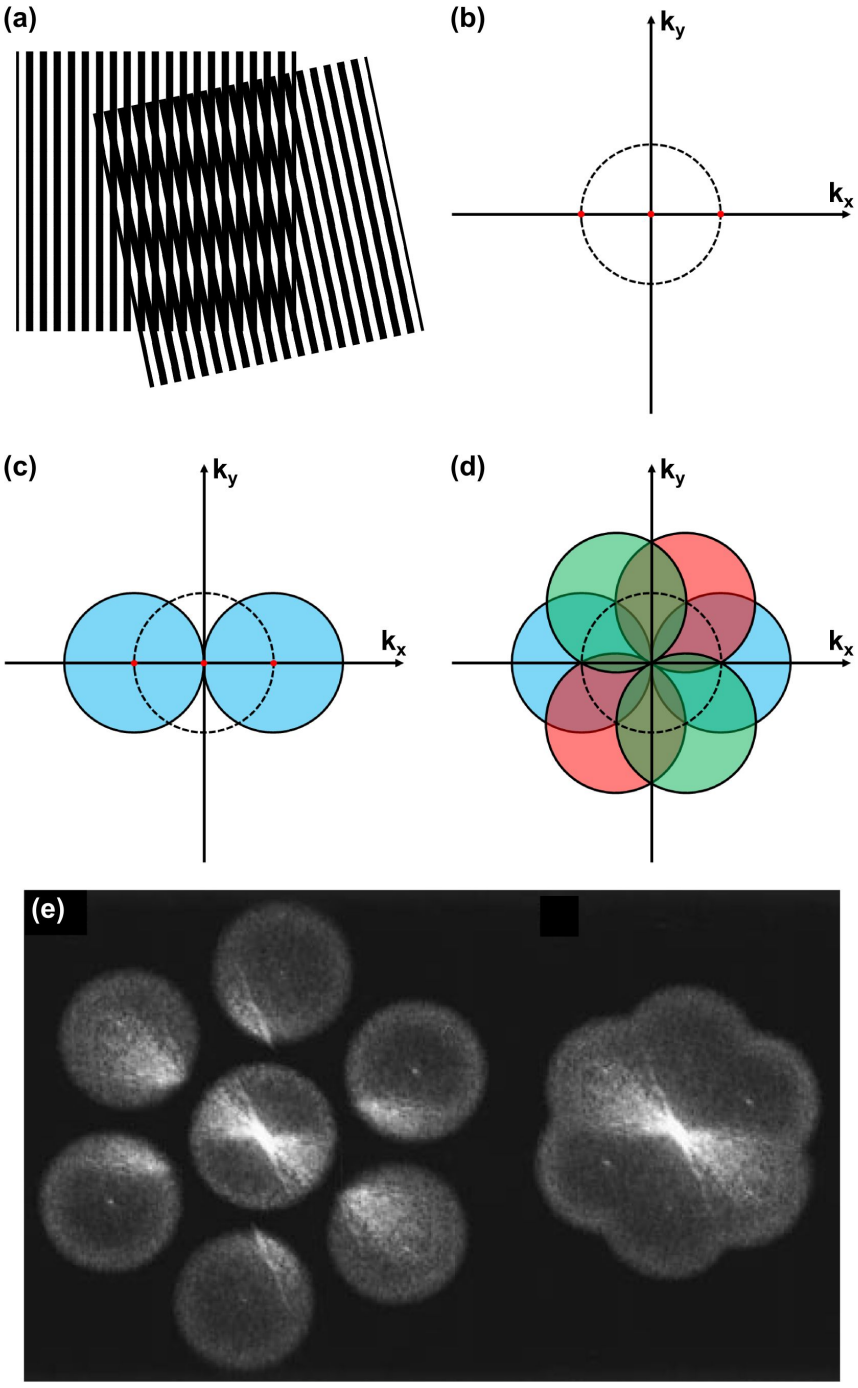

FIGURE A.2: (a) Example of Moiré fringes produced from two high-frequency gratings. (b) Normal support of OTF (dashed circle) and Fourier components of a periodic illumination with frequency $\boldsymbol{\nu_{max}} = k_{x,max}$ (red dots). (c) Extended Fourier regions (blue filled circles) which produce Moiré fringes within the support of the OTF. (d) The Fourier components which can be detected by 3 successive rotations of the grating in the lateral plane. (e) Separated (left) and restored (right) Fourier components from 2D-SIM acquisitions in a real sample. Figures (a-d) adapted with permission from, and (e) used with permission from [99].

Fourier ptychography [253] have been exploited for separation of the spectral regions with fewer phase-shifted images. Combination of the separate Fourier regions and generation of a super-resolution image can be performed simply using a generalised Wiener filter:

$$\hat{\tilde{S}}(\boldsymbol{k_r}) = \frac{\sum_m O^*(\boldsymbol{k_r} + m\boldsymbol{\nu})\tilde{D}_m(\boldsymbol{k_r} + m\boldsymbol{\nu})}{\sum_{m'}|O(\boldsymbol{k_r} + m'\boldsymbol{\nu})|^2 + w^2} A(\boldsymbol{k_r}) \tag{A.25}$$

where $\hat{\tilde{S}}(\boldsymbol{k_r})$ is the estimate of the sample distribution $\tilde{S}(\boldsymbol{k_r})$ and is the super-resolved image, $\tilde{D}_m(\boldsymbol{k_r} + m\boldsymbol{\nu})$ are the Fourier components of the acquired images associated with the $m = -1, 0 + 1$ frequency components of the grating illumination, w^2 is the Wiener parameter corresponding to the signal-to-noise ratio of the acquired images, and $A(\boldsymbol{k_r})$ is an apodization function, generally chosen to be a 3D triangle function centred on the origin and extending to the edge of the extended OTF support [32, 193].

The resolution enhancement is only achieved along the axis defined by $\boldsymbol{\nu}$. To achieve resolution enhancement along all directions in the lateral plane, the Fourier space must be extended in all dimensions equally. This can be achieved by using an illumination pattern that varies along multiple directions, however, this can require many images to separate all the spectral regions and compute a super-resolved image [99]. More commonly, the orientation of the 1D patterned illumination is rotated to act along different directions. Three pattern orientations, separated by $60°$ suitably fills the lateral Fourier plane (Fig. A.2(d))[99]. The separated Fourier components and their reconstruction are shown for a real sample in Fig. A.2(e)[99]. It is trivial to extend equation (A.25) to incorporate multiple grating orientations. A super-resolved image, breaking the diffraction limit by a factor of two, requires a total of nine images (three orientations each with three phase shifts), this is much fewer in comparison to other super-resolution techniques, however, the trade-off for increased speed is loss of spatial resolution as other super-resolution techniques can achieve significantly greater resolution.

Lateral and axial resolution enhancement with coherent illumination

Despite the excellent improvement of lateral resolution, the technique described above still has a poor axial resolution. As has already been discussed, the optimal grating

frequency for resolution enhancement is not optimal for axial resolution enhancement. To achieve three-dimensional resolution enhancement, 2D-SIM may be combined with other techniques which provide axial enhancement such as standing wave microscopy [251] or I^5M [254]. The combination of 2D-SIM with I^5M, I^5S, has already been demonstrated to provide resolution approximately 100nm in 3D [255], however, this technique requires a complex optical system and requires illumination of and collection of emitted fluorescence from the sample through two high NA objective lenses. In a much simpler setup, 3D resolution enhancement can be achieved with a single objective lens through illumination which varies periodically both laterally and axially as is discussed below.

So far, only the case of a two-dimensional (2D) PSF and illumination pattern has been considered, here this will be extended to consideration of the full, three-dimensional (3D) aspects. In general, periodic illumination takes the form:

$$I(\boldsymbol{r_{x,y}}, z) = \sum_m I_{z,m}(z) I_{r,m}(\boldsymbol{r_{x,y}}) \tag{A.26}$$

where $I_{z,m}(z)$ and $I_{r,m}((r_{x,y})$ are pure harmonic functions along the z-axis and in the lateral plane respectively, and m is finite. In the previous case examined in Appendix A.1, $m = 0, \pm 1$, $I_{r,m}(\boldsymbol{r_{x,y}}) = \frac{\mu}{2} \exp\left(im[\boldsymbol{\nu} \cdot \boldsymbol{r_{x,y}} + \phi]\right)$, and $I_{z,m} = 1$.

This can be achieved through illumination by three plane-waves:

$$I(\boldsymbol{r}) = \sum_p \sum_q \boldsymbol{E_p^*} \cdot \boldsymbol{E_q} e^{i(\boldsymbol{k_q} - \boldsymbol{k_p})\boldsymbol{r}} \tag{A.27}$$

which produce a 3D interference pattern containing only spatial frequencies only equal to the pairwise difference vectors $\boldsymbol{k_q} - \boldsymbol{k_p}$. This yields a periodic intensity grid containing 7 unique Fourier components arranged as shown in Fig. A.3(a).

If the illumination pattern is kept fixed with respect to the focal plane of the microscope then the axial intensity pattern modulates the PSF of the microscope rather than the sample fluorophore distribution and yields an image:

$$D(\boldsymbol{r}) = \sum_m D_m(\boldsymbol{r}) \tag{A.28}$$

$$D_m(\boldsymbol{r}) = ([HI_{z,m}(z)] \otimes [SI_{r,m}(\boldsymbol{r_{x,y}})])(\boldsymbol{r}) \tag{A.29}$$

The Fourier transform of $D_m(\boldsymbol{r})$ is given by:

$$\tilde{D}_m(\boldsymbol{k_r}) = O_m(\boldsymbol{k_r})[\tilde{S} \otimes \tilde{I}_{r,m}])(\boldsymbol{k_r}) \tag{A.30}$$

$$O_m(\boldsymbol{k_r}) = (O \otimes \tilde{I}_{z,m})(\boldsymbol{k_r}) \tag{A.31}$$

As above, $I_{r,m}(\boldsymbol{r_{x,y}})$ are harmonic functions, their Fourier transforms will be delta functions, and so equation (A.30) becomes:

$$\tilde{D}_m(\boldsymbol{k_r}) = O_m(\boldsymbol{k_r})\tilde{S}(\boldsymbol{k_r} - \boldsymbol{\nu_m}) \tag{A.32}$$

The grating frequencies replicate the OTF in the pattern shown in Figs A.3(c) and (d), and, when rotated in the lateral plane 3 times to fill the Fourier space homogeneously, Fig. A.3(e).

The grating frequencies that axially shift the spectral components of the object are symmetric around $z = 0$ and so their projections onto the $x-y$ plane are equal. As such, these components can be described by a single lateral frequency shift and a modified OTF which incorporates both the positively and negatively shifted axial components. Therefore, $m = 0, \pm 1, \pm 2$ fully describes the image formed from a 3D intensity pattern created from 3-beam interference, and only 5 phase-shifted images are required to achieve resolution enhancement along the axial direction and one lateral direction simultaneously.

The Wiener filter (equation (A.25)) can easily be extended to include the frequency dependent OTFs, $O_m(\boldsymbol{k_r})$, and is expressed below for all grating phases, m, and rotations, d:

$$\hat{\tilde{S}}(\boldsymbol{k_r}) = \frac{\sum_d \sum_m O_m^*(\boldsymbol{k_r} + m\boldsymbol{\nu_d})\tilde{D}_{d,m}(\boldsymbol{k_r} + m\boldsymbol{\nu_d})}{\sum_{d'} \sum_{m'} |O_{m'}(\boldsymbol{k_r} + m'\boldsymbol{\nu_{d'}})|^2 + w^2} A(\boldsymbol{k_r}) \tag{A.33}$$

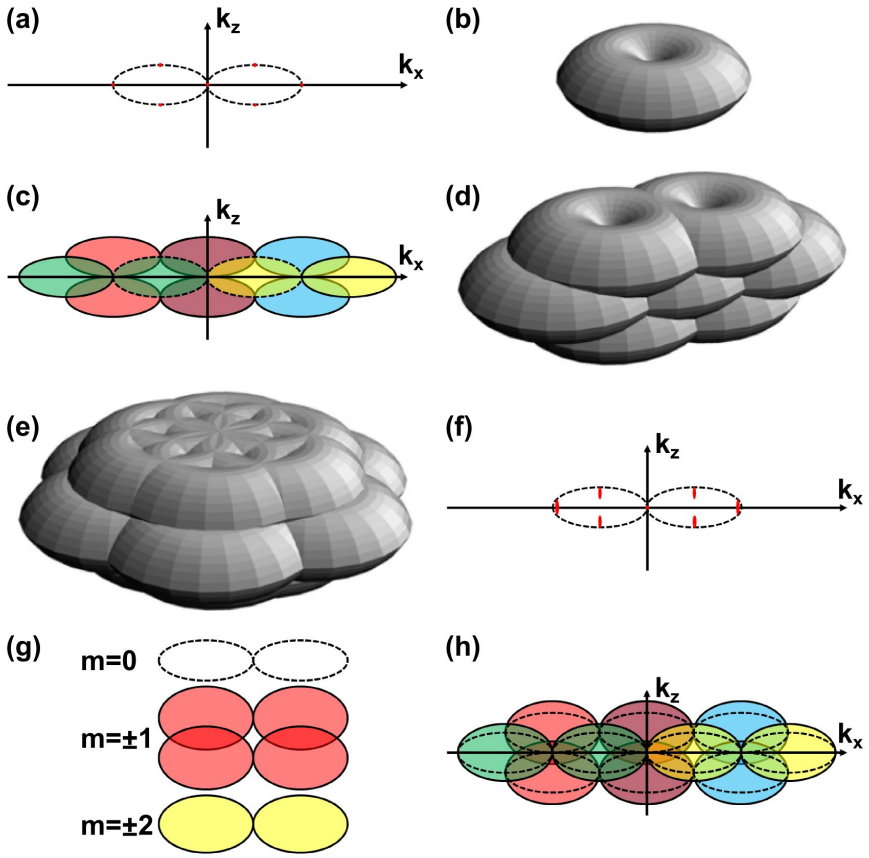

FIGURE A.3: (a) Cross-sectional and (b) 3D view of normal OTF support (dashed region in (a)) showing Fourier components of 3D illumination grating (red dots) with spatially coherent illumination. (c,d) The Fourier components which form Moiré fringes within the support of the OTF (filled regions, various colours represent different regions). (e) 3D view of the Extended Fourier space of the image available after 3 successive rotations of the grating around the z-axis. (f) Axial broadening of the illumination Fourier components with spatially incoherent illumination (red dots). (g) Comparison of the effective OTFs for $m = 0, \pm 1, \pm 2$ for the Fourier components in (e), and (h) resulting extended Fourier space of image. The outline for the coherent case is shown in (h) for comparison (dashed lines). Figures (a,c,f-g) adapted with permission from, and (b,d,e) used with permission from [32].

Lateral and axial resolution enhancement with spatially incoherent illumination

To demonstrate the method of 3D resolution doubling by structured illumination, Gustafsson *et al* also developed a novel approach to generate the required 3D intensity distribution based on spatially incoherent illumination [32].

In this approach, laser light is passed through a rotating holographic diffuser and coupled into a multi-mode (MM) fibre before being delivered to a diffraction grating to produce the three beams which interfere in the sample. The rotation rate of the diffuser controls the spatial coherence which is chosen to produce a time-averaged uniform intensity over the integration time of the camera. Each point in the three diffracted beams which are interfered to produce the 3D intensity distribution is therefore only coherent with the corresponding point in each of the other diffracted orders, this causes a wider distribution of Fourier components in the illumination pattern. As shown in Fig. A.3(f), this manifests as an axial broadening of the non-zero Fourier components (Fig. A.3(g)). This, in turn, axially elongates their OTF and allows slightly higher axial resolution to be achieved compared to the case of spatially coherent illumination (Fig. A.3(h)).

The use of spatially incoherent illumination also serves to reduce the axial extent of the illumination pattern, which should reduce photobleching and phototoxic effects away from the plane of imaging [32]. A similar approach has been used by Chen *et al* to reduce the axial extend of the illumination in structured illumination based light-sheet imaging [46].

A.3 Structured illumination microscopy in the non-linear regime

The structured illumination techniques described up to this point have assumed a linear response of the fluorophore to the incident illumination intensity. This criteria is not always satisfied and can be broken in a controlled manner quite simply. Saturation of the excited state of the fluorophore is a prime example of the non-linear behaviour that can be exhibited in the fluorescence emission. Such a nonlinearity serves to distort the periodic illumination pattern used in SIM and so higher harmonics appear in the

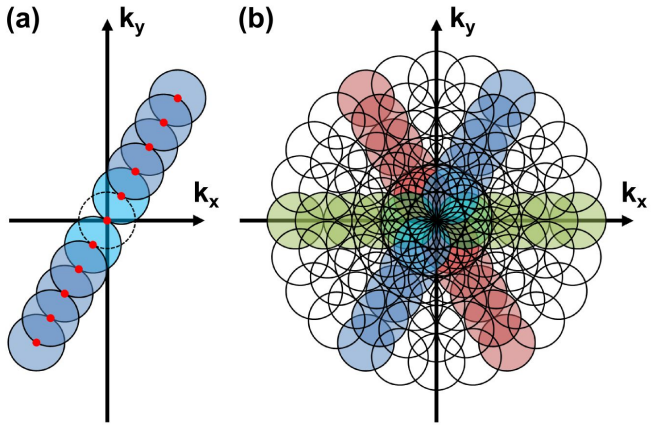

FIGURE A.4: (a) Fourier components of non-linear 2D-sIM intensity pattern (red dots), additional frequency components accessible to linear SIM (light blue circles) and NL-SIM (dark blue circles). (b) Fourier space accessible with 3 rotations of non-linear illumination (coloured circles) showing necessity for many more rotations (12 rotations shown). Figure adapted with permission from [100].

Fourier transform of the illumination. These harmonics enable Moiré fringes from even higher spatial frequencies of the sample to become visible to the microscope.

A number of non-linear responses have been utilised to demonstrate non-linear SIM (NL-SIM), most notably fluorophore saturation [100, 101] and the use of photoswitchable fluorophores [102–104]. Multi-photon excitation (nPE) fluorescence also yields a non-linear fluorophore response, for example 2-photon excitation (2PE) fluorescence is proportional to the square of the illumination intensity and so can produce a strong second harmonic, 2ν. However, the harmonics of nPE techniques for NL-SIM are misleading as the illumination wavelength is longer than the equivalent single-photon excitation (1PE) wavelength (2 times longer for the case of 2PE) and this negates some of the improvement. nPE fluorescence techniques have been successfully utilised for NL-SIM through combination with temporal focusing [256, 257] although only a 2 times enhancement of the resolution can be achieved with the second harmonic rather than 3 times which would be achieved with 1PE.

In theory, NL-SIM can give unlimited resolution providing enough harmonics of the grating can be generated [100]. The limiting factor becomes one of practical considerations, as the number of illumination phases required to separate and restore each Fourier components to its correct location increases with the number of harmonics and

the number of pattern rotations required to fill the lateral plane also increases. To further extend this to 3D-SIM necessitates the acquisition of even more images. The large number of image acquisitions required to compute a super-resolved image places great strain of the fluorophore, which must not become photobleached over the acquisition of a single super-resolved image. As such, only NL-SIM utilising the first 2 or 3 harmonics of the illumination pattern has been viable for biological samples.

Appendix B

Use of the Nikon N-SIM structured illumination microscope

This Appendix describes the basic operation of the Nikon N-SIM structured illumination microscope which is used in Chapters 7 and 8. The N-SIM microscope is controlled through Nikon NIS-Elements Advanced Research software.

B.1 Sample preparation

In order to achieve a good image with SIM, consideration must be given to the sample preparation prior to imaging.

The Nikon N-SIM has 3 illumination wavelengths (405nm, 488nm, and 561nm) and so is suitable for imaging most blue, green, and red fluorophores but care must be taken when choosing fluorophores to minimise cross-talk between spectral channels.

The periodic illumination is produced by a fixed diffraction grating and is designed for use with a single objective lens (Nikon, Plan Apo TIRF 100x/1.49 Oil DIC H N2). The lateral resolution of SIM with this objective is expected to be approximately $100-120$nm (wavelength dependent) and the FOV is limited to a region approximately $30 \times 30\,\mu\mathrm{m}^2$. These factors must be considered when designing an experiment and preparing a sample, the features of interest must be resolvable and must be sufficiently contained within the FOV.

Temporal resolution is another key factor: the N-SIM can achieve temporal resolution of approximately 1 2D SR image (9-15 acquired frames) in 1s in one colour channel. Switching to a different colour channel requires mechanical changes in the microscope

and introduces a significant delay. Multi-colour acquisition is therefore much slower and not suitable for high frame-rate timelapse studies.

The microscope objective requires calibration for the thickness of coverslip in order to minimise spherical aberration (see Appendix B.2.2). In order to maintain a valid calibration, the same thickness of coverslip should be used. No. 1.5 thickness coverslips are recommended although the thickness, specified as $170\,\mu\mathrm{m}$, typically ranges from $140 - 200\,\mu\mathrm{m}$. As such, coverslips must be sized before use and only those with thickness of $(170 \pm 10)\,\mu\mathrm{m}$ should be used. Alternatively, coverslips with tighter tolerances can be bought. Coverslips should be clean and only fresh immersion oil should be used to place these on the objective lens. Nikon recommends Nikon brand Type NF immersion oil for SIM as this has low autofluorescence and minimises chromatic aberration.

Slides should be mounted level and rigidly on the microscope to minimise sample drift.

B.2 N-SIM calibration

The microscope must be calibrated for optimal performance. There are three major steps to fully calibrate the N-SIM for imaging.

B.2.1 Optical fibre axis alignment

The first step is to align the optical fibre that delivers illumination into the microscope body. The SIM illumination is performed by a MM fibre coupled laser bank which illuminates a diffraction grating and is subsequently imaged into the sample via the microscope objective lens.

The lateral and axial position of the output facet of the MM fibre can be adjusted by micrometre accuracy positioning screws. This is aligned as follows:

- The SIM objective lens height is adjusted to form an in-focus image of a sample. This position is fixed, the sample is removed and the objective cleaned.
- The condenser lens on the illumination pillar is removed and a target mounted on the illumination pillar of the microscope is switched to the active position.

- Without adjusting its height, the objective turret is rotated to an empty position.
- The SIM grating block is removed from its housing.
- The "Widefield" imaging option is selected in the N-SIM panel within the Elements software and "Live" acquisition is selected.
- The fibre positioning screws are adjusted until the beam is a sharply focused circle, centred on the target.
- The previous two steps are then repeated with the grating block replaced. Small adjustments only should be required.
- The SIM objective lens is then reselected with the objective turret and the beam re-centred on the target. Small adjustments only should be required.

The fibre is then aligned.

B.2.2 Correction collar adjustment

The SIM objective lens features an adjustable correction collar to correct for spherical aberration due to the refractive index mismatch between the coverslip and the sample medium. The correction collar must be adjusted for a particular thickness of coverslip.

The following procedure is used to determine the optimal position of the correction collar:

- A dilute sample of 100nm fluorescent beads is prepared and allowed to settle and adhere to the coverslip prior to imaging.
- The correction collar is set to one particular position (labelled 0.13-0.19 on the objective casing) and the bead sample is adjusted to best focus.
- The laser intensity and camera integration time are adjusted to give suitable signal.
- A $10\,\mu\mathrm{m}$ z-stack is acquired around the focal position to measure the 3D PSF of the microscope (see Fig. B.1)
- The above is repeated for all correction collar positions.

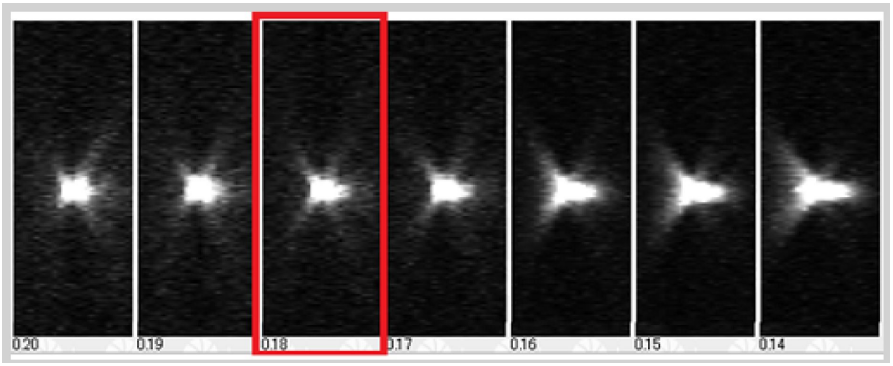

FIGURE B.1: N-SIM correction collar adjustment. 3D PSFs acquired as described in the main text for different correction collar positions (labelled under each PSF). The most symmetric PSF is highlighted. Position 0.18 is the optimal correction collar position in this case. Figure taken from the Nikon N-SIM operation manual (ver. 2.8).

- The acquired PSFs are compared and the correction collar position giving the most symmetric PSF is selected as the optimal.

A Wizard in the Elements software guides the user through the above procedure.

B.2.3 Grating focus adjustment

It is now necessary to align the focal plane of the structured illumination grid with the focal plane of the microscope to ensure the best contrast. This is achieved by adjusting the position of the SIM grating block.

The offset of structured illumination grid and image planes is determined as follows:

- Use the same sparse bead sample as for the correction collar adjustment.
- Adjust to the best focus.
- Using the 'Correction Ring Navi' Wizard, start a 1D-SIM z-stack acquisition around the focal plane.
- Select an isolated beam in the image stack, the software automatically plots the axial profile to determine the bead position and therefore image plane position (see Fig. B.2).
- The SIM grating position is then moved by piezo to match the image plane.

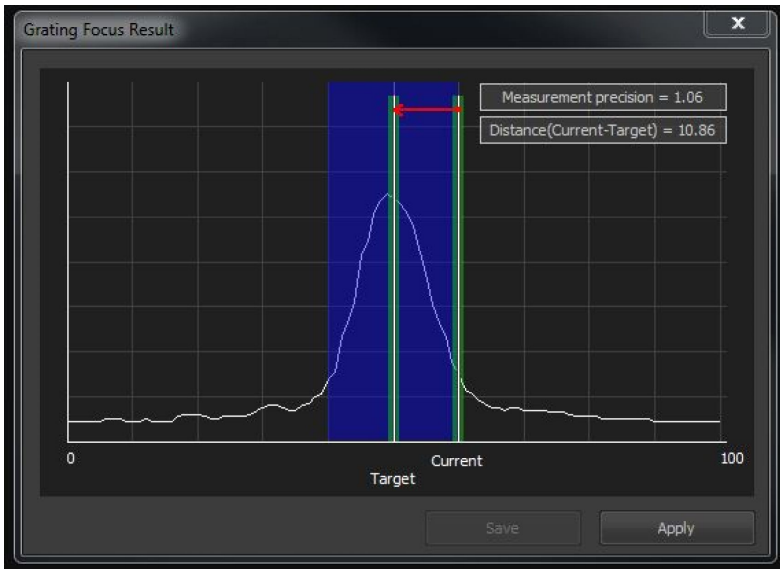

FIGURE B.2: N-SIM grating focus adjustment. Axial PSF of isolated 100nm fluorescent bead. Green vertical lines indicate current and new grating focus positions, at the start and end of the arrow respectively. The blue shaded area indicates the range of the grating piezo. The new grating position is the peak of the axial profile as determined from a fitted model to the data. Figure taken from the Nikon N-SIM operation manual (ver. 2.8).

B.3 Image acquisition

Prior to starting a SIM image acquisition, the illumination intensity and camera exposure must be set appropriately. As individual image frames are combined to yield a SR image, the signal must be within the linear range of the camera (EMCCD; Andor iXon+). The camera has a 14-bit dynamic range, giving 16384 quantised values. The camera is linear with incident intensity up to a signal of about 4000 and the illumination intensity and exposure time must be set to produce a maximal signal within this range. Signal levels above this could produce artefacts in the reconstructed images and signal significantly lower than this will have low SNR.

Once set for all colour channels, the order of acquisition can be set. 6-dimensional (6D) image stacks can be acquired, $I(x, y, z, \lambda, t, r)$, where x, y, and z are the standard microscope coordinates, λ is the wavelength channel, t is time, and r is a positional offset in the lateral plane allowing for multiple ROIs to be imaged. The acquisition parameters and order are set and acquired automatically.

Images can be acquired in a standard widefield epi-fluorescence mode, or with 2D-

and 3D-SIM modalities. Multiple imaging modes cannot be combined as part of the same imaging sequence. For example, it is not possible to set a timelapse experiment where a 3D-SIM image is acquired for the green channel while a widefield image is acquired for the red channel at each corresponding time-point. Figure B.3 shows a 3-colour image of a test slide (Invitrogen, FluoCells Prepared Slide No. 1) acquired with standard epi-fluorescnece (Fig. B.3(a)) and 3D-SIM (Fig. B.3(b) and B.3(c)).

B.4 Image reconstruction

There is some control given over the parameters used for reconstruction of a SR image from recorded raw data.

3D-SIM z-stacks allow processing of the entire z-stack as a related dataset, utilising a "pre-deconvolution" step which reduces the influence of out-of-focus signal from other $z-$planes on the reconstruction algorithm. The reconstruction algorithm has two parameters that can be varied. The "Illumination modulation contrast" which influences the shape of the MTF of the microscope. This can be set to "auto" which fits a function to the MTF from experimental data. Figures B.3(d-f) shows the effect of varying the illumination modulation contrast. Additionally, "High resolution noise suppression" can be set. This controls pixel noise but can also smooth out high resolution features in the image. Figures B.3(d-f) shows the effect of varying the high resolution noise suppression.

Figure B.3 shows that there is little effect on the image by changing the illumination modulation contrast, more extreme values may show changes in image quality but 'Auto' was used most commonly. The high resolution noise suppression has the most significant effect on data. In Fig. B.3(g) the image contains more single pixel variations whereas in Fig. B.3(i) these variation are not present but the high resolution features appear slightly blurred. $N = 1.00$ was used for the majority of SIM reconstructions.

In 2D-SIM mode, there is no "pre-deconvolution" step and each image plane is processed separately. There is an additional parameter, "Out of focus blur suppression" which suppresses low frequency features similarly to the high resolution noise suppression parameter.

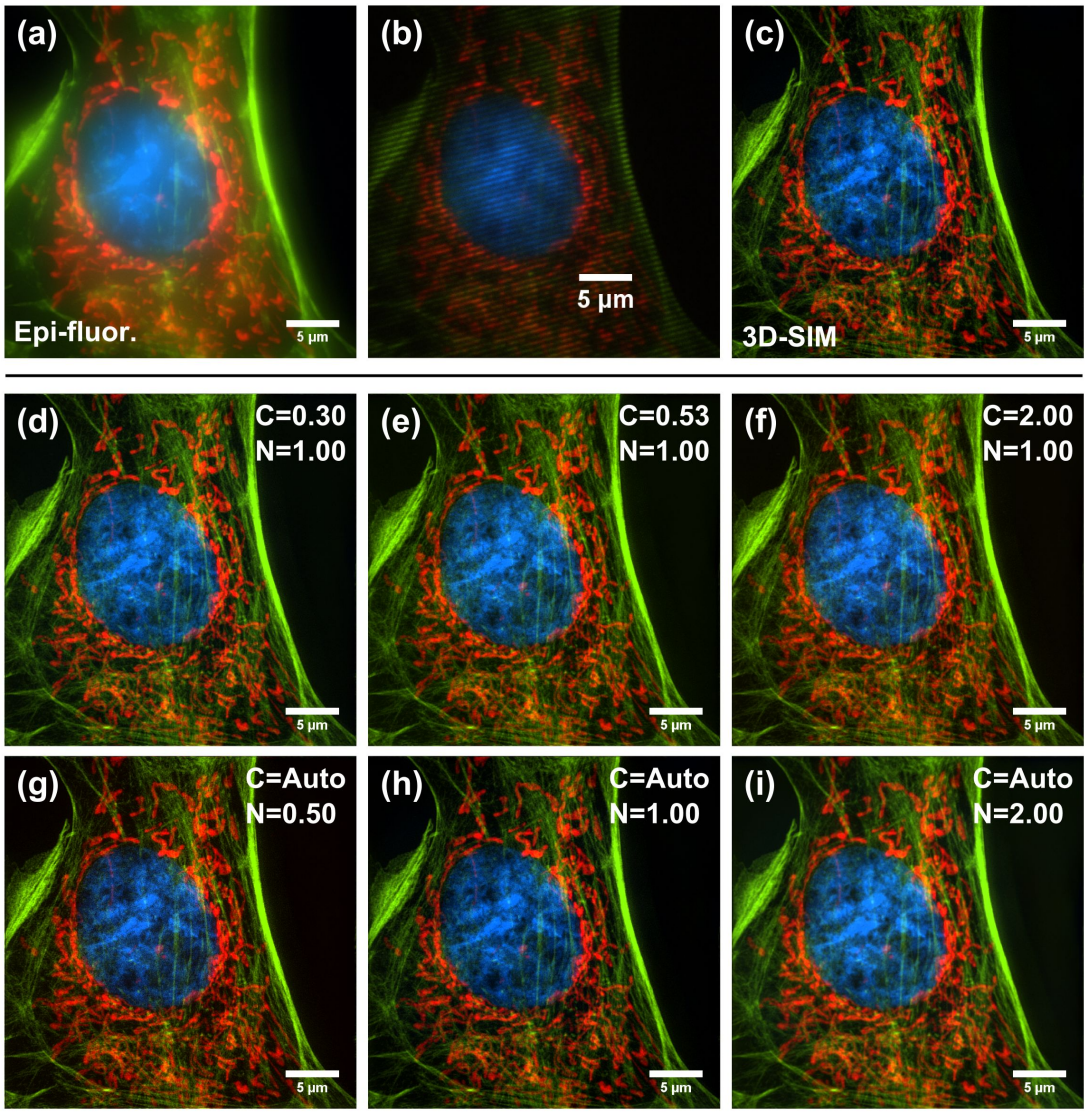

FIGURE B.3: Effect of varying reconstruction parameters on SIM image. Epi-fluorescence (a), recorded 3D-SIM raw data (b), and reconstructed 3D-SIM (c) images of BPAE cells (Invitrogen, FluoCells Prepared Slide No. 1) showing actin filaments (green), mitochondria (red), and DNA (blue). The modulation contrast parameter, C, is varied in the middle row; (d) $C = 0.30$, (e) $C = 0.53$, and (f) $C = 2.00$. The high resolution noise suppression parameter, N, is varied in the bottom row; (g) $N = 0.50$, (h) $N = 1.00$, and (i) $N = 2.00$. In (c), $C =$ Auto, $N = 1.00$.

Appendix C

Addressing a spatial light modulator

This Appendix describes how pupil function engineering can be achieved using a spatial light modulator (SLM) and related principles which are used to simulate the profile of a beam.

C.1 Complex field manipulation with phase only control

The SLM is a square array of liquid crystal cells, each of which can apply a phase delay to a small region of the incident light field. By control of the phase delay at each pixel, the phase profile of the beam can be controlled.

Phase control gives some freedom, but restricts access to some beams types. Additionally, the modulation efficiency of an SLM is never 100% as this will depend on the fill-factor of the device. The practically achieved modulated beam will contain the super-position of the desired modulation and an unmodulated beam. This will result in inconsistencies in the beam profile.

Complex (amplitude and phase) modulation of the field can be achieved by modulating the desired profile with a blazed grating. The desired modulation is then achieved in the first-diffracted order with 100% modulation efficiency (of the light within the first-order).

The phase profile to create a blazed grating has the form:

$$M_{blazed}(u, v) = \exp[2\pi i(T_u \cdot u + T_v \cdot v)] \tag{C.1}$$

where (u, v) are normalised pupil coordinates zero-centred on the SLM active region, T_u and T_v scale the frequency of the grating along the $u-$ and $v-$axes respectively.

Amplitude modulation is achieved by turning off different spatial regions of the blazed grating.

An apodization function allows the effective NA of the illumination to be controlled.

$$M_{apodization}(u,v) = H(1 - \sqrt{u^2 + v^2}) \tag{C.2}$$

where H is the Heaviside step function.

The same principle enables the generation of a Bessel beam by applying the apodization function:

$$M_{Bessel}(u,v) = H(1 - \sqrt{u^2 + v^2})H(\sqrt{u^2 + v^2} - 1 + \beta) \tag{C.3}$$

Wavefront correction was also performed to correct for aberrations in the optical train to ensure experimental results were as close to theoretical predictions as possible, this was achieved using the method described by Čižmár, Mazilu, and Dholakia [194]. Once the correction mask, $M_{wavcorr}$, was determined it was additionally modulated on the SLM profile.

The full profile displayed on the SLM was the phase component of the product of the blazed grating, apodization, wavefront correction, and the desired modulation:

$$M_{SLM}(u,v) = M_{apodization}(u,v) \cdot M_{blazed}(u,v) \cdot M_{wavcorr}(u,v) \cdot M_{desired}(u,v) \tag{C.4}$$

Figure C.1 shows examples of the masks described above to be displayed on a 600×600 pixel area of a 800×600 pixel SLM (Hamamatsu, LCOS X10468-04), corresponding to a maximum effective NA of the SLM of 0.6. Figure C.1(g-i) displays the full phase profiles to yield Gaussian, Bessel10, and Airy7 beams with $\mathrm{NA} = 0.42$ as used in Chapter 4.

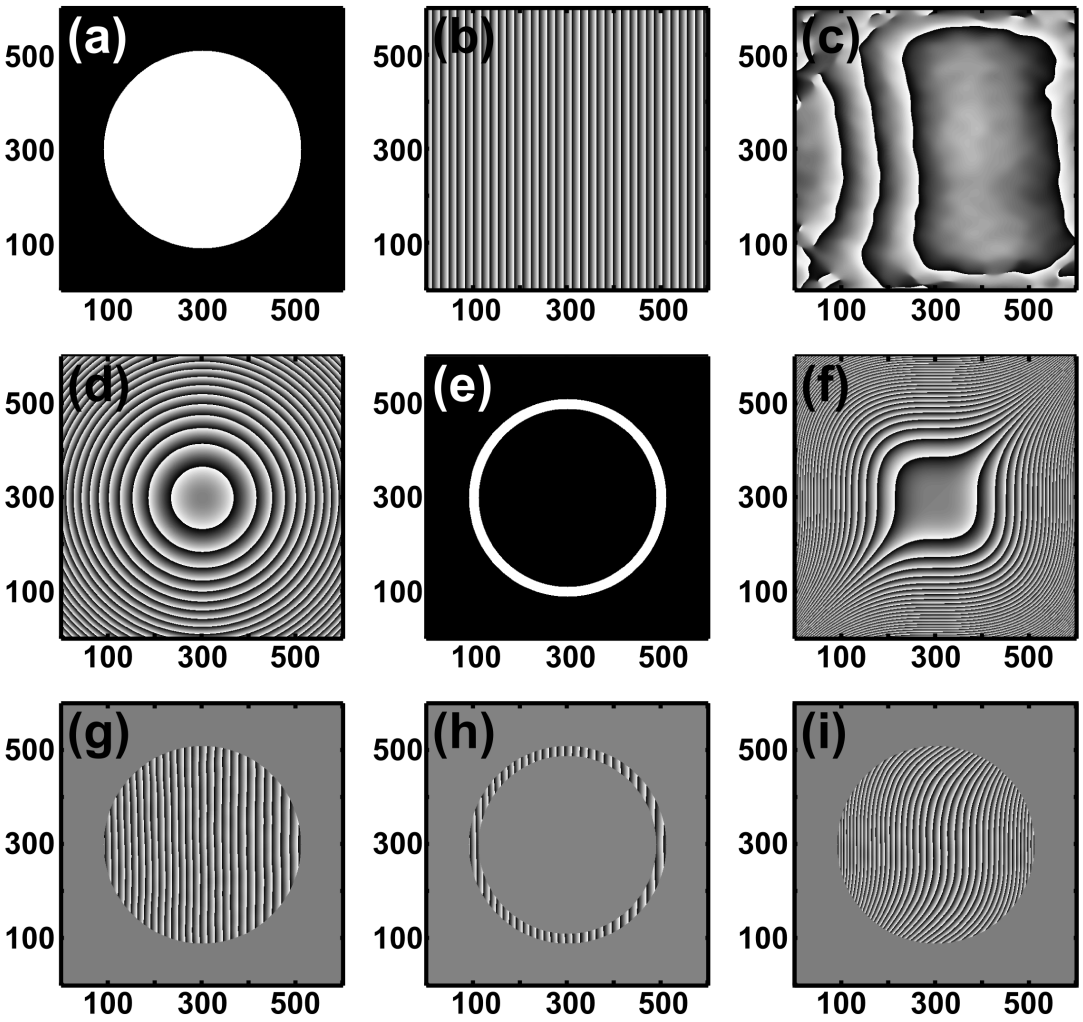

FIGURE C.1: SLM profiles for complex field modulation. Various amplitude-only (a,e; range: $0:1$), phase-only (b,c,d,f; range: $0:2\pi$), and complex (g,h,i; range: $0:2\pi$) field profiles using a 600×600 pixel area of a 800×600 pixel SLM. (a) apodization mask corresponding to $\mathrm{NA}=0.42$, (b) blazed grating with $T_u=10$, $T_v=0$, (c) wavefront correction phase mask for systematic aberrations, (d) defocusing phase mask with $d=5$, (e) Bessel ring apodization with $\beta=0.1$, (f) Airy cubic phase mask with $\alpha=7$, (g) full Gaussian mask, product of (a,b,c), (h) full Bessel10 mask, product of (a,b,c,e), and (i) full Airy7 mask, product of (a,b,c,f).

C.2 Simulating beam profiles from pupil functions

The desired pupil functions described above and elsewhere in this Thesis were used to simulate 3D beam profiles.

The electric field distribution in the sample volume is calculated as the Fourier transform of the electric field distribution in the SLM plane. Only the desired modulation is considered, the SLM is assumed to have 100% modulation efficiency, and there are no systematic aberrations in the optical train. From this, the intensity profile can be determined in the focal plane of the illumination objective lens, $I(x, y, 0)$, where x and y refer to the lateral focal plane of the illumination objective and z is the longitudinal coordinate on the optic axis of the illumination objective.

The intensity distribution in axially offset planes can be determined by applying a defocussing term to the field applied in the SLM plane. The defocus is given by:

$$M_{defocus}(u, v) = \exp[2\pi i d(u^2 + v^2)] \tag{C.5}$$

where d is the defocus parameter, related to the physical axial displacement, z, by:

$$d = z\frac{n}{\lambda}\left(1 - \sqrt{1 - \left(\frac{\mathrm{NA}}{n}\right)^2}\right) \tag{C.6}$$

$M_{defocus}(u, v)$ is shown in Fig. C.1(d) for $d = 5$. Repeated calculation with different d allows the full 3D intensity profile of the beam, $I(x, y, z)$, to be determined.

Appendix D

Derivation of light-sheet properties

This Appendix derives expressions for the axial resolution and FOV of single-photon excitation Gaussian, Bessel, and Airy light-sheet as discussed in Chapter 4.

D.1 Axial resolution and field-of-view with Gaussian illumination

An apertured Gaussian beam will focus to a diffraction limited spot, its MTF is given by:

$$MTF_G(\nu_z) = \frac{2}{\pi}\left(\arccos(\nu_{z,max}) - \nu_z\sqrt{1-\nu_z^2}\right) \tag{D.1}$$

Taking a practical threshold for the noise floor as 5%, the maximum spatial frequency achieved by the Gaussian beam, in normalised coordinates, is $\nu_z = 0.88$. The practically attainable resolution can then be determined from the modified Abbe criteria[1]:

$$r_{x,y} = \frac{\lambda}{2\,\mathrm{NA}\,\nu_{z,max}} \tag{D.2}$$

This yields a maximum attainable axial resolution with the Gaussian beam of $r_G =$ 720nm with the same experimental parameters as used in the simulations described in Chapter 4.2.2.

[1]The modified Abbe criteria is subscripted x, y, referring to the lateral coordinates of the beam. However, due to the light-sheet geometry, this is representative of the axial resolution of the microscope system.

The FOV of the Gaussian beam can be estimated from the axial extent of the Gaussian focal spot given by equation (2.2).

$$FOV_G = 2\frac{2\lambda n}{\mathrm{NA}^2} \tag{D.3}$$

The additional factor 2 in equation (D.3) is due to the symmetric nature of the focal spot and the definition of the axial extent of the spot by equation (2.2) which is from the peak to the first intensity minimum. Therefore the approximate FOV of a Gaussian light-sheet is $FOV_G = 16\,\mu\mathrm{m}$.

D.2 Axial resolution and field-of-view with Bessel illumination

Considering Bessel beam formation as the Fourier transform of a thin annulus [26], with pupil function:

$$P_B(\boldsymbol{u_r}) = \frac{1}{\sqrt{\pi\beta(2-\beta)}} H(1-\boldsymbol{u_r})H(\boldsymbol{u_r}-1+\beta) \tag{D.4}$$

where $\boldsymbol{u_r}$ is the radial normalised pupil coordinate, H denotes the Heaviside step function, and β is the fractional width of annulus (width of annulus/radius). The first term in equation (D.4) ensures the total beam intensity is unity.

The MTF of the Bessel beam can calculated from the autocorrelation of the pupil function. This is approximated geometrically by:

$$MTF_B(\nu_z) = \frac{\beta}{\nu_z\pi\sqrt{1-\nu_z}(2-\beta)} \tag{D.5}$$

The support (magnitude) of the MTF is dependent on the value of β. Taking a linear approximation of the denominator in ν_z and combining with equation (D.2) using the same 5% threshold as for the Gaussian beam yields the expression:

$$r_B \approx \frac{\lambda}{2\,\mathrm{NA}}\frac{0.05(2-\beta)\pi}{\beta} \tag{D.6}$$

As β is typically small ($\beta \ll 1$), this can be further simplified to:

$$r_B \approx \frac{0.05\pi\lambda}{\mathrm{NA}\,\beta} \tag{D.7}$$

which shows that the achievable resolution with a Bessel beam is approximately inversely proportional to the width of annulus used to form the Bessel beam.

The FOV of the Bessel beam will be given by the propagation range over which constructive interference occurs on axis. By symmetry, at any distance from the illumination objective, rays from a given radial coordinate will interfere constructively on axis. Therefore, the end of this range will occur when destructive interference occurs between rays originating from inner and outer edges of the annulus. This phase difference is given by:

$$\Delta\phi = 2\pi d\beta(2-\beta) \tag{D.8}$$

where d is the defocus parameter (see Appendix C). Again, for small β, this becomes:

$$\Delta\phi \approx 4\pi d\beta \tag{D.9}$$

The defocus parameter is given by:

$$d = x\frac{n}{\lambda}\left(1-\sqrt{1-\left(\frac{\mathrm{NA}}{n}\right)^2}\right) \tag{D.10}$$

where x is the on-axis displacement from the beam waist.

Destructive interference occurs for $\Delta\phi \geq \pi$. Combining with equations (D.9) and (D.10) yields:

$$4\pi x\frac{n}{\lambda}\left(1-\sqrt{1-\left(\frac{\mathrm{NA}}{n}\right)^2}\right)\beta \geq \pi \tag{D.11}$$

The estimated FOV of the Bessel beam is $2x$, rearranging (D.11) gives the expression:

$$FOV_B \approx \frac{\lambda}{2n\beta}\frac{1}{1-\sqrt{1-(\mathrm{NA}/n)^2}} \tag{D.12}$$

Similarly with equation (D.7), the FOV of a Bessel beam depends inversely on the annular width. These relations demonstrate the inherent trade-off that exists when using a Bessel beam for light-sheet illumination, increasing the FOV inherently reduces the resolution and *vice versa*. The trade-off with Bessel illumination is less restrictive than for Gaussian illumination, doubling r_G will quarter FOV_G as this scales with NA^{-2} whereas doubling r_B can be achieved simply by varying β and will only half FOV_B as this scales with β^{-1}.

Two Bessel beams were chosen to demonstrate this trade-off. In order that relatively good axial resolution was still achievable, and to ensure sufficient power could be transmitted into the sample, β was kept fairly large. Bessel5 and Bessel10 refer, respectively, to Bessel beams with an annular width of 5% and 10%. Their achievable axial resolution and FOV are summarised in Table D.1.

Beam type	**Bessel10**	**Bessel5**
$\boldsymbol{r_B}$ **[µm]**	1.99	3.98
$\boldsymbol{FOV_B}$ **[µm]**	39.1	78.2

TABLE D.1: Analytical Bessel light-sheet resolution and field-of-view or selected β.

D.3 Axial resolution and field-of-view with Airy illumination

An Airy beam may be formed from the pupil function:

$$P_A(u,v) = \frac{H(1-\boldsymbol{u_r})}{\sqrt{\pi}} \exp[2\pi i\alpha(u^3+v^3)] \tag{D.13}$$

where u and v are normalised pupil coordinates corresponding to the z- and y-axes respectively, $\boldsymbol{u_r} = (u^2+v^2)^{1/2}$, and α is the strength of the cubic modulation.

The MTF of the Airy beam oscillates strongly for large α but can be approximated using the stationary phase approximation [191] as:

$$MTF_A(\nu_z) = \frac{1}{\sqrt{48|\alpha\nu_z|}} \tag{D.14}$$

Taking a 5% threshold of the Airy MTF and substituting into equation (D.2) yields an achievable resolution of:

$$r_A = 0.12\alpha\frac{\lambda}{2\,\mathrm{NA}} \tag{D.15}$$

From equation (D.15), it would appear that super-resolution information, beyond the diffraction limit can be achieved with the Airy beam as for $\alpha < 8.33$, r_A will be smaller than $\lambda/2\,\mathrm{NA}$. However, equation (D.15) is based on an approximation of the Airy MTF, for example setting $\alpha = 0$ produces a Gaussian beam but with infinite resolution which is clearly wrong. For $\nu_z \to 0$ or $\nu_z \to 1$ (as is the case when considering the resolution limit) the Gaussian MTF is a more valid approximation. Therefore, what is correctly inferred from equation (D.15) is that the resolution achieved by an Airy beam is diffraction limited for $\alpha \leq 8.33$. For $\alpha > 8.33$, an increase in α will result in a decrease in resolution.

To determine the FOV of the Airy beam, the propagation range over which the Airy beam "core" (lobe of maximum intensity) exists. Due to the nature of the Airy beam, a different approach is required to that taken for the Bessel beam. Consider the full pupil function of the Airy beam including defocus:

$$P_A(u, v; d) = \frac{H(1 - \boldsymbol{u_r})}{\sqrt{\pi}} \exp[2\pi i\alpha(u^3 + v^3)] \exp[2\pi i d\boldsymbol{u_r}^2] \tag{D.16}$$

Shifting the origin of the pupil plane can eliminate the quadratic defocus term. For simplicity, this is shown for the case of a 1D pupil function, $P(u; d)$, using the coordinate shift:

$$u' = u - \frac{d}{3\alpha} \tag{D.17}$$

the total phase profile across the pupil becomes:

$$\alpha u^3 - du^2 = \alpha u'^3 - \left(\frac{d^2}{3\alpha}\right)u' - \frac{2d^3}{27\alpha^2} \tag{D.18}$$

As equation (D.18) shows, there is no quadratic term in u' after the origin shift.

The intensity distribution near the "focus" of the Airy beam depends mainly on the pupil phase near the origin as rapid phase shifts, which occur far from the origin due to the cubic nature of the pupil phase profile, are cancelled out by destructive interference. Therefore the axial extent of the Airy beam can be estimated by considering the defocus at which the shifted origin lies at the edge of the pupil aperture, *i.e.* when $d = 3\alpha$. Combining with equation (D.10) to relate d to the physical beam displacement results in a FOV for the Airy beam of:

$$FOV_A = \frac{6\alpha\lambda}{n} \frac{1}{1 - \sqrt{1 - (\mathrm{NA}/n)^2}} \tag{D.19}$$

Table D.2 summarises the achievable resolution and FOV for Airy beams with various α-values.

$\boldsymbol{\alpha}$	2.5	5	10	20
$\boldsymbol{r_A}$ **[µm]**	0.72	0.72	0.76	1.52
$\boldsymbol{FOV_A}$ **[µm]**	117.3	234.5	469.0	938.0

TABLE D.2: Analytical Airy light-sheet resolution and field-of-view for selected α.

Table D.2 shows the non-linear nature of the resolution/FOV trade-off for Airy beams. For low values of α, there is no loss in resolution when increasing the FOV, when increasing α beyond 8.33, there is a slight reduction in resolution when the FOV is increased, and for large α, the resolution decreases inversely with the increase in FOV, the same as for the Bessel beam.

Appendix E

Theory of principal component analysis for image filtering

This Appendix summarises the theoretical underpinning of PCA, as used for image filtering in Chapter 8.

The spatial covariance matrix of a movie, M, is defined as:

$$C_{ij} = \sum_{n} \sum_{m} M^{i}_{nm} M^{j}_{nm} \tag{E.1}$$

where M^{i}_{nm} corresponds to the value of the n^{th} pixel in the m^{th} row of the i^{th} frame of a movie. This covariance matrix is symmetric, positive, and semi-definite. It describes the correlations between frames i and j of the movie. The covariance matrix can be represented by an eigenvector decomposition with real, positive eigenvalues as:

$$\lambda^{(k)} V^{(k)}_{i} = \sum_{j} C_{ij} V^{(k)}_{j} \tag{E.2}$$

where $V^{(k)}_{i}$ is the k^{th} eigenvector with corresponding eigenvalue, $\lambda^{(k)}$. The eigenvectors form an orthonormal basis. The eigenvectors and their eigenvalues are ordered by magnitude of eigenvalue, starting with the largest eigenvalue and decreasing. The first eigenvector corresponds to the fist principal component (PC). The k^{th} PC, as defined in the image space, is given by:

$$M^{(k)}_{nm} = \frac{1}{\sqrt{\lambda^{(k)}}} \sum_{i} M^{i}_{nm} V^{(k)}_{i} \tag{E.3}$$

The adaptive filter projects each frame onto the PCs, determining the coefficient, c_k^i, for how much the k^{th} PC describes the i^{th} frame:

$$c_k^i = \sum_n \sum_m M_{nm}^i M_{nm}^{(k)} \tag{E.4}$$

The inverse process is then performed to recompose the frames using only the relevant PCs, giving the filtered frames, $\tilde{M}_{nm}^i$:

$$\tilde{M}_{nm}^i = \sum_{k=1}^{k_{max}} c_k^i M_{nm}^{(k)} \tag{E.5}$$

where k_{max} defines the last PC which contains relevant information on the motion of the particle.

Appendix F

Protocols: Sample preparations

This Appendix contains details of how samples used in experiments throughout this Thesis were prepared.

F.1 Sample preparations for experiments presented in Chapter 4: Light-sheet microscopy using an Airy beam

F.1.1 Amphioxus muscle block

A juvenile amphioxus (*Branchiostoma lanceolatum*, gender not determinable at age) was humanely killed by an overdose of ethyl 3-aminobenzoate methanesulfonate (Sigma, MS-222) and was fixed in 4% (w/v) paraformaldehyde (PFA) in MOPS buffer (0.5M NaCl, 2mM $MGSO_4$, 1mM EGTA, 0.1M morpholinopropanesulfonic acid buffer, pH 7.5) for 1 h at room temperature and then washed three times in PBT (1x phosphate buffered saline (PBS) solution, 0.1% Triton X-100). The 'skin' of the amphioxus was peeled off. The specimen was permeasbilised in PBT for 1 h at room temperature (RT). A ribonuclease (RNase) treatment was then performed, consisting of a brief wash in 2x SSC (0.3M NaCl, 0.03M sodium citrate, pH 7.0) followed by incubation with $100\mu g/mL$ deoxyribonuclease-free (DNase-free) RNase A (Promega) in 2x SSC for 20 min at $37°C$ and three washes with 2x SSC. Non-specific binding sites were blocked with 5% normal goat serum (NGS), 1.5% bovine serum albumin (BSA), 0.1% Triton X-100 in PBS solution (0.01M PBS, 0.0027 M KCl and 0.137 M NaCl, pH 7.4) for 1 h at RT. For visualisation of actin filaments, the specimen was stained overnight at $4°C$ under continuous agitation with Alexa Fluor 488 Phalloidin (Invitrogen) diliuted 1:40 (v/v) in 1.5% BSA,

0.1% Triton X-100 PBS. After a brief wash in 2x SSC, the sample was immersed in a 1:1650 (v/v) dilution of propidium iodide (PI; Invitrogen) in 2x SSC for 15 min at RT for nuclear counterstaining. The sample was then rinsed several times in 2x SSC and embedded in 1% low-melting point (LMP) agarose (Peqlab, peq-GOLD) on the sample mount and allowed to set for 10 min. before imaging.

F.1.2 Photobleaching study sample

Homogeneously fluorescent samples were prepared by embedding Cy3-streptavidin (Invitrogen) at a high concentration within a polyacrylamide (PAA) gel matrix. The pore size of the gel matrix is believed to isolate the Cy3-streptavidin in the sample volume, preventing diffusion of the fluorophores.

A solution of 15% acrylamide in 1x Tris-borate-EDTA buffer was mixed in a 1:1 ratio with Cy3-streptavidin in buffer yielding a final concentration of 10µM. 0.7% 1x Ammonium persulfate (Sigma; APS) and 0.07% 1x TEMED (Sigma) was added to cause polymerisation of the acrylamide for formation of the PAA matrix and left overnight to set.

F.2 Sample preparations for experiments presented in Chapter 5: Application of Airy light-sheet microscopy to imaging in turbid tissue

All animal experiments were reviewed and approved by the University of St Andrews Animal Ethics and Welfare Committee under Dr Javier Tello's Home Office Project License 70/7924. All *in vivo* experiments were performed by Dr Javier Tello and Ms Sanya Aggarwal only.

F.2.1 Viral infusion *in vivo*

Adult female heterozygous mice (*Kiss1*$^{tm1.1(cre/EGFP)Stei}$) were anaesthetised with isofluorane, and adenoassociated viral particles (AAV; AAV1/2-Ef1a-DIO-mCherry-wPRE; 1.75×10^{11}gc/ml were injected bilaterally into the hypothalamic arcurate nucleus using stereotactic guidance (coordinates: AP -1.6, ML ± 0.3, DV -5.9) with a pulled glass

pipette and pressure injection at a volume of 400nL/side, at a rate of 75nL/min. After surgery, mice were returned to their cages and tissue was collected after 3 weeks to allow for AAV activation. Mice were culled by deep anaesthetisation with an overdose of sodium pentobarbital (100mg/kg) and transcardially perfused with 0.1M PBS (pH 7.4) followed by 4% PFA in PBS (pH 7.4). Brains were post-fixed overnight in 4% PFA in PBS and subsequently cryopreserved in 30% sucrose in 0.1M PBS. The brains were sectioned using a Compresstome vibratome (Precisionary Instrucments VF-300) at a thickness of 400 µm.

F.2.2 Fluorescent bead infusion *in vivo*

Adult female heterozygous mice (*Kiss1*$^{tm1.1(cre/EGFP)Stei}$) were anaesthetised with isofluorane, and fluorescent beads (Duke Scientific R600, 600nm diameter polystyrene, red fluorescence), diluted 1:50 in PBS, were injected bilaterally into the hypothalamic arcurate nucleus using stereotactic guidance (coordinates: AP -1.6, ML ± 0.3, DV -5.9) with a pulled glass pipette and pressure injection at a volume of 500nL/side, at a rate of 75nL/min. Mice were culled 2h following bead injection and post-fixed as described above.

F.2.3 Tissue clearing with TDE

Tissue sections were optically cleared using TDE as described by Constantini *et al* in the section, "Optical clearing with TDE" [200]. This is described below.

Tissue sections were cleared with serial incubations in 10mL of 20% and 47% (v/v) 2,2'-thiodiethanol (TDE) in 0.01M PBS, each for 1h at 37°C under continuous agitation.

Optically cleared tissue sections were embedded in 1% LMP agarose gel made with 47% TDE/PBS buffer and immersed in 47% TDE/PBS during imaging.

F.3 Sample preparations for experiments presented in Chapter 6: Advanced beam shaping strategies for Airy light-sheet microscopy

F.3.1 Zebrafish larva

A 14 days post fertilisation (14-dpf) zebrafish larva (*Danio rerio*, gender not determinable at age) was humanely killed by an overdose of ethyl 3-aminobenzoate methane sulfonate (Sigma, MS-222). Schedule 1 techniques were used in compliance with the Animals (Scientific Procedures) Act regulations and are authorised by the Animal Welfare and Ethics Committee of the University of St Andrews. The zebrafish was then fixed in 4% (w/v) PFA in PBS overnight at $4°$C. The tissue was then permeabilised by washing three times in PBT (1x PBS, 0.1% Triton X-100). Muscle fibres were visualised by staining actin filaments with Alexa Fluor 555 Phalloidin (Invitrogen). The zebrafish larva was stained overnight under continuous agitation with Alexa FLuor 555 Phalloidin diluted 1:100 (v/v) in PBT. The specimen was then rinsed three times in PBT and embedded in 1.5% LMP agarose within a poly(ethylene) (PE) tube and allowed to set for 10 min. before imaging.

F.4 Sample preparations for experiments presented in Chapter 7: Structured illumination microscopy for diagnosis of nephrotic disease

F.4.1 Preparation of kidney tissue for SIM

Tissue sections were prepared for imaging by SIM using standard indirect immunofluorescence staining. Sections of $5\,\mu\mathrm{m}$ thickness were cut from the frozen tissue block using a Tissue-Tek Cryo3 Microtome/Cryostat (Sakura Finetek, 5805) and mounted on Colorfrost Plus Slides (Thermo Fisher Scientific, 12-550-17). Sections were warmed to room temperature, washed twice for 1 min. with phosphate buffered saline (PBS, Becton Dickinson and Company, B11248), then fixed for 10 min. in freshly made 2%

paraformaldehyde (PFA; Electron Microscopy Sciences, Prill's form, 19200) in Dulbecco's PBS (pH 7.4; Life Technologies, 14200-075). The sections were washed a further three times in PBS for 1 min. each, permeabilised in 0.2% Triton X-100 in PBS (Sigma-Aldrich, T9284) for 20 min., and washed three more times in PBS. Sections were then incubated in wash buffer (0.05% Tween 20 in PBS; Dako, S1966) supplemented with 1% bovine serum albumin (BSA; Jackson ImmunoReseach Labs, 001-000-162) for 5 min. then blocked for 20 min. at room temperature with 5% normal goat serum (Vector Labs, S1000) in antibody diluent (Life Technologies, 003218) with 1% BSA. Slides were incubated for 30 min. with 100μL per slide of rabbit polyclonal anti-podocin antibody (Sigma-Aldrich, P0372) diluted 1:500 in antibody diluent with 1% BSA, washed 3 times in wash buffer, incubated for a further 30 min. with fluorescein isothiocyanate (FITC)-conjugated goat anti-rabbit antibody (Sigma-Aldrich, F0382), and washed three more times with wash buffer. Coverslips (24 x 50mm) were then added with Vectashield anti-fade mounting medium with DAPI (Vector Labs, H-1200) and sealed with nail varnish to prevent dying of the sample.

F.4.2 Preparation of kidney tissue for TEM

For comparison with SIM images, TEM images of kidney biopsies were taken as part of routine diagnosis processed by standard EM preparation and imaging methods [224]. Briefly, biopsy tissue of $1-2$mm maximal dimension were fixed in cacodylate-buffered 4% formaldehyde-2.5% glutarahyde solution for at least 1 hour, postfixed in 1% osmium tetroxide, dehydrated with aqueous ethanol solutions and acetonitrile, and embedded in Araldite-Epon resin. Thin sections (100nm) of the embedded tissue were cut using an ultramicrotome (Leica, Ultracut), then mounted on 3mm copper grids, stained with 1% uranyl acetate-lead citrate, and imaged with a JEOL 1400 TEM equipped with a side-mounted CCD (GATAN, 785 ES1000W) at magnifications between $1000-20000$x.

F.5 Sample preparations for experiments presented in Chapter 8: Integrated optical trapping and microscopy

F.5.1 B3Z T-cell hybridoma

B3Z cells were cultured in suspension using Dulbecco's modified Eagle's medium (DMEM) supplemented with 10% fetal calf serum (FCS) and the antibiotics penicillin (100units/mL) and streptomycin (100mg/mL) at $37°$C in a humidified atmosphere of 5% CO_2 in air. Prior to the experiment, cells were pelleted, washed in fresh medium and loaded with the calcium indicator Fluo-4 (Life Technologies, Fluo-4, AM, cell permeant, F-14201) as per the manufacturer's instructions: Fluo-4 stock solution (1mM Fluo-4 in dimethyl sulfoxide (DMSO)) was mixed in a 1:1 ratio with Pluronic F-127 (20% solution in DMSO, Life Technologies, P-3000MP) and added to the cells at a final concentration of 0.1mM in fresh medium and incubated at $37°$C for 30 minutes. The cells were then washed twice in imaging medium (phenol-red free DMEM supplemented with 2% charcoal stripped FCS (Life Technologies, 12676-011) plus penicillin and streptomycin as above.

Antibody conjugated beads were prepared by passive adsorption of $3.1\,\mu$m polystyrene beads coated with protein G (0.5% (w/v), Spherotech, PGP-30-5) with mouse anti-CD3 (1mg/mL, eBioscience, 16-0032) and anti-CD28 (1mg/mL, eBioscience, 16-0281) antibodies. 2μg of each antibody solution was added to 100μL of the protein G coated bead solution, vortexed, and incubated an room temperature under continuous agitation for 1 hour. The beads were then pelleted and washed 5 times in 1mL of sterile phosphate buffered saline (PBS) and the beads finally resuspended in 3mL sterile PBS.